Measurement of the Local Properties of Multiphase Flows

Nickolaos Panagiotopoulos

A thesis submitted to the University of Huddersfield in partial fulfilment of the requirements for the degree of Doctor of Philosophy

The University of Huddersfield

April 2009

Declaration

No portion of the work referred to in this thesis has been submitted in support of an application for another degree or qualification of this or any other university or other institute of learning.

Acknowledgements

I would like to express my gratitude to my supervisor, Gary Lucas, for giving me the opportunity to carry out this research. I would also like to thank him for his support and advice during the research, and for reading all the draft copies of this thesis. But most of all I would like to thank him for the experience I gained through his scientific expertise, judgemental reasoning, research curiosity, and altering my personality and judgement so I can have the foundations for scientific achievements, and behavioural elegance as an engineer.

I would like to thank my second supervisor, Rakesh Mishra, for the vital and productive conversations we had regarding my research. I would also like to thank him for his essential information given to me and cooperation during the research.

I would like to thank the technicians at the University of Huddersfield for their help in manufacturing, and repairing, the varied equipment that I have needed; and their patience when I was asking them for favours during lunch times. As part of the parallel research program at Leeds University I would like to thank Mi Wang, and the other members of the Process Tomography Unit, for the their help in the experiments carried out on the dual-plane ERT system.

Outside work I would like to acknowledge the moral and materialistic support of my family who I know always meant well even if I didn't show it. Last, but by no means least, I would like to thank Terrie for her almost endless support and patience throughout my research.

I would like to acknowledge the financial assistance of EPSRC (grant no. GR/L59088).

Abstract

Flows of mixed fluids in pipes are frequently encountered in several areas of engineering, such as chemical, petroleum and nuclear. Two key parameters characterising such flows are the local volume fraction distribution and the axial velocity distribution of the dispersed phase. In order to achieve a further understanding of the flow properties, vector velocities are important too. A common intrusive method that is used for acquiring these parameters is the local conductivity probe. The reason is that conductivity probes are more accurate than other measuring techniques, such as ERT (Electrical Resistance Tomography) systems, and are therefore used for the calibration and validation of ERT systems. Also the measurements from conductivity probes show a more representative distribution of volume fraction and velocity of the dispersed phase than other non intrusive methods. They are also useful for validating data produced by CFD (Computed Fluid Dynamics) simulations.

In this thesis, research has been done on designing probes, and improving the related signal processing algorithms, and several experiments have been run in multiphase loops for measuring the local volume fraction and velocity of the dispersed phase in vertical and inclined pipes and in swirling flows. All these attempts have recognised an extra problem that is not negligible when using local conductance probes. This problem is the interaction between the probe and the bubble. It is known that local probes alter the true value of the bubble's vector velocity due to the fact that bubbles are slowed down by the probe.

A number of experiments were performed and a comparison between ERT and local conductivity probes was made. Both techniques gave velocity distributions of the dispersed phase which do not agree, showing that ERT is unable to accurately measure the gas velocity and volume fraction profiles.

Furthermore the current thesis presents results from dual sensor and four sensor local conductivity probes in steady vertical and inclined air-water and oil-water flows and in steady swirling flows, and a proposed new design for fabricating a rotary index dual sensor probe with a new algorithm for the signal processing scheme is given. This new type of conductivity probe has a relatively small frontal area that reduces the bubble-probe interaction hence the probe's effect on the dispersed phase is less that of other types of probe.

Table of Contents

List of figures

List of tables

Nomenclature

A	coefficient that must be obtained from calibration for King's law calibration procedure.
A	voltage when bubble is present (section 2.2.2).
A	the cross-sectional area of the flow.
A_0	voltage when bubble is absent.
a_{max}	the maximum (or the peak value) of the volume fraction in the pipe.
b	geometrical parameter of a system.
B	coefficient that must be obtained from calibration for King's law calibration procedure.
c	celerity in the liquid medium.
c_1	Constant used in chapter 8.
C	an empirical constant.
C_0	the Zuber-Findlay distribution parameter.
d	diameter of a bubble.
d_{SM}	bubble mean diameter.
E	is the output voltage from the bridge.
f	Frequency.
F	the frictional pressure loss.
f	the single-phase friction factor (section 7.3.2).
g	the gravitational constant.
H	Harmonic average.
I	measured photon flux (section 2.1.14).
I	Current.
I_0	initial measured photon flux.
j_l	the local homogeneous velocity.
K	the meter factor for the device (chapter 7).
K	Calibration factor (chapter 9).
K_{hy} K_ε	Constants used in chapter 8.

K_0	a constant of integration.
L	the distance between the transmitter and receiver
M	the hydraulic radius of the flow loop working section.
n	coefficient that must be obtained from calibration for King's law calibration procedure.
n	Exponent used in chapter 8.
N	number of bubbles.
n_c	the refractive index of the continuous phase.
$\hat{n}_v$	the unit vector in the direction of **V.**
p	Exponent in the power law formula for velocity.
$p(s,\theta)$	the measured attenuation that corresponds to a projection of attenuation.
q	Exponent in the power law formula for volume fraction.
Q_d	the dispersed phase volumetric flow rate.
Q_g	gas volumetric flow rate.
Q_w	flowrate of the water.
r	position vector.
Re	Reynolds number.
R_i	the internal radius of the working section.
R_{ref}	Reference resistance.
R_s	Resistance of the water.
s	Distance.
S	sound dispersion.
S_g	the gas conductance.
S_{th}	threshold conductance.
S_w	the water conductance.
T	transmittance (section 2.2.2).
T	sampling period.
t_{1f}	the first time a bubble makes contact with the front sensor.
t_{1r}	the first time a bubble makes contact with the rear sensor.
$t_{2f.}$	the last time a bubble makes contact with the front sensor.

t_{2r}	the last time a bubble makes contact with the rear sensor.
U_{ds}	dispersed phase superficial velocity.
u_{dl}	Local dispersed phase axial velocity.
$\overline{u}_{d,ref}$	Reference value of global mean dispersed phase axial velocity.
$\overline{u}_{d,est}$	Estimated value of global mean dispersed phase axial velocity.
$u_{b,i}$	the velocity of an individual bubble.
u_e	is the fluid velocity.
$\overline{u_{est}}$	Estimated mean gas velocity.
u_{gl}	mean local axial bubble velocity.
$\overline{u_g}$	Mean gas velocity.
$\overline{u_{g,ref}}$	Reference mean gas velocity.
u_{gs}	air superficial velocity.
u_{hy}	Oil droplet velocity in chapter 8.
U_h, u_h	Homogeneous velocity (mixture superficial velocity).
u_L	Local axial liquid velocity used in chapter 8.
u_{t0}	Terminal rise velocity.
u_o	Local oil velocity.
$\overline{u}_{o,probe}$	Mean axial oil velocity in the flow cross section measured by the four sensor probe.
$\overline{u}_{o,ref}$	Reference mean axial oil velocity in flow cross section.
$u_{o,\max}$	Maximum local oil velocity.
u_{os}	Oil Superficial Velocity.
u_r, u_z, u_θ	Radial, axial and azimuthal velocity components.
u_{t0}	the velocity of a single particle of the dispersed phase rising through the static continuous phase.
u_w	Local axial water velocity.
U_{ws} *or* u_{ws}	Water dispersed phase superficial velocity.
V	Velocity vector of the droplet.

v	the magnitude of the vector **V.**
V_a	output voltage from operational amplifier.
V_f	threshold voltage for the front sensor.
V_{in}	Input voltage from sensor.
v_{ref}	Reference of the magnitude of the vector velocity.
v_{meas}	Measured amplitude velocity of the vector velocity.
v_r, v_z, v_θ	Calculated radial, axial and azimuthal velocity components from the four sensor probe.
v_r', v_z', v_θ'	Compensated radial, axial and azimuthal velocity components from the four sensor probe.
V_{out}	Output voltage from circuit.
V_r	threshold voltage for the rear sensor.
V_r	the radial velocity component.
V_{xi}	x-axis velocity.
V_{yi}	y-axis velocity.
V_{zi}	z-axis velocity component of the bubble.
V_θ	the azimuthal velocity component.
α	Local oil or air volume fraction.
$\overline{\alpha}$	Mean volume fraction.
α_A	local interfacial area concentration.
$\overline{\alpha}_{est}$	estimated average volume fraction.
α_l	Local volume fraction.
$\overline{\alpha}_{ref}$	volume fraction reference measurement.
β	the azimuthal angle between the y-axis and the projection of vector **V** onto x-y plane.
β_{meas}	Measured Azimuthal angle of the vector velocity.
β_{ref}	Reference of the Azimuthal angle of the vector velocity.
γ	the polar angle between the z-axis and the vector **V.**
γ_{meas}	Measured polar angle of the vector velocity.
γ_{ref}	Reference of the Polar angle of the vector velocity.

$\delta t_{1,i}$	time intervals of i^{th} bubble for first contact.
$\delta t_{2,i}$	time intervals of i^{th} bubble for last contact.
$\delta t_{min}, \delta t_{max}$	Time delays used in processing probe signals.
ΔP	Pressure drop in the pipe.
$\Delta\Phi$	phase difference between the light signals.
ε	local droplet diffusivity.
$\overline{\varepsilon}_{abs,\gamma}$	mean value of the absolute error for polar angle.
$\overline{\varepsilon}_{abs,\beta}$	mean value of the absolute error for azimuthal angle.
$\overline{\varepsilon}_{v}$	mean percentage error in the measured bubble velocity magnitude.
ε_G	phase volume fraction (gas).
ε_L	phase volume fraction (liquid).
θ	angular position.
λ	the light wavelength.
ρ_G	density of gas.
ρ_L	density of liquid.
$\sigma_{abs,\alpha}$	standard deviation.
τ_w	the wall shear stress.
ψ	pipe inclination angle.

1. Introduction.

The aim of this research is to develop instruments that can measure properties of multiphase flows. Specifically, these properties are the local volume fraction, the local axial velocity, and the local vector velocity of the dispersed phase. Primarily, these instruments were required to be used for validation of other measurement devices. But the extensive research and development on their use make them useful in their own right for investigating flow behaviour in multiphase flows.

Due to the fact that these devices are used in a multiphase flow environment, it is necessary to describe briefly the basic physics behind the multiphase flows. In general, there is a fundamental division between single phase and multiphase flows. In the first case a single substance is flowing. In the second case, several fluids or conceptually similar materials are flowing at the same time. Once this second possibility is considered, the physics becomes extremely complex. Also in multiphase flow, the several materials that flow together are not mixed (such as oil and water). Therefore, there are several combinations that can be regarded as multiphase flows. These include gas-liquid flows, liquid-liquid flows, liquid-solids flows, gas-solids flows, and gas-liquid-solids flows. The current investigation deals with gas-liquid flows and liquid-liquid flows, or to be more specific, with air-water and oil-water flows. More specifically, the current research deals with multiphase flow in circular cross section pipes and focuses mainly on bubbly flows. Due to the fact that the behaviour of this type of flow changes with the inclination of the pipe, the current project also focuses on multiphase flows in vertical and inclined flows (up to 30^0 degrees inclination from the vertical). Finally, the multiphase flow domain that was investigated was upward bubbly flow.

Next, the basic properties of multiphase flows are described followed by a description of areas of application in which they are encountered.

1.1 Properties of a Multiphase flow.

There are four principal flow regimes for vertical gas-liquid multiphase flows. The number of these regimes is not definite. In [1] the number of the flow regimes that are recognised for vertical flows is 16. But as it is mentioned in [1] the reason for this, is that the physics of multiphase flows is complex and a large number of descriptions can be used.

For the gas-liquid flow, it can be said that several flow patterns appear that depend on the superficial velocities of the two fluids. When the liquid superficial velocity is low and the gas superficial velocity is in the range from zero to about 0.6096 ms^{-1} (in a pipe of internal diameter 26mm) then the gas appears in the form of relatively small bubbles that differ in their size. The number of bubbles per unit volume and the rate at which they coalesce increase with the gas superficial velocity and the bubbles' size becomes bigger. This flow pattern is called *bubbly flow*. If there is a further increase of the gas superficial velocity, coalescence among the bubbles is increased and cap shaped bubbles appear, denoting the onset of the *slug flow* regime. With further increase of the gas superficial velocity, the bubbles become longer, nearly span the pipe and are separated by the liquid phase. These bubbles are called *Taylor bubbles*. Instability of these large gas bubbles appears when the gas superficial velocity is increased even further. This type of flow pattern is called *churn* or *froth flow*, and it is characterized by a chaotic behaviour. The flow is highly turbulent. Increasing even more the gas superficial velocity cause the *annular flow* regime to occur. This flow regime is characterised by a thin layer of water at the pipe's wall and

the rest of the pipe is occupied by the gas with some water droplets in it. Finally, at slightly higher gas velocities, water droplets from the thin liquid film are captured by the gas and are distributed in the whole cross section of the pipe, resulting in a *mist flow*. [2][3]

For the liquid-liquid flow it is noticeable that the flow patterns are similar to gas-liquid flows. They also, follow the same sequence. But there are some differences due to the fact that the viscosities, densities, and interfacial tensions of the fluids are different. For example although cap shaped oil bubbles can form, large oil Taylor bubbles are rarely observed.

In the current research the flow regime that is studied for air-water and oil-water systems is the *bubbly flow* regime.

For inclined multiphase flows, different flow patterns will be observed compared to vertical flows. Due to the action of gravity on the components there is a tendency for stratification to occur in inclined flows. The heavier component has the tendency to go to the bottom side of the pipe wall while the lighter component does the opposite. Hence different levels of stratification occur, which depend on the density of the materials and the amount of inclination. There is not much extensive work on the study of inclined multiphase flows. Some studies of these flow conditions can be read in [4]-[10][14], where the effect of inclination on the flow regime is discussed. In the current thesis investigation and analysis of inclined flows is undertaken.

Some key parameters that are used in order to quantify multiphase flows are the *mean phase volume fractions, phase superficial velocities and actual phase velocities*. *Mean phase volume fraction* is the time averaged fraction of the volume which is occupied by a phase. It is a dimensionless number between 0 and 1. *Phase*

superficial velocity is the velocity that a phase would have if it was flowing alone in the pipe. *Actual phase velocity* is the mean velocity with which a particular phase travels in the pipe. Note that in a steady state multiphase flow the local volume fraction and local velocity of a particular phase may vary in the flow cross section and this is particularly true for inclined flows.

The main properties that are considered in the current research are the *local volume fraction* and the *local actual velocity* (both axial and vector velocity) of the dispersed phase. The reason for studying these properties is that in many industries (e.g. oil industry, chemical industry, and nuclear plants), the knowledge of volume fraction and velocity profiles of the dispersed phase is important for the optimal control of processes, the maximum exploitation of resources, and the safety of the personnel. Some reasons why gas velocity and volume fraction profiles are important include [11-13]:

(a) Knowledge of the local gas volume fraction distribution is essential when calculating the pressure gradient in inclined gas-liquid pipelines.

(b) Optimization of chemical processes is vital in chemical engineering applications (e.g bubble column reactors) when bubbling gases into liquid solutions. Therefore, knowledge of gas-liquid interface conditions is important for determining their reaction kinetics.

(c) Advanced nuclear reactor concepts rely on extreme high heat removal, only possible through liquid boiling. In this case, minor changes in local parameters can drastically change the flow conditions in steam-water systems. As a result, knowledge of the gas volume fraction and velocity is important for producing reliable accident-safety calculations.[12-13]

1.2 Presence of multiphase flows and the need for measuring their properties.

Multiphase flows are present in several processes and industries. The main ones are:

- Oil and gas industry.
- Mining Industry.
- Nuclear plants.
- Chemical Industry.

1.2.1 Oil and gas industry.

In the oil industry multiphase flows appear in all the stages of oil production. These are during the drilling procedure, and at the oil extraction procedure. During the drilling a "*drilling mud*", which is a mixture of water, clay and other chemical materials, is pumped into the well in order to lift the rock pieces that are produced from the drilling up to the surface for removal[14][15].

It is essential that the flow rates of the mud and rock cuttings are known at various points in the well in order to prevent accidents such as collapsing of the well or drill bit becoming stuck into the well [14]. Therefore multiphase flow measurements are needed for this kind of operation.

During the extraction of oil from the well, multiphase flow is often present. Usually after the drilling of the hole, a pump is placed on the top to extract the oil. But there are cases where the oil is too heavy to be pumped. Therefore another technique is used to extract the oil and it is called "*enhanced oil recovery*". This technique involves the drilling of another well close to the original one and pumping steam into the second well. The pressure that is created, pumps the oil to the surface. Sometimes

water and gas are injected into the second well for better extraction efficiency. So, it is obvious that during the extraction of oil, gas and water may also flow upwards in the well. Therefore, measurements of the multiphase flow properties in the well or at the well head are important in order to quantify the flow [16][17].

1.2.2 Mining industry.

In the mining industry one of the methods that is used to transport the extracted minerals is using pipelines and water. This method is called "*Hydraulic transportation*". This method involves the placing of the solids into the pipeline and the use of a liquid (usually water) as a medium of transporting. Transportation of the mineral can be done even over large distances. As reported by Seshadri et al [18], the transportation of solids using pipelines is a better method than the traditional ones. The reasons are that (i) it is techno-economically attractive, and (ii) it offers a high degree of efficiency, reliability and round the year availability. Also, this method is environmentally friendly, making it even more desirable as a way of transportation [18]. This is another example of a multiphase flow (solids-liquid) in which several key flow parameters must be monitored for proper functioning of the installation. One of these parameters is the solids volume fraction for pressure drop prediction along the pipe's length. This must be known in order to reduce building and operating costs [14][19][20]. Also as Suhashini and Nigam state in [21], quantitative information and reliable estimates of hydrodynamic properties about this kind of operation are essential for a safe and economic design and efficient function, especially when capital and operating costs become competitive [21].

1.2.3 Nuclear plants.

Another area of engineering where multiphase flow is present is in nuclear plants. To be more specific two phase flow occurs in the cooling equipment of a nuclear reactor. The nuclear reactor uses radioactive materials to heat the water. The resultant steam drives a steam turbine which in turn spins a generator to produce power. Then the steam is cooled down before it re-enters into the steam generator. This steam-water flow is a two phase flow. It is essential to know the steam bubble size distribution and the local steam volume fraction distribution since these parameters are important for calculating heat transfer, which is an important parameter for the efficiency of operation of the nuclear reactor and for the safety of the personnel as well [5]. Also, models of flow patterns of the two phase flows are important for the design, optimisation and safety analysis in nuclear plants as stated by Dirk Lucas et al [22].

1.2.4 Chemical Industry.

A vast number of multiphase flows occur in chemical processes. In gas-liquid reactions sufficient contact of the two phases is important in order to have *optimal performance*. Examples include chlorination, oxidation and aerobic fermentation reactions. In these kinds of reaction the interfacial area per unit volume and the mass transfer rate of the two phases are important parameters that must be measured for a better overall performance of the process [23].

Improved manufacturing techniques of microstructures made possible the development and assembly of microchemical devices. These devices are better than the common batch reactors due to the fact that they use minimal amounts of fluids, they have high heat and mass transfer rates, and short reaction times. In these

microchemical reactors multiphase flows are present. It is highly desirable to know the characteristics of the multiphase flows in these microstructures in order to properly design, develop and operate them. Knowledge of flow patterns, volumetric content, pressure drop, liquid film thickness, and the mixing quality is essential [24] [25].

During fermentation reactions in chemical and biochemical processes foam (a mixture of gas and liquid) is often produced. Depending on the conditions of the process different effects may occur. Loss of sterility may happen from excessive foaming. Also, in order to store the unwanted foam, over sizing of vessels must occur. This increases the costs of the process. So it is important to monitor and control the different types of foam that can occur during these processes [26].

Bubble columns are multiphase reactors which are used in chemical and biochemical industries. They have advantages over other multiphase reactors. These are the simplicity of their construction, very good heat and mass transfer rate properties, absence of mechanical moving parts, high thermal stability, good mixing, low power consumption, and low operational costs. In these reactors gas is injected into a continuous liquid. Applications of bubble columns include oxidation and chlorination reactions, in which kinetically slow gas-liquid reactions take place. The reactor geometry, the primary gas distribution, the operational conditions, and the physico-chemical properties of the two phases can all affect the size, velocity, shape, and interfacial area of the bubbles. Also, in some applications it is important to quantify the bubble coalescence. Therefore it is obvious that these bubble properties must be measured in order to build a representative model of the bubble columns for better operational efficiency [27].

Another device that is used widely in the chemical industry and involves multiphase flow is the riser. Gas and solids flow co-currently upward. One example of the use of this process is in fluid catalytic cracking (FCC), which is used in many industrial processes. This type of multiphase flow has a complex behaviour due to the existence of turbulence. This complexity introduces many difficulties in designing, scaling up and optimising the operation of the chemical reactor. Therefore it is essential to know the physics behind these complex flows. Measurements of phase volumetric distributions are important for understanding the behaviour of such gas-particulate flows [28].

Finally, in fluidised beds and sieve plate reactor towers, is important to know the bubble diameter, and the phase volume fractions [29][30][31][32].

This section has given examples of processes where multiphase flows are present. In these sectors of engineering, reliable methods of measuring properties of the multiphase flow are needed in order to maximise efficiency and reduce operational costs.

1.3 Aim of the project.

The aim of this thesis is to research the design and application of local conductivity probes. The probes are able to measure local volume fractions and local velocities in bubbly two phase flows. By traversing the probes throughout the flow cross section, profiles of local volume fraction and local velocity can be extracted. The data produced from this method can be used among other things for calibrating and validating electrical resistance tomography (ERT) systems.

ERT is increasingly being used in the process industry for measuring volume fraction distributions in two phase flows. Industrial sectors such as sewage treatment,

the oil industry, the food industry, and the mineral processing industry are examples of where the ERT technique is applied. It is important to mention that “dual plane” ERT has also been developed and it is able to measure the local axial velocity distribution of the dispersed phase. Note also that ERT can be used in inclined multiphase flows, where highly skewed profiles maybe observed. Some aspects of the ERT technique, however, require improvement. In particular, the accuracy of the dispersed phase axial velocity distribution obtained using dual-plane ERT is highly dependent upon the separation of the image planes and the acquisition rate (frames per second) of the data. Also, due to the fact that the resultant volume fraction and velocity profiles obtained from ERT may not be valid, it is important to have reference measurements available against which they can be compared [14][33]. These reference measurements must be taken using a local probe, acquiring point by point data in the flow cross section. One promising candidate local probe is the local conductivity probe. As previously mentioned, the data acquired from local conductivity probes can be used for validation and calibration of ERT and can also indicate weaknesses of ERT (therefore providing a better understanding of the ERT technique). It is important to mention that the acquired data from local conductivity probes can also be used for validating CFD analysis of bubbly two phase flows.

It is obvious from the above that the primary purpose of the project is to provide a benchmark against which ERT data can be validated. Therefore, the aim of the thesis is to research the design and fabrication of local conductivity probes along with their associated signal processing algorithms. Specifically, the thesis aims to research the design and construction of dual and four sensor ‘needle’ conductivity probes and their corresponding signal and data processing. It also aims to use these probes in air-water and oil-water flows, both vertical and inclined. Finally a major

aim is to overcome one of the disadvantages of intrusive conductivity probes, namely the influence of the bubble-probe interaction on the measurement.

2. Literature Review.

Measuring techniques for multiphase flow can be categorised in two main fields. These are the *invasive techniques* and the *non-invasive methods*. The former is when the measurement is acquired from inside the environment where the phenomenon takes place, whereas the latter occurs when the measurement is taken from outside the environment where the phenomenon of interest takes place. In addition, each of these fields can be separated into two categories depending on the resolution and accuracy of the measurement that is required. These two subcategories are *local measurements* and *global measurements*. The local measurements involve the process in which a specific characteristic in a multiphase flow is measured in a predefined position in the pipe. In other words, measurement of the characteristic is made at a single point in the test environment. Global measurements are made when average values of the multiphase flow are of interest. It can be said that it is possible to have measurements that are *invasive* and either *global* or *local*. Any decision taken regarding the technique and the type of measurement that has to be used depends on the requirements and specifications of the project. For example, one of the differences between the *local* and *global* measurements is that the former has much better spatial resolution of a flow characteristic than the latter. But in general the *global* one can give average information of a fluid property in shorter time than *local* measurements. Regarding the technique, one of the differences between *invasive* and *non-invasive* methods is their applicability in a specified environment. A non-invasive technique that uses laser light as the medium for observation might be inappropriate in a working environment where the pipes are metallic or not transparent for the wavelength of the laser; but a Pitot tube can be more appropriate.

Next, a more detailed description for various measurement methods will be presented, and it will give a better idea and understanding of the different techniques currently in use.

2.1 Non-invasive techniques.

There are a large number of non-invasive multiphase flow measurement techniques. Some of them are used to measure local characteristics (point measurement in the cross section of the pipe) of the multiphase pipe flow, and others can measure global characteristics (average measurements of the whole system) in a multiphase pipe flow. Depending on the principles of their operation, some devices detect fluctuations of the measured property, and others average long-term behaviour of a property. Also, one technique can yield more than one characteristic. Table 1 shows a number of non-invasive techniques that are used today in industry and in academia [34].

	Technique	**Measured characteristics**	**Type of measurement**
1	Pressure drop	Phase volume fraction, flow regime	Global
2	Pressure fluctuation	Flow regime, turbulence characteristics	Global
3	Dynamic gas disengagement	Bubble size distribution, phase volume fraction	Global

4	Tracers	Phase volume fraction, mixing characteristics and phase velocity	Global
5	Conductimetry	Phase volume fraction	Local and Global
6	Neutron absorption, γ-ray absorption, X-ray absorption	Phase distribution and phase volume fraction	Local and Global
7	Light attenuation	Phase volume fraction and interfacial area	Global
8	Ultrasound attenuation	Phase volume fraction, and phase velocity	Global
9	Photography and image analysis	Bubble/drop size shape, flow regime	Global
10	Radiography	Bubble/drop size and shape, flow regime	Local and Global
11	PIV	Disperse phase velocity fields	Local
12	NMR	Phase volume fraction, phase velocity, wetting efficiency	Local and Global
13	Laser Doppler anemometry and phase Doppler anemometry	Liquid velocity, gas velocity, and bubble size	Local
14	Polarography (microelectrodes)	Wall shear stress	Local
16	Tracking of radioactive particles	Velocity fields and	Local

		trajectories	
17	Γ- or X-ray tomography	Phase volume fraction distribution	Local
18	Capacitive or resistive tomography	Phase volume fraction distribution	Local
19	Ultrasonic tomography	Phase volume fraction distribution	Local

Table 1 Non-invasive techniques.

2.1.1 Pressure drop.

Time averaged pressure drop is a technique that can be characterised as global. This means that it gives average information of the multiphase flow in a pipe. The information that it yields in a non-horizontal two phase flow is the volume fractions of the different phases (provided there is a density contrast between the phases) and hence, with reference to a flow pattern map, it may also provide information on flow regime. The pressure drop is measured between two different points in the pipeline separated by a vertical distance Z using a differential pressure transducer. In this technique the pressure tappings are at the pipe wall. The technique relies upon measurement of the hydrostatic pressure drop and hence care must be taken to eliminate the effects of frictional pressure loss [34][35].

For a gas-liquid, flow the formula that is used for relating the measured pressure drop ΔP to the phase volume fractions ε_L (liquid) ε_G (gas) is:

$$\frac{\Delta P}{Z} = g\left(\rho_L \varepsilon_L + \rho_G \varepsilon_G\right) + \left(\frac{(\Delta P)_f}{Z}\right) \tag{1}$$

Where g is the gravitational constant, ρ_L, ρ_G are the density of liquid and gas respectively and $\frac{(\Delta P)_f}{Z}$ is the calculated frictional pressure gradient. Since $\varepsilon_G = 1 - \varepsilon_L$, eq. 1 can be used to determine both ε_L and ε_G. Flow regime transitions may be measured from the time averaged values of measured pressure drop.

2.1.2 Pressure fluctuation.

Another way of determining the flow regime in multiphase flows is by analysing the fluctuations in pressure drop. Pressure drop is measured at the pipe wall, but the interest is focused on the small fluctuations that appear on the signal. Matsui (1984) [36], Glasgow et al (1984) [37], Drahos and Cermak (1989) [38], Drahos et al (1991) [39], Drahos et al. (1992) [40], Vial et al. (2000) [41], Johnson et al., (2000) [42], are some of the many that used numerical techniques in order to interpret the fluctuations in the differential pressure signal, and more details can be read from the corresponding references. It is important to mention that the differential pressure signal can be produced by several different measurement methods such as electrical current from microelectrodes embedded in the wall or from the more common diaphragm differential pressure cell. Although this way is direct, it needs careful analysis in order to avoid over-interpretation of the fluctuations, due to the fact that there are some limits (time resolution of the method) within the techniques used for measuring pressure fluctuations. Many numerical methods have been proposed by a number of authors regarding the interpretation of the differential pressure fluctuations. In literature one can find statistical methods [39], [43], spectral analysis [44], fractal analysis [40], [45], [46], [47], chaotic analysis [48], [42], [49], and time-frequency

analysis [50], [41]. Detailed descriptions of these methods can be reviewed in the corresponding references.

2.1.3 Dynamic gas disengagement technique (DGD).

The dynamic gas disengagement technique involves the interruption of the gas into a bubble column or reactor. At that time the liquid level is measured or the pressure at different levels of the reactor (or column) as a function of time. This method can be used to determine the global gas and solid volume fractions in a slurry bubble column or the structure of the gas volume fraction in bubble columns. [34]

The liquid level can be measured by various ways, such as: visual observation, and pressure profile [51]. Camarasa et al. report that the use of DGD involves the acceptance of three basic assumptions. These are [52]:

1. the dispersion is axially homogeneous when the gas feed is interrupted,
2. there is no bubble-bubble coalescence or break-up happening during disengagement,
3. the bubble disengagement of each bubble class is not influenced by other bubble classes.

But the work of [53] shows that assumptions 2 and 3 are not valid for a two dimensional bubble column.

2.1.4 Tracing techniques.

As table 1 shows, tracing techniques are used for measuring the mean phase volume fraction of one of the phases, and for characterising mixing of phases. They can be used for any type of multiphase flow. Therefore they can be divided in three

categories, which are the tracing of the liquid phase, tracing of the gas phase, and tracing of the solid phase.

2.1.4.1 Tracing of the liquid.

One way for tracing the liquid phase is to measure the residence time distribution (RTD) of a tracer. This method is a well known technique and details can be found in [54-56]. Most of the times the tracer is salt tracer and the measuring technique is Conductimetry. But there are other tracers that are used too. Some of them are the coloured tracers used in non-aqueous liquids, and radioactive isotope tracers, a method that is non-invasive [57][58]. Sakai et al. [59] has proposed a new technique using a non-radioactive tracer and it is non-invasive too. The characteristic of the specific tracer is that it interacts with neutrons. Besides the disadvantage of the requirement of a neutron source, this method can be used under high pressure and temperature conditions.

For the interpretation of the flow behaviour in a reactor a model is used. Depending on the complexity of the system the model might be a simple one with a few parameters only to be determined, or a complex one with many parameters to be calculated. The values of these parameters are adjusted so they can fit the experimental data. Usually in simple systems a two-parameter model is adequate to describe the global behaviour of the flow in the reactor. One of the parameters is the RTD and the other can be a characteristic of mixing (e.g. recirculation rate between stirred cells, axial dispersion coefficient). Examples of these simple cases can be found in [60][61].

In the more complicated systems, the models need more than two parameters in order to give reliable results. This case raises the question of how sensitive are the

models to the change of the parameters. Therefore, careful investigation should be conducted in order to check the agreement between the model and the experiment [34].

2.1.4.2 Tracing of the gas-phase.

Due to the fact that there is no completely insoluble gas, hence absorption and desorption phenomena occur, investigation of gas-phase dispersion is more difficult than for liquid-phase tracers. In [62] an example of this behaviour can be seen. Simultaneous gas-liquid mass transfer and gas and liquid dispersion is necessary to be considered for tracing the gas phase. Finally, an interesting method is suggested by Lübbert [63]. This method uses stochastic distribution of the tracer and cross correlates the outlet signal with the inlet signal.

2.1.4.3 Tracing of the solids phase.

One of the applications in which solid tracers are used is fluidisation. Three kinds of tracers are used for solid tracing [34]:

- *Coloured tracers*. Qualitative information on the mixing of the solids is achieved through investigating the behaviour of layers of particles in different colours. This method has been used by Fortin [34].
- *Magnetic tracers*. Two concentric loops are situated around the column. The signal measured in the inner loop when electric current is present in the outer loop, depends on the magnetic properties in the column at the level of the loop [34].
- *Fluorescent tracers*. A fluorescing substance that is able to be absorbed by the solids is used as a tracer. This method is used for liquid-solid slurries [34].

2.1.5 Conductimetry.

In cases where the multiphase mixture is electrically conductive, for example multiphase mixtures for which water is the continuous phase, it is possible to measure the mixture conductivity between two electrodes in the pipe. The conductivity in this case is related to the water volume fraction. The greater the amount of water relative to the amount of gas or solids, the bigger the measured conductivity, and vice versa. But the measured conductivity also depends on the spatial distribution of the phases and on the temperature. Differences of up to 20% between predictions and measurements have been reported. It is also advisable to calibrate a conductimetry device before use. However this technique has been used by various scientists such as Begovich and Watson [64], Uribe-Salas et al. [65], and by Shen et al. [66].

2.1.6 Radiation attenuation techniques.

It is well known that all kinds of radiation are attenuated when they cross a medium. This medium might be solid or liquid or gas or a multiphase mixture. No matter what is the medium, the attenuation depends on the type of radiation that is used and the density of the medium along the path which the radiation travels. In multiphase flows three methods are used as measuring techniques. These are:

- *X-ray, γ-ray or neutron absorption radiography*. There is a significant difference in the absorption coefficients between solids, gas, and liquids. As a result, the overall attenuation, measured along the path of the beam between the transmitter and the receiver, can be used to infer the relative amounts of the different materials present. Spatial resolutions of about

100μm can be achieved if X-rays are used. The disadvantages of this technique are the price and safety considerations [34].

- *Light attenuation*. A similar concept to the above technique is to use light instead of a radioactive source. The light attenuation depends on the specific interfacial area of the dispersed phase. Of course the liquid must be transparent. Also, care should be taken in order to avoid parasitic light sources [34].
- *Ultrasound attenuation*. An ultrasound source imports mechanical motion to the atoms of the surrounding environment. This is a high frequency acoustic wave. The attenuation depends on the material in which the wave travels, different types of materials giving different attenuations. Attenuation also depends on the number of interfaces between different types of material through which ultrasound passes. The advantage of this technique is that it is not limited to transparent liquids as with for example optical methods [34].

2.1.7 Photographic techniques.

This method involves the taking of pictures of the flow in order to post-process them and to allow various properties of the multiphase flow to be quantified. It requires transparent pipe walls and transparent liquid. Using this technique, information about the flow at the vicinity of the wall can be extracted. In gas-liquid flows, for very low values of gas volume fraction, high speed cameras can also be used to give information on the bubble velocity, size and shape close to the pipe centre. Image processing can be used as a method for analysis of the flow. Mean

bubble diameter, and sphericity are some of the other properties that can be measured [52]67][68][69].

2.1.8 Radiographic techniques.

This method of measurement uses the same principle as the photographic technique but instead of light, X-rays are used. The method can be used in a non transparent fluid, but only one layer of bubbles can be observed reliably [70].

2.1.9 Particle image velocimetry.

This method is used for measuring velocity fields. The principle of operation is that a laser sheet illuminates a slice of the multiphase fluid. Pictures are taken at short time intervals. Measuring the distance between the same particles in successive images and knowing the time interval between successive images, particle velocity vectors can be calculated. One main problem that occurs using this method is the identification of the same particle in successive images. But different methods have been proposed for solving this problem. Another disadvantage is that the technique is limited to relatively low values of the mean dispersed phase volume fraction. A more comprehensive description about the method can be found in [71][[72][73].

2.1.10 NMR imaging.

NMR stands for nuclear magnetic resonance. It is a method that is used in medical imaging. But it has started to be used in engineering too. In general radio frequency pulses and magnetic gradient pulses interact with the spins of the nuclei positioned in a static magnetic field. More information can be found in [74][75][76].

2.1.11 Laser Doppler anemometry (LDA) technique.

The principle of operation of LDA is that, if there is a relative motion between a wave source (which in this case is a laser) and a wave receiver (e.g. a bubble in the liquid), then there is a Doppler shift of wave frequency related to the bubble velocity. LDA measurements are very fast allowing rapid measurement of velocity fluctuations. One of the problems that can occur using this method is that small particles in the liquid can cause liquid velocities measured by LDA to be mixed with bubble velocities [11].

A second technique (also mistakenly referred to as LDA) uses interference fringes from two intersecting laser beams to create a small volume with patterns of light and dark in the direction of flow. As a tiny particle moves across these patterns it reflects light of sinusoidal varying intensity into a photodetector. The frequency of the sinusoidal variations of light intensity is related to the particle velocity and the separation of the interference fringes. This second technique is more suited to finding the local velocity of, for example, a liquid seeded with tiny particles.

A derived technique of LDA is Phase Doppler Anemometry (PDA). Figure 1 shows a PDA schematic.

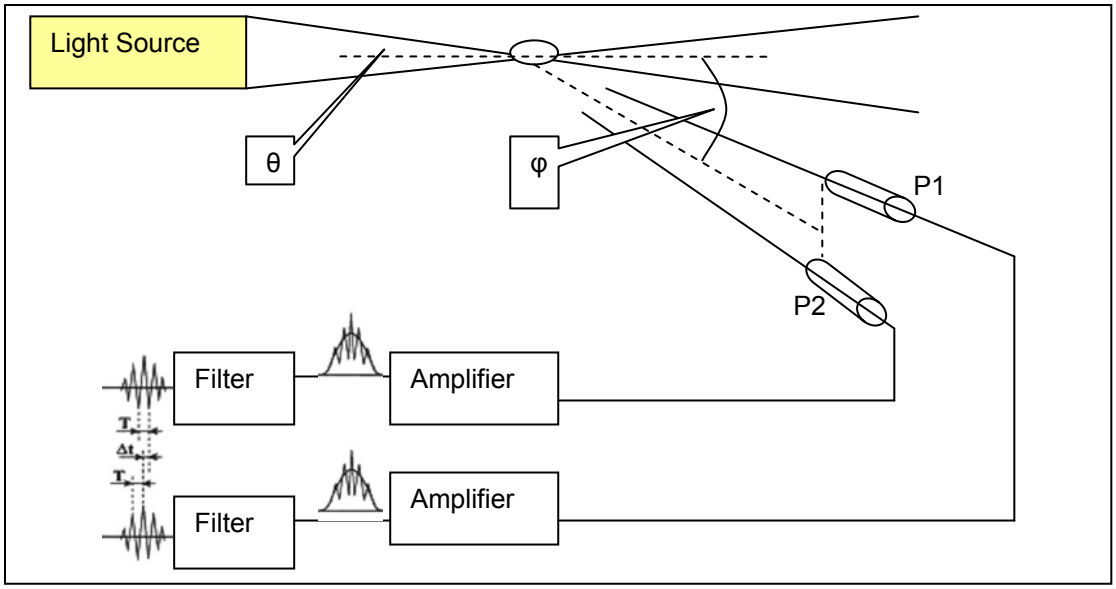

Figure 1. PDA equipment [11]

As can be seen, the laser Doppler signal is measured by two detectors. If the geometry of the systems is known, then the phase difference between the two signals gives the size of the particles in the flow. So, if T is the time between the reflected signal from two successive interference fringes measured by one detector, Δt is the time lag between the reflected signal from the same interference fringe measured by both detectors, then a phase difference ΔΦ can be calculated by:

$$\Delta\Phi = 2\pi\frac{\Delta t}{T} \tag{2}$$

Therefore, if λ is the light wavelength, n_c is the refractive index of the continuous phase, b a characteristic of the geometry of the system, then the bubble diameter d can be calculated by:

$$d = \frac{1}{2b}\frac{\lambda}{\pi n_c}\Delta\Phi \tag{3}$$

More information regarding LDA, PDA and their applications can be found in [75][77][78][[79].

2.1.12 Polarographic technique.

This technique is used for measuring local wall stress. This method is based on the fast electrochemical reduction of a reagent dissolved in the moving medium. Usually, the electrochemical system that is used is hexacyanoferrate III, and after the reduction it becomes hexacyanoferrate. The electrode potential is adjusted so that the reagent concentration on the electrodes is zero. As a result, the mass transfer on each probe depends only on local hydrodynamic parameters. A simple equation that describes how the wall shear stress τ_w depends on the supplied current I is:[80][81]

$$\tau_w = CI^3 \tag{4}$$

Where C is an empirical constant the value of which depends on the liquid dynamic viscosity, the width of the electrode within the flow, and the diffusion coefficient. The advantage of this technique is that it is a non-invasive method; it can be miniaturised, and gives information regarding velocity fluctuations near the wall. But it requires conducting liquid and a method of support for the electrolyte [80][81].

2.1.13 Radioactive tracking of particles.

This method uses neutrally buoyant spheres that contain radionucleides that emit γ-rays. A number of detectors around the column or pipe receive the transmitted rays. Thereafter, determination of the position of the particle in the flow is possible. The final result is that trajectories of the particles can be measured. Usually this type of measurement is used to validate CFD calculations, to determine axial dispersion coefficients of the solid, and to yield global circulation patterns. The only

disadvantage of this technique is the long and complicated calibration procedure that is needed [82][83].

2.1.14 X- or γ ray tomography.

Similar in principle of operation to the radioactive measuring techniques, this method is used to obtain data from many points in the cross section of the bubble column or pipe in which multiphase flow occurs. The reconstruction procedure involves the inversion of a 2D Fast Fourier Transform since the measured attenuations are linearly proportional to the density of the material. If *f(x,y)* represents the distribution of the phases inside the column or pipe, the measured attenuation $p(s,\theta)$ that corresponds to a projection of attenuation for a given angular position θ and a given distance *s* from the centre of the pipe, can be expressed as [34]:

$$p(s,\theta) = K \ln\left(\frac{I}{I_0}\right) = \int_{L_{S,\theta}} f(x,y)dl \tag{5}$$

where *I* and I_0 are respectively the photon flux measured at cylindrical coordinates *s* and θ when (i) the column or pipe is crossed by two-phase flow and (ii) when it is filled by only one phase. *K* is a constant.

If P(S,Θ) is the one-dimensional Fourier Transform of p(s,θ), the function *f(x,y)* can be reconstructed [34] by using the inverse Fourier transform of P(S,Θ) as follows:

$$f(x,y) = \frac{1}{4\pi^2}\int_0^{\pi}\int_{-\infty}^{\infty} P(S,\Theta)|S|e^{jS(x\cos\theta + y\sin\theta)}dSd\theta \tag{6}$$

The difference between the X-ray technique and the γ-ray method is that the former is used in low attenuation materials (due to low energy levels) but the spatial resolution is better (1x1 mm^2 for X-rays) than the later method (1x1 cm^2 for γ). More information regarding the method and its application can be found in [84][85][86].

2.1.15 Electrical tomography.

This method of tomography has fast dynamic characteristics, relatively low cost and easy installation, but the measured signal is a non-linear function of the phase fractions. The reconstruction procedures are not easy to implement and the spatial resolution is moderate (of the order of few mm^2). The technique is able to give information about local volume fractions and with some modifications (e.g. dual-plane tomography), local velocities of the dispersed phase. Electrical tomographic systems have been used in bubble columns, three-phase pipes and trickle beds. Many recent advances have been made in the optimisation of the reconstruction algorithms.[87][[88][89][90][91]. The electrical tomography method uses two different concepts for its implementation. The first is the use of the change of electrical resistance that appears between two electrodes in a conductive multiphase mixture. This method is Electrical Resistance Tomography or ERT. The second uses the change of capacitance between two electrodes in a non-conductive multiphase mixture. This method is called Electrical Capacitance Tomography or ECT. More information regarding ERT will be presented later in the current thesis.

2.1.16 Ultrasonic tomography.

This method obtains a tomographic image through a cross section of a pipe using ultrasonic waves. The wave propagation depends on the phase fraction and the

phase distribution. In gas liquid flow this method is used when the volume fraction of the dispersed gas is about 0.2. This limitation occurs due to the fact that for large gas volume fractions, there is significant attenuation of the ultrasound, which can reduce the depth of investigation into the pipe [34].

2.2 Invasive techniques.

Although non-invasive techniques can give the required information (see third column in table 1) that is needed for a process, there are limitations that make them unsuitable for a number of applications. In addition non-invasive techniques often provide insufficient depth of investigation into the flow. Therefore invasive methods may be preferred. Also in some industrial operating conditions, non-invasive techniques become ineffective because of the pipe walls, bubble number density, etc; furthermore non-invasive methods are not always easy to apply and install, and often they are very expensive [34].

As a result, much research has been performed into invasive techniques. Table 2 shows the main invasive measuring methods that exist for multiphase flows.

	Technique	**Measured characteristics**	**Type of Measurement**
1	Heat transfer probe (hot film anemometers)	Dispersed phase local volume fraction, phase local velocity, liquid RMS velocity	Local
2	Ultrasound probe • Attenuation technique	Gas volume fraction, interfacial area, bubble	Local

	• Doppler technique	diameter, bubble velocity	
3	Pitot tube	Flow velocity and direction, pressure drop, liquid velocity	Local
4	Needle probes (conductivity and optical)	Gas volume fraction, dispersed phase velocity, bubble chord distribution	Local

Table 2. Invasive techniques [34].

2.2.1 Heat transfer probes.

The main device that represents this type of group is the hot wire or hot film anemometer. The principle of its operation is based on the fact that when a probe is electrically heated then heat exchange occurs between the probe and the surrounding environment. The convective heat transfer between the probe and the environment, which might be liquid or gas, depends on the Reynolds number Re and Prandtl number. If Prandtl number is assumed constant then conventing heat can be calculated from:

$$N_u = A + B \cdot \mathrm{Re}^{-0.5} \tag{7}$$

The electric current through the probe is controlled by a Wheatstone bridge which in turn is connected with a regulation amplifier and a high pass filter [34]. The calibration procedure follows King's law [141], which is:

$$E^2 = A + B \cdot u_e^n \tag{8}$$

where A, B, n are coefficients that must be obtained from calibration (for both equations 7 and 8), and E is the output voltage from the bridge. These coefficients are dependent on the physical properties of the fluid around the probe (density, viscosity, thermal conductivity) and on the geometry of the sensor, u_e is the fluid velocity. Usually, for the calibration procedure a Pitot tube is used as a reference measuring technique. Also, due to the fact that the sensor's characteristics can change rapidly, it is recommended to calibrate the probe daily [34].

The hot film sensor is very small in dimensions (25-100μm thickness) and of the order of a millimetre in length. It is made of quartz substrate for thermal insulation, covered with platinum or nickel and protected from oxidation by a thin layer (1 to 2 μm thickness) of quartz. Also, it is possible to have multiple sensors in one probe for multi-directional measurements. Figure 2 shows a picture of one, two and three sensor hot film probes [34].

Figure 2. Hot film anemometry probes. From left to right: one sensor, two sensor, and three sensor probes [34].

Hot film anemometry can also be used for measuring local phase fraction in gas-liquid and liquid-liquid phase fraction. It can also be used for measuring the local turbulence properties of the continuous phase in such flows. More information regarding its application and methods can be found in [92][93][94][95][96].

Due to their fragile nature, hot film probes are not used in multiphase flows that have solids with high momentum. Also, it is desirable that the temperature in the

flow is kept constant. Care must be taken when it is used due to the fact that errors in measurements may arise from several factors. These factors are: flow disturbance due to the probe, calibration curve uncertainty, signal treatment, signal amplification, signal interpretation in turbulent flow, and non-uniform temperature [92][93][97][98].

Based on hot film anemometry, another device has been developed that uses a similar principle of operation but different measuring technique. These are probes that are based on mass transfer instead of heat transfer. In this type of probe micro-electrodes rely on the Polarographic technique using a radox system. Polarography is a voltammetric measurement. Its response is determined by combined diffusion/convection mass transport. Polarography is a subcategory measurement system of the general category of linear-sweep voltammetry. The radox system is a set of electrodes that operate in an electrochemical environment. The output of the electrodes depends on whether the reaction on it is a reduction or oxidisation. The most common reaction is the oxidisation of hexacyanoferrate II to hexacyanoferrate III (see also section 2.2.12). Of course the liquid must be conductive. Details for this technique can be found in [99][100][[101].

2.2.2 Ultrasound probes.

There are two types of techniques that are used with ultrasound probes. The first one uses transmitted wave characteristics such as attenuation in order to make a measurement. The other type uses the characteristics of the reflected wave from a bubble and involves Doppler techniques. Both techniques use a receiver and a transmitter aimed at the measurement point in the flow. In the case of the Doppler technique the transmission and reception of the ultrasound are performed using the same probe [34].

In general, the structure of an ultrasound probe consists of a piezo-ceramic disk linked to a damping device included in a metal tube. These probes are able to be used even in aggressive environments; they can be used in temperatures up to 140^0C and at pressures up to 20MPa. Figure 3 shows a diagram of an ultrasound probe [34][102][103].

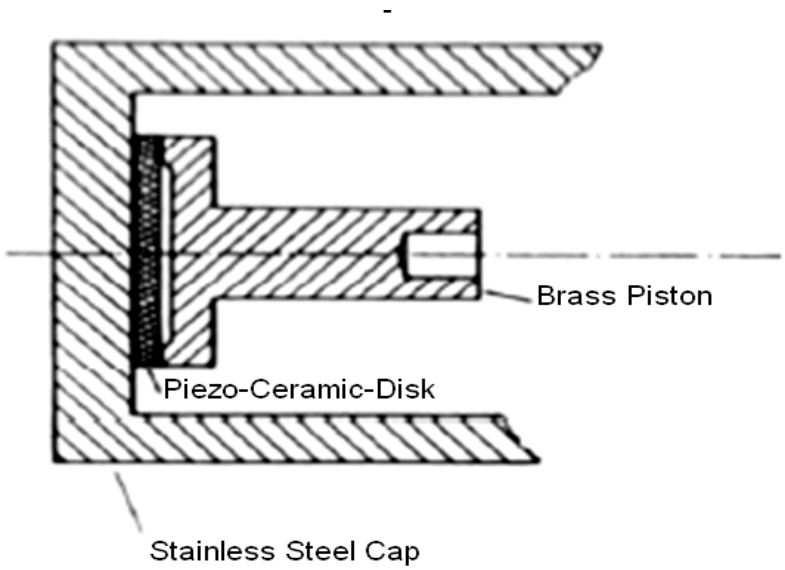

Figure 3. Cross-section of an ultrasound Doppler probe from [102].

The principle of its operation is that acoustic pressure waves are generated within the piezo-ceramic disk causing vibrations. The disk transforms these waves into a voltage signal which in turn can be acquired by a computer through a data acquisition card. The frequencies that are used range between 0.2 and 5 MHz. Also, the focal distance of these probes is about 0.2 to 0.3 m; therefore no disturbance of the flow occurs [34].

As previously mentioned, there are two techniques that can be implemented with ultrasound probes. In the first method, transmittance T is evaluated through the voltages A (when bubble is present) and A_0 (when bubble is absent) measured at the receiver probe. Transmittance T depends on the distance L between the transmitter and receiver, bubble size and shape, and wave characteristics such as frequency f and

celerity c in the liquid medium. So, knowing the transmittance T, the bubble mean diameter d_{SM} and sound dispersion S, then the local interfacial area concentration α_A or the gas volume fraction ε_G can be calculated using the following formula[34][104]:

$$\alpha_A = \frac{-8\ln(T)}{SL\left(k\frac{d_{SM}}{2}\right)} = \frac{6\varepsilon_G}{d_{SM}} \tag{9}$$

where

$$k = \left(\frac{2\pi}{c}\right) f \tag{9a}.$$

The other technique is called the *pulse echo technique*. Due to the fact that gas-liquid interfaces are very good reflectors (acoustic impedance is different in gas and liquid), pulsed signals are emitted into the fluid and their echo is received. Wave characteristics are altered and these changes correspond to the characteristics of the multiphase flow. Using the Doppler method it is possible to acquire information regarding gas volume fraction. The frequency of the pulse emission is around 10kHz. Also, the shorter the pulse, the weaker the echo distortion will be [105].

2.2.3 Pitot tubes.

Pitot tubes are used in single phase flows to acquire the local axial flow velocity. Figure 4 shows a simple drawing of this devise.

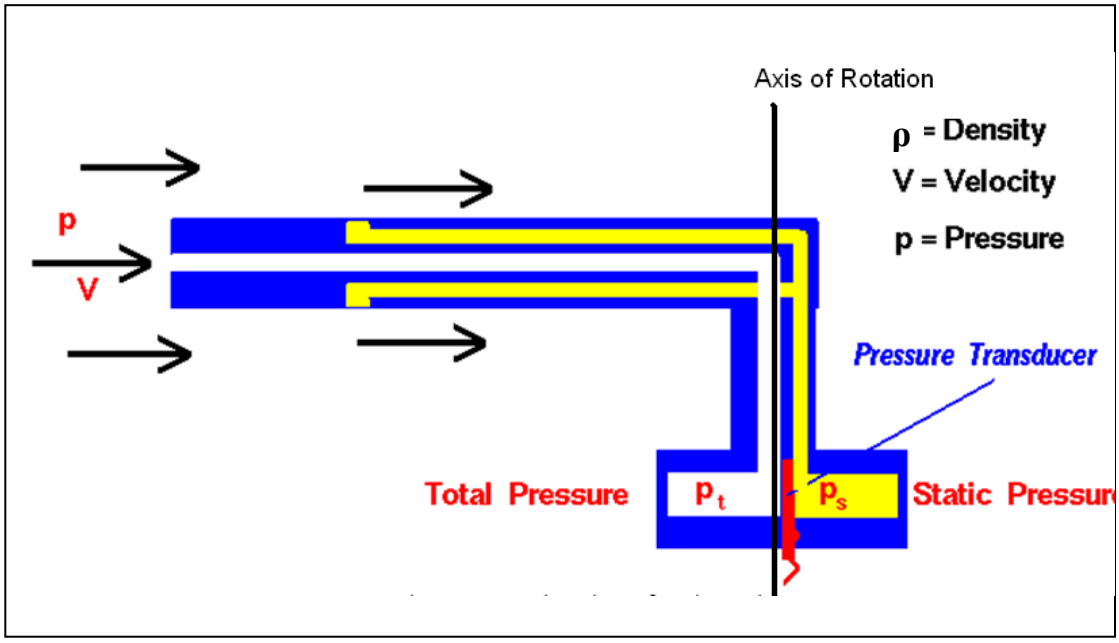

Figure 4. A drawing of a Pitot tube.[140]

But with the appropriate procedure they can also be used for multiphase flows. They are made to be thin (1-2mm in diameter) in order to disturb the flow as little as possible. A Pitot tube usually has a central hole and four interconnected side holes. The central hole measures the total pressure and is connected to the high pressure side of a differential pressure transducer. The four interconnected side holes measure static pressure and are connected to the low pressure side of the differential pressure transducer. The flow velocity magnitude can be simply calculated from the measured differential pressure using Bernoulli's equation. One way of using a Pitot tube is to rotate the probe around its own axis until the four side holes give the same value of pressure. In that way direction of flow can be determined [34].

When a Pitot tube is used in bubbly flow, care must be taken to hinder bubbles from entering into the nozzles [106][97]. The estimated error of Pitot tubes is around 4%. Although they might be difficult to use, they are robust and can be applied to hostile environments. Calibration must be performed if they are going to be used in

bubbly flows. The reason is that bubble slip velocity must be taken into account in the vicinity of the probe during the calibration procedure [34].

2.2.4 Needle probes.

The main characteristic about these probes is that they are thin and they are sharp ended. They are positioned so they face the flow direction in their design. They are able to measure local gas volume fraction and local gas velocities. There are mainly two types of needle probes: (i) optical fibre probes and (ii) conductivity probes. The number of tips or the number of needles they use is one or two. With one needle they are able to measure only the local volume fraction of the dispersed phase in gas-liquid and liquid-liquid flows. With two needles it is possible to measure the local velocities of the dispersed phase. Lately, four and five needle probes have been fabricated, which also measure vector velocities and bubble shape respectively. [12][113]

Optical probes are usually made of optical fibres and usually they are protected by a layer which does not cover the tip of the fibre. In cases where the probe is going to be used in hostile environments the tip of the fibre is made from sapphire. The tip diameter is usually between 50 to 200μm. The light beam that is used can be infra-red. When the tip is surrounded by liquid the beam is absorbed by the medium. But when gas surrounds the tip then the light is reflected back to a photodetector[136]. Figure 5 shows one and two sensor optical probes [107][108].

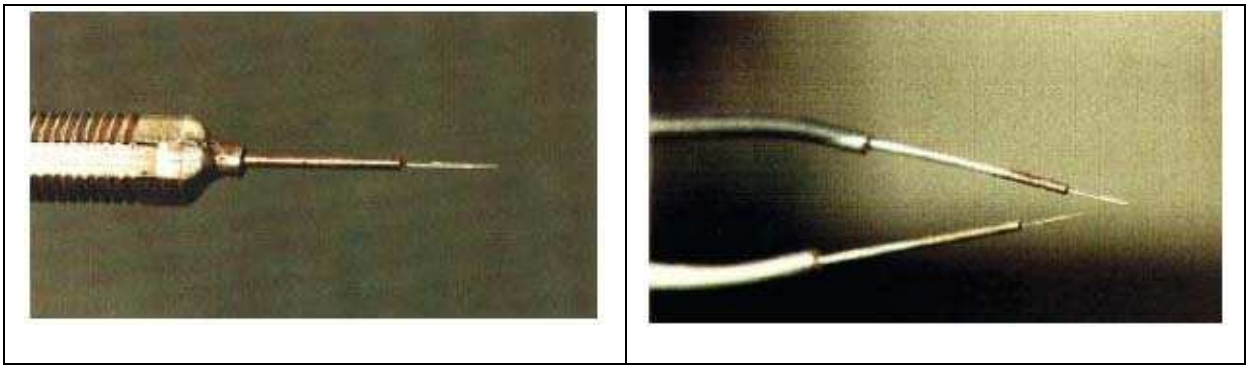

Figure 5. From left to right: One sensor optical probe, two sensor optical probe from [34].

Conductivity probes use metal needles as the sensors. The diameter of the needles is smaller than 400μm. They are covered with a non-conductive waterproof layer except at the tip of the needles. The tips are the actual sensors. The electronic circuit that supports these probes measures the conductance between the tip of the needle and the body of the probe, which is metal. When the tip is surrounded by liquid then the measured conductivity is high. When a bubble strikes the probe the tip is surrounded by gas and the measured conductivity is very low. Hence measurements can be acquired of the times when the bubble surface contacts the probe. As is the case with optical probes, a one needle probe can be used to measure local volume fraction and a two needle probe measures the local dispersed phase velocity. In the last decade four sensor probes have been also been designed and used. For more information regarding conductivity probes refer to [109][110][111][112][113] and also the remainder of this thesis.

Some of the problems that occur when needle probes are used include errors introduced by (i) the bubble-probe interaction (ii) incorrect probe orientation (iii) non-uniform bubble shape (iv) turbulence (v) statistical bias (large bubbles are likely to be hit by the probe more times than the small ones), and (vi) the signal (and data) processing scheme.

In the current thesis, dual and four sensor probes have been designed, fabricated and applied to a range of multiphase flows. An extensive and more detailed discussion regarding their characteristics will be presented in chapter 3.

3. Theory of the dual sensor probe.

It is important to mention the objectives the dual sensor probe must fulfil. It must be used in a bubbly air-water flow or in a bubbly oil-water flow. It must be able to measure local volume fraction and local bubble axial velocities. It should be able to take the measurements in vertical and in inclined flows.

With the use of the two conductive sensors, it is possible to acquire measurements of local volume fraction and local axial bubble velocities. One sensor is needed for the local volume fraction measurement, and both sensors are needed for the local velocity measurements. Also, due to the fact that water is conductive, but oil and air are not, the measured conductance is the property that is used in order to obtain the required information for the local volume fraction and the local velocity measurements. Therefore, a conductive dual sensor probe is one of the candidates that fulfils all the objectives and it is the one that was used in the current research.

3.1 Background Theory.

The operation of the dual sensor conductance probe is based on the changes of the electrical conductance in a multiphase flow. Let us assume that the probe is positioned vertically facing an oncoming bubbly air-water flow, and the surface of the gas bubble makes contact with the front sensor for the first time at some time t_{1f}, and the last time at t_{2f}. Before proceeding, it is important to note that in [118] Mishra et al showed that in multiphase flows the bubbles of the dispersed gas (in a gas-liquid flow) and disperse droplets (in a liquid-liquid flow) have an oblate spheroidal shape as they move in the continuous liquid, and that they have a plane of symmetry normal to the direction of motion. Continuing the previous assumption, let's also assume that the gas bubble surface makes first contact with the rear sensor at time t_{1r} and last

contact at time t_{2r}. The conductance measured at each sensor will change due to the bubble's presence. Figure 6 shows the bubble striking the sensors at the contact times described above.

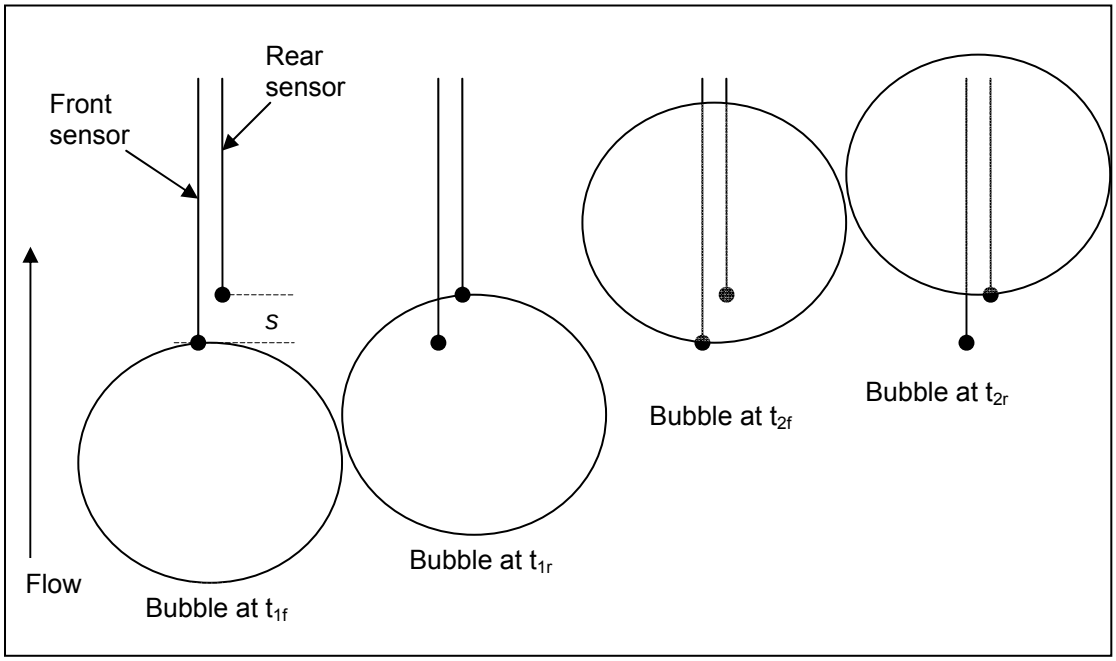

Figure 6. Bubble strikes dual sensor probe at different time intervals.

Based on the above, when the bubble first strikes the front sensor, the conductivity will fall sharply as the tip of the sensor is immersed in air (which is a non-conductive material) instead of water (which has high conductivity). As long as the tip of the sensor stays in the bubble's interior, the measured conductance stays low. When the bubble leaves the front sensor, then the conductance will sharply rise since water will surround the sensor's tip. The same events happen with the rear sensor. Figure 7 shows the conductance changes for both sensors and the times of these occurrences.

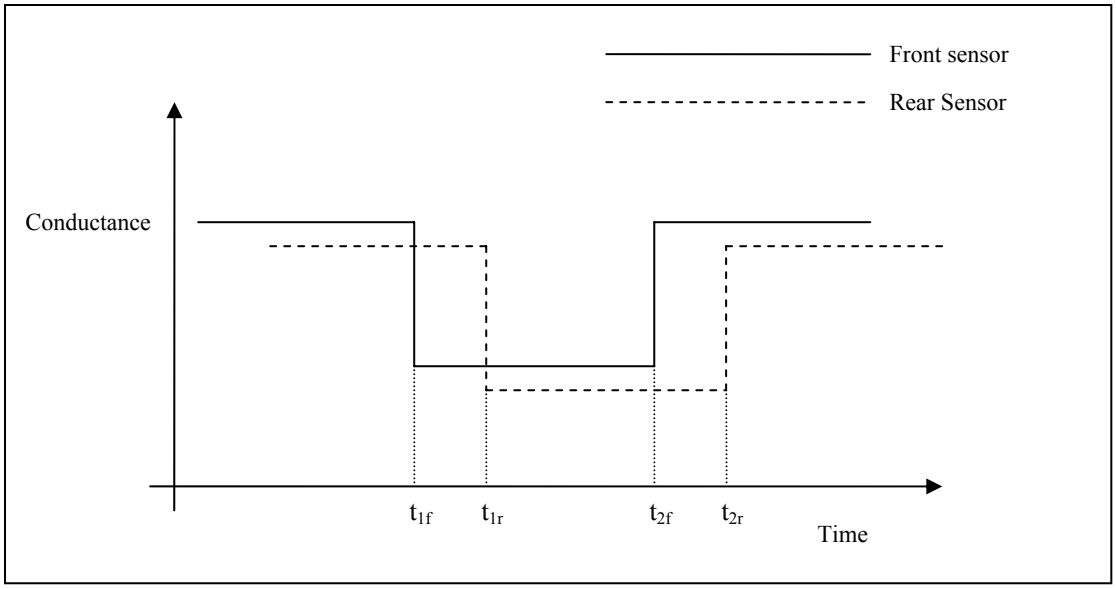

Figure 7. Ideal signals obtained from a bubble striking a dual sensor probe.

Suppose N bubbles hit both the front and the rear sensors during a sampling period T. For the i^{th} bubble, two time intervals $\delta t_{1,i}$ and $\delta t_{2,i}$ may be defined as follows:

$$\delta t_{1,i} = t_{1r,i} - t_{1f,i} \tag{10}$$

and

$$\delta t_{2,i} = t_{2r,i} - t_{2f,i} \tag{11}$$

The mean local axial bubble velocity u_{gl} at the position of the probe is then given by:

$$u_{gl} = \frac{2s}{N} \sum_{i=1}^{N} \frac{1}{\left(\delta t_{1,i} + \delta t_{2,i}\right)} \tag{12}$$

where s is the axial distance between the tips of the sensors. If the bubbles have a plane of symmetry normal to their direction of motion then use of equation (12) minimizes the errors in the calculated value of u_{gl} due to the effects of curvature of bubbles that hit the probe 'off centre', as demonstrated by Steinemann and Buchholz [114].

The mean local volume fraction α_l of the bubbles at the position of the probe can be estimated from the conductance signal from either the front or the rear sensor. If the front sensor's signal is considered, then α_l can be calculated by [14][118]:

$$\alpha_l = \frac{1}{T} \cdot \sum_{i=1}^{N} \left(t_{2f,i} - t_{1f,i} \right) \tag{13}$$

Where T is the overall sampling period as described above. It is important to mention that in real, as opposed to ideal, vertical upward air-water flows the velocities of the air bubbles are not purely axial. They have small lateral components as well. In [115] it is shown that these lateral velocity components can cause the surface of the bubble to strike both sensors nearly at the same time. This will make the values of $\delta t_{1,i}$ and $\delta t_{2,i}$ very small. Since, $\delta t_{1,i}$ and $\delta t_{2,i}$ are in the denominator of equation (12), the outcome will be a very large value for u_{gl}, which will not correspond to reality. Therefore, one way for minimising the effect of this problem in typical vertical bubbly multiphase flows, is to make the distance s (see figure 5) to be in the range between $0.5d$ and $2d$, where d is the diameter of the bubble [115].

It is important to mention that equation (12) is one of several averaging formulae that exist to calculate u_{gl}. Specifically it is the result of the simple mean value formula that everybody knows and uses in daily life activities (whenever is

required). Another average equation that could be used is the *harmonic average*. If q_1, q_2, …., q_n are real numbers then the *harmonic average* is:

$$H = \frac{N}{\sum_{i=1}^{N} \frac{1}{q_i}} \tag{14}$$

This type of average is used when mean values of rates must be calculated or when the variable is at the denominator. In the current case, the variables, which are the $\delta t_{1,i}$ $\delta t_{2,i}$, are at the denominator. So, based on the statistics [116], it is proper and sound to use the harmonic average in order to calculate the mean local bubble velocity. Therefore if $u_{b,i}$ is the velocity of an individual bubble then:

$$u_{b,i} = \frac{2s}{\delta t_{1,i} + \delta t_{2,i}} \tag{15}$$

Applying the concepts illustrated by equations (14) and (15), the harmonic mean of the local velocity u_{gl} of the dispersed gas phase is given by:

.

$$u_{gl} = \frac{N}{\sum_{i=1}^{N} \frac{1}{u_{b,i}}} = \frac{2sN}{\sum_{i=1}^{N} (\delta t_{1,i} + \delta t_{2,i})} \tag{16}$$

Equations (12) and (16) do not give the same result. Specifically, based on the measurements that will be shown in the next chapters, equation (12) overestimates the mean local velocity, whereas equation (16) underestimates u_{gl} but it gives results closer to the reference value.

In order to show what actually happens, let's assume that three bubbles hit the probe (this means that N=3), and their corresponding velocities are $u_{b,1}$=0.25ms^{-1}, $u_{b,2}$=0.3ms^{-1}and $u_{b,3}$=0.2ms^{-1}, and the distance between the tips of the sensors is s=0.0025m. Based on these, the corresponding time intervals for each bubble are $\delta t_{1,1} = \delta t_{2,1}$=0.01sec, $\delta t_{1,2} = \delta t_{2,2}$=0.0083sec, $\delta t_{1,3} = \delta t_{2,3}$=0.0125sec. Using equation (12) for calculating the mean bubble velocity yields:

$$u_{gl} = \frac{2(0.0025)}{3}\left(\frac{1}{2(0.01)} + \frac{1}{2(0.0083)} + \frac{1}{2(0.0125)}\right) = 0.25ms^{-1} \tag{16a}$$

But using equation (16) the local mean bubble velocity is:

$$u_{gl} = \frac{2(0.0025)3}{\left(2(0.01) + 2(0.0083) + 2(0.0125)\right)} = 0.2435ms^{-1} \tag{16b}$$

The author's opinion is that equation (16) (and hence (16b)) is the proper one due to the soundness of the statistical argument. It also eliminates the possibility of isolated incidences of very small $\delta t_{1,i}$ and $\delta t_{2,i}$ for a given bubble causing a very large contribution to the mean bubble velocity.

The same example can be described as having one bubble that travels distance s for δt_1, then the same distance for δt_2, and finally the same distance for δt_3. The average speed of the bubble is 0.2435msec^{-1} and not 0.25msec^{-1}. Finally, it is important to note that the equation used for the calculation of the mean bubble velocities in the current thesis was equation 16, whilst in previous work [14] equation 12 was used.

4. Construction of the dual sensor probe and its ancillaries.

4.1 Probe design and fabrication.

The main concept of the probe's operation is that each sensor injects current into the multiphase mixture which then flows to a common electrode. This common electrode is the metal tube that supports the sensors and is the main body of the probe. Figure 8 shows the main concept of the dual sensor conductance probe.

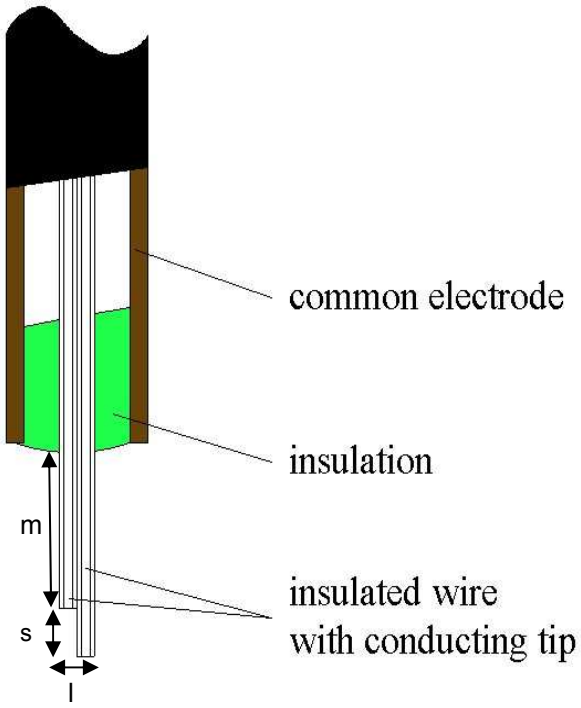

Figure 8. Dual sensor probe design concept.

As can be seen from figure 8, the sensors are covered with an insulating material and only their tips are exposed to the flow. As long as the probe is immersed in the water (which is a conductive medium) then current flows from each sensor to the common electrode. When a bubble of air or oil strikes a sensor then the current flow between the tip of the sensor and the main body of the probe is interrupted and no current flows, due to the fact that air and oil are non-conductive media.

Also, the probe is positioned in the flow in such a way that the tips of the sensors face the oncoming flow. It is proper to mention that the longest sensor is referred as the front sensor and the shortest one as a rear sensor. So, the air or oil bubbles strike first the front sensor and then the rear sensor.

Three parameters characterise the dual sensor probe. These are the axial distance *s* between the tips of the sensors, the distance *m* between the tip of the rear sensor and the main body of the probe, and the lateral distance *l* between the centre lines of the sensors. From all these three parameters the one that most significantly affects the performance of the probe is the distance *s*. As described by Wu et al in [115] the distance *s* must be between 0.5*d* and 2*d*, where *d* is the mean diameter of the bubbles of the dispersed phase. Generally, the reason behind this rule is that if the distance is longer than the 2*d* then it is difficult to correlate the signals from the two sensors. If the distance is shorter than 0.5*d* then limitations in the acquisition procedure occur. For the probes used in the experiments, the axial sensor separation *s* was typically 5mm and 2.5mm whilst the lateral sensor separation was typically 1mm. Since the mean bubble diameter in the experiments was about 5mm, the value for *s* was comfortably within the range suggested by Wu et al. [115]. The distance *m* from the tip of the rear sensor to the support tube was typically about 10mm.

The components and materials chosen for fabricating the probes were the following:

- 0.3mm diameter stainless steel acupuncture needles as sensing electrodes.
- Stainless steel tubing as common electrode (2.65mm O/D, 2.1mm I/D).
- Resin based two component glue for bonding parts.
- Waterproof model paint and silicon coating for insulating the needles.

- 30 AWG silver-plated copper wire for connecting the needles with the measurement electronics.
- Silver loaded conducting paint for connecting wire to the needles.

The reason for using acupuncture needles was that they have very small diameter (0.3mm), they are rigid, and they have a straight uniform shape. The small needle diameter is an advantage due to the fact that it minimises the interaction between the sensor and the bubble, thereby minimising the probe influence on the bubble's characteristics and dynamics. The rigidity and the uniform shape of the needles give the advantages of repeatably assembling sensors with similar characteristics.

The stainless steel tube holds and supports the sensors and works as the common electrode. There are no critical parameters regarding the tube. The only thing that should be mentioned is that the top of the tube is bent at an angle of 90^0, to enable it to emerge through the pipe wall when it is mounted in the traverse mechanism, a device that is going to be described in chapter 7.

Two coatings have been used for insulating the needles. One is a waterproof paint, and the other was initially an insulating varnish. The waterproof paint isolates the sensor from the water so no contact with it could occur (which would create false measurements). The insulating varnish creates an extra protective layer for the sensor from the environment. Due to the fact that the varnish coating was difficult and time consuming to apply on the sensors, this technique was abandoned and changed into applying a silicon coating to the fabricated sensors. This method was easier and less time was spent, but the coating was not entirely uniform. However the performance of the probe was not appreciably affected because of this non-uniformity.

The steps that were used for the construction of the dual sensor probe are described below.

Step 1: cut the stainless steel tube, the needles and the wire to length; use different colour wire for the 2 sensors.

Step 2: to achieve small lateral needle spacing bend blunt end of one needle so as to allow sufficient space for wires to be connected to needles.

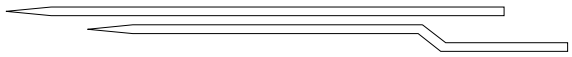

Step 3: clean needles from dust and grease and remove wire insulation of first few millimetres and twist around blunt end of needles.

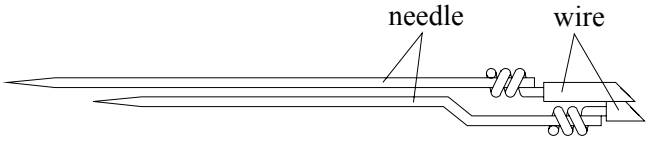

Step 4: apply conducting paint to glue the wire-needle connections.

Step 5: clean needles and apply paint/varnish coatings of sufficient thickness on all conducting areas (needle and conducting paint).

Step 6: remove insulation from tips of needles with fine sand paper.

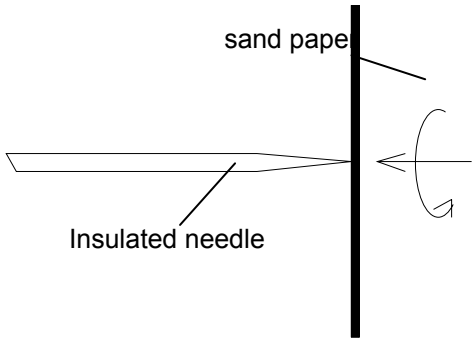

Step 7: arrange needles in parallel with required axial and lateral spacing, use two pieces of magnetic foil to hold needles in place, then glue assembly.

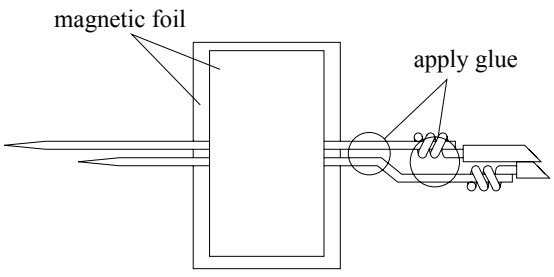

Step 8: insert needle assembly into stainless steel tube and bond with two component glue. Glue far end of tube where wires come out for strain relief of needles.

Step 9: measure probe dimensions. A shadowgraph was used for measuring the probe's dimensions.

So, following the above procedure, the assembled dual sensor probe is shown diagrammatically in figure 9 (right). A picture of two dual sensors that have been made is shown in figure 9 (left).

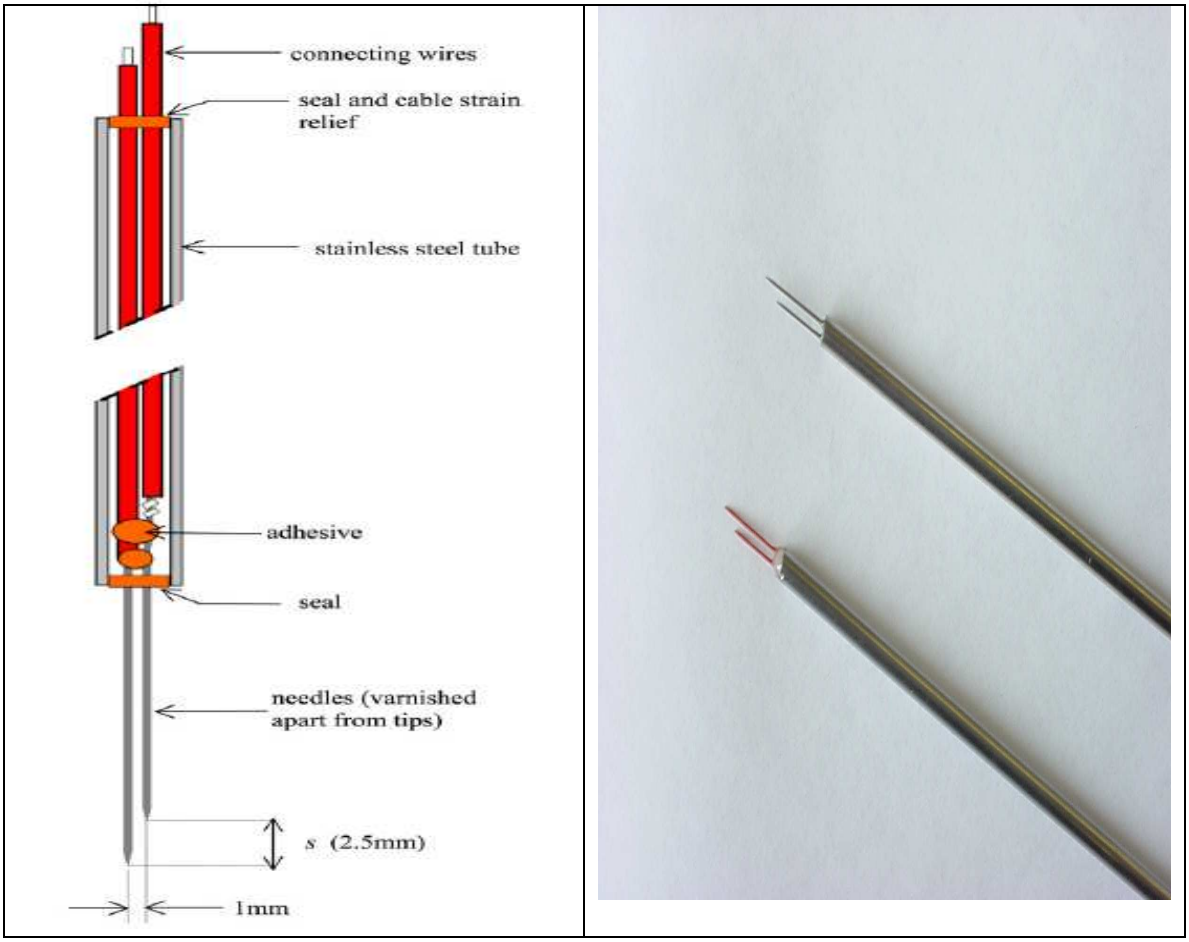

Figure 9. Left: Schematic of dual sensor probe. Right: Two of the many dual sensor probes that have been fabricated.

To measure the distance between the tips of the sensors after the fabrication, the University's shadowgraph was used. This system has a maximum magnification of 100x. Using a caliper rule with a resolution of 0.02mm for taking measurements on

the shadow-graph screen, the maximum theoretical resolution is therefore 0.2μm, but is limited by the precision by which ruler and shadow boundary can be lined up.

4.2 The interface circuit.

The purpose of the interface circuit is to transform changes of conductance into voltage changes. There are two types of circuit that can satisfy the objective. One is to use an ac-based circuit and the other is to use a dc-based circuit. The advantage of an ac circuit is that the problem of electrolysis is reduced. The disadvantage is that a demodulator is needed, which in turn requires a low-pass filter. This would filter out high frequency components during the transitions which occur when a bubble strikes a sensor. This in turn would make accurate identification of the transition times more difficult. A dc-based circuit does not need a demodulator and a low pass filter; therefore high frequency signal components will not be eliminated. The disadvantage of the dc-based circuit is that it causes electrolysis. Due to electrolysis, the performance of the probe is reduced. The reasons for this are that (i) particles from the insulation may become loosened and (ii) dirt or particles that exist in the flow are attracted by the tips of the sensors due to the fact that the electrical field is more intense at the tips of the sensors. The result of the latter event is that the sensor tips can become partially or wholly covered by a non-conducting film of dirt and the acquired signal's characteristics are altered, creating errors in the signal processing scheme. The solution for this problem is to clean the tips of the probe when it is observed that the probe's performance has started to deteriorate. Of course this means that an extra maintenance procedure must be implemented. Figure 10 shows how the tip of a sensor is affected by the electrolysis and improved after cleaning procedure.

Figure 10. Sensor tip – before electrolysis (left), after electrolysis (middle), and after cleaning (right). Images are from shadow-graph.

The type of interface circuit that was used in the experiments was a dc-based circuit using a non-inverting amplifier. The output voltages when the tip of the probe is immersed in water or in a non-conducting medium (air or oil) are derived below. Figure 11 shows the dc-based circuit diagram that was used in the experiments.

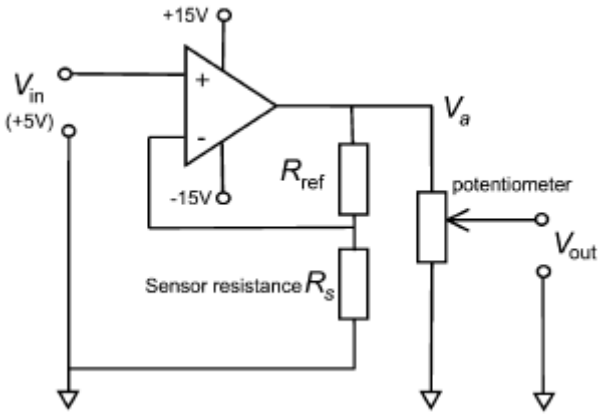

Figure 11. Outline diagram of circuit used to measure conductance changes. R_{ref} is typically 1.5 MΩ.

Note that the circuit shown in the figure 11 is connected with one sensor. So, for a dual sensor probe two of these circuits are used one for each sensor. The main advantage of this circuit is that when the sensor is immersed in conducting water, V_{out} is equal to the positive rail voltage and will therefore not drift or fluctuate. Due to the sharp gradients that occur when a non-conducting bubble strikes the sensor, identification of the contact time is thus made relatively easy.

The output voltage V_a from the operational amplifier in the circuit shown in figure 11 is:

$$V_a = V_{in}\left(1 + \frac{R_{ref}}{R_s}\right) \tag{17}$$

When the tip of a given acupuncture needle is immersed in water R_s is relatively small compared to R_{ref} (which has a typical value of 1.5 MΩ) and so V_a saturates at the positive rail voltage used to supply the operational amplifier (+15V). When the tip of the acupuncture needle is immersed in air or oil bubble, the quantity R_{ref}/R_s approaches zero and so V_a approaches V_{in} (+5V). The potentiometer shown in figure 14 is used to scale the voltage V_a from each sensor to provide an output voltage V_{out} which covers the full range of the analogue to digital converters of the data acquisition system that was used and which will be described later.

Figure 12 shows typical voltage output voltage signals from two such circuits when a bubble strikes both sensors.

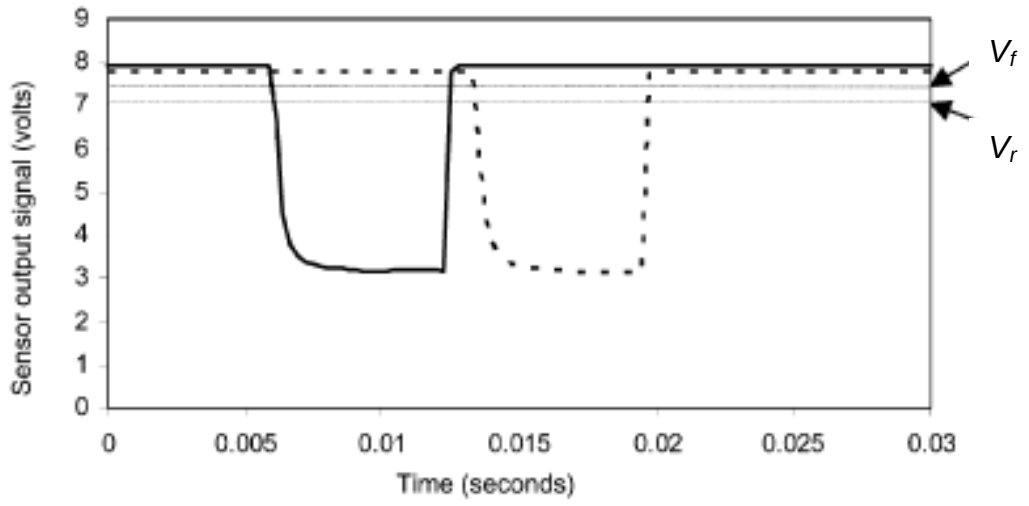

Figure 12. The solid and dashed lines are portions of real output signals obtained from the front and rear sensors, respectively.

4.3 Signal processing scheme.

The dual sensor probe described in the previous section was used to make measurements in vertical upward, bubbly air–water and oil-water flows in an 80 mm

internal diameter pipe as will be described later in this thesis. At each flow condition, the dual sensor probe was successively moved to distinct spatial locations in the flow cross-section using an automatic traversing mechanism, which will also be described later. At each spatial location, the probe was used to obtain signals from the flowing air bubbles for a period of 30s and these signals were then stored on a computer hard drive with the appropriate file format for later processing. After data was taken at each of the distinct spatial locations in the flow cross-section, it was processed off-line in the following manner.

Real signals from the two sensors are shown in Fig. 12. It was found [129] that the best estimates for the mean local gas volume fraction α_l and the mean local axial bubble velocity u_{gl} were obtained if threshold voltages V_f and V_r were defined for the front and rear sensors, respectively, as shown in Fig. 12. This need to use threshold voltages arises from the fact that there is a small reduction in the measured conductance from a given sensor just before a bubble of the dispersed phase actually touches the sensor. This initial drop in conductance is probably due to the air or oil bubble partially blocking the flow of electrical current through the water from the sensor tip to the earthed probe body. For a similar reason, the measured sensor conductance does not return to its maximum value until a short time after the bubble has ceased to be in contact with the sensor. Thus, the times $t_{1f,i}$ and $t_{2f,i}$ at which the surface of the i^{th} bubble comes into contact with the front sensor occur when the output voltage from the front sensor is at a value V_f. Similarly, the times $t_{1r,i}$ and $t_{2r,i}$ at which the surface of the i^{th} bubble comes into contact with the rear sensor occur when the output voltage from the rear sensor is at a value V_r. For a given flow condition, the values of V_f and V_r were calculated as follows by making use of a

reference measurement $\overline{\alpha}_{ref}$ of the area averaged gas or oil volume fraction, obtained using a differential pressure global measurement technique (see chapter 7)[129].

If we consider the front sensor, an initial value of V_f is guessed and then the local gas or oil volume fraction is obtained for each of the spatial locations of the probe using Eq. 13. If, at the j^{th} spatial location, the mean local dispersed phase volume fraction is $\alpha_{1,j}$ then an estimate $\overline{\alpha}_{est}$ of the area average volume fraction can be made using the following expression [129]

$$\overline{\alpha}_{est} = \frac{\sum_{j=1}^{81} \alpha_{1,j} A_j}{A} \tag{18}$$

where A is the cross-sectional area of the flow and where A_j is the cross sectional area of the j^{th} of the discrete regions into which the flow cross-section is divided, the j^{th} discrete region corresponding to the j^{th} spatial location of the probe. If $\overline{\alpha}_{est}$ is not equal to $\overline{\alpha}_{ref}$ (a reference measurement of the global mean volume fraction as described in chapter 7), then the threshold voltage V_f is adjusted and the process repeated. When $\overline{\alpha}_{est}$ and $\overline{\alpha}_{ref}$ are equal, the relevant value of V_f is used to determine the bubble contact times $t_{1f,i}$ and $t_{2f,i}$ which in turn are used, in conjunction with Eq.13, to produce the measurements of the local volume fraction of the dispersed phase which are shown in this thesis. A similar procedure to that outlined above is used to determine the threshold voltage V_r for the rear sensor, from which the bubble contact times $t_{1r,i}$ and $t_{2r,i}$ are determined. Note that this method for setting the threshold voltages is very straightforward because the reference measurement $\overline{\alpha}_{ref}$ is very simple to make. The technique described herein therefore represents a significant

improvement over the complex and often subjective signal processing techniques described elsewhere; see for example Liu [117] [129]

Once $t_{1f,i}$, $t_{2f,i}$, $t_{1r,i}$ and $t_{2r,i}$ have been found for a given probe location at a particular flow condition, Eq. 16 can be used to determine the local axial dispersed phase velocity u_{dl} at that spatial location of the probe. However, two additional signal processing features were introduced, as described below, to make the local axial bubble velocity estimates as accurate as possible. As described previously (section 3.1), bubbles with significant lateral velocities can strike both the front and rear sensors virtually simultaneously giving rise to very small values for $\delta t_{1,i}$ and $\delta t_{2,i}$ and hence (with reference to Eq. 14) causing gross overestimates in the value of u_{dl}. In an attempt to counteract this phenomenon, a minimum time interval dt_{min} was introduced such that [129]: if $\delta t_{1,i} < \delta t_{min}$ or $\delta t_{2,i} < \delta t_{min}$ then the i^{th} bubble is ignored when calculating u_{dl}. This is referred to as "Criterion 1" of the signal processing scheme. For a given flow condition, the value of δt_{min} was found in the following way. A global mean velocity $\overline{u}_{d,ref}$ of the dispersed phase was obtained from reference measurements of the dispersed phase volumetric flow rate Q_d and the area average disperse phase volume fraction $\overline{\alpha}_{ref}$ using the relationship below [129]:

$$\overline{u}_{d,ref} = \frac{Q}{A\overline{\alpha}_{ref}} \tag{19}$$

An estimate $\overline{u}_{d,est}$ of the mean dispersed phase velocity can then be obtained using the following expression [129]

$$\bar{u}_{d,est} = \frac{\sum_{j=1}^{81} u_{d1,j}\alpha_{1,j}A_j}{\sum_{j=1}^{81} \alpha_{1,j}A_j} \tag{20}$$

where for the *jth* probe location $u_{d1,j}$ is calculated from Eq.16 and $\alpha_{1,j}$ is calculated from Eq. 13. With δt_{min} set to zero (in the Criterion 1) $\bar{u}_{d,est}$ is generally greater than $\bar{u}_{d,ref}$. However, for any particular flow condition, a value of δt_{min} can be found for which $\bar{u}_{d,est}$ is equal to $\bar{u}_{d,ref}$. For the given flow condition, this value of δt_{min} was subsequently used in calculating values of the local axial velocity u_{dl} from Eq. 16, in conjunction with Criterion 1. A typical value for δt_{min} was 2.5×10^{-4}s [129].

An extra criterion was also used for calculating the local axial dispersed phase velocity, in order to eliminate a further potential source of error. The following argument will be applied only to the case of bubbly air-water flows however it is easily adapted to the case of bubbly oil-in-water flows. The slip velocity of a 5mm air bubble in static water is approximately equal to $0.25 ms^{-1}$ and so in a vertical upward air–water flow, the maximum time taken for a gas bubble to travel the axial distance *s* between the two sensors of the probe would be expected to be *s*/0.25 (close to the pipe walls it could take slightly longer than this because, as noted by Steinemann and Buchholz [114], there may be a moderate down flow of water at the walls). So, for example if *s*=5mm the maximum time taken for a bubble to travel between the front and rear sensor is about 0.02s. A time interval δt_{max} can be defined (which is slightly greater than *s*/0.25) and which represents the maximum expected transit time of a gas bubble between the two sensors of the dual sensor probe. If, for what is assumed to be the i^{th} bubble, either $\delta t_{1,i}$ or $\delta t_{2,i}$ is greater than δt_{max} then it is highly unlikely that a

single bubble is responsible for producing the signals at the two sensors. A more likely explanation is that the bubble striking the front sensor misses the rear sensor and that, slightly later, a different bubble strikes the rear sensor having missed the front sensor (the phenomenon of missing bubbles is discussed in detail by Liu [117]). To prevent inaccuracies in the estimate of u_{dl} the following criterion was introduced [129] (for air-water experiments): if $\delta t_{1,i} > \delta t_{max}$ or $\delta t_{2,i} > \delta t_{max}$ then what is assumed to be the i^{th} bubble is ignored when calculating u_{dl}. This is referred to "Criterion 2" of the signal processing scheme.

Criterion 2 was particularly helpful in ensuring that values of the local axial dispersed phase velocity u_{dl} were not underestimated. In the present investigation, for air water flows, a conservative value of δt_{max} equal to 0.05s was employed (for oil-water flows the value of 0.008s was taken). The local axial bubble velocity profiles shown in chapter 8 were obtained using Eq. 16 in conjunction with the Criteria 1 and 2.

5. Theory of the four sensor probe.

The four sensor probe is able to measure more characteristics of the dispersed phase in bubbly flows than the dual sensor probe. These characteristics are the volume fraction (which is a property that is measured by the dual sensor probe too), and the vector velocity of the bubble. The dual sensor probe measures only the magnitude of the bubble's velocity in the axial direction. The four sensor probe is able to measure the velocity magnitude and the direction of the bubble. For this extra information another two sensors are needed, hence the concept of the four sensor probe. So, this type of device has one lead sensor and three rear sensors. Next a detailed description and analysis of the four sensor probe is presented.

5.1 The model.

5.1.1 Preliminary information and assumptions.

Before describing the model and analysis of the four sensor probe, it is proper to present the assumptions and the conditions that should be taken account before the model is applied. The probe and the corresponding model are applicable to bubbly multiphase flows, where the continuous phase is a conducting liquid and the dispersed phase is a non-conductive gas or liquid. In the current research, the probe and its model were used in air-water and oil-water bubbly flows.

The following assumptions are made for the development of the model used to determine the bubble/droplet vector velocity from measurements from the four sensor probe:

- Each droplet (or bubble) has a plane of symmetry normal to its direction of motion. Such droplet shapes include spheres and oblate spheroids. As it is reported in [118], oil droplets or gas bubbles of the dispersed phase are

flattened in their direction of motion due to their velocity relative to the continuous phase. Experimental observations that occurred in [118] showed that oil droplets with small diameters (about 4mm) had spherical shapes, while bigger droplets tended to have oblate spheroidal shapes with a major axis length up to about 8mm.

- The droplets strike the front sensor first and then the rear sensors.
- The surface of each droplet hits all four sensors twice. The first time is when the droplet initially contacts a sensor. The second time is when the droplet leaves the sensor.
- The sensors do not alter the droplet's characteristics (shape and velocity vector).
- When a droplet strikes a sensor, the sensor output signal has a shape similar to those shown in figure 12 in chapter 4.

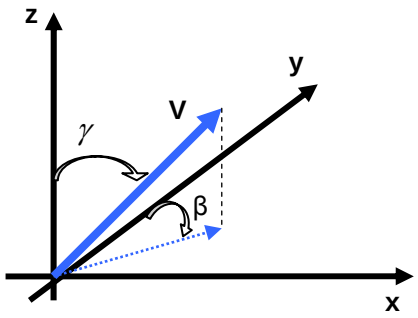

Figure 13. Vector V in a 3D polar coordinate system and its projection on to the x-y plane.

The velocity vector **V** of the droplet can be represented mathematically using the coordinate system shown in figure 13.

$$\mathbf{V} = v\left(\sin\gamma\sin\beta\,\mathbf{i} + \sin\gamma\cos\beta\,\mathbf{j} + \cos\gamma\,\mathbf{k}\right) \tag{21}$$

or

$$\mathbf{V} = v\hat{n}_v \tag{22}$$

where γ is the polar angle between the z-axis and the vector **V**, β is the azimuthal angle between the y-axis and the projection of vector **V** onto x-y plane, v is the magnitude of the vector **V**, $\hat{n}_v$ is the unit vector in the direction of **V**, and **i, j, k** are the unit vectors in the direction of the x, y, and z axes respectively. So, in order to find the velocity vector of a bubble it is necessary to find the three parameters that define it. These are the polar angle (γ), the azimuthal angle (β), and the velocity magnitude (v).

5.1.2 Derivation of the equations that describe the velocity vector.

Let us assume that a bubble moves with a velocity vector **V** (which can be described from equations 21 and 22) and strikes the four sensor probe. Also, let us take the case where the bubble strikes the front sensor (which has 0 as an index) and then strikes the rear sensor with 1 as an index. Figures 14 and 15 show this case.

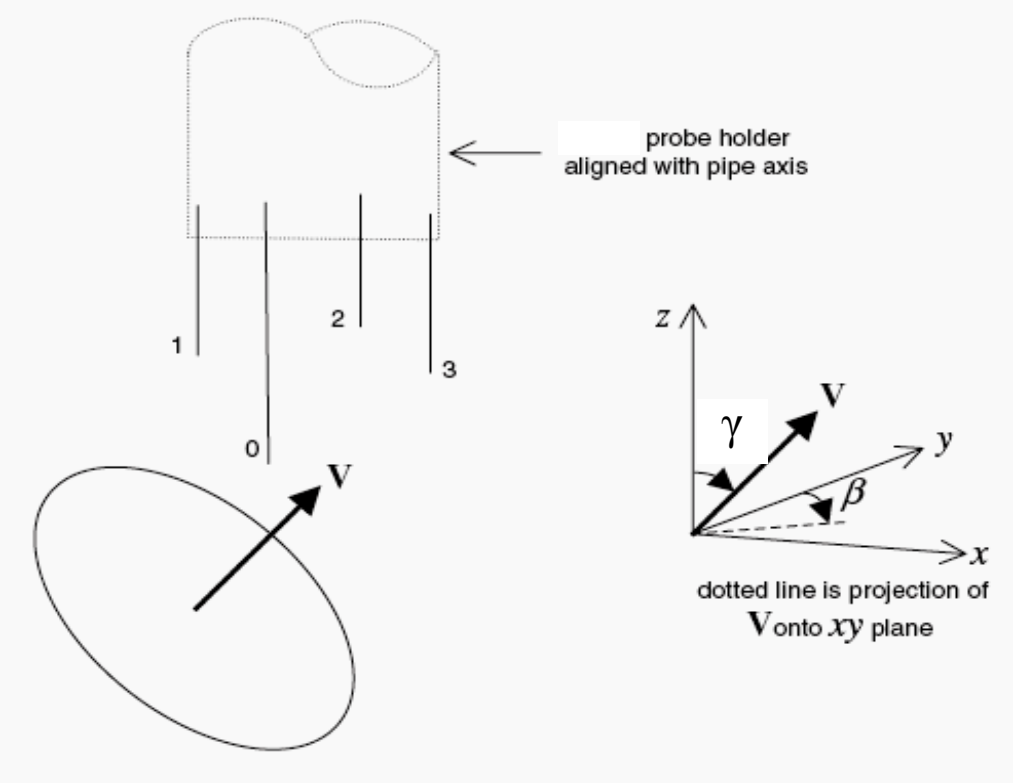

Figure 14. Bubble with vector velocity moving across the four sensor probe.

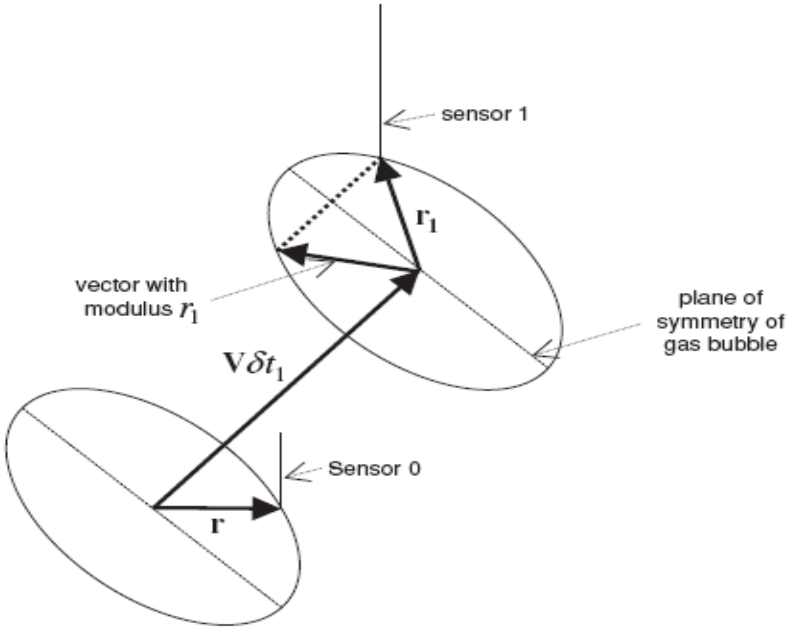

Figure 15. Motion of bubble between front sensor 0 and rear sensor 1.

When the bubble strikes the front sensor 0 for first time then a position vector **r** is created between the centre of the bubble and the point that contacts the sensor (see figure 15). This position vector can be expressed as $\mathbf{r}=r\hat{\eta}_i$, where $\hat{\eta}_i$ is a unit vector. After some time δt_1 the bubble strikes the rear sensor 1, which is located at (x_1,y_1,z_1) with respect to the front sensor. The position vector $\mathbf{r_1}$ of this point of contact with sensor 1 relative to the centre of the droplet can be given as that:

$$\mathbf{r_1} = \left(\mathbf{r} + x_1\mathbf{i} + y_1\mathbf{j} + z_1\mathbf{k} - \mathbf{V}\delta t_1\right) \tag{23}$$

From equation (23) the following equation can be written, where r_1 is the magnitude of $\mathbf{r_1}$:

$$(\mathbf{r} + x_1\mathbf{i} + y_1\mathbf{j} + z_1\mathbf{k} - \mathbf{V}\delta t_1)\,.\,(\mathbf{r} + x_1\mathbf{i} + y_1\mathbf{j} + z_1\mathbf{k} - \mathbf{V}\delta t_1) = r_1^2 \tag{24}$$

Expanding the bracket in equation (24), and writing $\mathbf{V} = v\hat{\eta}_v$ and $\mathbf{r} = r\hat{\eta}_i$ we have:

$$\begin{aligned} &r^2 + rx_1(\hat{\eta}_i.\mathbf{i}) + ry_1(\hat{\eta}_i.\mathbf{j}) + rz_1(\hat{\eta}_i.\mathbf{k}) - rv\delta t_1\ (\hat{\eta}_i.\hat{\eta}_v) + rx_1(\hat{\eta}_i.\mathbf{i}) + x_1^2 - x_1 v\,\delta t_1(\hat{\eta}_v.\mathbf{i}) \\ &+ ry_1(\hat{\eta}_i.\mathbf{j}) + y_1^2 - y_1 v\,\delta t_1(\hat{\eta}_v.\mathbf{j}) + rz_1(\hat{\eta}_i.\mathbf{k}) + z_1^2 - z_1 v\,\delta t_1(\hat{\eta}_v.\mathbf{k}) - rv\,\delta t_1(\hat{\eta}_v.\hat{\eta}_i) \\ &- vx_1\delta t_1(\hat{\eta}_v.\mathbf{i}) - vy_1\delta t_1(\hat{\eta}_v.\mathbf{j}) - vz_1\delta t_1(\hat{\eta}_v.\mathbf{k}) + v^2\delta t_1^2 = r_1^2 \end{aligned} \tag{25}$$

Which can be written as

$$\begin{aligned} &v^2\delta t_1^2 - v\,\delta t_1\left[2r\,(\hat{\eta}_i.\hat{\eta}_v) + 2x_1(\hat{\eta}_v.\mathbf{i}) + 2y_1(\hat{\eta}_v.\mathbf{j}) + 2z_1(\hat{\eta}_v.\mathbf{k})\right] + \\ &\left[x_1^2 + y_1^2 + z_1^2 + 2rx_1(\hat{\eta}_i.\mathbf{i}) + 2ry_1(\hat{\eta}_i.\mathbf{j}) + 2rz_1(\hat{\eta}_i.\mathbf{k}) + r^2 - r_1^2\right] = 0 \end{aligned} \tag{25a}$$

The equation 25a is quadratic in δt_1 and has two solutions for δt_1 which are:

$$\delta t_{1a} = \frac{-b - \sqrt{b^2 - 4ac}}{2a} \tag{26}$$

$$\delta t_{1b} = \frac{-b + \sqrt{b^2 - 4ac}}{2a} \tag{27}$$

where

$$a = v^2 \tag{28}$$

and

$$b = -v\left[2r\,(\hat{\eta}_i.\hat{\eta}_v) + 2x_1(\hat{\eta}_v.\mathbf{i}) + 2y_1(\hat{\eta}_v.\mathbf{j}) + 2z_1(\hat{\eta}_v.\mathbf{k})\right] \tag{29}$$

and

$$c = \left[x_1^2 + y_1^2 + z_1^2 + 2rx_1(\hat{\eta}_i.\mathbf{i}) + 2ry_1(\hat{\eta}_i.\mathbf{j}) + 2rz_1(\hat{\eta}_i.\mathbf{k}) + r^2 - r_1^2\right] \tag{30}$$

The first solution for δt_1 is δt_{1a} and is the time interval between the first contact of the bubble with the front sensor 0 and the first contact of the bubble with the rear sensor 1. The second solution for δt_1 is δt_{1b} which is the time interval between the first contact of the bubble with the front sensor 0 and the last contact of the bubble with the rear sensor 1. Based on the assumption that the bubbles have a plane of symmetry normal to their direction of motion, it is valid to conclude that r_1 is

the same for the first and last contacts of the droplet with the rear sensor. Therefore with reference to figure 15, the terms *a, b,* and *c* have the same values for the first and last contacts and so equations (26) and (27) can be combined into:

$$\delta t_{1a} + \delta t_{1b} = -\frac{b}{a} \tag{31}$$

Applying equations (28) and (29) to equation (31), the result is:

$$\delta t_{1a} + \delta t_{1b} = \frac{\left(2r\left(\hat{n}_i \cdot \hat{n}_v\right) + 2x_1\left(\hat{n}_v \cdot \mathbf{i}\right) + 2y_1\left(\hat{n}_v \cdot \mathbf{j}\right) + 2z_1\left(\hat{n}_v \cdot \mathbf{k}\right)\right)}{v} \tag{32}$$

Using the same procedure for the other two rear sensors, the corresponding equations are:

$$\delta t_{2a} + \delta t_{2b} = \left[2r\left(\hat{\eta}_i.\hat{\eta}_v\right) + 2x_2\left(\hat{\eta}_v.\mathbf{i}\right) + 2y_2\left(\hat{\eta}_v.\mathbf{j}\right) + 2z_2\left(\hat{\eta}_v.\mathbf{k}\right)\right]/v \tag{33}$$

$$\delta t_{3a} + \delta t_{3b} = \left[2r\left(\hat{\eta}_i.\hat{\eta}_v\right) + 2x_3\left(\hat{\eta}_v.\mathbf{i}\right) + 2y_3\left(\hat{\eta}_v.\mathbf{j}\right) + 2z_3\left(\hat{\eta}_v.\mathbf{k}\right)\right]/v \tag{34}$$

Looking at the equations (32-34) one observes that there are three equations with four unknowns, which are $r, v, \hat{n}_i, \hat{n}_v$. This problem can be overcome by considering the time δt_{0b}, which is the time between the first and last contact of the bubble with the front sensor only. Therefore, applying the same concept that was used for deriving equations (32-34) to the front sensor, another equation is produced which is:

$$\delta t_{oa} + \delta t_{ob} = \left[2r\,(\hat{\eta}_{\mathrm{i}}.\hat{\eta}_v) + 2x_0(\hat{\eta}_v.\mathbf{i}) + 2y_0(\hat{\eta}_v.\mathbf{j}) + 2z_0(\hat{\eta}_v.\mathbf{k})\right]/v \tag{35}$$

But $x_0 = y_0 = z_0 = 0$ (since the origin of the coordinate system is the tip of the front sensor). So, equation (35) can be written as:

$$\delta t_{oa} + \delta t_{ob} = \left[2r\,(\hat{\eta}_{\mathrm{i}}.\hat{\eta}_v)\right]/v \tag{36}$$

But since the time starts when the bubble hits the front sensor for the first time, it is sound to accept that $\delta t_{0a} = 0$.

Based on the above, it is sound and valid to subtract the time quantity δt_{0b} from equations (33-35). Therefore defining δt_{11}, δt_{22} and δt_{33} as follows:

$$\delta t_{11} = \delta t_{1a} + \delta t_{1b} - \delta t_{0b} \tag{37}$$

$$\delta t_{22} = \delta t_{2a} + \delta t_{2b} - \delta t_{0b} \tag{38}$$

$$\delta t_{33} = \delta t_{3a} + \delta t_{3b} - \delta t_{0b} \tag{39}$$

From equations 33-35 and 37-39 the final equations that describe the vector velocity of a bubble that hits a four sensor probe are derived as follows:

$$x_1 \sin\gamma \sin\beta + y_1 \sin\gamma \cos\beta + z_1 \cos\gamma = \frac{v\delta t_{11}}{2} \tag{40}$$

$$x_2 \sin\gamma \sin\beta + y_2 \sin\gamma \cos\beta + z_2 \cos\gamma = \frac{v\delta t_{22}}{2} \tag{41}$$

$$x_3 \sin\gamma \sin\beta + y_3 \sin\gamma \cos\beta + z_3 \cos\gamma = \frac{v\delta t_{33}}{2} \tag{42}$$

These three equations (40-42) have three unknowns. So, it is possible to solve them and find the formulae to give the polar angle γ, the azimuthal angle β, and the velocity magnitude v of the velocity vector of the bubble.

5.1.3 Solution of the equations and the derived formulae.

The solution of equations (40-42) is shown below. From (40) solving for v:

$$v = \sin\gamma\left(V_{x1}\sin\beta + V_{y1}\cos\beta\right) + V_{z1}\cos\gamma \tag{43}$$

where V_{xi}, V_{yi}, and V_{zi} are equal to $\frac{2x_i}{\delta t_{ii}}, \frac{2y_i}{\delta t_{ii}}, \frac{2z_i}{\delta t_{ii}}$ respectively and i is the index for the rear sensors which takes values from 1 to 3. Applying equation 43 to 41 gives:

$$\sin\gamma\left(V_{x1}\sin\beta + V_{y1}\cos\beta\right) + V_{z1}\cos\gamma = \sin\gamma\left(V_{x2}\sin\beta + V_{y2}\cos\beta\right) + V_{z2}\cos\gamma \Rightarrow$$

$$\tan\gamma\left(V_{x1}\sin\beta + V_{y1}\cos\beta\right) + V_{z1} = \tan\gamma\cdot\left(V_{x2}\sin\beta + V_{y2}\cos\beta\right) + V_{z2} \Rightarrow$$

$$\tan\gamma = \left(\frac{V_{z2} - V_{z1}}{\left(V_{x1} - V_{x2}\right)\sin\beta + \left(V_{y1} - V_{y2}\right)\cos\beta}\right) \tag{44}$$

Applying equation 43 to 42 and doing the same algebraic manipulations:

$$\tan\gamma = \left(\frac{V_{z3} - V_{z1}}{\left(V_{x1} - V_{x3}\right)\sin\beta + \left(V_{y1} - V_{y3}\right)\cos\beta}\right) \tag{45}$$

Equating equations 44 and 45 gives:

$$\left(\frac{V_{z2}-V_{z1}}{(V_{x1}-V_{x2})\sin\beta+(V_{y1}-V_{y2})\cos\beta}\right)=\left(\frac{V_{z3}-V_{z1}}{(V_{x1}-V_{x3})\sin\beta+(V_{y1}-V_{y3})\cos\beta}\right)\Rightarrow$$

$$\frac{V_{z3}-V_{z1}}{V_z-V_{z1}}=\frac{(V_{x1}-V_{x3})\sin\beta+(V_{y1}-V_{y3})\cos\beta}{(V_{x1}-V_{x2})\sin\beta+(V_{y1}-V_{y2})\cos\beta}$$

After some algebraic manipulations, the equation for calculating β in its final form is:

$$\tan\beta=\frac{\left(\frac{z_1}{\delta t_{11}}-\frac{z_2}{\delta t_{22}}\right)\left(\frac{y_1}{\delta t_{11}}-\frac{y_3}{\delta t_{33}}\right)-\left(\frac{z_1}{\delta t_{11}}-\frac{z_3}{\delta t_{33}}\right)\left(\frac{y_1}{\delta t_{11}}-\frac{y_2}{\delta t_{22}}\right)}{\left(\frac{z_1}{\delta t_{11}}-\frac{z_3}{\delta t_{33}}\right)\left(\frac{x_1}{\delta t_{11}}-\frac{x_2}{\delta t_{22}}\right)-\left(\frac{z_1}{\delta t_{11}}-\frac{z_2}{\delta t_{22}}\right)\left(\frac{x_1}{\delta t_{11}}-\frac{x_3}{\delta t_{33}}\right)} \tag{46}$$

Once γ (eq. 44) and β (eq. 46) have been determined the magnitude v of the vector can be found using any one of the three equations (40)-(42) by substituting the relevant values for γ and β. It is interesting to point out that for the γ angle there are two equations (44 and 45) for calculating it.

5.1.4 Comments on the model.

From the solutions, it is obvious that in order to calculate the bubble vector velocity the dimensions of the probe must be measured and also the time delays of each sensor when a bubble strikes the probe. Note that the dimensions of the probe are the x, y, and z distances of the tips of the rear sensors, having the tip of the front sensor as the origin of a 3D Cartesian space. Also, knowing the velocity magnitude v, the polar angle γ, and the azimuthal angle β it is possible to compute the velocity components V_z, V_r, V_θ of the bubble in a pipe coordinate system as follows..

$$V_\theta = v\sin\gamma\sin\beta \tag{47}$$

$$V_r = v \sin\gamma \cos\beta \tag{48}$$

$$V_z = v \cos\gamma \tag{49}$$

Eqns 47, 48 and 49 assume that the probe is aligned in the pipe such that the probe's increasing z-axis is in the direction of the pipe axis (in the direction of the flow) and the probe's increasing y-axis lies along a radius of the pipe (in the direction from the pipe centre to the pipe wall). Thus V_z can be considered as the axial velocity component of the bubble, V_r can be considered as the radial velocity component and V_θ can be considered as the azimuthal velocity component. Based on these definitions it is obvious that a positive axial velocity means that the bubbles go upwards (if the probe faces the bubble's direction), a positive radial velocity means that the bubbles go away from the centre of the pipe, and a positive azimuthal velocity means that the bubbles have a clockwise motion as observed looking towards the oncoming flow.

It is important to mention that the mean local volume fraction of the dispersed phase α_l can be calculated by:

$$\alpha_l = \frac{1}{T}\sum_{n=1}^{N}\left(\delta t_{0b}\right)_n \tag{50}$$

Where T is the total time of the sampling process, and N is the number of bubbles that strike the front sensor.

6. Construction of the four sensor probe and its ancillaries.

6.1 Preliminary analysis prior to the fabrication of four sensor probe.

One important requirement for the fabrication of the four sensor probe is that it must be small in dimensions. The reasons are that, the smaller the probe, the better it will be from a measurement accuracy point of view due to the fact that a bubble will strike each sensor twice. Also, if the probe is small enough, the interaction between the sensors and the bubbles will be small, minimising any alteration to the bubble velocity vector. However, there are constraints on how small the probe can be due to the method of construction of the probe. One constraint is that the probe is fabricated by hand. This means that the accuracy of positioning the sensors is limited by human factors especially the human inability of the eye and hand movement to place the sensors with very small errors. Another constraint comes from the fact that the smaller the dimensions of the probe the higher the sampling rate needed in order to acquire a reliable and representative signal from the output of the probe. Also the smaller the probe, the smaller the associated time delays (δt_{11}, δt_{22}, δt_{33}, described in Chapter 5) and the more accurately they have to be measured. The dimensions of the probe affect the maximum polar angle γ that can be measured. Mishra et al. in [118] investigated how the probe's dimensions influence the maximum polar angle for different bubble sizes. Figure 16 and 17 show this effect.

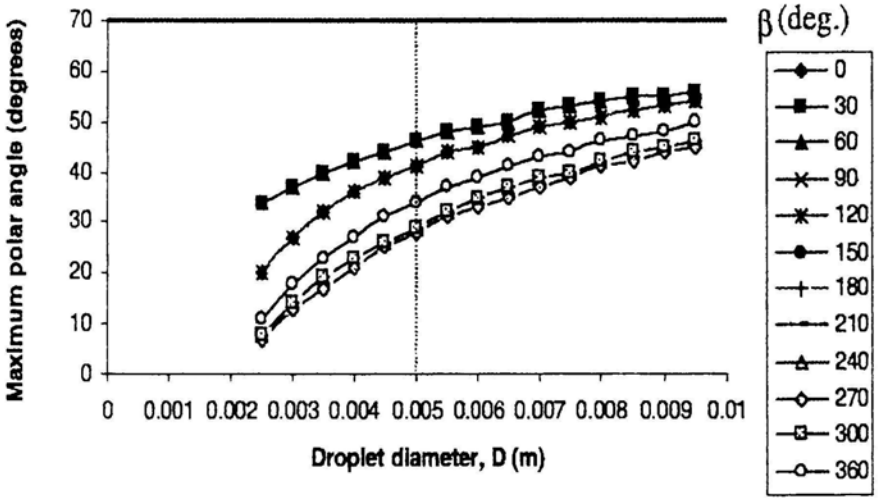

Figure 16. Variation of γ_{max} with different droplet diameters and azimuthal angles β for $d_1=d_2=d_3=1$mm from [118].

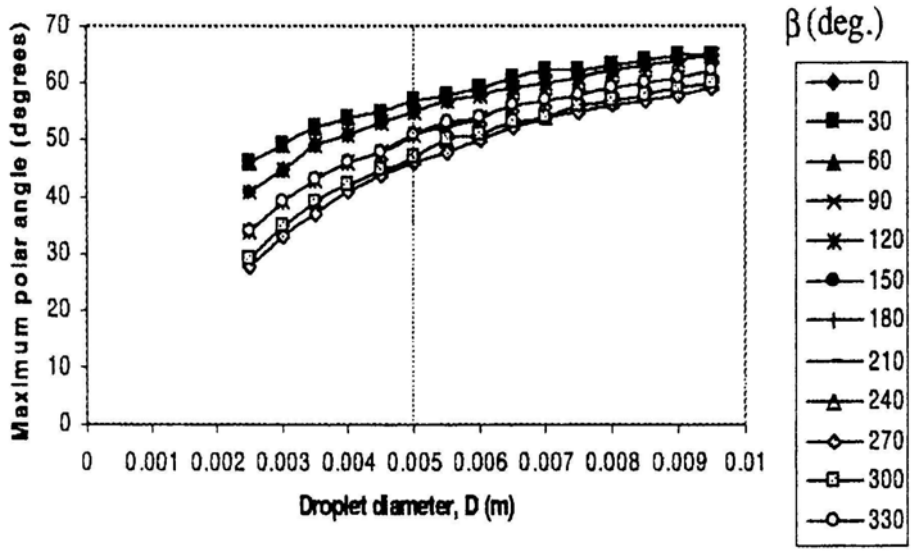

Figure 17. Variation of γ_{max} with different droplet diameters and azimuthal angles β $d_1=d_2=d_3=0.5$mm from [118].

As can be seen from figure 16 and 17, increasing the droplet diameter increases the maximum polar angle γ that can be measured. Also, making the probe smaller increases the range of polar angles for which the bubble's velocity vector can be measured. The dotted line in both plots shows the γ_{max} values when the bubble's diameter is 5mm. In the current research, the droplets' diameter in the bubbly multiphase flow experiments is around 5mm. For this size of bubble, when the

separation of the sensors is approximately 1mm, the maximum polar angle that can be measured (for all β) is about 27^o. This means that for flows where the droplets have 5mm diameter they will strike each rear sensor twice for γ up to 27^o. In the case where the separation of the sensors is 0.5mm, the value of γ_{max} increases to about 45^o. Also, from figure 16 it is shown that the influence of β on γ_{max} is less for smaller size probes [118]. A simple sketch that shows the above reasoning in a graphical way is given in figure 18.

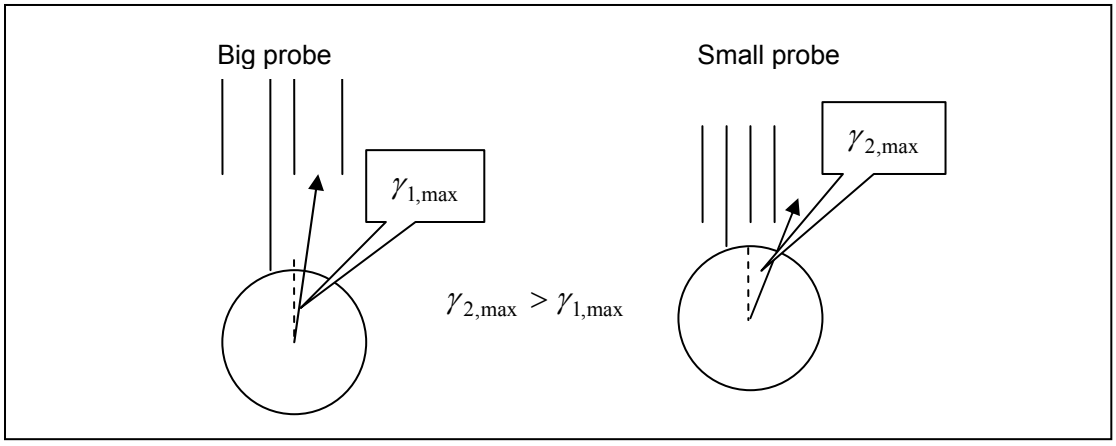

Figure 18. Maximum polar angle is affected by probe's dimensions ($\gamma_{i,max}$ is the maximum polar angle for which the bubble strikes all four sensors).

Based on the above, two types of probe have been fabricated. The code names are 4s1/4s4 and 4s3. With reference to the probe coordinate system, the positions (x_1, y_1, z_1), (x_2, y_2, z_2), (x_3, y_3, z_3) of sensors 1, 2, and 3 with respect to sensor 0 (which is the front sensor) are shown in tables 3 and 4.

Probe 4s1/4s4	X (mm)	Y(mm)	Z(mm)
Sensor 1	0.7889	1.060	1.1778
Sensor 2	0.0556	1.830	1.1223
Sensor 3	-1.1222	0.960	1.0556

Table 3. Measured dimensions of the 4s1/4s4 four sensor probe.

Probe 4s3	X (mm)	Y(mm)	Z(mm)
Sensor 1	1.384	-0.988	1.200
Sensor 2	0.263	-1.713	0.640
Sensor 3	-0.988	-1.318	1.800

Table 4. Measured dimensions of the 4s3 four sensor probe.

Figure 19 shows the method that was used for measuring the probe's dimensions in x-y plane and in z plane.

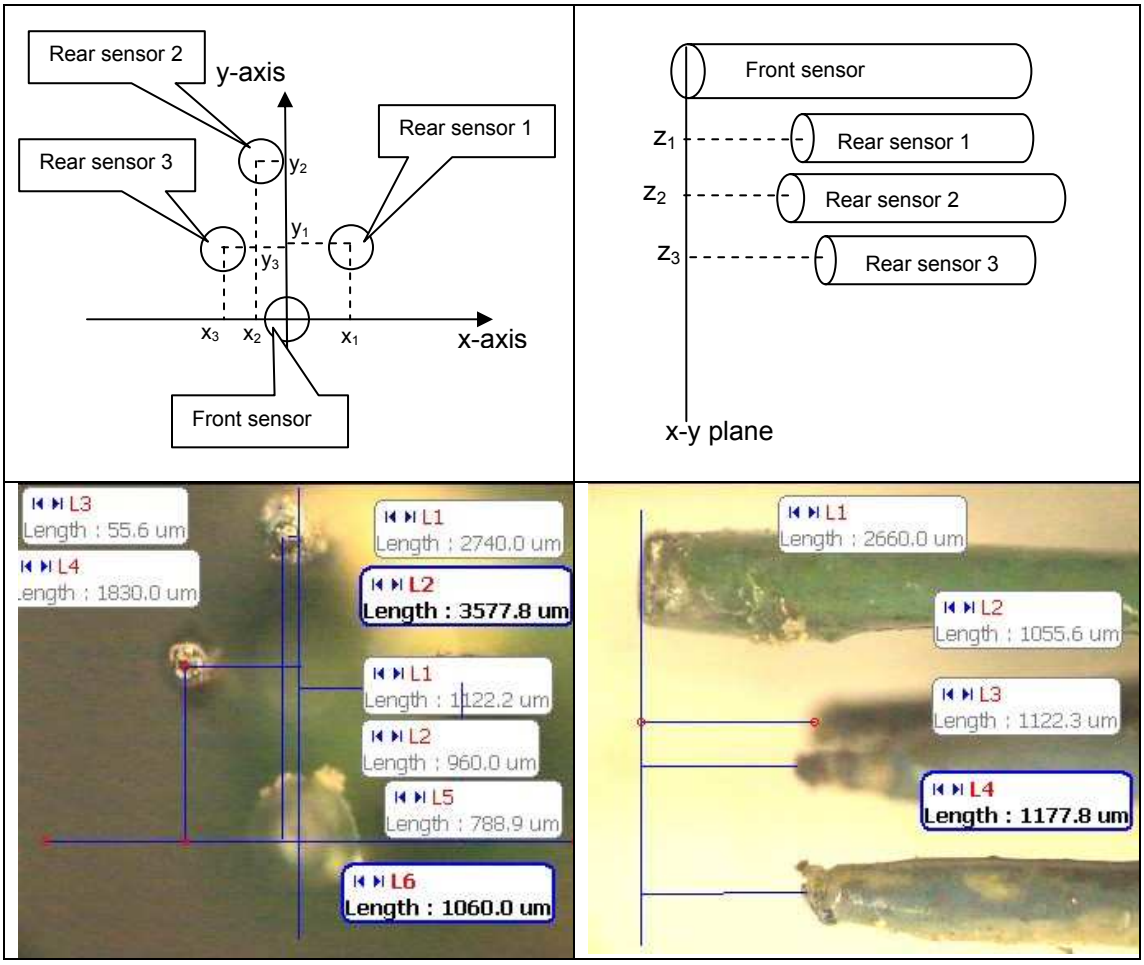

Figure 19. Measuring probe's (4s1/4s4) dimension in X-Y plane (top left and bottom left) and in Z-plane (top right, and bottom right) using a microscope. The top figures show the concept behind the procedure. The bottom picture show how the concept was implemented by using microscope and the relevant software for measuring the distances of the sensors having as reference the front sensor.

The two images shown in figure 19 were taken by using a microscope and the utilities of the supporting software. The bottom left image was used for measuring the probe's dimensions in the x-y plane having as a reference the front sensor which can be seen

as the middle dark point of the picture. The bottom right image was used for measuring the probe's dimensions in the z-direction having as a reference the front sensor, which is the longest dark element in the picture. The software used for acquiring the images and measuring the relevant distances, uses several parameters that had to be set up a priori. These parameters are the magnification factor, the focal point and the type of lenses. Based on this information several calculations are performed by computer in order to adjust the number of pixels in the image with the distance in each direction. The scale is in μm. In this procedure, it is important to position the probe in the same way as it is installed in the pipe. This action, if not correctly performed, imposes an error which is added in the uncertainty budget of the whole measuring procedure. Also, looking at the right picture of figure 19, it might seem that front sensor (the longest dark element) is not exactly parallel with the z-axis of the probe coordinate system. This is not an error due to the positioning of the probe in the measuring procedure, but an error in aligning the front sensor with the probe holder. The misalignment looks huge due to the magnification. In fact, the z-axis of the probe coordinate system passes through the tip of the needle forming sensor 0 and is parallel to that part of the probe holder denoted ww in figure 20. The y-axis of the probe coordinate system passes through the tip of the needle forming sensor zero and is parallel to the line denoted vv in figure 20. It is very important to accurately measure the positions of the tips of the rear sensors in the x, y and z directions relative to the position of the tip of sensor 0 (see chapter 5). For this reason it is important to position and hold the body of the probe appropriately when measurements are being undertaken using the microscope.

6.2 Fabrication of four sensor probes and associated circuitry.

The procedure for assembling the four sensor probes is similar to that which was used for the fabrication of dual sensor probes described in chapter 4. Four stainless steel acupuncture needles were used, the tips of which formed the sensors of the probe. The rigidity, small diameter (0.3mm), and the uniform shape make acupuncture needles the best candidate for this kind of application. The needles were mounted inside a stainless steel tube with an outer diameter of 4mm. Each sensor was painted with waterproof paint and insulating varnish. The tips of each needle were scratched with fine emery paper, so that the conductance between the tip of each needle and the stainless steel tube could be measured. One end of the stainless steel tube (vv in figure 20), was bent by exactly 90^0 relative to the other end of the stainless steel tube (ww in figure 20) so that it could be fitted to a traverse mechanism (which will be described later in the chapter 7). Figure 20 shows the schematic of the four sensor probe (right) and a picture of two real probes (left).

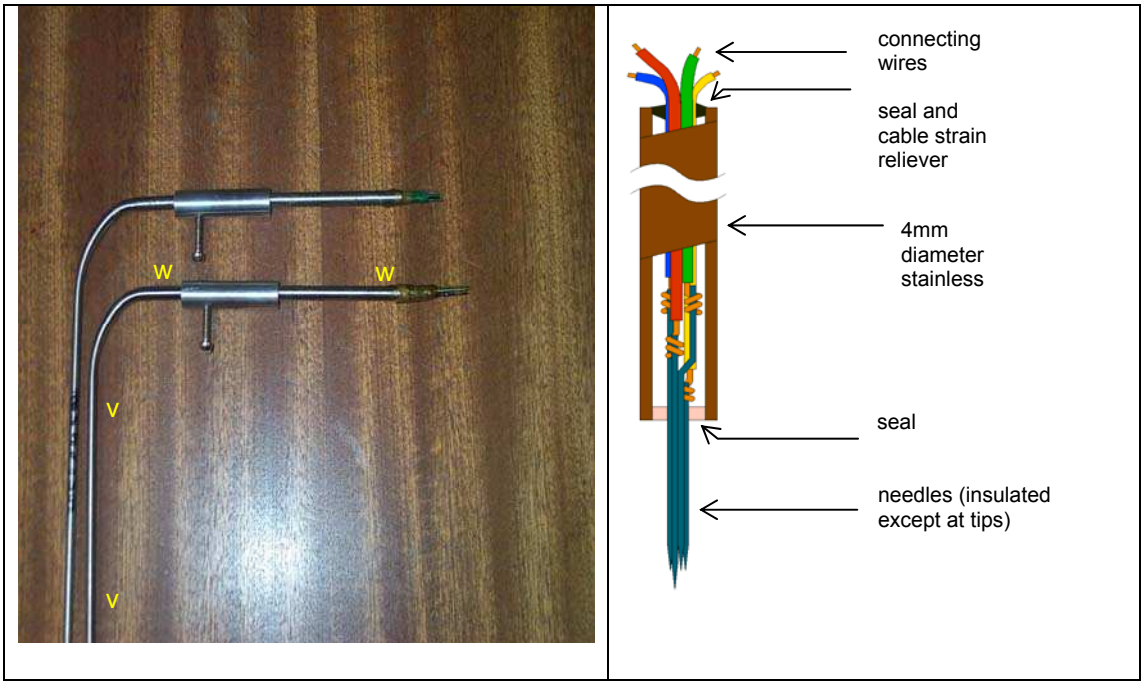

Figure 20. Four sensor probes in reality (left), and in design (right).

Each sensor was connected to a separate electronic circuit that transformed changes of conductance at the needle tip into voltage changes. The circuit that was used is the same as the one that was used for the dual sensor probe which was described in section 4.2. It is obvious that four of these circuits were needed, one for each sensor. As before, the common electrode is the main body of the probe. Figure 21 shows typical output voltages from the circuits when a bubble strikes the four sensor probe.

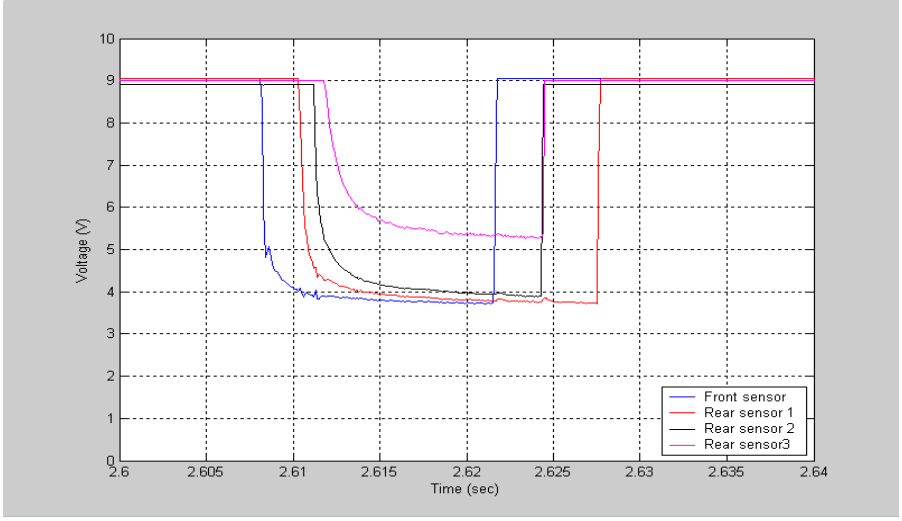

Figure 21. Signals from the four sensor probe, when a bubble strikes all sensors.

6.3 Signal processing scheme.

The signal processing scheme for the four sensor probe is similar to that used for the dual sensor probe described in chapter 4. Thresholds are applied to the signal of each sensor in order to identify the contact times of the bubble with each sensor. Lucas et al [119] showed that provided the transient responses of the four sensors are similar, when a bubble hits the probe, then the measured time intervals δt_{11}, δt_{22}, and δt_{33} are very close to the true values even if incorrect thresholds have been used.

The next step in the signal processing scheme is to identify the bubbles that strike all four sensors. This procedure involves two steps. The first step involves applying Criterion 1 and Criterion 2 (see section 4.3) successively to sensor pairs 0-1, 0-2 and 0-3, for each bubble whose surface is suspected of contacting all four sensors

twice. If Criterion 1 and Criterion 2 are satisfied a third criterion is used in order to increase the probability that the signals under consideration from each sensor are all caused by the same bubble. To illustrate this third criterion refer to figure 22, which shows signals from the four sensors which are thought to be caused by the same bubble. Suppose t_0, t_1, t_2 and t_3 represent the times when the bubble surface first contacts sensors 0, 1, 2 and 3 respectively. Suppose times t_4, t_5, t_6 and t_7 represent the times when the bubble surface last contacts senses 0, 1, 2 and 3 respectively. Criterion 3 states that if {t_1 and t_2 and t_3 are all greater than t_0} and {if t_5 and t_6 and $t_7$are all greater than t_4} then the sensor signals (as shown in figure 22) can all be assumed to come from the same bubble.

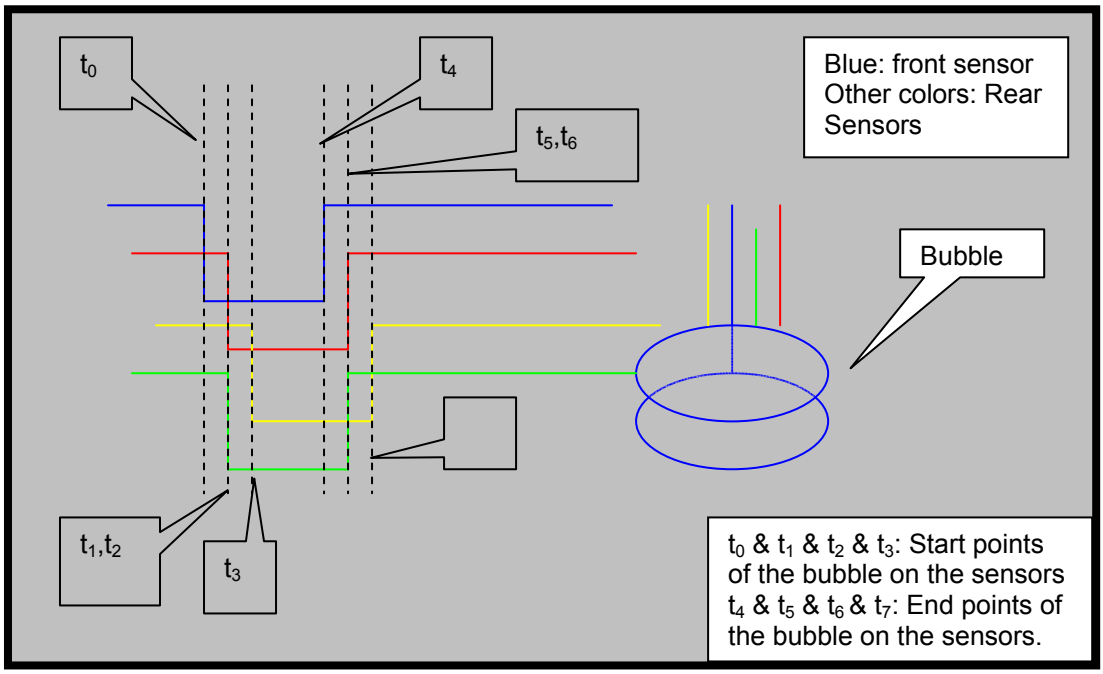

Figure 22. Ideal situation of a bubble striking the four sensors and the corresponding time.

The reason behind this "Criterion 3" is that the first contacts of the bubble with the rear sensors must happen after the first contact of the bubble with the front sensor. The same applies for the last contacts. If this happens then the δt_{ii} (see chapter 5) will all be positive and the signal processing scheme can do the calculations properly. If Criterion 3 is not satisfied then the inputs to the signal processing scheme may be

erroneous and the results do not correspond to reality for predominantly vertically upward flows.

After identifying the bubbles that hit all sensors, the next process is to calculate the time intervals δt_{ii} from the equations 37, 38, and 39. Knowing the time intervals and the position of each rear sensor with respect to the front sensor then using equations 46, 44 or 45, and 43 it is possible to calculate the azimuthal angle β, the polar angle γ, and the magnitude v of the velocity vector. Also, using equations 47, 48, and 49 the velocity components V_θ, V_r, and V_z can be calculated.

At each spatial location in the flow cross section the procedure outlined above is used to process data for many individual bubbles. From these many bubbles (typically 50 to 100 bubbles) average values for v, γ and β can be obtained. This procedure is repeated for each spatial location in the flow cross section at which it is required to obtain velocity vector data for a given set of flow conditions. Note that the local volume fraction can be calculated using eq. 50.

7. Experimental apparatus.

In order to carry out the measurements using the dual and four sensor probe, two main flow rigs were needed. These are a two-phase flow loop for air-water experiments, and a different multiphase loop for oil-water experiments. On these flow loops several reference measurement devices were used including a thermal mass flow meter for measuring air flow rate, a differential pressure sensor for measuring the global dispersed phase volume fraction, turbine meters for measuring liquid flow rate, a temperature sensor and data acquisition systems for acquiring data from the probe and reference measurement devices. Also, for accurately positioning the probe in the pipe and moving it to predefined positions, a traverse mechanism was used. The next sections will describe all of these devices and their functions in detail.

7.1 The two-phase flow loop for air-water experiments.

Pictures of the multiphase loop and its schematic are shown in figures 23 and 24. This facility is capable of producing the necessary air-water flow conditions relevant to the current investigation in the 2m long 80mm i.d. Perspex working section. The different flow conditions require a variety of air and water flow rates, and different gas volume fractions. Also, it was necessary to be able to position the working section (i.e. the part of the multiphase loop where the measurements take place, and in which the different multiphase flow regimes described in section 1.1 occur) at different inclination angles from the vertical, in order to produce non-uniform flows. Some flow conditions also required the flow to undergo swirl and for these conditions a swirler was used in the working section. The multiphase loop includes several instruments for the acquisition of reference data, and for the control of the flow conditions. These will be discussed later.

Figure 23. The air-water two-phase loop.

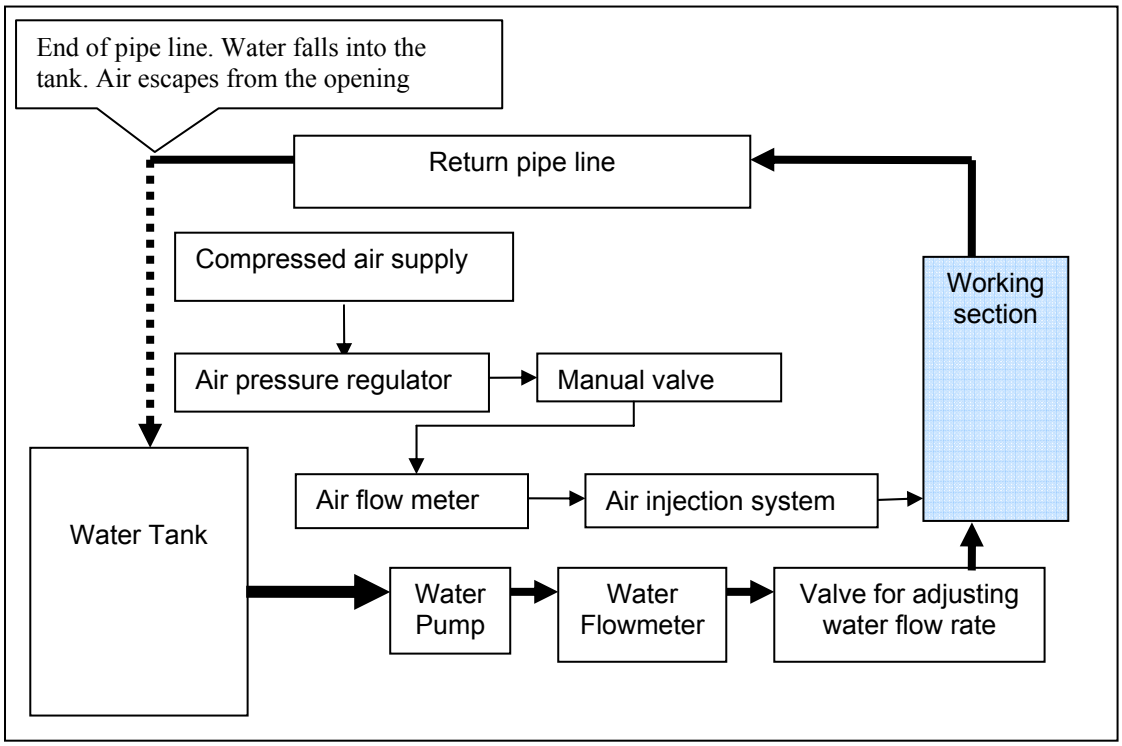

Figure 24. Schematic of air-water two-phase loop.

As previously mentioned, the air-water loop is able to produce flows with water as the continuous phase and air as the dispersed phase. Based on figure 24, water was pumped into the working section through a turbine meter in order to

measure the volumetric flowrate of the water Q_w. From the turbine meter the water flowed into the base of working section. Pressurised air from the laboratory compressed air supply was passed through a regulator and a mass flow meter. The air was injected into the base of the working section via a series of 1mm diameter holes. The holes were equispaced around the circumference of the pipe. The resulting air bubbles had an oblate spheroidal shape with the major axis typically about 5mm to 8mm long. The mass flow rate of the air was measured before it entered the working section using the thermal mass flow meter. Measurements of the pressure and temperature made within the working section enabled the mean air volumetric flow rate Q_g in the working section to be determined. The air superficial velocity u_{gs} was then calculated using

$$u_{gs} = \frac{Q_g}{A} \tag{51}$$

where A is the flow cross-sectional area within the working section. The air-water flow passed through the working section where the measurements took place. The axial distance between the point in the working section where the probe was located and the base of working section was 1.5m (18.75 internal pipe diameters), in order to ensure that the flow was developed at the axial location of the probe.

The inclination of the working section from the vertical could be changed. For the current research the inclinations that were used were 0^0, 15^0, and 30^0 from the vertical. Also, where a swirler was needed, a six vane swirler was installed four pipe diameters upstream of the probe. The swirler angle was 20^o, meaning that the inclination of the vanes with respect to the central vertical metal support was 20^0 (see figure 32).

In the working section, a differential pressure measurement was made in order to measure the mean air volume fraction $\overline{\alpha}_{ref}$. A detailed description of the specific method is presented in section 7.3.2.

7.2 The two-phase loop for oil-water experiments.

The oil-water facility has to be capable of producing the necessary oil-in-water flow conditions relevant to the current investigation. The different flow conditions require a variety of oil, and water flow rates, and values of oil volume fraction. For the flow conditions that required the oil droplets to have lateral motion as well as vertical motion, a swirler was used in the working section. The multiphase loop includes several instruments for the acquisition of reference measurements, and for the control of the flow conditions, which are described later.

For the current investigation, the flow loop of the University of Huddersfield was used. This was capable of producing many different oil-water flow conditions. Also, the reference measurement devices were in place and calibrated. Pictures of the multiphase loop and its schematic are shown in figures 25 and 26.

Based on figure 26, the experiments were carried out in the 80mm internal diameter, 2.5m long, vertical, perspex working section of the oil-water flow loop. The working section is shown in figure 25 and it will be discussed in detail later in this chapter. The oil and water were stored in a 2m long by 1m wide by 1.25m high stainless steel separator tank (see figure 27).

Figure 25. The oil-water loop. The tank and the pumps (top-left), the pumps the valves and the turbine meters (top-right), and the working section (bottom).

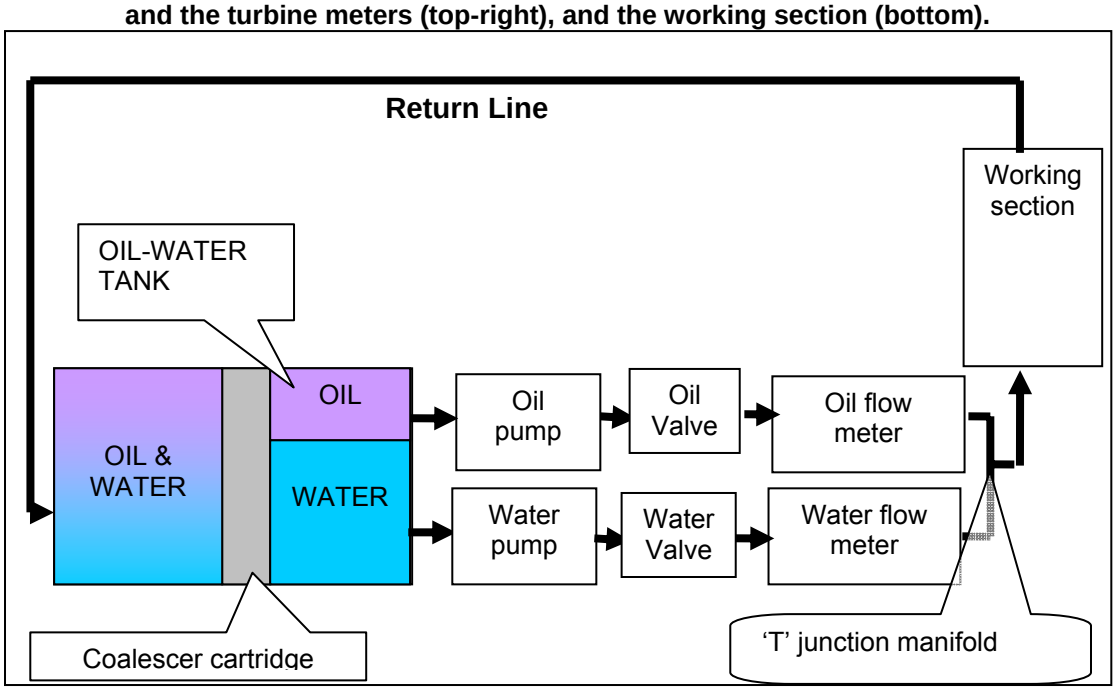

Figure 26. Schematic of oil-water multiphase loop.

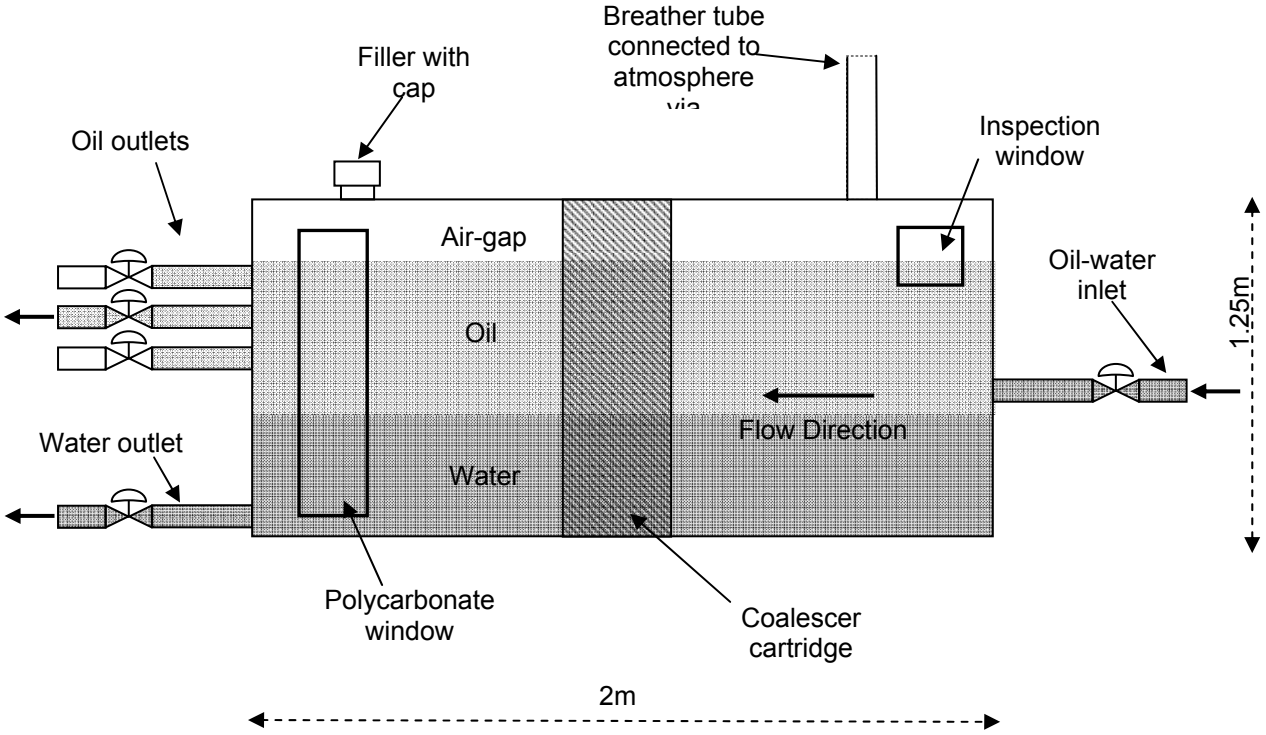

Figure 27. Oil-water tank.

The water outlet was located close to the base of the tank, the oil outlet was selected using one of three manual valves (as shown in figure 27), the choice of valve being dependent upon the position of the oil-water interface, which was in turn dependent upon the amounts of oil and water stored in the tank at any given time. The position of the oil water interface was clearly visible through a transparent polycarbonate window in the side of the tank. On leaving the tank the oil and water were conveyed through separate flow lines prior to being mixed together in a manifold just upstream of the working section. The oil and water flow lines each contained the following items of equipment; (i) a pump capable of pumping up to about $20\,m^3hr^{-1}$ of liquid at 3 bar gauge pressure: (ii) an electro-pneumatic control valve: and (iii) a turbine flow meter.

For each flow line the liquid flow rate was controlled using a separate Proportional-Integral-Derivative (PID) controller. The output signal from the relevant

turbine meter was passed through a frequency-to-current converter, the 4-20mAmp output from which formed the 'measured value' input to the relevant PID controller. This 'measured value' was compared with the 'set point' flow rate, entered into the PID controller by the operator, and a 4-20mAmp control signal was generated which was sent to the appropriate electro-pneumatic control valve. In this way, the oil and water flow rates into the flow loop working section could be individually controlled with good precision (better than 0.5% of set-point flow rate) for long periods of time. On emerging from the flow loop working section the oil-water mixture was piped back to the inlet of the separator tank in the form of a 'primary dispersion' [NB: one definition of a 'primary dispersion' that is relevant here is that the oil droplets are *not* so small that they cannot readily separate from the mixture under the influence of gravity]. Gravity induced separation of the oil and water in the tank was accelerated with the aid of a 350mm long coalescer cartridge (see figure 27) which spanned the cross section of the separator tank. The oil used in the experiments described in this thesis was Shellsol D70 with a density of $790\,\mathrm{kgm^{-3}}$, a kinematic viscosity of about $2\,\mathrm{mm^2 s^{-1}}$ at $20^{o}\mathrm{C}$ (i.e. 2 centistokes, which is approximately twice the viscosity of water) and a flashpoint greater than $70^{o}\mathrm{C}$.

Due to the high flashpoint temperature of the oil, the room in which the flow loop was housed was classified as a 'zone 2' area, i.e. an area in which an explosive atmosphere would be present for less than 10 hours per year but still sufficiently likely to require controls over ignition sources. To this effect, and to comply with other UK health and safety legislation, a number of safety features were incorporated into the flow facility and the room in which it was housed. These included: (i) the flow loop was surrounded by a bund of sufficient height to contain spillage of the entire liquid contents of the flow loop and separator tank: (ii) an extractor fan was

mounted in an external wall of the room in which the flow loop was housed and was run whilst the loop was being operated to prevent any possible build up of oil vapour: (iii) flameproof motors were used on the pumps and on the extractor fan and flameproof cabling and lighting were used throughout the room housing the flow loop: (iv) all electrical switchgear, electrical sockets, data acquisition and control equipment were sited in the main part of the laboratory outside the room containing the flow loop, with the operator observing and controlling the experiments via a large window in the wall of the room containing the flow loop: (v) automatic fire detection equipment was installed around the flow loop: (vi) a 50mm diameter breather tube connected the air gap above the oil to atmosphere via an external wall to prevent inadvertent overpressurisation of the tank.

A number of other safety features were used including: the use of oil resistant Viton gaskets and seals throughout; electrical earthing of the separator tank to prevent the build up of electrostatic charge; and the use of splash guards around hot surfaces, such as the electric motors of the oil and water pumps, to minimize the possibility of ignition of any oil that might leak from the flow loop under fault conditions. Detailed operating and emergency procedures were written, as were detailed schemes of inspection and maintenance. The flow loop operator was required to undergo training in these procedures prior to using the facility.

7.3 Reference measurement devices.

The reference measurement devices that are going to be described below were used in both the air-water and oil-water multiphase flow loops. Some of the instrumentation was common to both multiphase flow loops. Specifically, turbine meters were used for measuring liquid volumetric flow rate. A differential pressure

sensor and a swirler were devices used in both multiphase flow loops. The description of their operation follows.

7.3.1 Turbine meter.

Turbine meters were installed in the liquid lines of the flow loops. They were used to give measurement of the liquid volumetric flow rate, delivered by the relevant pumps. The principle of the turbine meter operation is that the number of rotations per second of the turbine rotor depends on the flowrate of the liquid. Therefore, by counting the frequency of rotations of the turbine rotor it is possible to acquire measurements of the water flow rate. The turbine meters are designed to have a linear relationship between the flow rate and the frequency of the rotation over a range of flow rates. The relationship can be expressed in the following formula:

$$Q = Kf \tag{52}$$

where Q is the liquid flowrate, f is the frequency of the rotor rotation, and K is the meter factor for the device, which can vary as the meter begins to wear. The meter factor K of the turbine meter for the water line of the air-water loop was $0.0462 m^3 h^{-1} Hz^{-1}$ over a design range of $3.41 m^3 h^{-1}$ to $40.88 m^3 h^{-1}$.

For the oil-water rig the meter factor for the water turbine flow meter was $0.03121 m^3 h^{-1} Hz^{-1}$ over a design range from $2.7 m^3 h^{-1}$ to $27 m^3 h^{-1}$. For the oil turbine flow meter the meter factor was $0.00541 m^3 h^{-1} Hz^{-1}$ over a design range of $0.9 m^3 h^{-1}$ to $9 m^3 h^{-1}$. The turbine meters of the oil-water loop were each connected to a separate PID controller. The PID controllers calculated, for each of the oil and water flow lines, the error between the desired flow rate and the current flowrate. Depending on

the magnitude of the error a signal was sent to the electropneumatic valve of the relevant flow line in order to adjust the flow rate to the desired value. In other words, there was no need to check and manually adjust the water and oil flow rates, since the PID controllers brought the flow rates to the set point values, programmed into the PID controller by the operator.

7.3.2 Differential pressure transducer

A Honeywell ST-3000 differential pressure sensor was installed in the working section of both flow loops. This instrument was used to measure the differential pressure across a 1 metre length of the working section. Both differential pressure transducers were configured such that the lines connecting the high and low pressure sides of the transducer to the pressure tappings on the working section were filled with water. A flushing system was installed on each dp cell in order to ensure that no air or oil could be trapped in either the sensor or the water filled measurement lines. The measured differential pressure was used to calculate the volume fraction of the air or the oil as shown below.

The method of calculating the volume fraction of the dispersed phase is as follows and as described in [120]. Assuming that the pressure tappings (which are in the working section) are separated by a distance h, the working section is inclined by ψ degrees from the vertical and that the lines connecting the pressure tappings to the dp cell are water filled, then the volume fraction $\overline{\alpha}_{ref}$ of the dispersed phase can be calculated as:

$$\overline{\alpha}_{ref} = \frac{\Delta P + F}{(\rho_w - \rho_d) g h \cos\psi} \tag{53}$$

where g is the acceleration due to gravity, ΔP is the measured differential pressure, ρ_w and ρ_d are the densities of water and dispersed phase respectively and F is the frictional pressure loss. This frictional pressure loss, with reference to [120], can be calculated from:

$$F = \frac{fh\rho_w U_h^{\,2}}{2M} \tag{54}$$

where f is the measured single-phase friction factor for the working section and M is the hydraulic radius of the working section given by:

$$M = R_i \tag{55}$$

where R_i is the internal radius of the working section. In equation 54 U_h is the homogeneous velocity, which is the sum of the water and dispersed phase superficial velocities U_{ws} and U_{ds} respectively. In detail:

$$U_h = U_{ws} + U_{ds} \tag{56}$$

where

$$U_{ds} = \frac{Q_d}{\pi R_i^2} \tag{57}$$

$$U_{ws} = \frac{Q_w}{\pi R_i^2} \tag{58}$$

and Q_w and Q_d are the volumetric flow rates of the water and the dispersed phase respectively.

7.4 Data acquisition cards.

Two different data acquisition cards were used in the experiments. The first data acquisition card was a DT2821A from "Data Translation". The data acquisition software used was GlobalLab. This is a DOS based data acquisition and analysis package from Data Translation. GlobalLab allowed the data acquisition card to be automatically controlled via a pre-written chain of commands called a macro. This data acquisition card was mainly used for the air-water experiments for obtaining signals from the dual sensor probe and for obtaining reference measurement data. A description of the software and how it links to the instrumentation for the air-water loop is given in section 7.6.1.

The second data acquisition card was a DAQ2006 from ADLINK. The software for controlling the card and acquiring the measurements is listed in appendix I. The software language that was used for the making of the program was Visual Basic 6. Also, for the building of the program the author used a file (D2kDask.bas), which includes all the functions that are needed in order to control the data acquisition. The maximum sampling rate of the DAQ2006 card is 250 kilosamples per second per channel. Every sample is 16 bits long, and the number of channels that can perform simultaneous sampling is four. This data acquisition card was used in the oil-water experiments only. Note that the software for using the card was part of a program (written in Visual Basic 6) that was also responsible for (i) controlling the motion of the traverse mechanism (ii) the synchronization between the motion of the traverse mechanism stepper motors and the data acquisition and (iii) the

communication between a main computer and a subsidiary computer responsible for acquiring the reference measurements using GlobalLab software. A description of the software for the oil-water loop and how it links to the instrumentation of the oil-water loop is given in section 7.6.2. The functionality of the traverse mechanism is explained in the next section.

7.5 Traverse mechanism.

In order to move the probe to predefined positions in the cross section of the pipe a traverse mechanism was used. This device was able to achieve two types of motion. These were a linear movement and a rotary movement. These two types of movement required the use of two stepper motors. One motor performed the linear motion, and the other motor performed the rotary motion. Note that due to the fact that the movement of the probe in the pipe is achieved by these two types of motion, the coordinate system that was used to define the spatial location of the probe in the flow cross section was a radial and angular (r,θ) coordinate system (or cylindrical polar coordinate system). The coordinate system has two variables, which are the r for the radial position (position from the centre of the pipe in the direction of the wall), and the θ for the angular position. Therefore, the linear traverse mechanism was responsible for the radial movement of the probe, and the rotary traverse mechanism was responsible for the angular movement of the probe.

Figure 28 shows the linear traverse mechanism. It consists of a linear stepper motor, guide rails, a clamping system, a traverse yoke, and a junction box. At the side of the wall of the pipe on which the linear traverse is mounted there was a small hole and the clamping system held the linear traverse mechanism in line with the small

hole so the probe could be inserted into the pipe through the hole. Also, the clamping system provided a mechanical support to the linear traverse. An O ring was used at

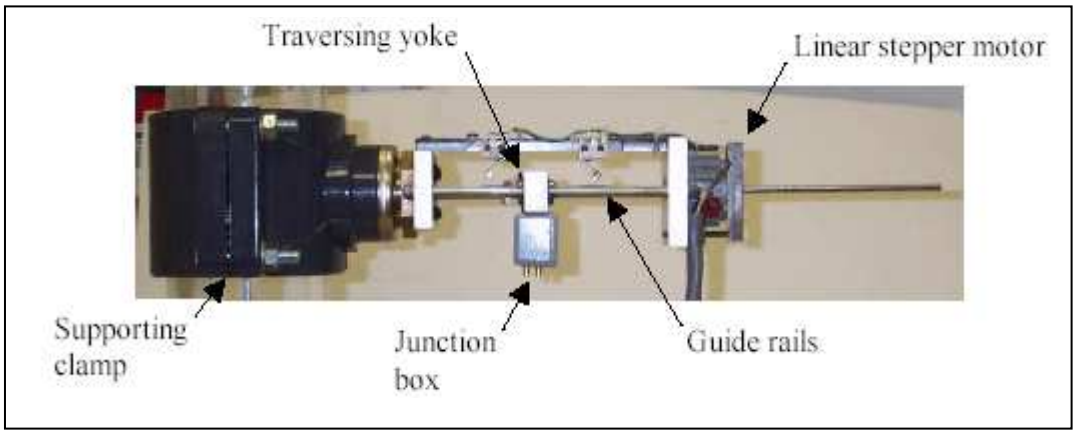

Figure 28. The linear traverse mechanism [14].

the small hole that the probe was inserted through in order to seal the hole and prevent any leakage. The probe was clamped close to the yoke in order to keep it stable and to follow the yoke's motion. The yoke was attached to two guide rails so it could slide forward or backwards achieving the radial motion of the probe into the pipe. Also the yoke was attached to the radial motion stepper motor shaft. While the motor was rotated, the shaft was screwed or unscrewed making it move forward or backwards. The result was to move the yoke forwards or backwards and in turn to move the probe forwards and backwards, achieving the desired radial motion of the probe. The junction box was used for connecting the wires that come out from the probe. Another set of wires was connected to the sockets attached on the junction box in order to connect the probe with the relevant electronic circuits. The linear traverse was capable of moving the probe in radial steps of 0.025mm.

For the angular motion a rotary mechanism was used. It consisted of a stepper motor, a geared ring, and the mechanical support to hold them together. The stepper motor was connected with a worm shaft that was attached to the geared ring. When

the stepper motor was rotated, the worm shaft rotated the ring. The ring was attached to the traverse mechanism pipe section which was then rotated relative to the rest of the working section. When this pipe section was rotated the coordinate θ defining the angular location of the probe in the flow cross section was changed. It is important to mention that the section of pipe, in which the whole traverse mechanism was attached, was fitted with sealed stainless steel bearings and radial shaft seals mounted into the end flanges. In this way leakage from the rotating pipe section was avoided. The rotary traverse was able to move the probe angularly in steps of 0.015^{o}. Figure 29 shows the whole traverse mechanism.

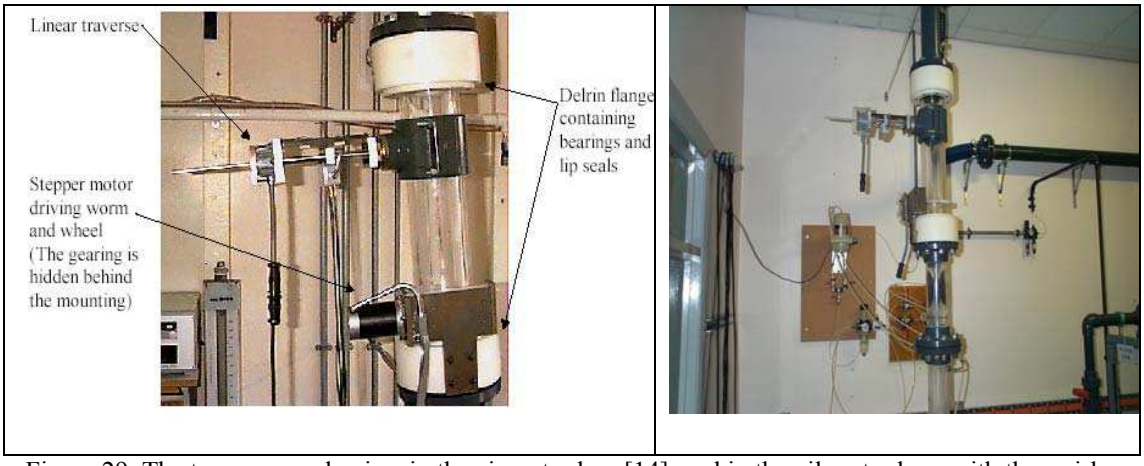

Figure 29. The traverse mechanism in the air water loop[14], and in the oil-water loop with the swirler just upstream of it (right).

The control of the two stepper motors in the traverse mechanism was achieved using a modular system supplied by RS Components Ltd. It was housed in a shielded rack. The system was connected with a PC using an RS-232 link. It was capable of controlling the small linear (radial) stepper motor (1 Amp) and the big rotary (azimuthal) (5 Amps) stepper motor.

7.6 Software.

To make the hardware perform all the appropriate tasks, software programs were constructed. The programs were responsible for (i) synchronizing the different devices based on a predefined timeline, (ii) acquiring data and storing them in pre-determined memory locations in a hard disk of a computer for later processing, (iii) moving the probe for pre-determined positions in the pipe, and (iv) acquiring the reference measurements and storing them in the hard disk of a computer for later processing. Due to the fact that two different multiphase loops were used, there were two different hardware set ups with two different software programs. Next a more detailed description of these programs is presented.

7.6.1 Software for air-water loop.

Figure 30 shows a block diagram of the set up for the air-water loop. As can be seen, the software is used (i) to control the two stepper motors on the traverse mechanism, (ii) to acquire data from the probe and (iii) to acquire reference measurements. The linear and rotary motors on the traverse mechanism are connected with the motor controller. The motor controller is connected with the PC through its serial port. The output signals of the probe are connected to a signal conditioning unit which in turn is connected with the DT2821A data acquisition card. Also, the reference measurements are connected to a second signal conditioning unit and this in turn is connected to the data acquisition card. So, the software must be able to communicate with the motor controller and send the appropriate commands in order

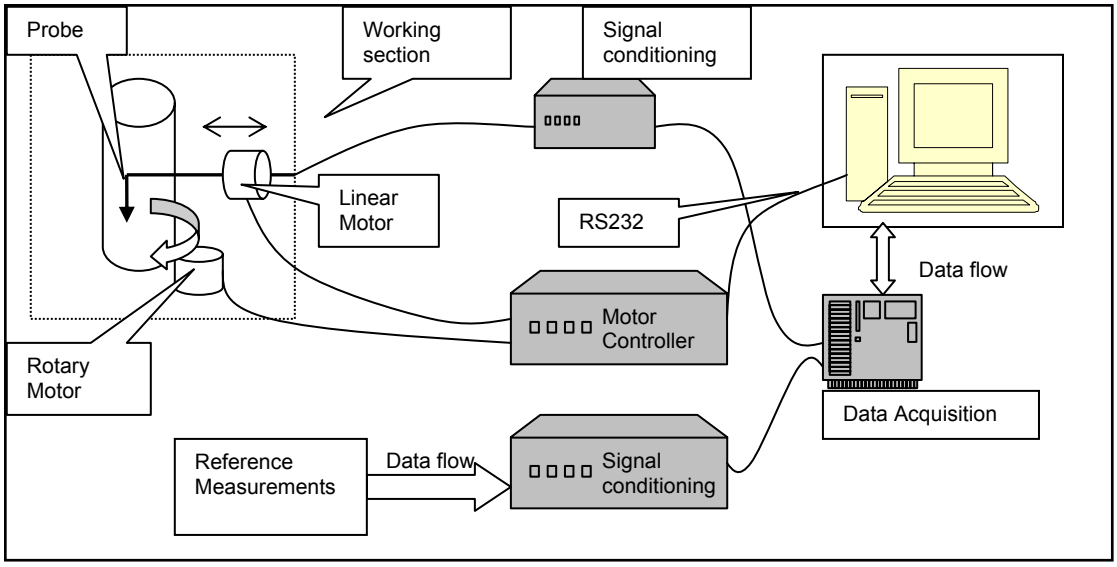

Figure 30. Hardware set up of the air water loop.

to move the probe to a predetermined position. Another task of the program is to communicate with the data acquisition system, acquire the measurements, and store them onto the hard disk.

7.6.2 Software for oil-water loop.

Figure 31 shows in a block diagram the oil-water set up. It is similar with the air-water set up but it includes one extra computer and the DAQ2006 data acquisition card. The extra computer (PC2) in the set up was responsible for communicating with the DAQ2006 and acquiring data from the probe. The other computer (PC1) was the same computer used in the air-water loop and it was responsible for acquiring the reference measurements and for controlling the traverse mechanism. The QBasic software used in PC1 was principally the same as that used in the air-water loop with some minor alterations. The software programme used in PC2 was written using Visual Basic 6.0.

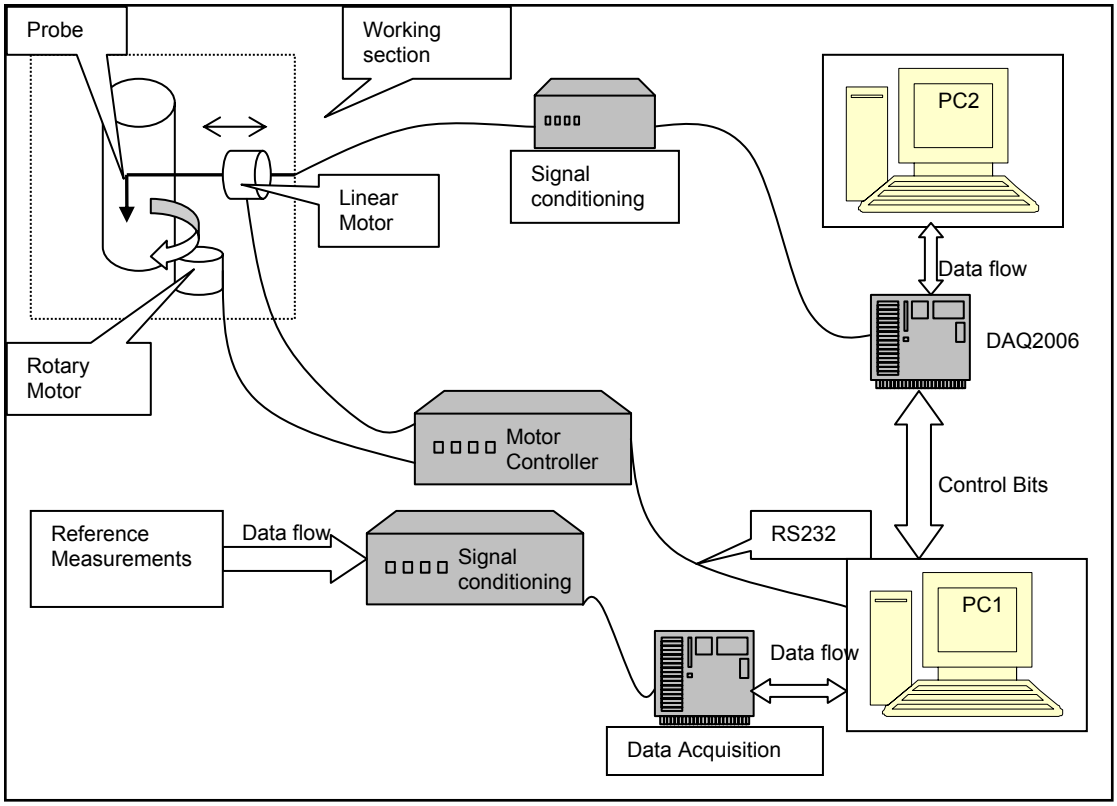

Figure 31. Hardware set up of the oil water loop.

Part of the minor alterations in the QBasic programme and part of the Visual Basic programme was to achieve the synchronization of actions between the two computers. For this purpose the digital I/O port of the DAQ2006 and the parallel port of PC1 were used for the synchronization by sending and receiving 4 control bits.

The master in the system was PC2 and the Visual Basic program was responsible for commanding PC1 when the stepper motors were going to move, and when to acquire the reference measurements. PC2 also controlled acquisition of measurements from the two and four sensor probes.

7.7 Swirler device.

Some of the experiments in the oil-water flow loop required the use of a swirler. The purpose of this device was to create a flow in which the oil droplets had significant azimuthal motion as well as vertical motion. This type of experiment

occurred when the four sensor probe was used and it was required to create bubble vector velocities that were not purely vertical.

A six vane swirler was installed four pipe diameters upstream of the probe. The swirler had six brass vanes welded to a 10mm diameter central brass hub. The design of the vanes was based on the criteria of Mathur [121]. The effective outer radius was 40mm. The swirler was housed in a flanged, 80mm internal diameter, clear pipe section. The swirler angle was 20^{o}. Figure 32 shows a picture of the swirler that was used in the experiments.

Figure 32. The swirler device in oil-water loop.

7.8 Experimental procedure for dual sensor probe.

7.8.1 Air-water experiments

The dual sensor probe was used in the air-water and oil-water multiphase loops. For the air-water experiments the experimental procedure was as follows. Initially, a program for the data acquisition was run in order to acquire measurements of the differential pressure when there was static water only in the flow loop working section. The acquired value was used later as a reference measurement for the calculation of the mean air volume fraction. The next step was to run the software program written in QBasic. The program initialised the communication between the

computer and the stepper motor controller of the traverse mechanism. Then, the procedure for positioning the probe into the centre of the pipe followed. The procedure involved the positioning of the probe to the pipe wall manually. Then the program asked the operator to input the dimensions of the pipe. The linear traverse mechanism moved the probe to the centre of the pipe, controlled by the motor controller. In this way it was ensured that the initial position of the probe when the experiments started was in the centre of the pipe. Then the water pump was started in order to achieve the desired water flow rate. Air was pumped into the working section at the desired volumetric flow rate. The air and water flow rates had values that made the multiphase flow to be in the bubbly regime. For the experiments at 0^o and 15^o inclination to the vertical the distance *s* (see figures 6 and 8) between the tips of the sensors of the dual sensor probe was 4.88mm, and for 30^o inclination the distance between the tips of the sensors of the dual sensor probe was 2.59mm. The code names of these two different probes that have 4.88mm and 2.59mm axial distances between the sensors are 2d1 and 2d2 respectively. Local gas volume fraction profiles and velocity profiles were obtained for values of water superficial velocity u_{ws} in the range $0.1\,\mathrm{ms}^{-1}$ to $1.14\,\mathrm{ms}^{-1}$, values of air superficial velocity u_{gs} in the range $0.183\,\mathrm{ms}^{-1}$ to $0.166\,\mathrm{ms}^{-1}$ and for pipe inclination angles θ away from the vertical of 0^o, 15^o and 30^o.

7.8.2 Oil water experiments

Table 5 shows all the data sets that were acquired from the dual sensor experiments for oil-water flows. Note that these data were taken for 0^0 inclination (vertical flow) only. Also, it is important to mention that three different types of dual sensor probes were used for these experiments. Their difference is the axial distance

between the tips of the sensors. The first probe with code name 2s1 had 2.6mm spacing between the tips; the second probe with the code name 2s2 had 2.7392mm spacing between the tips; and the last one with the code name 2s3 had 2.52mm spacing between the tips of the sensors. Also, the sampling period over which data was acquired at each probe position was increased. Instead of 30 seconds that was used in air-water experiments, 120 seconds were used for each data point. The sampling frequency for the dual sensor probe in the oil-water experiments was 10000Hz per channel.

Data Sets	Probe type	Q_W (m^3/h)	Q_O (m^3/h)
Data Set 1	2s1	5	0.5
Data Set 2	2s1	5	1
Data Set 3	2s1	5	1.5
Data Set 4	2s2	7.5	0.75
Data Set 5	2s2	7.5	1.5
Data Set 6	2s2	7.5	2.25
Data Set 7	2s3	7.5	0.5

Table 5 The experiments conducted in oil-water flow loop for dual sensor probe.

7.8.3 Movement of the traverse mechanism for the air-water and oil-water experiments using the 2 sensor probe.

During the experiments, the movement of the probe was predefined in order to know which data point corresponds to which position in the cross section of the pipe. This was done by deciding before the experiment how many data points were required. There were a number of options that could be chosen but the ones that were used were 88 points for air-water and 64 points for the oil-water experiments. For

each measurement point, data from the local probe was stored in a binary file that had the label "datadnnn.dat", where nnn is a 3 digit number. The 88 (or 64) points were evenly spread in the cross section of the pipe and the probe was moved to each position in order to acquire the measurements.

The way the data points were spread followed a pattern. The pattern was based on the number of diameters (or radii) and the number of points on each diameter (or radius) that should be considered in order to measure the desired number of data points. So, for 88 points the number of diameters that was chosen was 8 with 11 points in each diameter. This includes taking measurements at the pipe centre 8 times and so the actual number of independent data points was 81. For 64 data points the number of radii was 8 with 8 points in each radius. This includes taking data at the pipe centre 8 times and so the number of independent measurement points was 57. It should be noted that it is useful to take multiple measurements at the pipe centre. This is because it enables the stability of the flow to be checked periodically at a given set of flow conditions. If successive measurements at the pipe centre showed large variations during testing at a given set of flow conditions, it was usually found necessary to repeat the testing at those flow conditions.

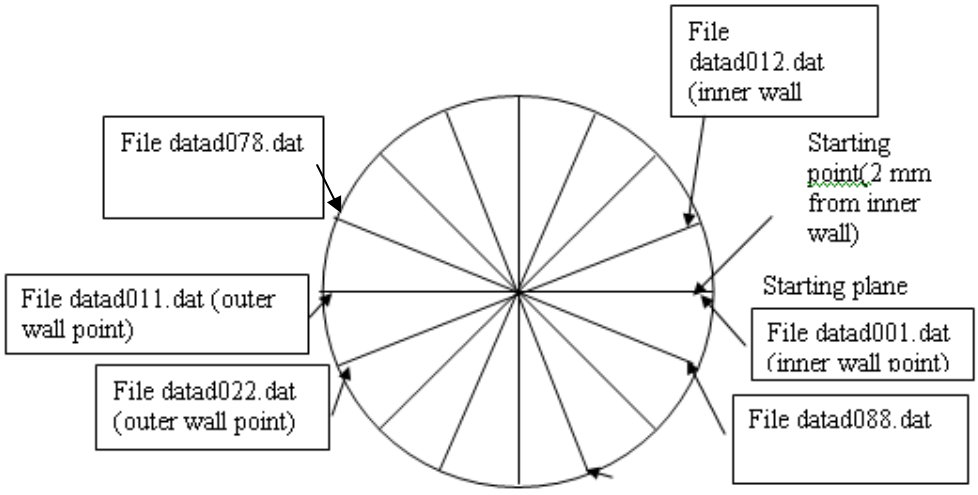

Figure 33. Details of the locations in the cross-section pipe at which 88 data points have been taken.

Figure 33 shows the data points laid in a virtual pipe cross section for 88 data points. Based on figure 33, when the air-water experiments were initiated, the probe was first moved to the pipe wall. Note that the centreline of the 4mm diameter probe was actually at a distance of 2mm from the wall pipe. Therefore the measurements that were taken at the boundary of the cross section of the pipe do not represent measurements which were precisely at the pipe wall. In that position, data was acquired for 30 seconds for air-water experiment and 120 seconds for oil-water experiments. Then the probe was moved to the next spatial location on the same diameter using the linear traverse mechanism. The procedure was repeated until the probe measured 11 points. Then the rotary traverse mechanism rotated the axis of motion of the linear traverse by $180^{o}/8$ or by 22.5^{0} (see figure 33). Then another 11 points were measured on the next diameter. The whole procedure continued until all the data points were measured. It is important to mention that during the procedure, the probe had to stop acquiring measurements in order to run a subroutine for taking reference measurements.

A similar procedure was used for the 64 spatial locations used in the oil-water tests, except for the small differences in the movement of the probe and the sampling period that were mentioned previously.

The dual sensor probe sampling frequency that was used for the air water experiments was 3750Hz per sensor, and the data acquisition was via a DT2821A board for the air-water experiments. For the oil-water experiments the dual sensor probe data acquisition was via a DAQ2006 with a sampling frequency of 10KHz per sensor. After accumulating all of the data, a shut down procedure was followed involving translation of the binary data files into text data files for later processing. Then, using software written in MatLab, processing of the data was performed. The

signal processing for the dual sensor probe has been described in chapter 4, and the MatLab software can be found in appendix II. Also, the reference data files were processed too, in order to know the exact flow conditions at which the results from the two sensor probe were obtained. The program for the reference data files was written in MataLab and can be found in Appendix III.

7.9 Experimental procedure for four sensor probe.

The experimental procedure for the four sensor probe was similar to that for dual sensor probes. The only differences between the procedures are the plotting of the data, the number of data points, and the placement of the swirler before the working section (described previously in the current chapter). The experiments were conducted in the oil-water flow loop. Note that for the four sensor probe, only 0^0 inclination (or vertical pipe) was used. Also, due the axisymmetric nature of the flow in which the four-sensor probe was used, results were only taken for one diameter of the pipe. The number of independent spatial locations on the diameter at which probe measurements were taken was 15. The results taken at each spatial location from the 4-sensor probe are (as mentioned in chapter 3 and 4) the mean local volume fraction, and the local oil droplet velocity vector, expressed in terms of axial, radial and azimuthal velocity components (in the pipe coordinate system), at the specific location of the probe. Table 6 shows the flow conditions that were used when acquiring data from the 4-sensor probe.

DATA SETS	Probe	Water Superficial Velocity u_{ws} (ms^{-1})	Oil Superficial Velocity u_{os} (ms^{-1})
SET 1 (without swirler)	4S3	0.276	0.0276
SET 2 (with swirler)	4S3	0.276	0.0276

Table 6. The experiments conducted in oil-water flow loop for the 4-sensor probe.

7.10 ERT system.

A number of experiments in the air-water and oil-water flow loops were conducted in collaboration with the University of Leeds. One of the aims of these experiments was to compare the volume fraction profiles and velocity profiles obtained from the conductivity probes with profiles obtained using Electrical Resistance Tomography (ERT). Therefore a brief description of the ERT system is given based on [122].

The ERT system is composed of three main parts. These are the sensors, the data acquisition system, and the image reconstruction system that is hosted in a computer. Figure 34 shows the block diagram of this system. Note that figure 34 shows a general concept of the ERT system.

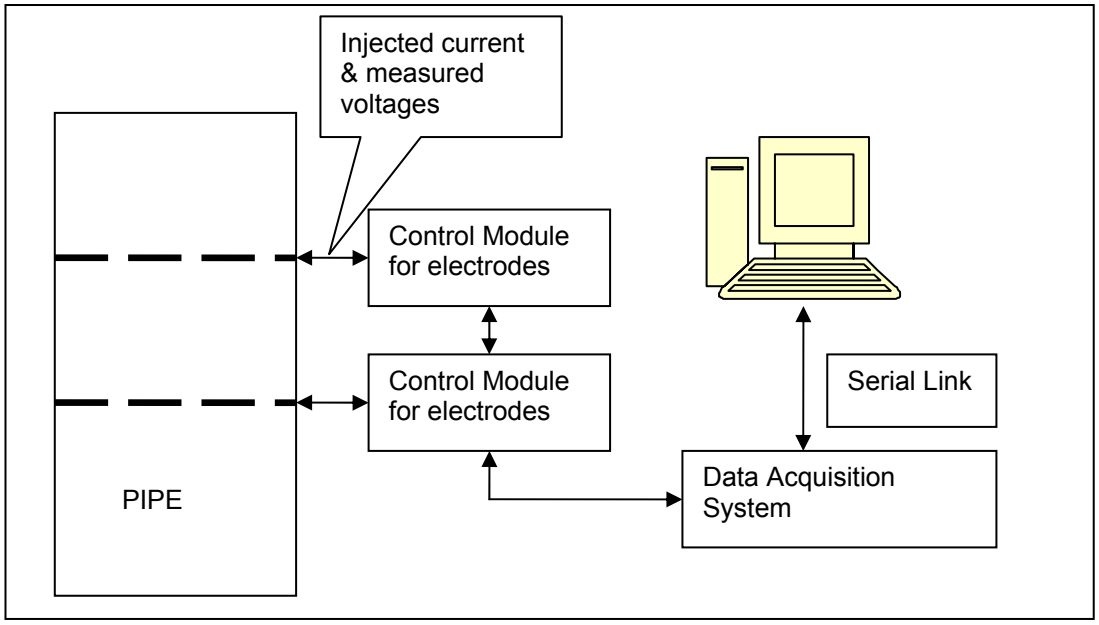

Figure 34. The structure of ERT system [122].

The electrodes in the ERT system are continuously in contact with the flow. The material that these electrodes are made of is metallic and can be fabricated from stainless steel, gold, platinum, or any other material that is a good electrical conductor. The electrodes are equispaced around the pipe wall. It is important to know the position of each electrode since this information is used in the reconstruction algorithm.

Figure 35. Dual plane ERT system .

The injected current should be constant and depending on the conductivity of the flow (which is dependent upon the volume fraction of the dispersed phase), changes in measured voltage occur. Note that one ring of electrodes is used to obtain images of the conductivity distribution in one plane, which corresponds to a particular cross section of the pipe. In the experiments in this thesis the ERT system had two sets of electrodes; therefore it "imaged" two planes. With this set up, it was possible to measure the local volume fraction (which can be measured using only one set of electrodes on one plane), and the local mean axial velocity of the dispersed phase (which requires two planes and the use of pixel-pixel cross correlation [122]. The distance between these planes needs to be known, and is 0.05m). The number of electrodes for each plane was 8.

The next part of the ERT system is the data acquisition system (DAS). Figure 36 shows the block diagram of the data acquisition system.

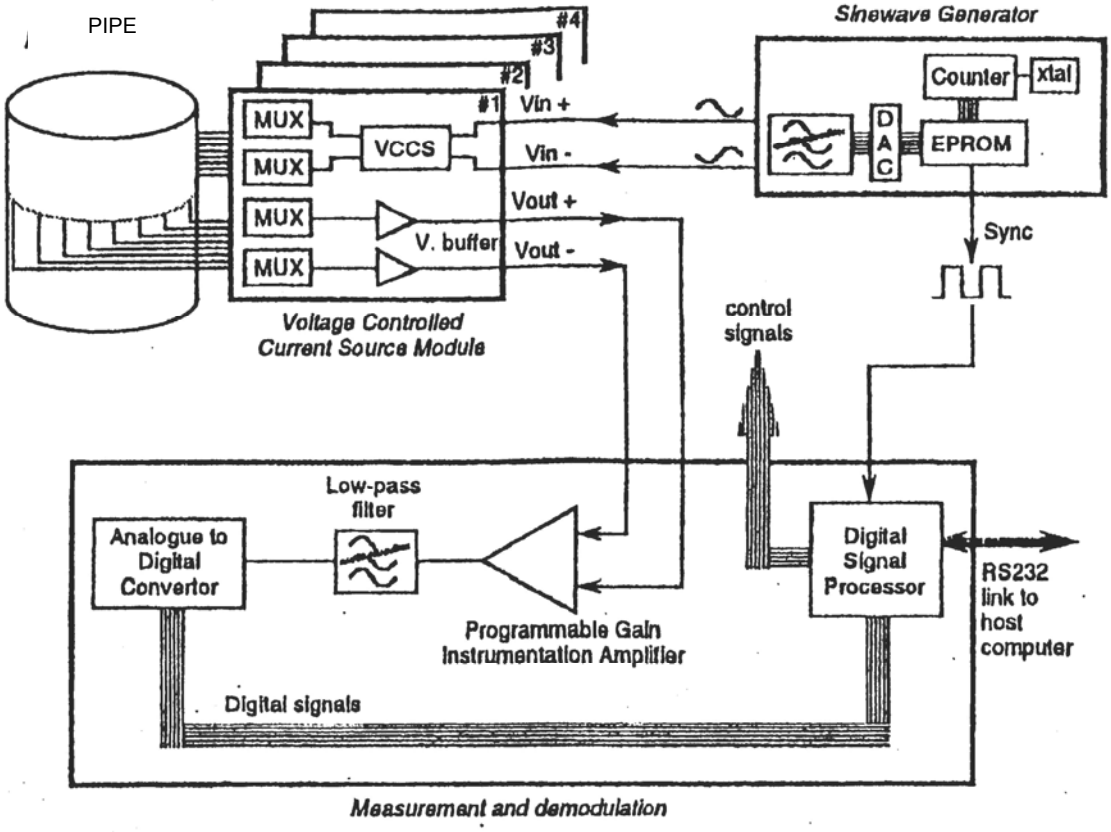

Figure 36. The ERT data acquisition system [122].

The DAS was housed in a portable unit that had four Eurocard sized printed circuit boards. These could perform the following functions: measurement, demodulation and control, waveform generation and synchronisation, multiplexer control, and power supply.

The final part of the ERT system is the algorithm that was used for collecting the data and reconstructing the images. There are four main strategies for collecting the data. These are the adjacent strategy, the opposite strategy, the diagonal strategy, and the conducting boundary strategy. Figure 37 shows the adjacent strategy applied in an ERT system.

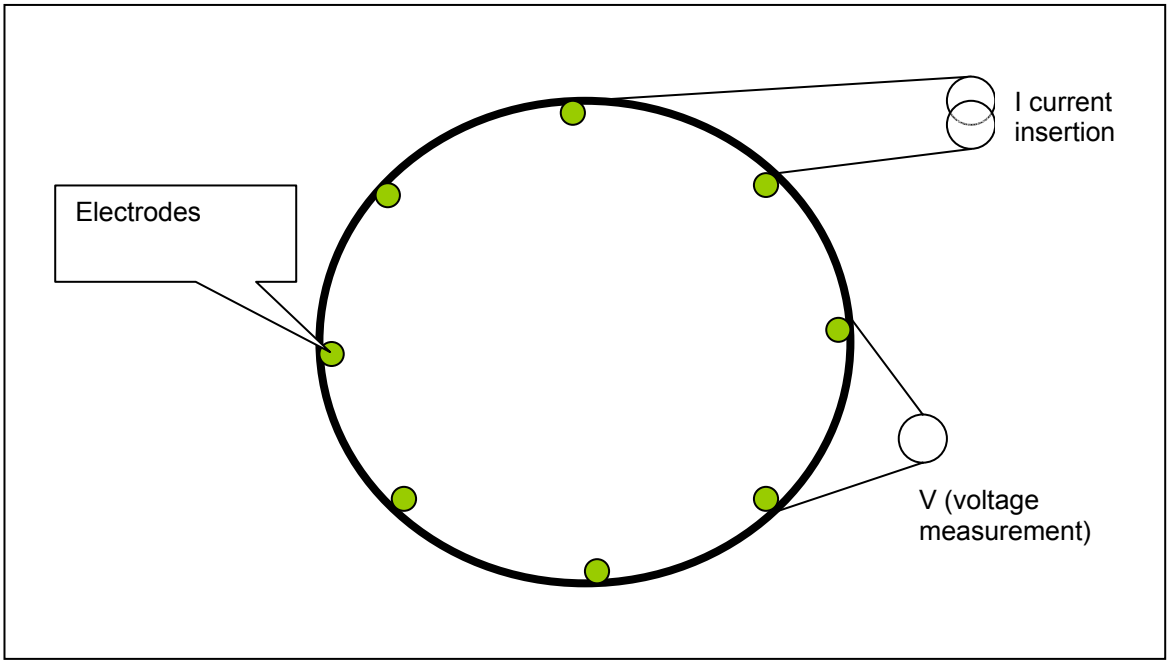

Figure 37. The adjacent strategy

Based on the figure 37, in the current investigation the "adjacent strategy" was used. This uses a pair of electrodes for injecting current into the flow, and another pair of electrodes for measuring the resultant voltage. With the same pair of electrodes injecting current into the flow another pair is used for measuring the voltage. This continues until all the electrodes have been used. Next another pair of electrodes is used for injecting current into the flow and the procedure repeats as before. The

advantage of this method is that it uses minimal hardware to implement and the image reconstruction needs minimal computer resources and it can be performed quickly. The disadvantage of this method is that there is non-uniform current distribution due to the fact that most of the current travels near the boundary electrodes, losing accuracy at the centre of the pipe.

After the data collection, the image reconstruction follows. The image reconstruction can be done off-line. More details regarding image reconstruction algorithms and the ERT system described above can be found in [122].

For the experiments that were conducted in the air-water loop an ITS P2000 ERT system in a dual-plane configuration [137] was used for measuring the local gas volume fraction distribution and the local axial velocity distribution. The adjacent electrode pair strategy with eight electrodes (Note that figure 35 shows a dual plane ERT system with 16 electrodes per plane, but for the experiments an 8 electrode dual plane ERT device was used. The device that was actually used is not shown because all of the electrode connections are permanently covered by a metallic screen) per sensing plane was applied. The amplitude of the injection current was 15 mA for all tests but two signal frequencies of 19.2 KHz and 38.4 KHz were used for every flow condition. The data collection rates were 95 dual-frames per second with 19.2 KHz and 134 dual frames per second with 38.4 KHz. The data collected from the low frequency excitation had a high signal to noise ratio and was used to reconstruct the local gas volume fraction distribution. The data collected with the high excitation frequency had a fast data acquisition rate and was used for velocity implementation. Two reconstruction algorithms were used: volume fraction distributions were reconstructed using the ‘SCG multistep image’ reconstruction algorithm [138] and velocity profiles were based on conductivity images which were reconstructed using

the MSBP algorithm [138]. About 8000 dual-frames of data per flow condition were recorded at 134 dual frames per second and then used to obtain one velocity distribution. The volume fraction distribution for each flow condition was reconstructed from the measurements obtained from 5000 frames obtained at 95 dual frames per second of data to give the 'steady state' local gas volume fraction distribution, averaged over a period of about 52.6 seconds.

Table 7 shows the flow conditions that were used in the ERT experiments. The "L" letter signifies low frequency (19.2KHz/95 dual frames per second), and the "H" letter signifies high frequency (38.4KHz/134 dual frames per second). The last 4 flow conditions with 'IN_' letters front of them indicate that they occurred when the pipe had 15^0 degrees inclination.

Data set	Water Superficial Velocity u_{ws} (ms^{-1})	Air Superficial Velocity u_{gs} (ms^{-1})
L1	0.6371	0.0647
H1	0.65	0.6515
L2	0.132	0.0158
H2	0.1295	0.0155
L3	0.1321	0.0329
H3	0.1295	0.0318
L4	0.3858	0.0138
H4	0.3858	0.0165
L5	0.3936	0.0295
H5	0.3936	0.0294

L6	0.3936	0.067
H6	0.3936	0.0669
L7	0.6603	0.0154
H7	0.6603	0.0154
L8	0.6603	0.0301
H8	0.6603	0.0301
L9	0.6603	0.0684
H9	0.6603	0.0684
L10	0.6603	0.1112
H10	0.6603	0.1113
L11	0.8986	0.0165
H11	0.8986	0.0165
L12	0.8986	0.0315
H12	0.8986	0.0316
L13	0.8986	0.0656
H13	0.8986	0.0657
L14	0.8986	0.1134
H14	0.8986	0.1134
L15	0.8986	0.1615
H15	0.8986	0.1612
L16	1.1446	0.0149
H16	1.1446	0.0149
L17	1.1524	0.0281
H17	1.1524	0.028

L18	1.1524	0.0639
H18	1.1524	0.0639
L19	1.1524	0.1078
H19	1.1524	0.1079
L20	1.1524	0.1572
H20	1.1524	0.1575
IN_L1	0.6448	0.0641
IN_H1	0.6448	0.0641
IN_L2	0.909	0.0638
IN_H2	0.909	0.0639

Table 7. The experiments conducted using the ERT system.

The air-water results from ERT were compared with the air-water results from the dual sensor probe as shown in subsequent chapters of this thesis.

8. Experimental results from dual sensor probes and discussion of results.

In this part of the thesis the results of the dual sensor probe experiments are shown. These include the air water experiments with 0^o, 15^o, and 30^o degrees of pipe inclination with respect to the vertical. Also, the oil water experiments are included with 0^o degrees inclination only.

This chapter also includes results from the ERT system taken in air-water flows that were vertical and inclined at 15^o to the vertical.

8.1 Dual sensor air-water results.

Local gas volume fraction and velocity profiles were obtained for values of water superficial velocity u_{ws} in the range $0.1\,\mathrm{ms}^{-1}$ to $1.14\,\mathrm{ms}^{-1}$, values of air superficial velocity u_{gs} in the range $0.018\,\mathrm{ms}^{-1}$ to $0.166\,\mathrm{ms}^{-1}$ and for pipe inclination angles ψ away from the vertical of 0^o, 15^o and 30^o. The profiles shown in figures 38 to 40 are results from a subset of these flow conditions. In figures 38 and 39 the colour red represents the maximum value of the local gas volume fraction α_l at a particular flow condition and the colour blue represents the minimum value of α_l at this flow condition. In figure 40 the colour red represents the maximum value of the local gas velocity u_{gl} at a particular flow condition and the colour blue represents the minimum value of u_{gl} at this flow condition. For the results shown in figures 38 and 39 α_l was typically calculated from between 600 and 1500 bubbles, where α_l was a maximum, and between 300 and 800 bubbles, where α_l was half the maximum value. For each flow condition the area-weighted mean gas volume fraction $\overline{\alpha}$ in the flow

cross section was calculated from the measured values of α_l and was found (on average for all of the flow conditions investigated) to be within 5% of the reference value of the mean gas volume fraction $\overline{\alpha}_{ref}$ obtained using the differential pressure measurement technique described in section 7.3.2. This gave good confidence in the accuracy of the measured values of α_l. For the results shown in figure 40 u_{gl} was typically calculated from between 600 to 1500 bubbles in the regions where α_l was close to the maximum value and from between 300 to 800 bubbles in regions where α_l was close to half the maximum value. It should be noted that the range of values of α_l is different for each of the graphs shown in figures 38 and 39 as indicated by the colour scale to the right of each graph. Also shown at the top of each graph is the reference value $\overline{\alpha}_{ref}$ of the mean gas volume fraction at that flow condition. Similarly, the range of values of u_{gl} shown in figure 40 is different for the different graphs that are shown.

The results shown in figures 38-40 are representative of all of the dual sensor air-water results that were obtained and detailed discussion of the results shown in figures 38-40 is given later in this chapter. In fact, additional measurements were obtained at other air-water flow conditions and, for completeness, these are shown (in the form of 3D graphs) in figures 41 to 59. Note that in figures 41 to 59, for every flow condition reference values are given of (i) the mean gas volume fraction; (ii) the superficial gas and water velocities and (iii) the mean gas velocity. Values of the mean gas volume fraction, the mean gas velocity and the superficial gas velocity which were obtained (by integration) from the local values of α_l and u_{gl} are also shown in figures 41 to 59 and are denoted ‘measured values’. It should be noted, with reference to figures 41 to 59 that, for some flow conditions, it was very difficult to

obtain accurate measurements of the local bubble velocity when the dual sensor probe was placed at certain locations close to the pipe wall (this was often because there were so few bubbles present at these probe positions). For these flow conditions and probe locations the value of u_{gl} was set equal to zero in figures 44 to 59. In figures 41 to 59 the pipe inclination angles ψ from the vertical are 0^o, 15^o and 30^o respectively.

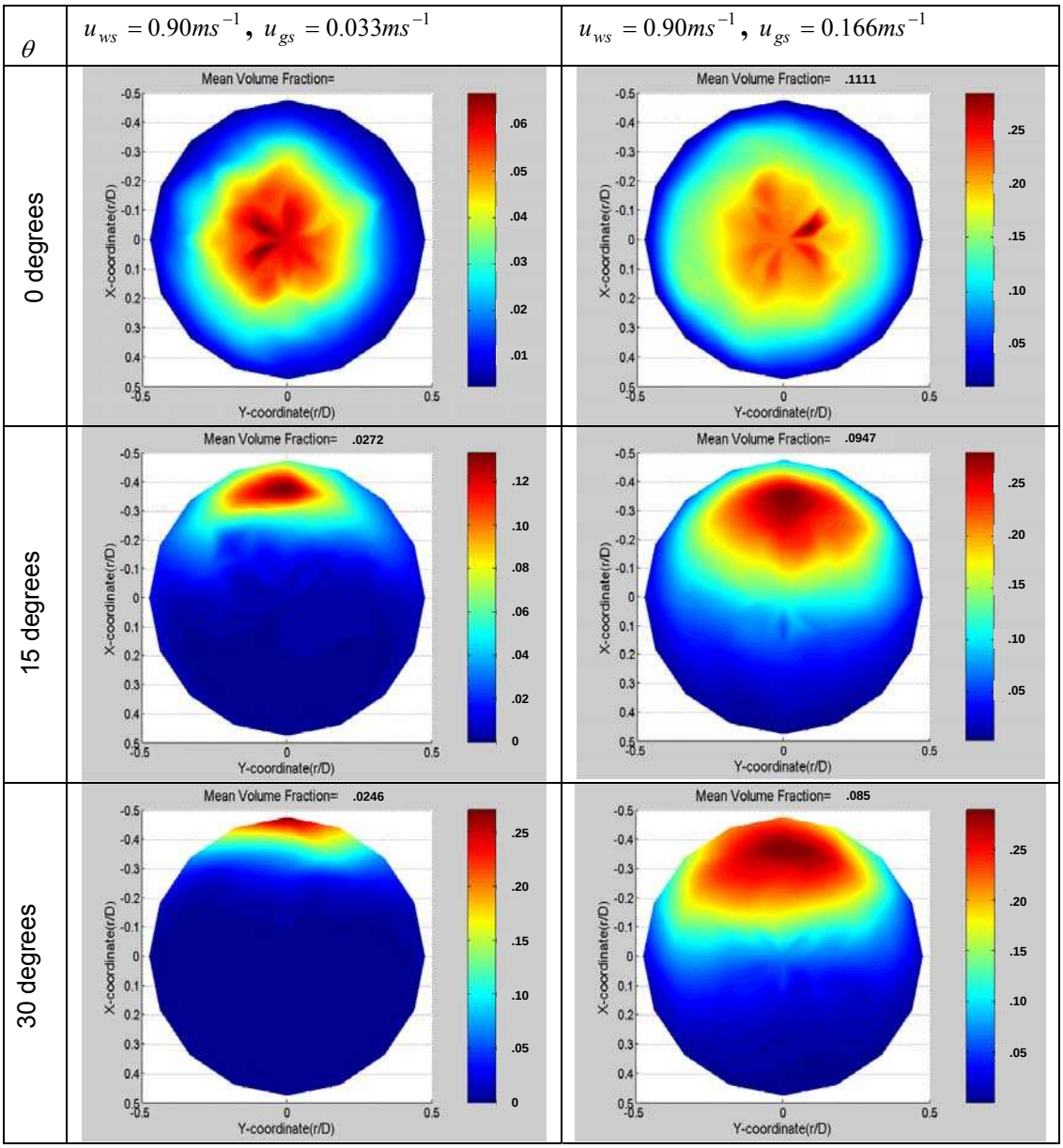

Figure 38 Local gas volume fraction distributions at constant water superficial velocity (case I left and case II right), r represents radial position, *D* is pipe diameter.

It should be noted that the range of values of α_l is different for each of the graphs shown in figures 38 and 39, as indicated by the colour scale to the right of each graph. Also shown at the top of each graph is the reference value $\overline{\alpha}_{ref}$ of the mean gas volume fraction at that flow condition.

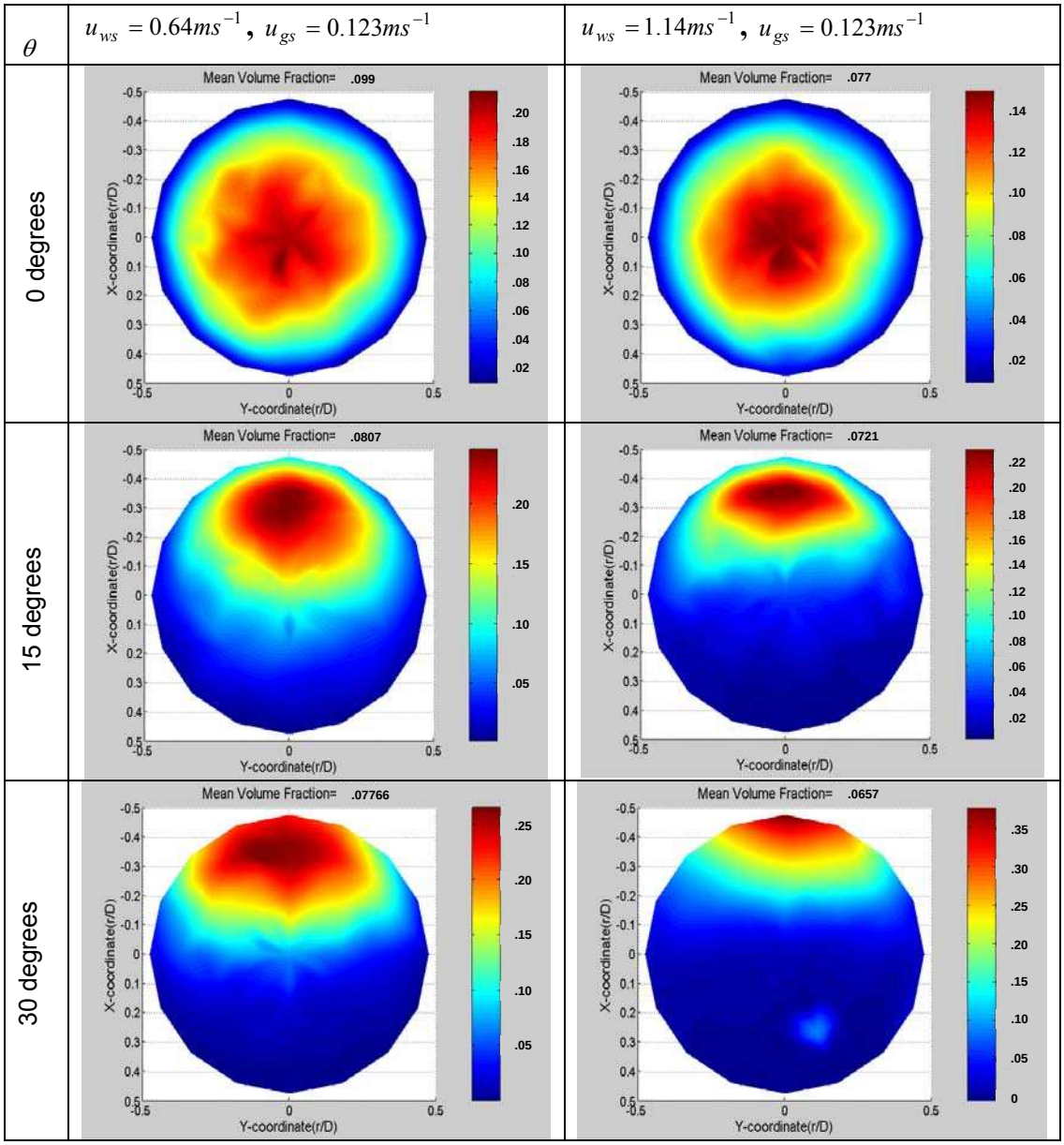

Figure 39. Local gas volume fraction distributions at constant gas superficial velocity (case III left and case IV right), r represents radial position, D is pipe diameter.

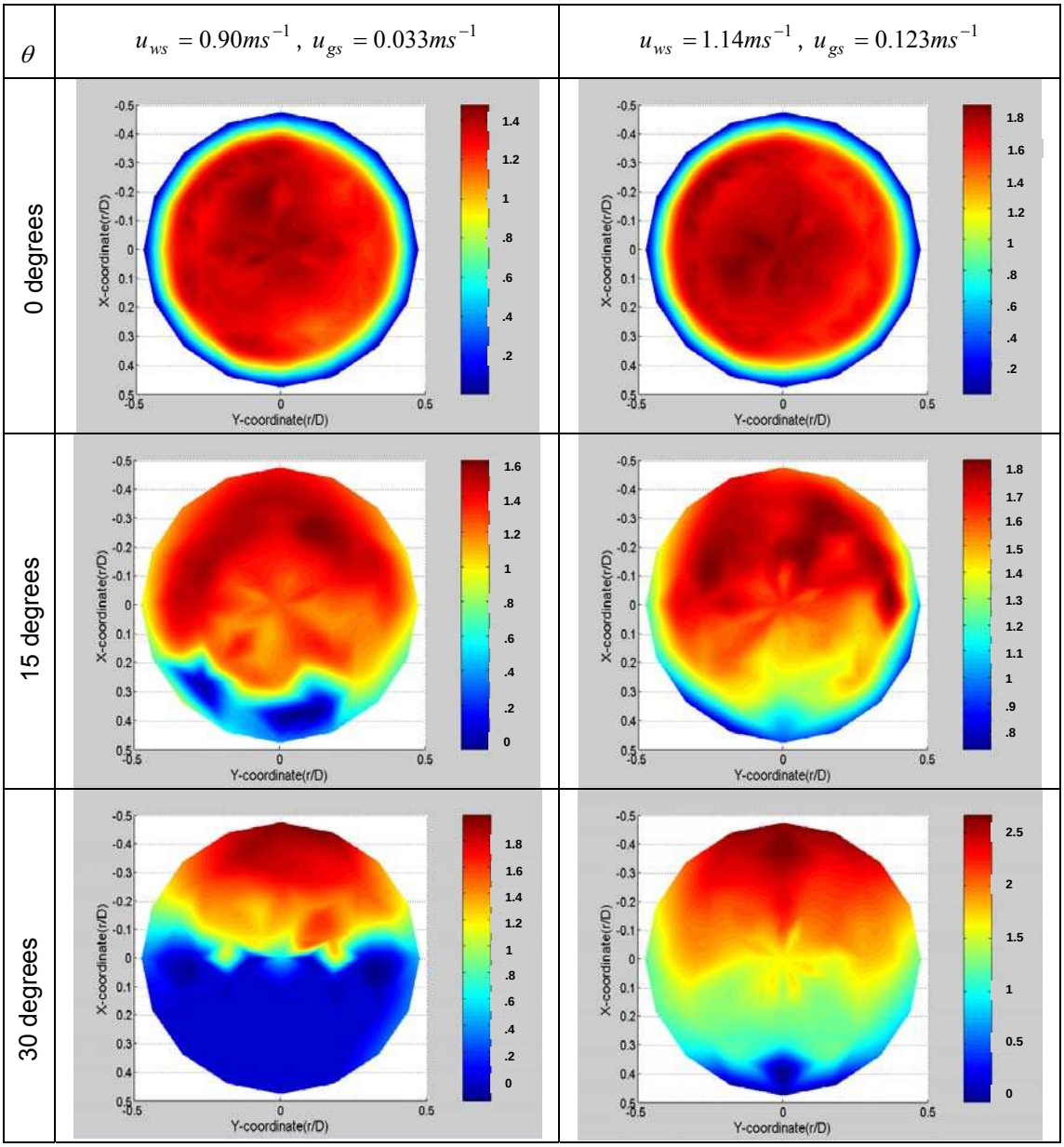

Figure 40. Local gas velocity profiles (case I left and case IV right), r represents radial position, D is pipe diameter (velocity is in ms^{-1})

The above results shown in the figures 38-40 are the ones that detailed analysis has been performed upon and which will be discussed in more detailed later in this chapter. In fact, more measurements have been acquired and processed for different flow conditions. It is worth showing the results of the other flow conditions. The next figures are shown in 3D view. Note that for every flow condition, the reference and the measured values of volume fraction, superficial gas and water

velocity, and the mean gas velocity are shown. The pipe inclination angles from the vertical are 0^0, 15^0, and 30^0. For all flow conditions there was good agreement between the reference volume fraction and the integrated local volume fraction in the flow cross section. Fair agreement was also found between the reference values of the mean and superficial gas velocities and the values of these variables obtained by integration of the local gas properties in the flow cross section (see Appendix II listing of matlab file "volint88new.m"). Below the formulas that are used in order to compute the local gas volume fraction $\overline{\alpha}_{est}$ and the local gas velocity $\overline{u}_{d,est}$ values are shown.

$$\overline{\alpha}_{est} = \frac{\sum_{j=1}^{81} \alpha_{1,j} A_j}{A} \tag{59}$$

$$\overline{u}_{d,est} = \frac{\sum_{j=1}^{81} u_{d1,j} \alpha_{1,j} A_j}{\sum_{j=1}^{81} \alpha_{1,j} A_j} \tag{60}$$

Reference Data
volume fraction=0.0364
superficial gas velocity=0.0183 msec^{-1}
superficial water velocity=0.1019 msec^{-1}
mean gas velocity=0.5017 msec^{-1}

Measured values
volume fraction = 0.0360
mean gas velocity = 0.5933 msec^{-1}
superficial gas velocity = 0.0214 msec^{-1}

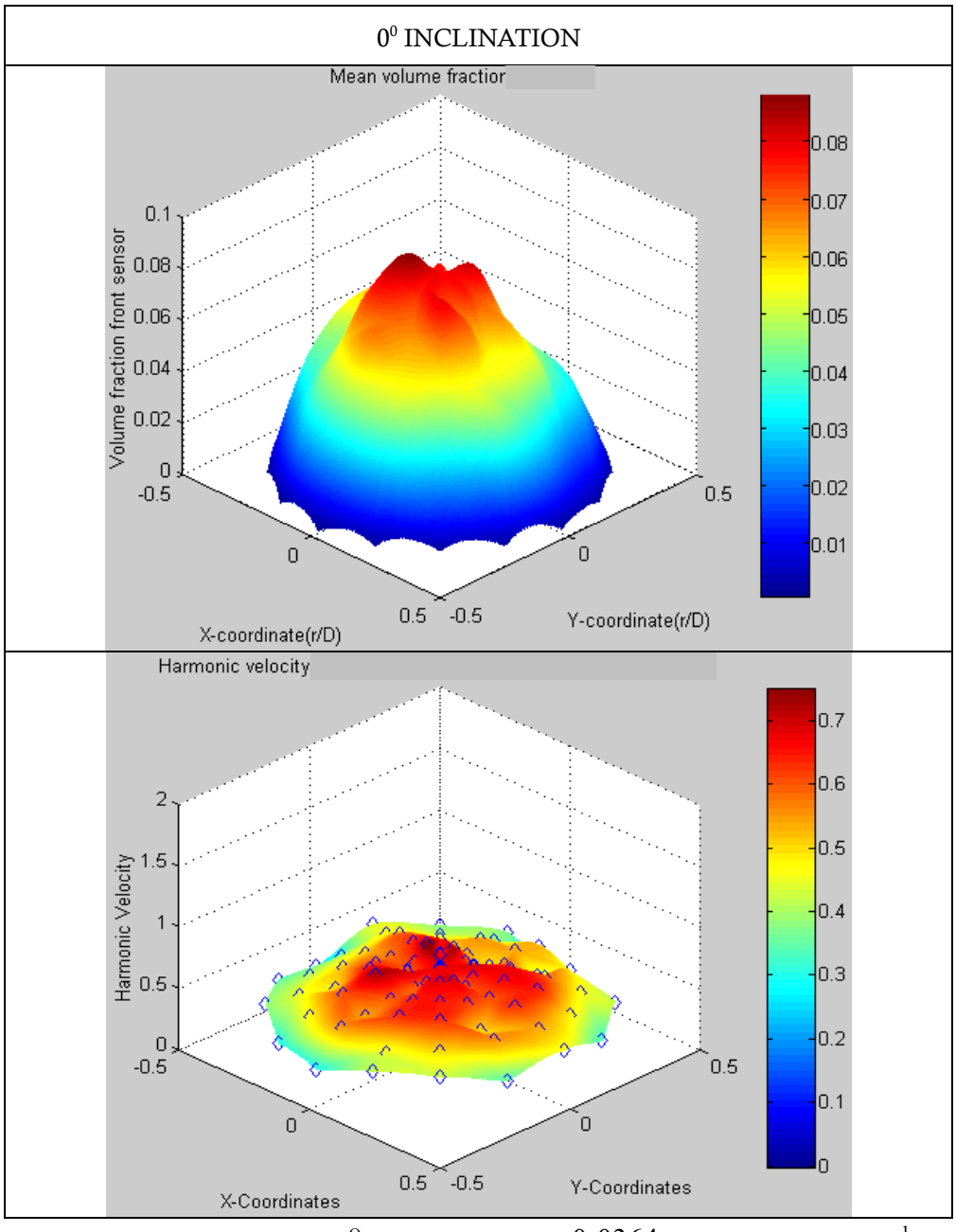

Figure 41. Dual sensor probe 0^{O} inclination $\alpha_{ref} = 0.0364$, $u_{ws} = 0.1019$ ms^{-1}, $u_{gs} = 0.0183$ ms^{-1}

Reference Data
volume fraction=0.0690
superficial gas velocity=0.0347 msec^{-1}
superficial water velocity=0.1019 msec^{-1}
mean gas velocity=0.5034 msec^{-1}

Measured values
volume fraction = 0.0637
mean gas velocity = 0.6230 msec^{-1}
superficial gas velocity = 0.0397 msec^{-1}

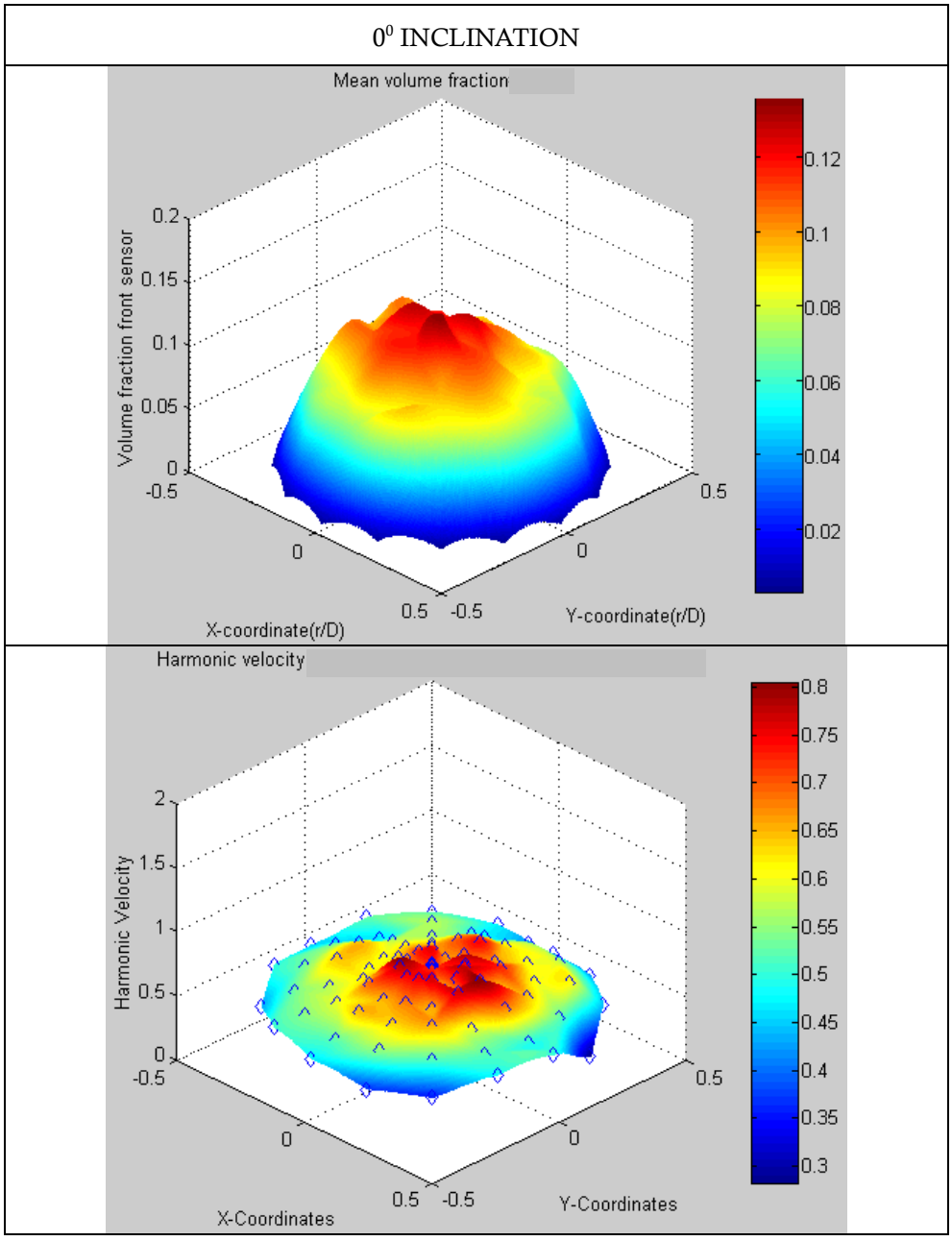

Figure 42 Dual sensor probe 0^{O} inclination $\alpha_{ref} = 0.0690$, $u_{ws} = 0.1019 \text{ ms}^{-1}$, $u_{gs} = 0.5034 \text{ ms}^{-1}$

Reference Data
volume fraction = 0.0378
superficial gas velocity = 0.0321 msec^{-1}
superficial water velocity = 0.3803 msec^{-1}
mean gas velocity= 0.8491 msec^{-1}

Measured values
volume fraction = 0.0416
mean gas velocity = 0.8486 msec^{-1}
superficial gas velocity = 0.0353 msec^{-1}

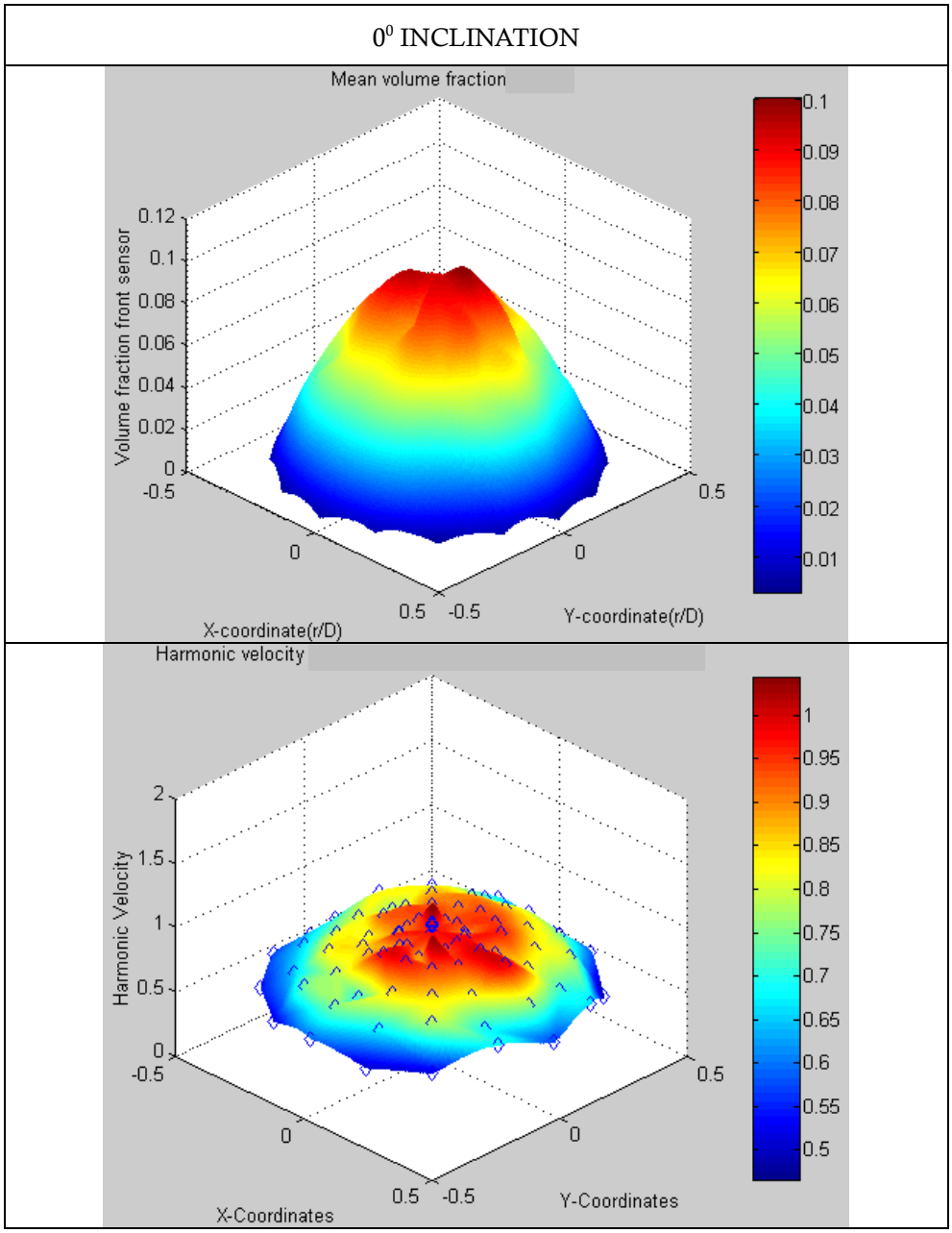

Figure 43. Dual sensor probe 0^{O} inclination $\alpha_{ref} = 0.0378$, $u_{ws} = 0.3803\,\mathrm{ms}^{-1}$, $u_{gs} = 0.8491\,\mathrm{ms}^{-1}$

Reference Data
volume fraction=0.0326
superficial gas velocity=0.0353 msec^{-1}
superficial water velocity=0.6412 msec^{-1}
mean gas velocity=1.0791 msec^{-1}

Measured values
volume fraction = 0.033
mean gas velocity = 1.0871 msec^{-1}
superficial gas velocity = 0.0359 msec^{-1}

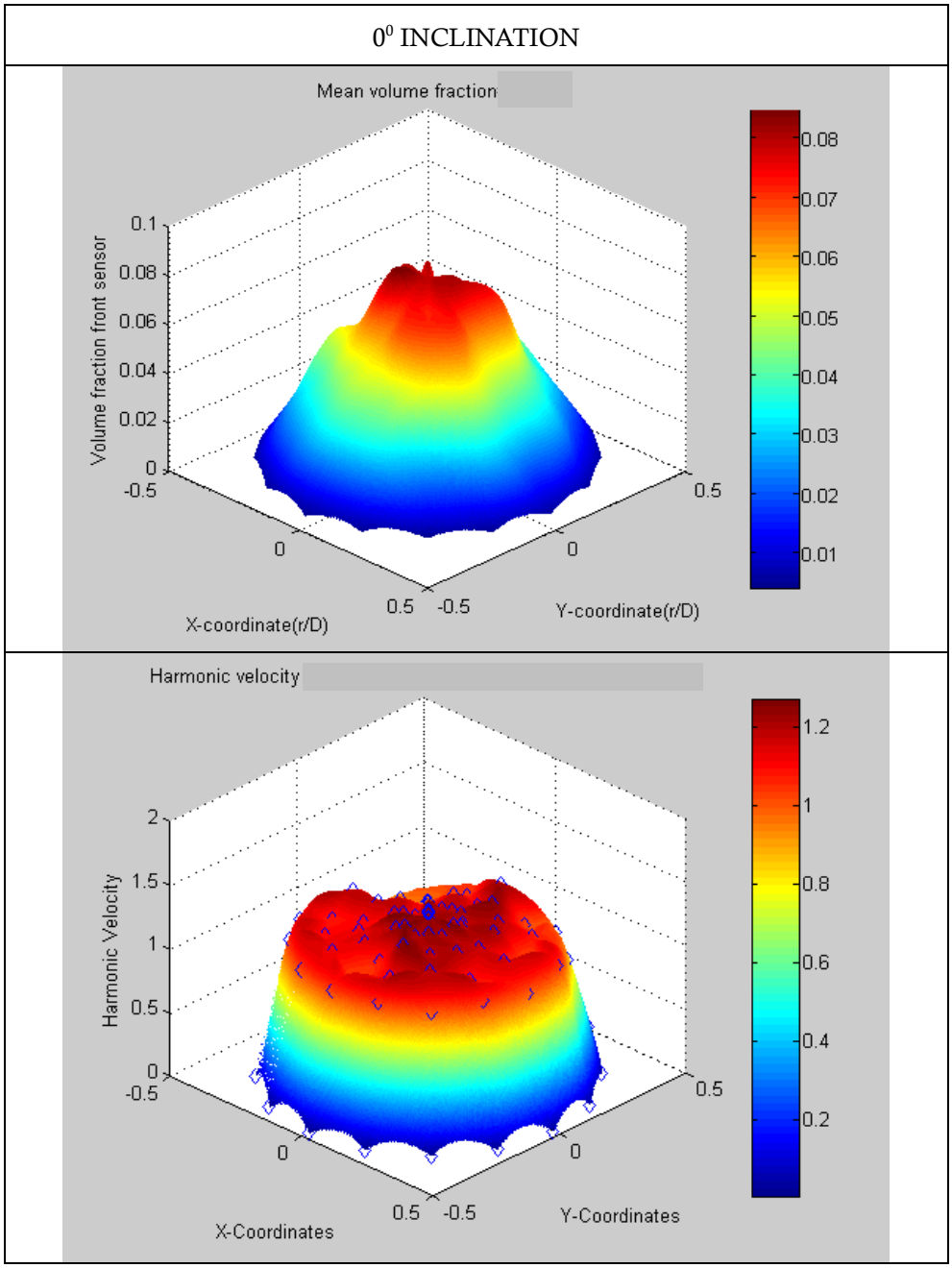

Figure 44. Dual sensor probe 0^{O} inclination $\alpha_{ref} = 0.0326$, $u_{ws} = 0.6412\,\mathrm{ms}^{-1}$, $u_{gs} = 0.0353\,\mathrm{ms}^{-1}$

Reference Data
volume fraction=0.0835
superficial gas velocity=0.1213 msec^{-1}
superficial water velocity=0.8775 msec^{-1}
mean gas velocity=1.4521 msec^{-1}

Measured values
volume fraction = 0.0795
mean gas velocity = 1.4515 msec^{-1}
superficial gas velocity = 0.1154 msec^{-1}

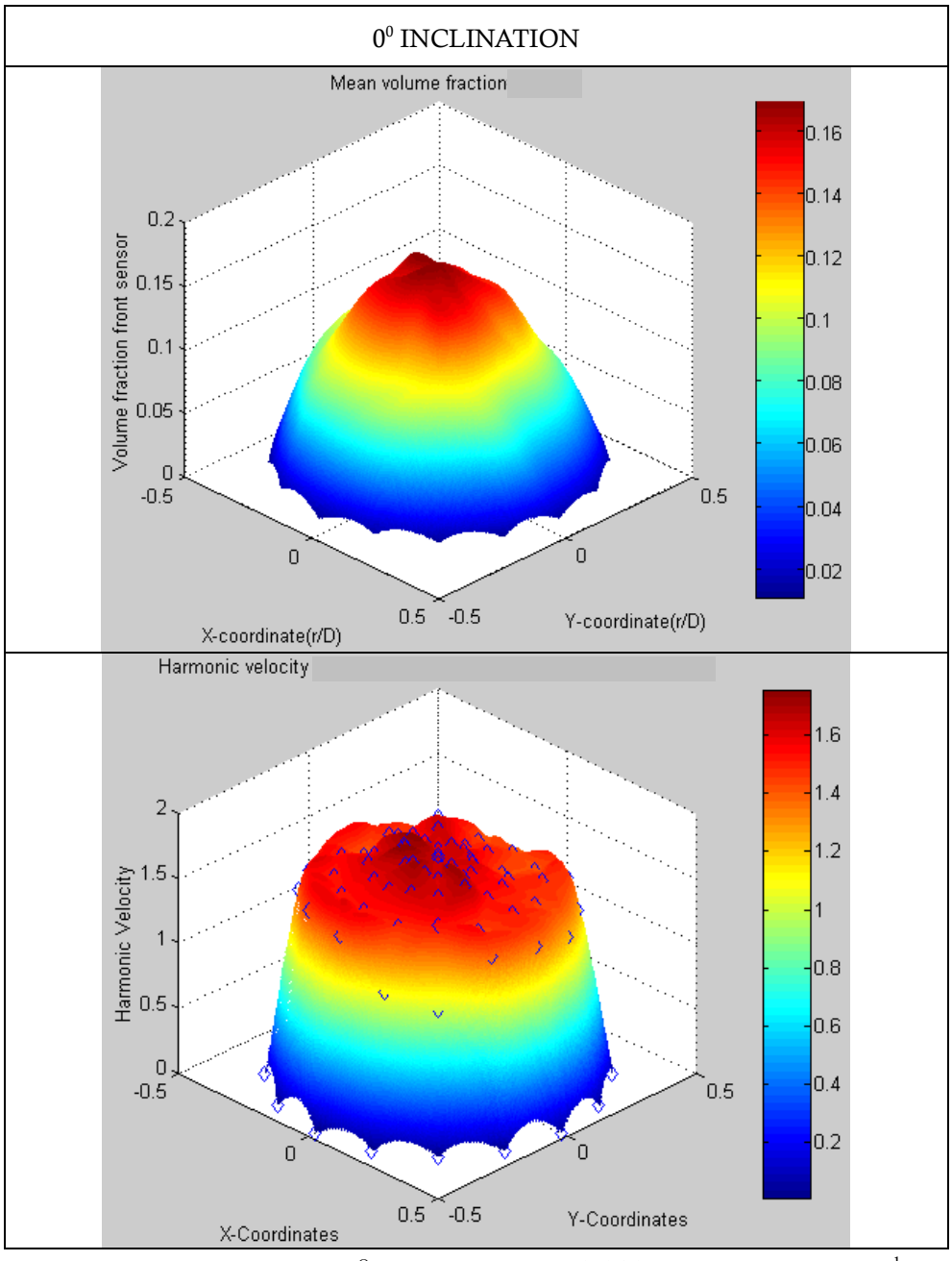

Figure 45. Dual sensor probe 0^{O} inclination $\alpha_{ref} = 0.0835$, $u_{ws} = 0.8775\,\mathrm{ms}^{-1}$, $u_{gs} = 0.1213\,\mathrm{ms}^{-1}$

Reference data
volume fraction = 0.0258
superficial gas velocity = 0.0334 msec^{-1}
superficial water velocity = 1.1417 msec^{-1}
mean gas velocity = 1.2919 msec^{-1}

Measured values
volume fraction = 0.0217
mean gas velocity = 1.3418 msec^{-1}
superficial gas velocity = 0.0292 msec^{-1}

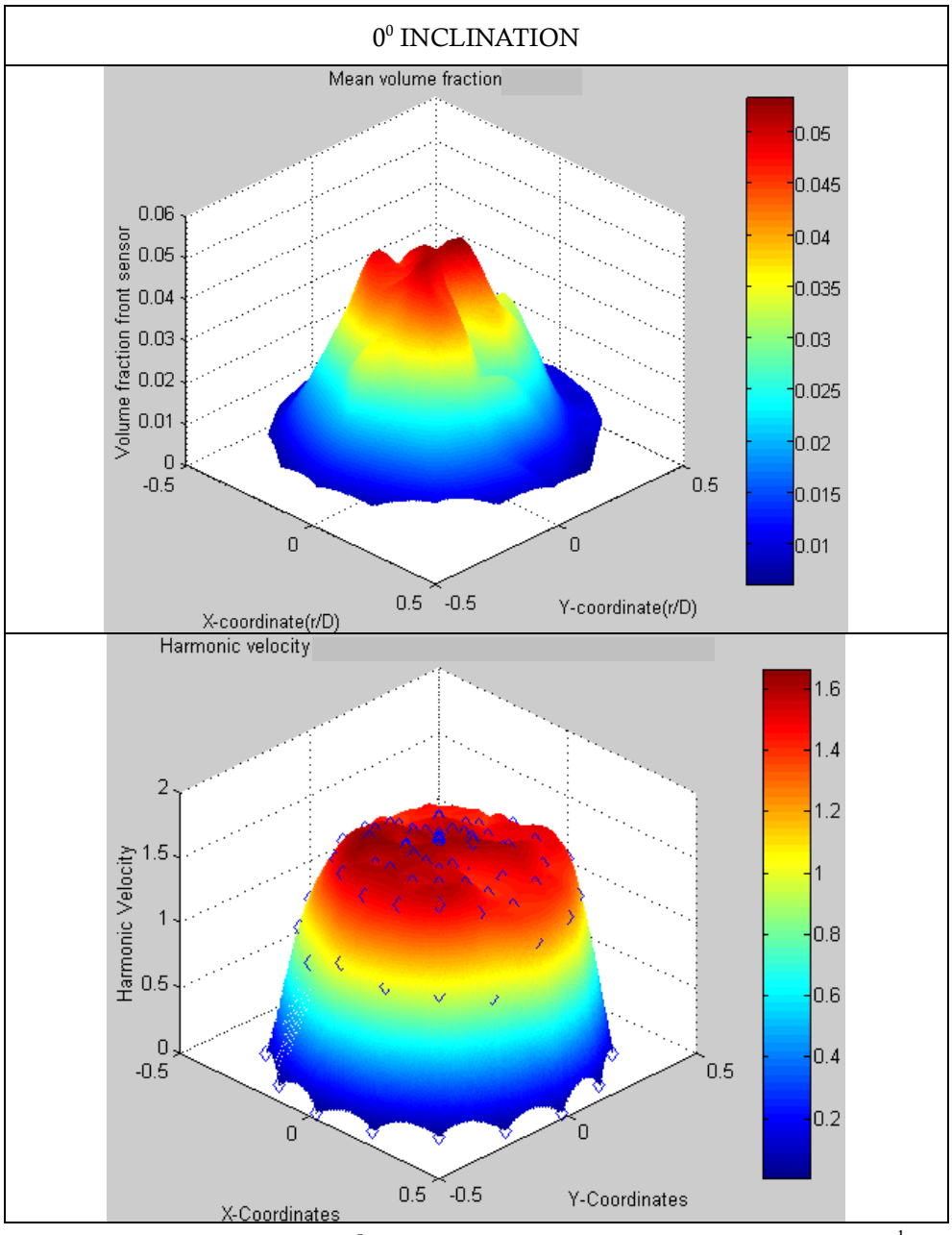

Figure 46. Dual sensor probe 0^{O} inclination $\alpha_{ref} = 0.0258$, $u_{ws} = 1.1417\,\mathrm{ms}^{-1}$, $u_{gs} = 0.0334\ \mathrm{ms}^{-1}$

Reference Data
volume fraction=0.0975
superficial gas velocity=0.164 msec^{-1}
superficial water velocity=1.1513 msec^{-1}
mean gas velocity= 1.6823 msec^{-1}

Measured values
volume fraction = 0.0932
mean gas velocity = 1.7006 msec^{-1}
superficial gas velocity = 0.1584 msec^{-1}

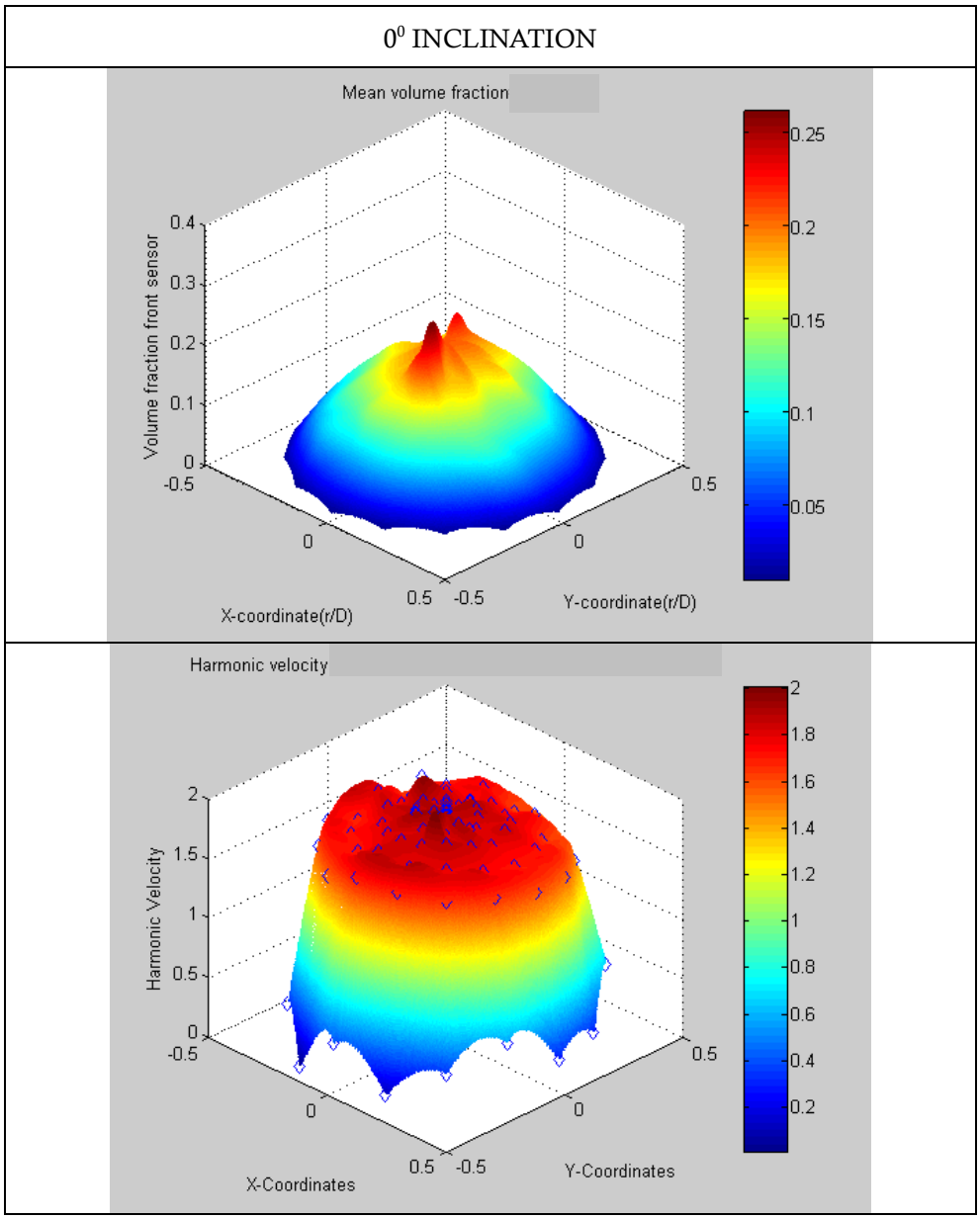

Figure 47. Dual sensor probe 0^{O} inclination $\alpha_{ref} = 0.0975$, $u_{ws} = 1.1513 \text{ms}^{-1}$, $u_{gs} = 0.164 \text{ ms}^{-1}$

Reference Data
volume fraction=0.0489
superficial gas velocity=0.0350 msec^{-1}
superficial water velocity=0.1106 msec^{-1}
mean gas velocity=0.7157 msec^{-1}

Measured values
volume fraction = 0.0439
mean gas velocity = 0.8159 msec^{-1}
superficial gas velocity = 0.0358 msec^{-1}

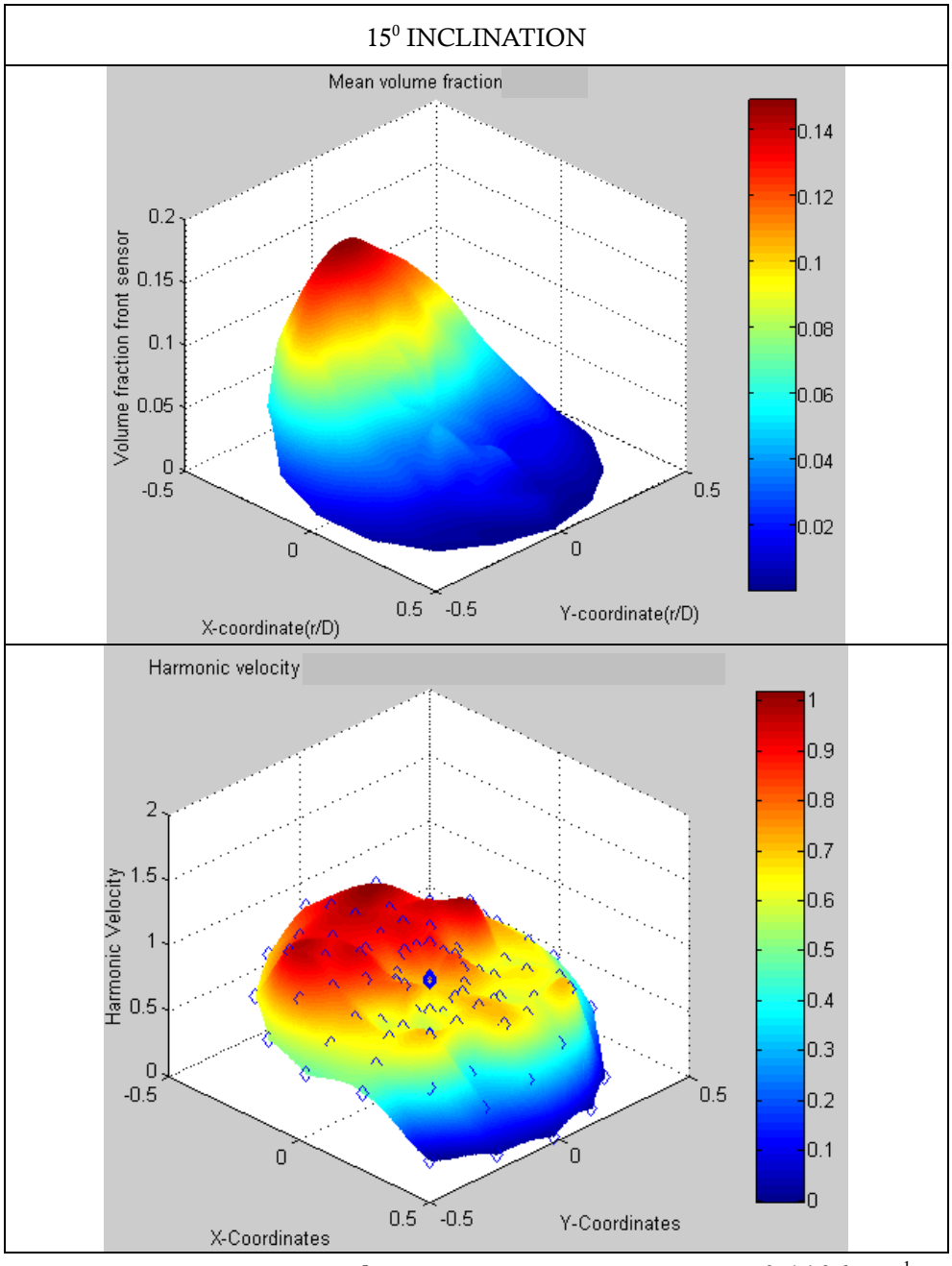

Figure 48. Dual sensor probe 15^{O} inclination $\alpha_{ref} = 0.0439$, $u_{ws} = 0.1106\,\mathrm{ms}^{-1}$, $u_{gs} = 0.0350\ \mathrm{ms}^{-1}$

Reference Data
volume fraction=0.0293
superficial gas velocity=0.0339 msec^{-1}
superficial water velocity=0.3783 msec^{-1}
mean gas velocity=1.1571 msec^{-1}

Measured values
volume fraction = 0.0291
mean gas velocity = 1.1492 msec^{-1}
superficial gas velocity = 0.0334 msec^{-1}

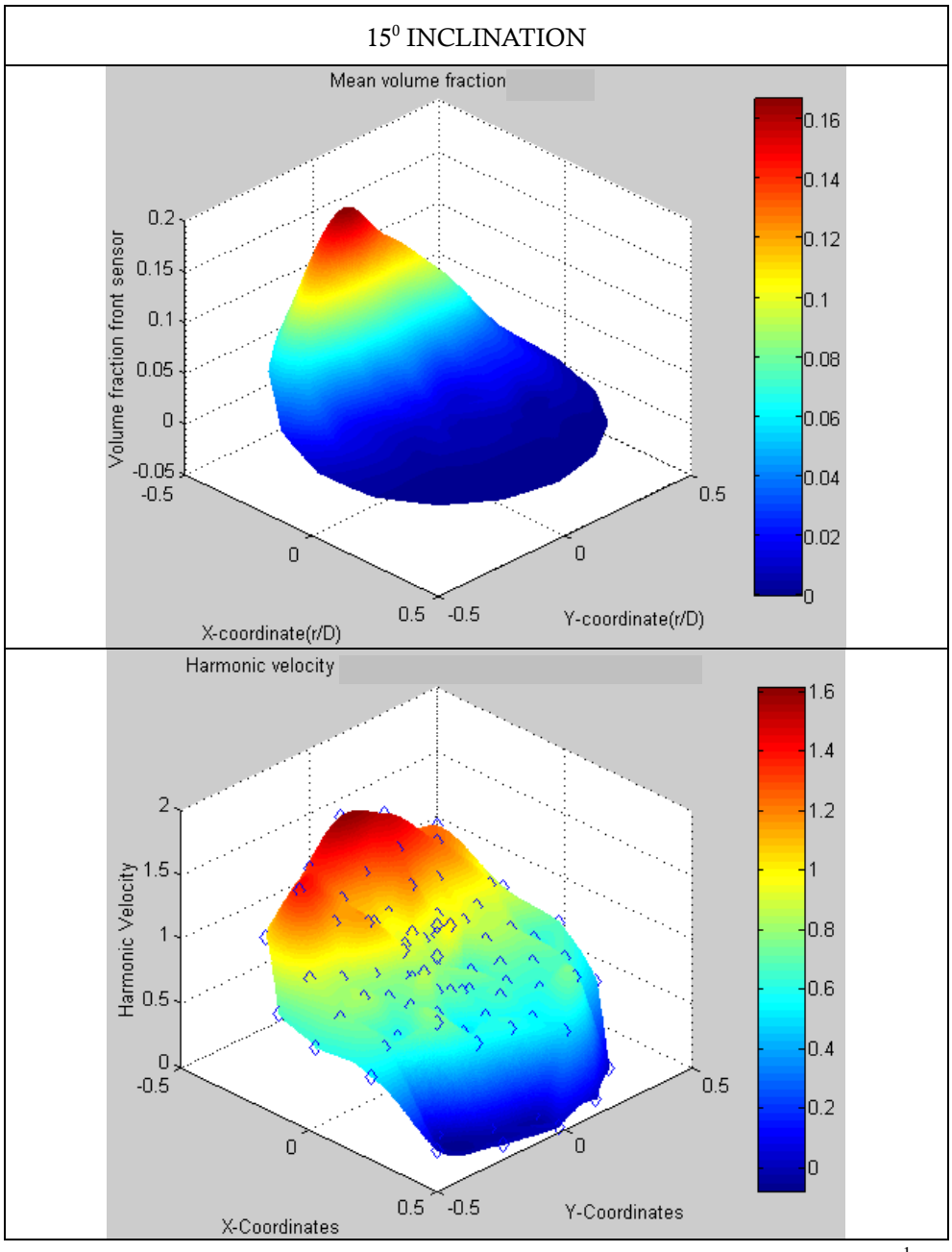

Figure 49. Dual sensor probe 15^{O} inclination $\alpha_{ref} = 0.0293$, $u_{ws} = 0.3783 \text{ms}^{-1}$, $u_{gs} = 0.0339 \text{ ms}^{-1}$

Reference Data
volume fraction=0.0238
superficial gas velocity=0.0358 msec^{-1}
superficial water velocity=0.6494 msec^{-1}
mean gas velocity=1.5018 msec^{-1}

Measured data
volume fraction = 0.0237
mean gas velocity = 1.4255 msec^{-1}
superficial gas velocity = 0.0338 msec^{-1}

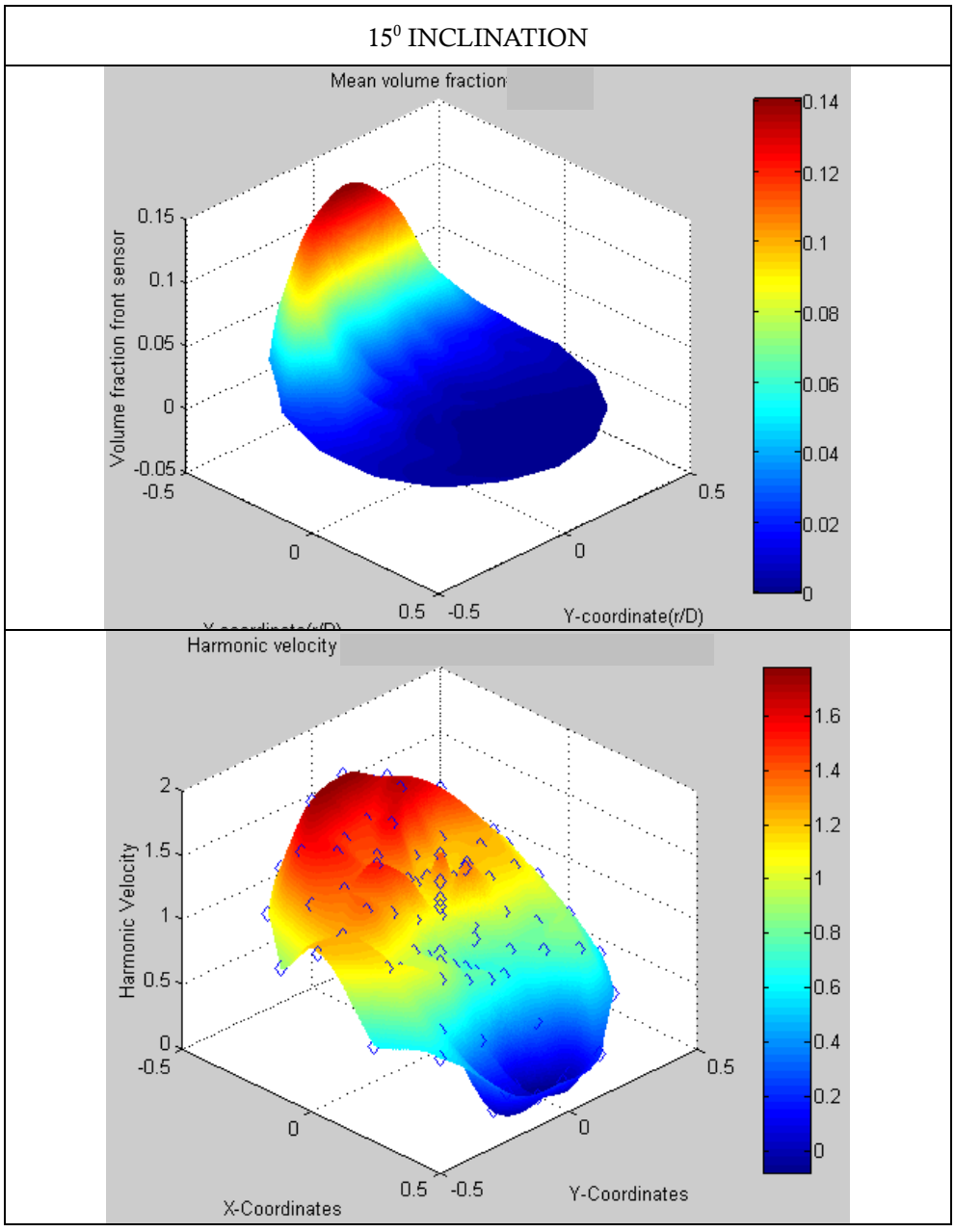

Figure 50. Dual sensor probe 15^{O} inclination $\alpha_{ref} = 0.0238$, $u_{ws} = 0.6494\,\mathrm{ms}^{-1}$, $u_{gs} = 0.0358\,\mathrm{ms}^{-1}$

Reference Data
volume fraction=0.0698
superficial gas velocity=0.1202 msec^{-1}
superficial water velocity=0.9074 msec^{-1}
mean gas velocity=1.7220 msec^{-1}

Measured values
volume fraction = 0.0627
mean gas velocity = 1.6234 msec^{-1}
superficial gas velocity = 0.1018 msec^{-1}

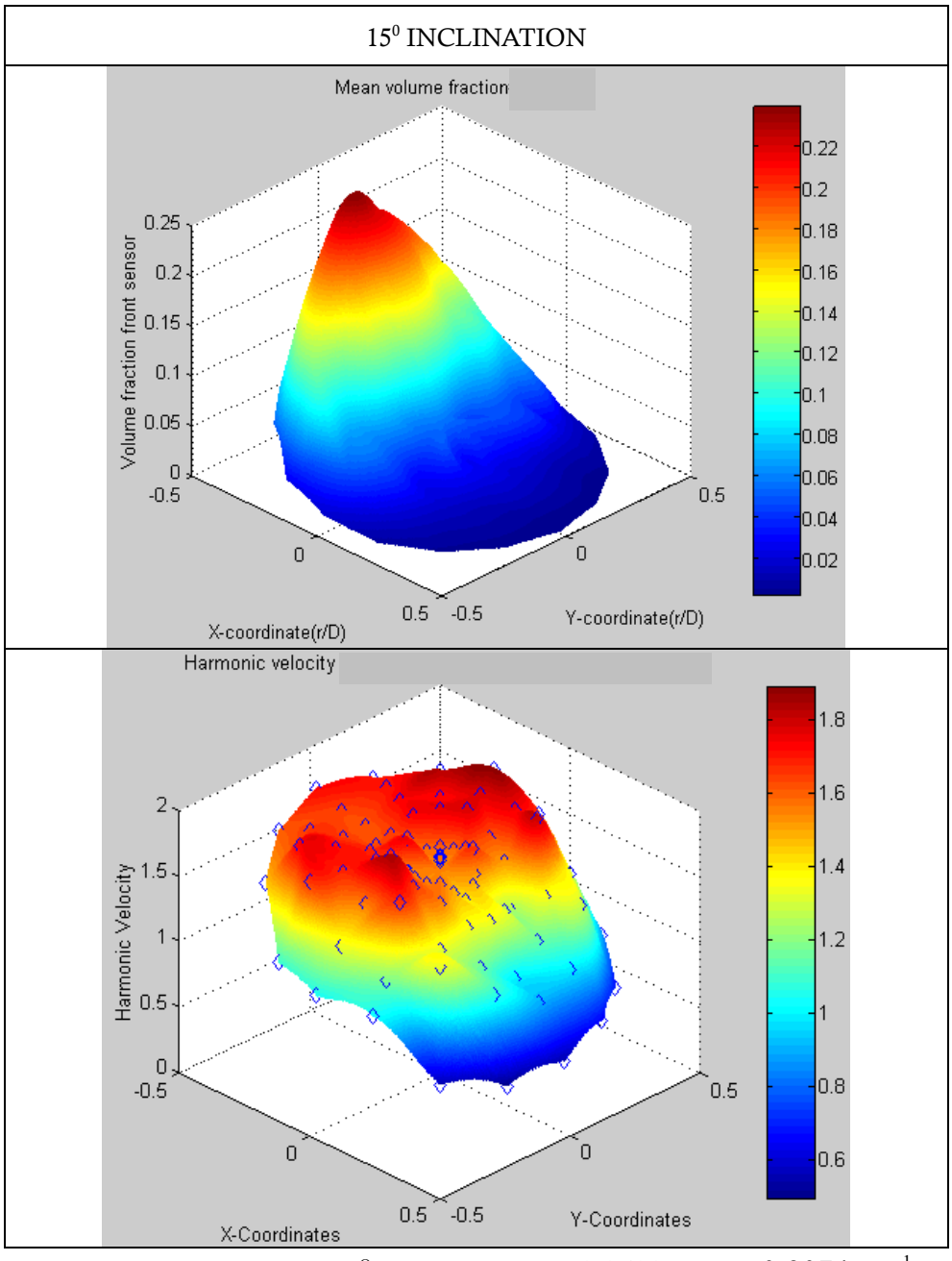

Figure 51. Dual sensor probe 15^{O} inclination $\alpha_{ref} = 0.0698$, $u_{ws} = 0.9074\,\mathrm{ms}^{-1}$, $u_{gs} = 0.1202\ \mathrm{ms}^{-1}$

Reference Data
volume fraction=0.0284
superficial gas velocity=0.0335 msec^{-1}
superficial water velocity=1.1472 msec^{-1}
mean gas velocity=1.1795 msec^{-1}

Measured values
volume fraction = 0.0202
mean gas velocity = 1.5019 msec^{-1}
superficial gas velocity = 0.0304 msec^{-1}

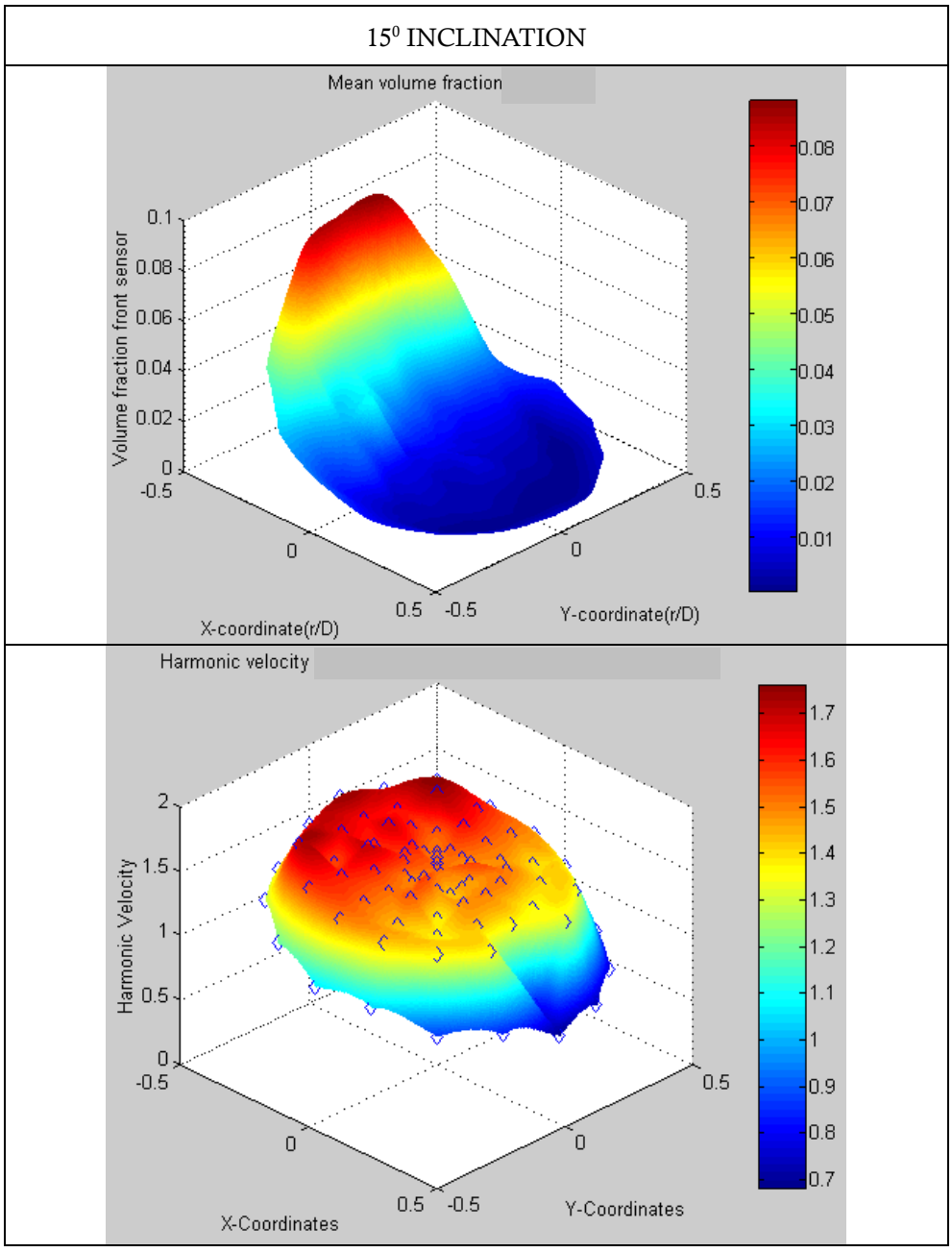

Figure 52. Dual sensor probe 15^{O} inclination $\alpha_{ref} = 0.0284$, $u_{ws} = 1.1472\,\mathrm{ms}^{-1}$, $u_{gs} = 0.0335\ \mathrm{ms}^{-1}$

Reference Data
volume fraction=0.0930
superficial gas velocity=0.1642 msec^{-1}
superficial water velocity=1.1470 msec^{-1}
mean gas velocity=1.7666 msec^{-1}

Measured values
volume fraction = 0.0733
mean gas velocity = 1.6907 msec^{-1}
superficial gas velocity = 0.1240 msec^{-1}

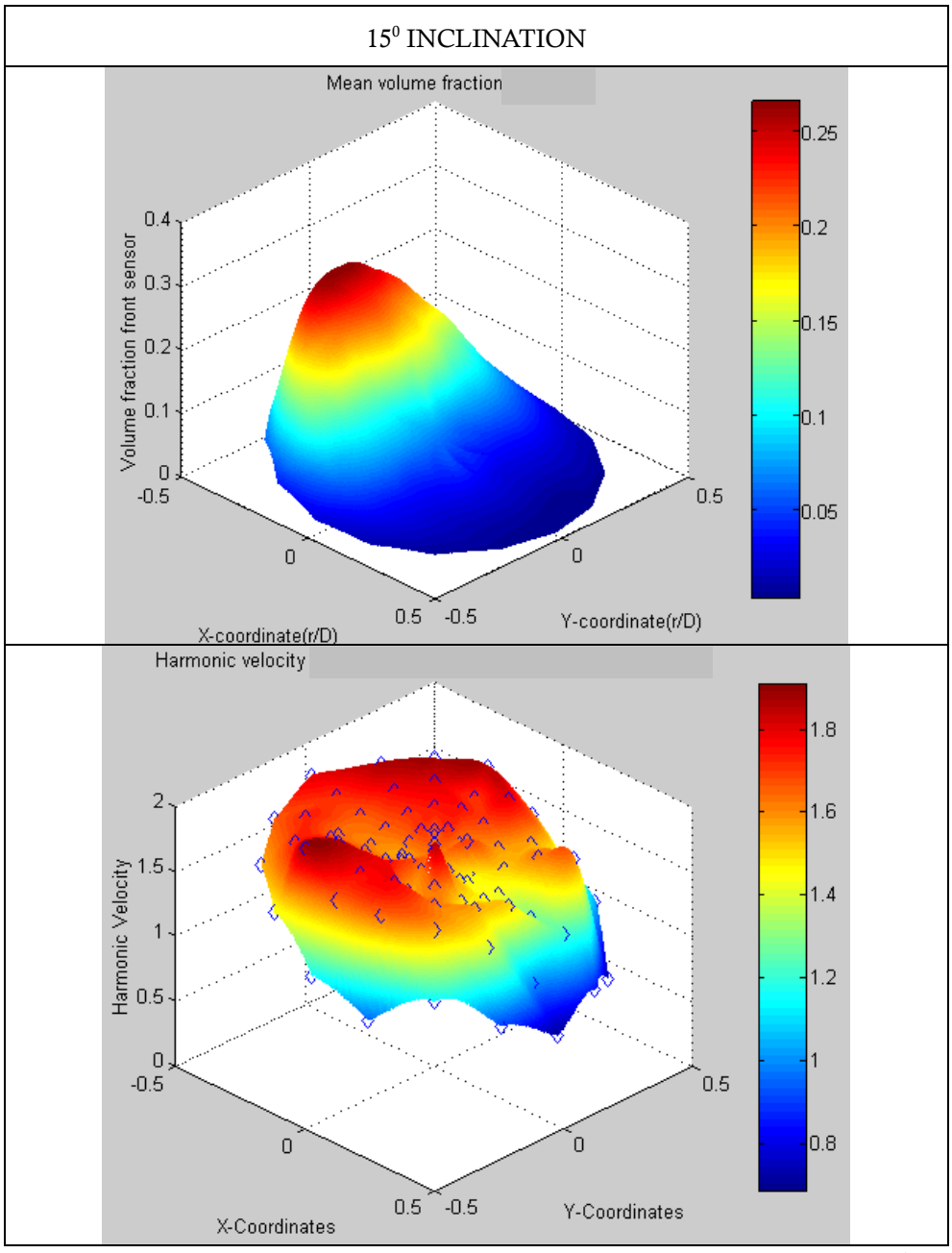

Figure 53. Dual sensor probe 15^{O} inclination $\alpha_{ref} = 0.0930$, $u_{ws} = 1.1470 \text{ms}^{-1}$, $u_{gs} = 0.1642 \text{ ms}^{-1}$

Reference Data
volume fraction=0.0394
superficial gas velocity=0.0345 msec^{-1}
superficial water velocity=0.1048 msec^{-1}
mean gas velocity=0.8750 msec^{-1}

Measured values
volume fraction = 0.0408
superficial gas velocity = 0.0418 msec^{-1}
mean gas velocity 30inc = 0.5126 msec^{-1}

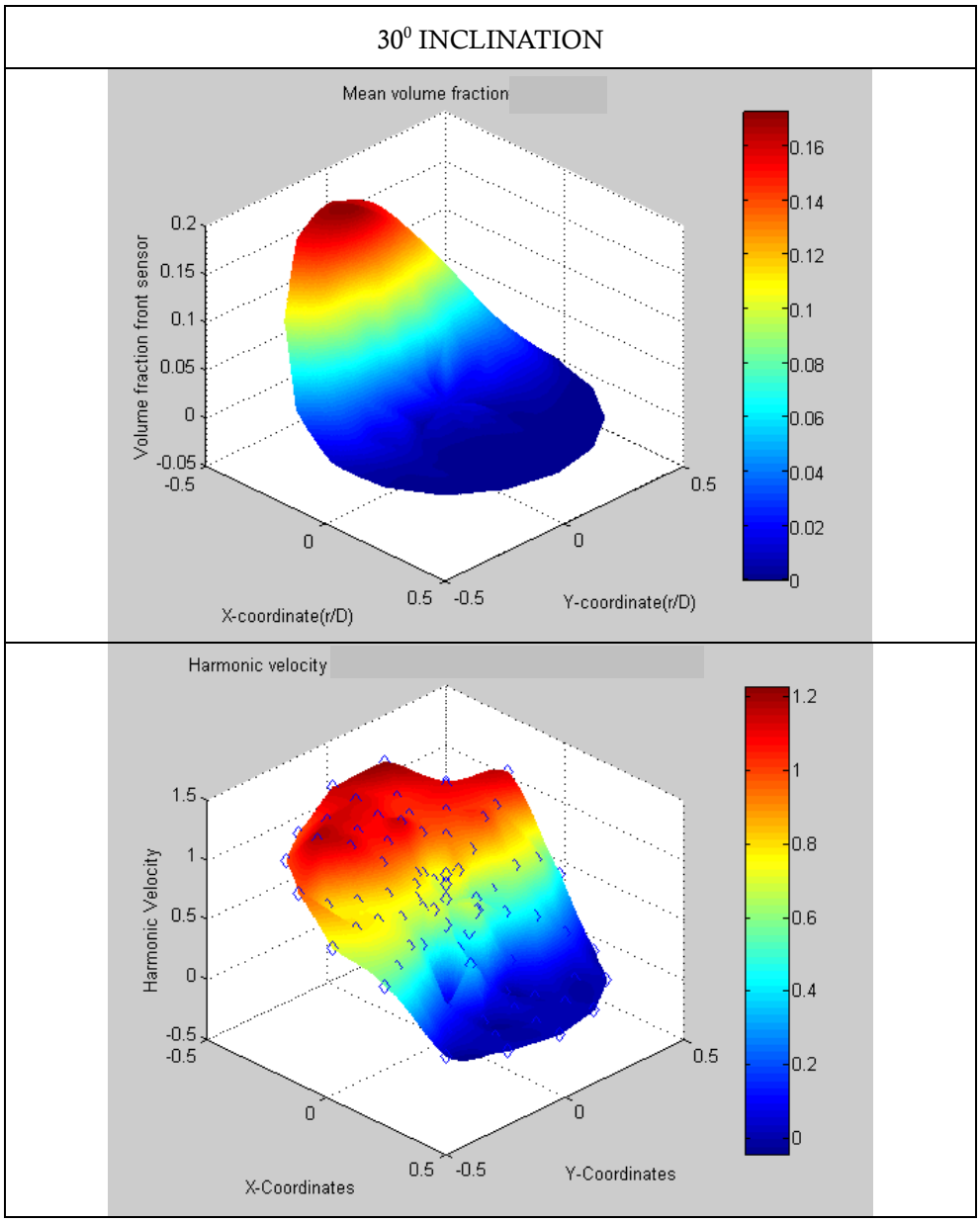

Figure 54. Dual sensor probe 30^{O} inclination $\alpha_{ref} = 0.0394$, $u_{ws} = 0.1048 \text{ms}^{-1}$, $u_{gs} = 0.0345 \text{ ms}^{-1}$

Reference Data
volume fraction=0.0270
superficial gas velocity=0.0327 msec^{-1}
superficial water velocity=0.3967 msec^{-1}
mean gas velocity=1.2095 msec^{-1}

Measured values
volume fraction = 0.0295
superficial gas velocity = 0.0358 msec^{-1}
mean gas velocity = 0.6073 msec^{-1}

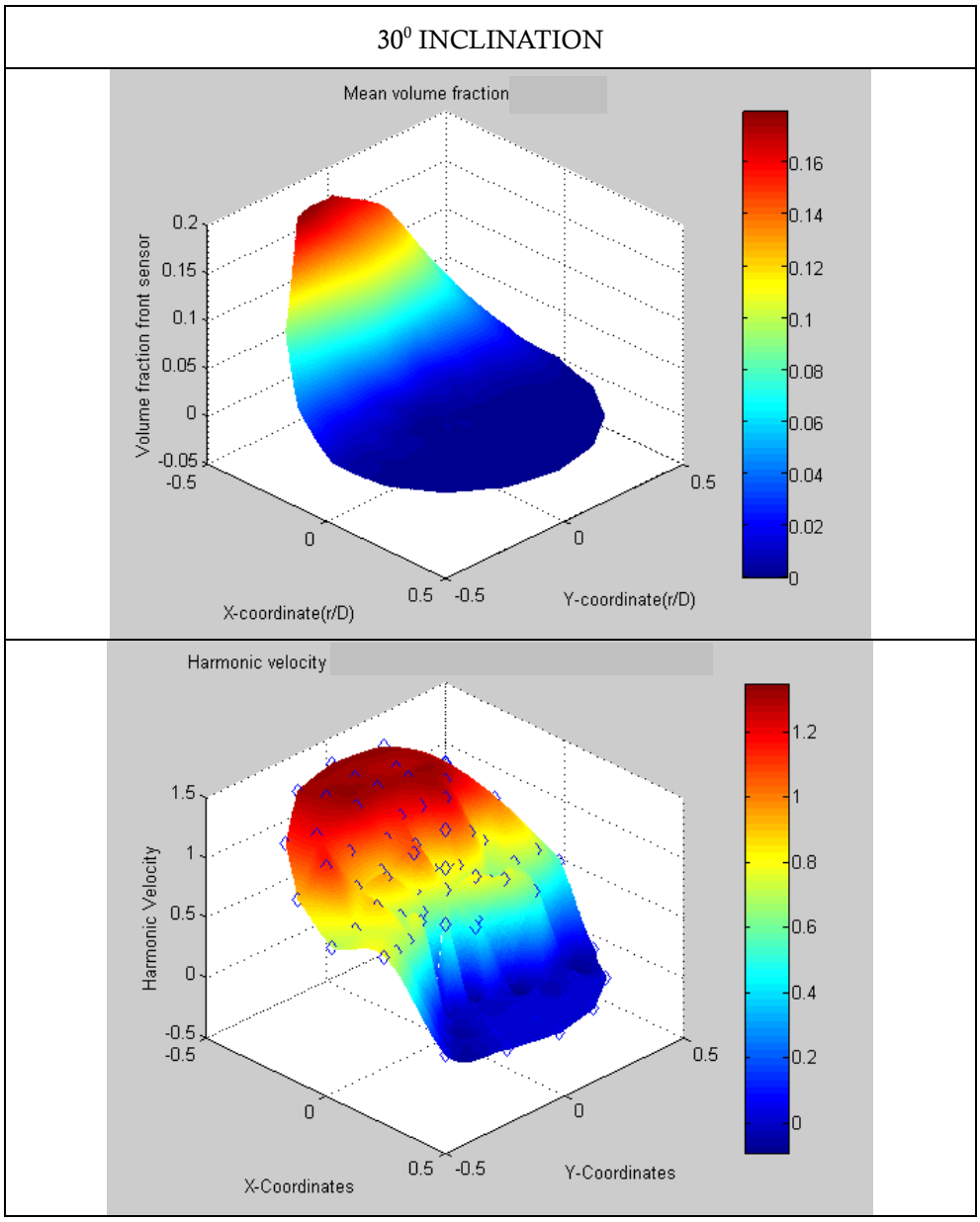

Figure 55. Dual sensor probe 30^{O} inclination $\alpha_{ref} = 0.0270$, $u_{ws} = 0.3967\,\mathrm{ms}^{-1}$, $u_{gs} = 0.0327\ \mathrm{ms}^{-1}$

Reference Data
volume fraction=0.0227
superficial gas velocity=0.0345 msec^{-1}
superficial water velocity=0.6501 msec^{-1}
mean gas velocity=1.5231 msec^{-1}

Measured values
volume fraction = 0.0248
superficial gas velocity = 0.0396 msec^{-1}
mean gas velocity= 0.7996 msec^{-1}

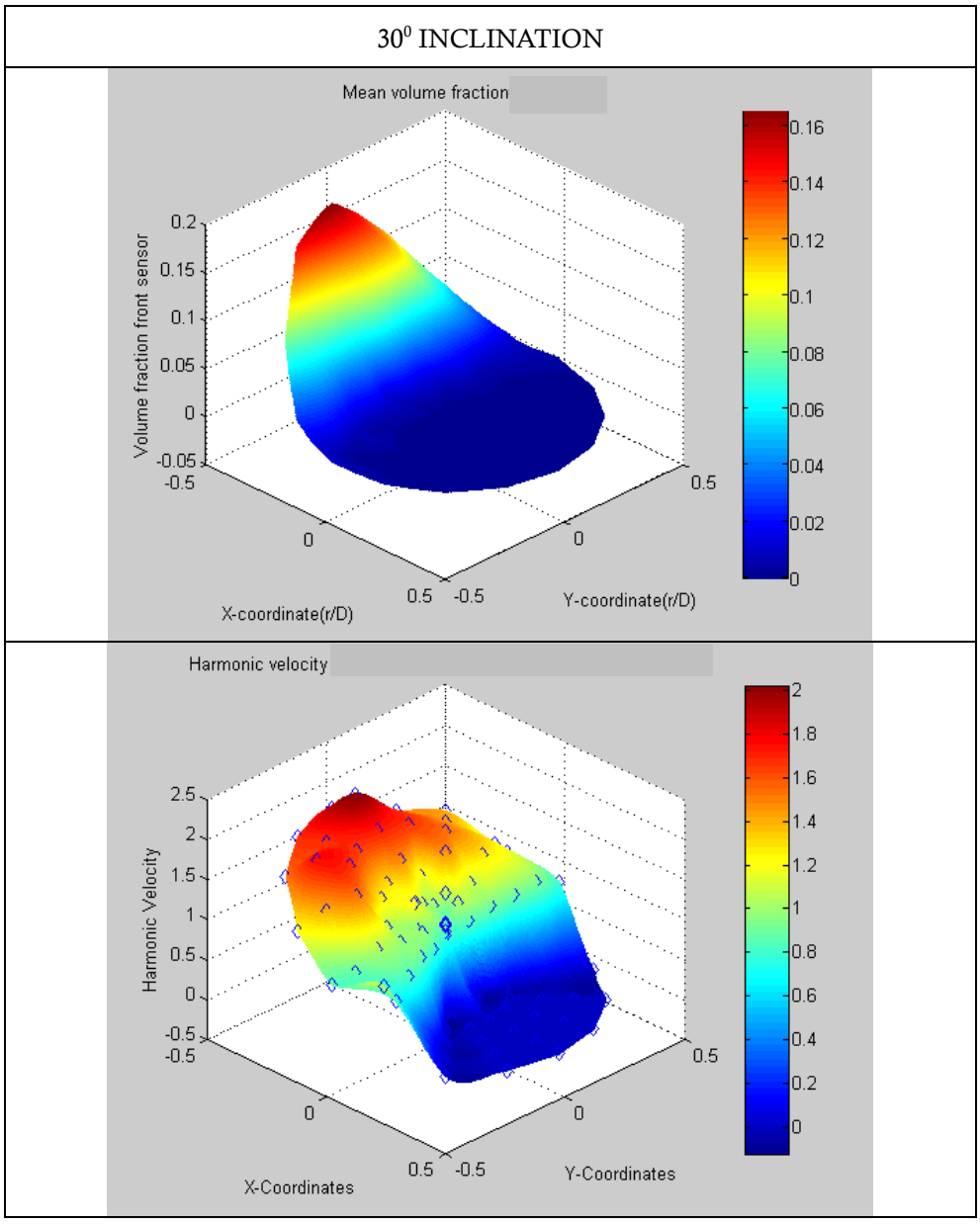

Figure 56. Dual sensor probe 30^{O} inclination $\alpha_{ref} = 0.0227$, $u_{ws} = 0.6501 \text{ms}^{-1}$, $u_{gs} = 0.0345 \text{ ms}^{-1}$

Reference Data
volume fraction=0.0649
superficial gas velocity=0.1179 msec^{-1}
superficial water velocity=0.8969 msec^{-1}
mean gas velocity=1.8167 msec^{-1}

Measured values
volume fraction = 0.0659
superficial gas velocity = 0.1211 msec^{-1}
mean gas velocity= 0.9181 msec^{-1}

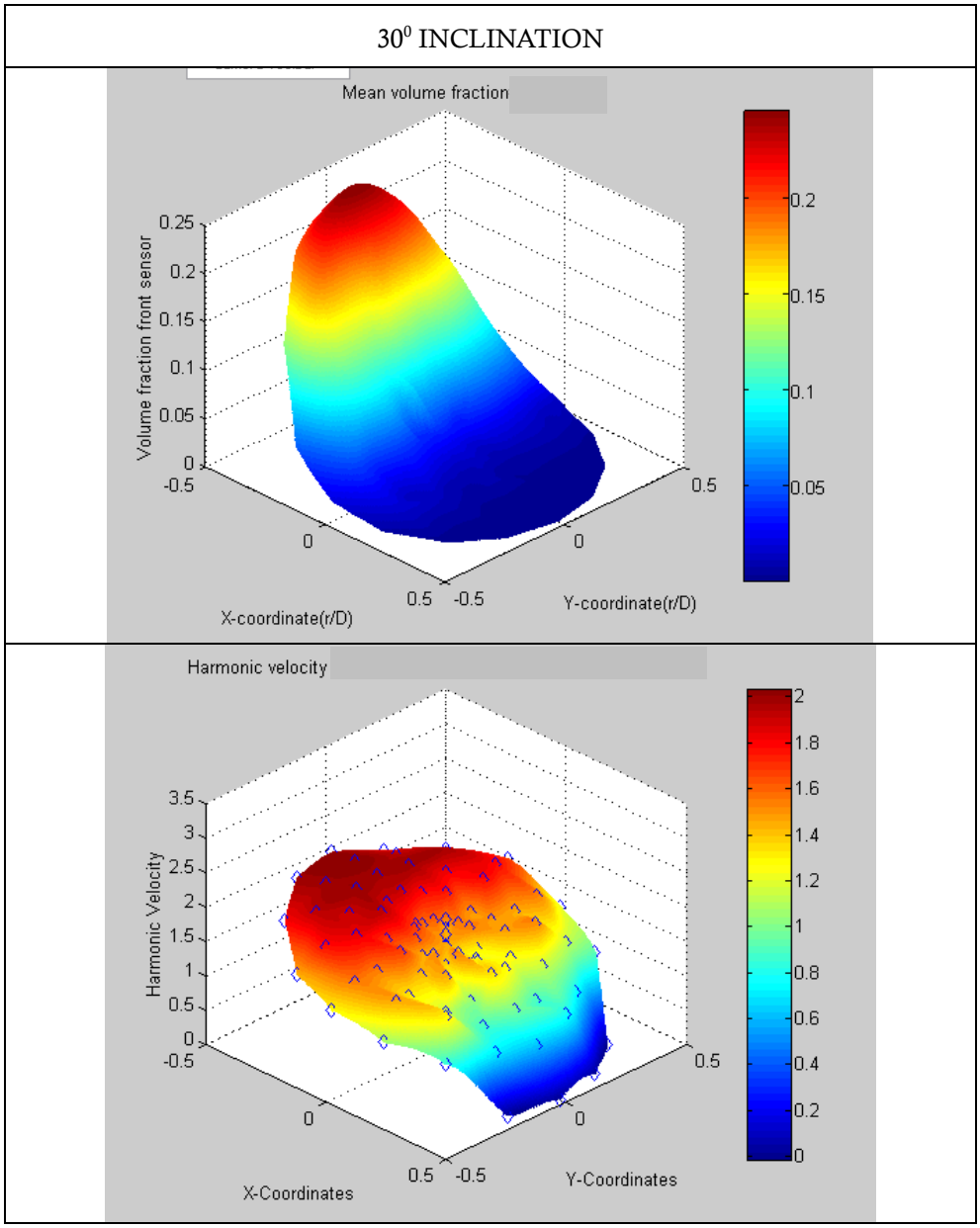

Figure 57. Dual sensor probe 30^{O} inclination $\alpha_{ref} = 0.0649$, $u_{ws} = 0.8969\,\mathrm{ms}^{-1}$, $u_{gs} = 0.1179\ \mathrm{ms}^{-1}$

Reference Data
volume fraction=0.0817
superficial gas velocity=0.1565 msec^{-1}
superficial water velocity=1.1397 msec^{-1}
mean gas velocity=1.9144 msec^{-1}

Measured values
volume fraction = 0.0807
superficial gas velocity = 0.1830 msec^{-1}
mean gas velocity = 1.1330 msec^{-1}

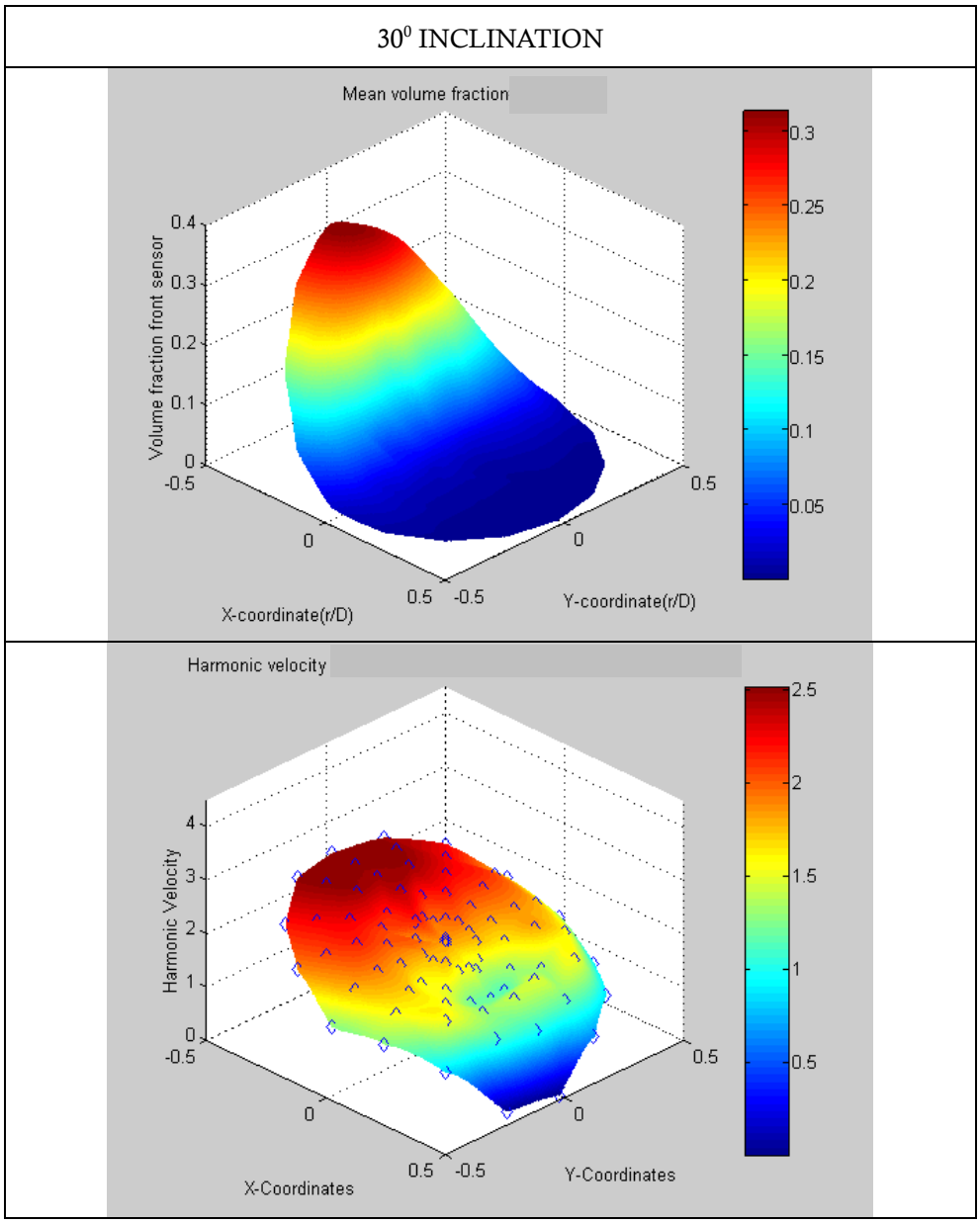

Figure 58. Dual sensor probe 30^{O} inclination $\alpha_{ref} = 0.0817$, $u_{ws} = 1.1397\,\mathrm{ms}^{-1}$, $u_{gs} = 0.1565\ \mathrm{ms}^{-1}$

Reference Data
volume fraction=0.0298
superficial gas velocity=0.0328 msec^{-1}
superficial water velocity=1.1418 msec^{-1}
mean gas velocity=1.1012 msec^{-1}

Measured values
volume fraction = 0.0273
superficial gas velocity = 0.0458 msec^{-1}
mean gas velocity = 0.8149 msec^{-1}

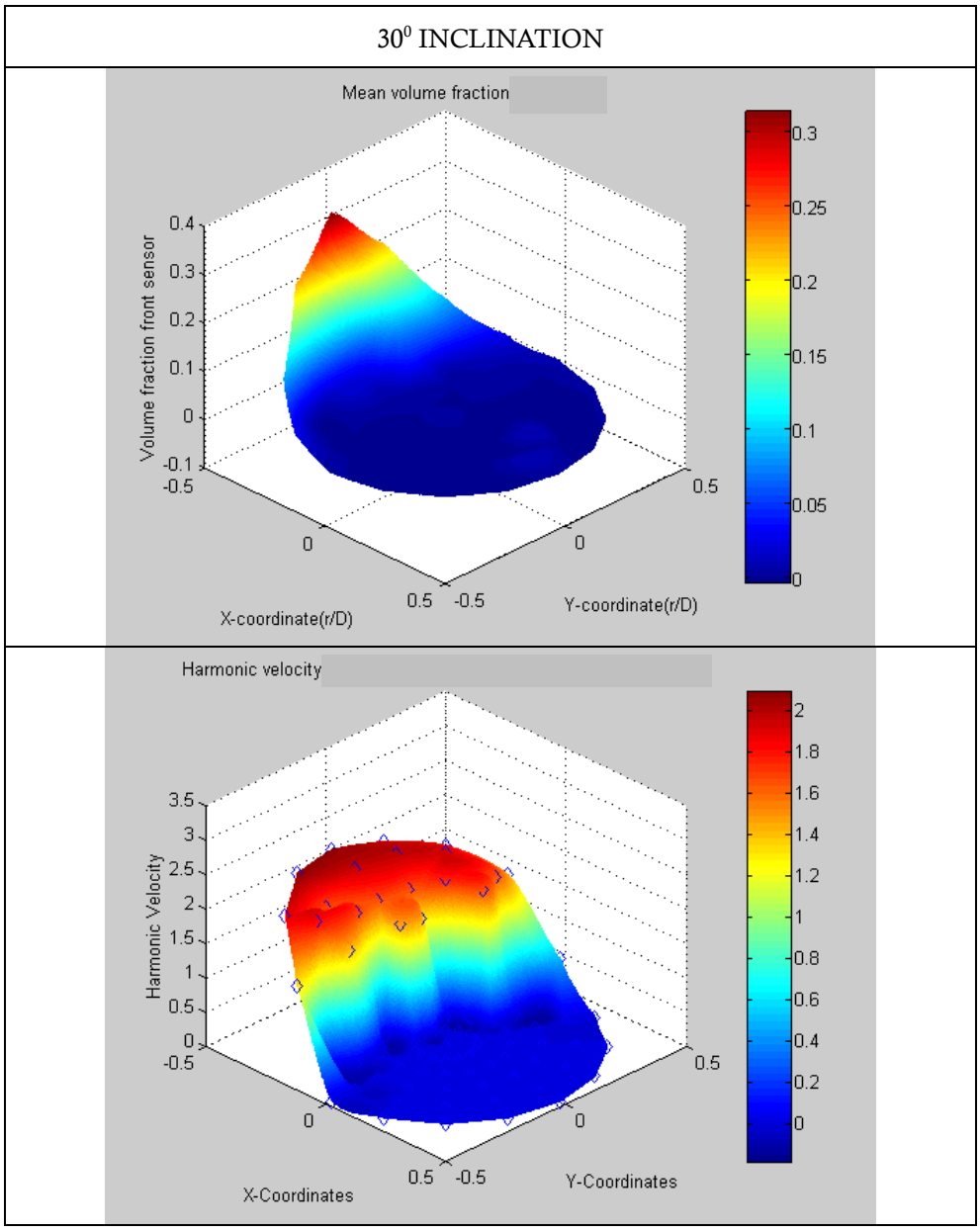

Figure 59. Dual sensor probe 30^{O} inclination $\alpha_{ref} = 0.0298$, $u_{ws} = 1.1418 \text{ms}^{-1}$, $u_{gs} = 0.0328 \text{ ms}^{-1}$

8.2 ERT experiments.

As mentioned before, a collaborative work occurred with Leeds University using dual plane electrical resistance tomography. Experiments were run for several flow conditions. These flow conditions are shown in table 5 in chapter 7. In this chapter only the results for some of the flow conditions are going to be presented. A table of the reference data for all the flow conditions appears. Then the plots of some volume fraction and velocity distributions in the cross section of the pipe are presented figures 60 to 61.

F. C.	Reference Volume fraction	Reference Mean Gas Velocity (m/sec)	Measured mean gas volume fraction by ERT	Measured mean gas velocity (m/sec) by ERT
H1	0.0558	1.1654	0.0546	1.3017
H2	0.0325	0.4781	0.0327	0.4871
H3	0.0607	0.5249	0.0589	0.7936
H4	0.0199	0.8322	0.0232	0.7358
H5	0.0344	0.8531	0.0415	0.7941
H6	0.0694	0.9627	0.0743	1.0217
H7	0.0123	1.2508	0.0086	1.2401
H8	0.0271	1.1125	0.0275	1.0243
H9	0.0555	1.2311	0.0537	1.1709
H10	0.0859	1.2950	0.0849	1.3259
H11	0.0156	1.0533	0.0073	0.9435
H12	0.0218	1.4506	0.0221	1.2883
H13	0.0480	1.3683	0.0443	1.4545
H14	0.0755	1.5026	0.0723	1.6379
H15	0.1008	1.5997	0.0983	1.6625
H16	0.0139	1.0679	0.0049	0.9666
H17	0.0213	1.3113	0.0707	1.1941

H18	0.0420	1.5244	0.0393	1.6395
H19	0.0628	1.7193	0.0620	1.6625
H20	0.0867	1.8172	0.0841	1.8951
IN_H1	0.0385	1.6633	0.0194	1.2628
IN_H2	0.0367	1.7405	0.0083	1.6575

Table 8. Reference data for the ERT experiments in 0^0 and 15^0 degrees inclination in air-water flow.

Next some air volume fraction and air velocity distribution plots are presented. Note that the velocity distribution plots have the same z-axis for comparison purposes.

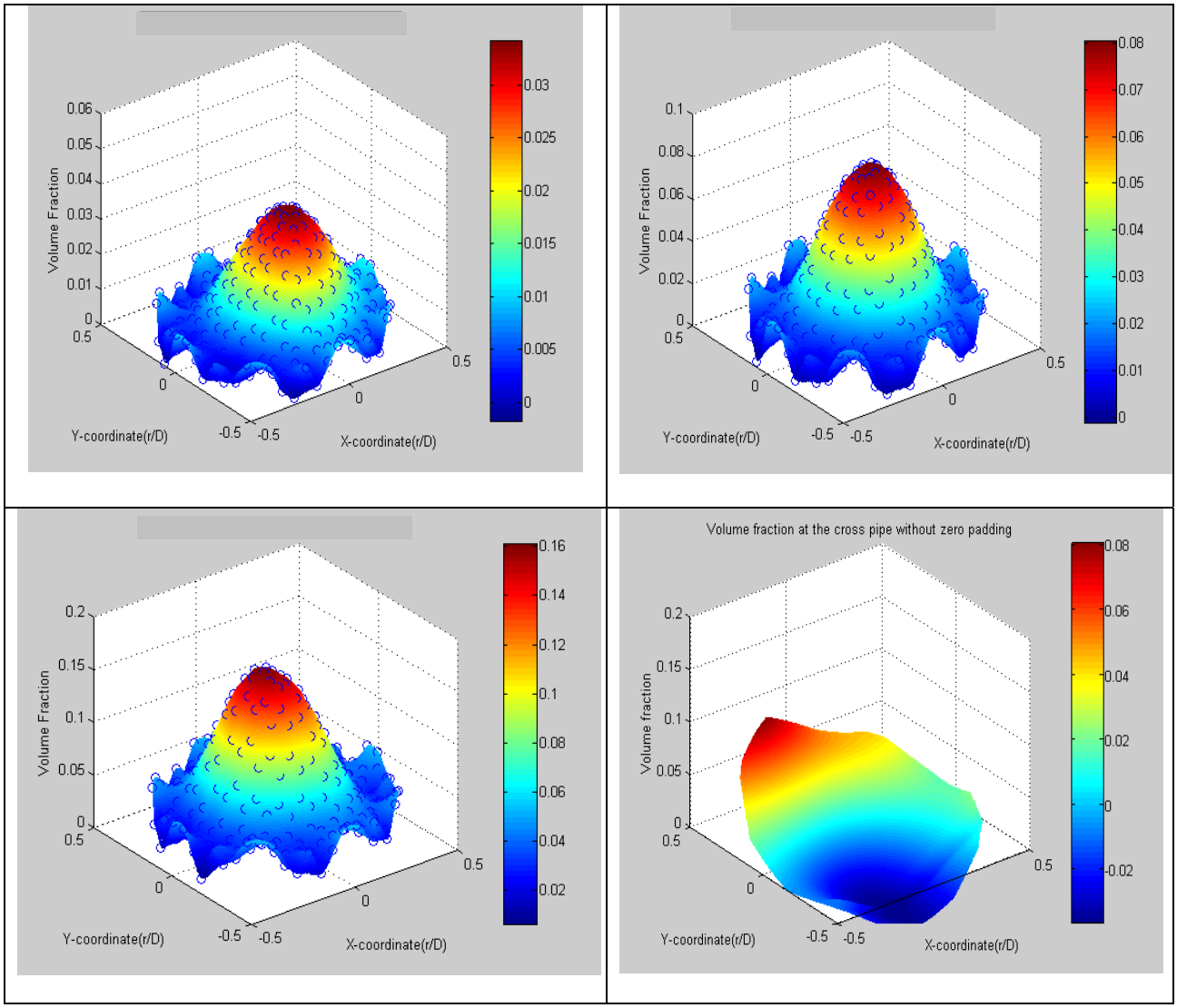

Figure 60. Pipe's cross section air volume fraction distribution (L7, top left), (L8, top right), (L9, bottom left), (IN_L2, bottom right). from ERT.

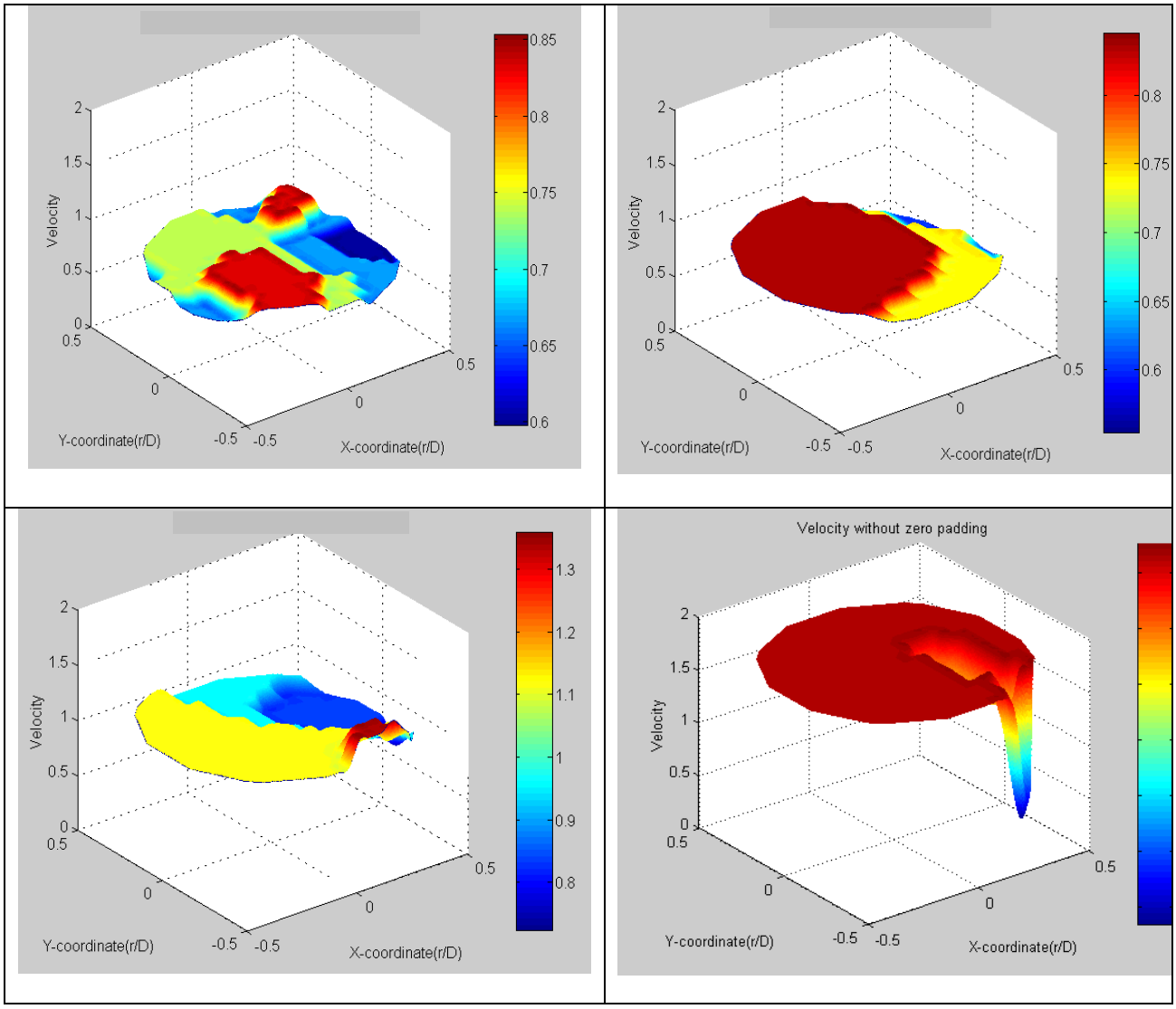

Figure 61. Pipe's cross section air velocity (H4, top left), (H5, top right), (H6, bottom left), (IN_H2, bottom right) from ERT.

These were the results of the ERT system for air-water flows.

8.3 Quantitative analysis of dual sensor probe and ERT results.

8.3.1 The gas volume fraction distribution in vertical upward, bubbly air-water flows

For $\psi = 0^o$, the local gas volume fraction profiles shown in figures 38 and 39 are essentially axisymmetric and can be described by a 'power law' expression of the form $\alpha_l = 0.5\overline{\alpha}(1 - r/R)^q (q+1)(q+2)$ where $\overline{\alpha}$ is the area-weighted mean value of

the gas volume obtained from the dual-sensor probe, R is the pipe radius and r represents radial position. [The fact that the vertical flow graphs shown in figures 38 and 39 are not entirely axisymmetric suggests that data perhaps could have been acquired for longer than the 30s sampling period that was actually used]. For the range of flow conditions investigated, it was found that the term q is related to $\overline{\alpha}$ by the correlation $q = 0.9014e^{-4.823\overline{\alpha}}$ with values of q in the range 0.6 to 0.8 (Lucas et al., 2004 [129]). In vertical bubbly gas-liquid flows the shape of the local gas volume fraction distribution can be dependent upon the mean gas bubble size (Hibiki and Ishii, 1999, [133]). For gas bubbles of about 5mm diameter and above such as those used in the present investigation 'power law profiles', with the maximum value of α_l occurring at the pipe centre, are commonly reported in the literature.

For the case where u_{ws}=0.90 ms^{-1} and u_{gs}=0.033 ms^{-1} (case I) it can be seen from figure 38 that as ψ is increased to 15^o most of the gas becomes located towards the upper side of the inclined pipe, however the peak value of α_l occurs a short distance away from the upper side of the pipe. For the same values of u_{ws} and u_{gs}, when ψ is increased to 30^o the gas moves even closer to the upper side of the inclined pipe and it is apparent from figure 38 that α_l tends to remain constant in 'bands' normal to the diameter joining the upper side of the pipe to the lower side.

For the case where u_{ws}=0.90 ms^{-1} and u_{gs}=0.166 ms^{-1} (case II) it is again clear that for ψ=15^o and ψ=30^o the peak value of α_l occurs a short distance away from the upper side of the pipe. For case II and for ψ=30^o it is again apparent that, away from the pipe wall, α_l is relatively constant in bands normal to the diameter joining the upper side of the inclined pipe to the lower side. However for ψ=30^o there is a much

greater tendency in case II, close to the pipe wall, for the contours of α_l to follow the curvature of the pipe wall, than was the situation for case I.

In figure 39 results are presented for the cases where u_{gs}=0.123 ms^{-1} and where u_{ws} takes values of 0.64 ms^{-1} (case III) and 1.14 ms^{-1} (case IV). It is interesting to note that for θ=15^o the gas bubbles are confined to a much smaller region of the flow cross section when u_{ws}=1.14 ms^{-1} than when u_{ws}=0.64 ms^{-1} even though the mean gas volume fraction is not vastly different. The same phenomenon is even more apparent for ψ=30^o. It has been proposed (Beyerlein et al., 1985, [134]) that when there is axial shear in the liquid phase, a gas bubble will experience a lateral force in the radial direction, causing it to move away from the faster moving liquid towards the slower moving regions. This lateral force is proportional to $-du_w/dr$ where u_w is the local axial liquid velocity and r represents the direction of increasing pipe radius. In figure 40 it is shown that large axial velocity gradients exist in inclined air-water flows. Although measurements were not obtained for the liquid velocity profile, previous research (Lucas, 1995, [135]) suggests that the local axial liquid velocity will attain a maximum value close to the upper side of the inclined pipe and then decay rapidly to zero at the pipe wall. For a given value of ψ, close to the pipe wall at the upper side of the inclined pipe the magnitude of du_w/dr will be greater for u_{ws}=1.14 ms^{-1} than for u_{ws}=0.64 ms^{-1}, and so each gas bubble will experience a greater force towards the upper side of the inclined pipe for u_{ws}=1.14 ms^{-1}. This causes the bubbles to be more tightly confined into a smaller region of the flow cross section as observed in figure 39.

In figure 40 local axial gas velocity profiles are shown for the cases where

u_{ws}=0.90 ms^{-1} and u_{gs}=0.033 ms^{-1} (case I) and for u_{ws}=1.14 ms^{-1} and u_{gs}=0.123 ms^{-1} (case IV). In figure 40 the colour red represents the maximum value of the local axial gas velocity u_{gl} at a given flow condition, whilst the colour blue represents the minimum value of u_{gl}. Again, the range of values of u_{gl} is different for each flow condition shown in figure 40 as indicated by the scale to the right of each graph. For each flow condition a volume-fraction-weighted mean gas velocity $\overline{u}_g$ was calculated from the measured values of u_{gl} and α_l. $\overline{u}_g$ was always found to be within 10% of the reference mean gas velocity given by $\overline{u}_{g,ref} = u_{gs} / \overline{\alpha}_{ref}$. This gave good confidence in the accuracy of the measured values of u_{gl}.

It is clear from figure 40 that for $\psi = 0^o$ the profile of u_{gl} is essentially axisymmetric however, as ψ is increased it is clear that the axial velocity of the gas bubbles becomes significantly greater at the upper side of the inclined pipe than at the lower side.

For example, for case IV and for $\psi = 30^o$ the axial gas velocity u_{gl} at the upper side of the pipe is greater than 2.5 ms^{-1} whilst at a distance of approximately $0.2R$ from the lower side of the inclined pipe u_{gl} is approximately equal to 0.75 ms^{-1}. This variation in the value of u_{gl} for inclined gas-liquid flows can be qualitatively explained as follows. In a steady state flow, at a given point in the flow cross section, there is a balance between the applied pressure gradient, which acts in the positive axial direction (i.e. the direction of flow) and gravitational and viscous forces which both act in the negative axial direction. With reference to an existing

model of inclined multiphase flow (Lucas, 1995 [135]) the local gravitational force is related to the mean local density of the multiphase mixture whilst the local viscous forces are related to the local axial velocity gradient of the multiphase mixture. In an inclined gas-liquid flow, the local density of the multiphase mixture is relatively small at the upper side of the inclined pipe due to the relatively high local gas volume fraction. As a consequence the local gravitational force acting on the fluid in the negative axial direction is much smaller at the upper side of the inclined pipe than at the lower side. This means that in a steady state flow, the local viscous forces acting on the fluid in the negative axial direction must be relatively high at the upper side of the inclined pipe and this, in turn, is manifested by the large local axial velocity gradients observed at the upper side of the pipe. This has many practical implications including the fact that in oil well drilling operations, when a gas kick occurs, the gas can reach the surface much more quickly in an inclined well than in a vertical well of the same overall length.

Van der Welle [128] suggested that the local gas volume fraction in vertical upward gas-liquid flows similar to those in the present study could be represented by a power law expression of the form

$$\alpha_l = \alpha_{\max}(1 - r/R)^q \qquad (61)$$

where $\alpha_{\max}$ is the maximum value of the local gas volume fraction, at a given flow condition, which occurs at the pipe centre, r is radial position within the pipe, R is the pipe radius and q is an exponent. For the local volume fraction distributions obtained in the present investigation, equation (61) was used to determine the exponent q for the volume fraction profiles obtained using the local dual-sensor probe and the ERT

system at each of the flow conditions investigated. This was done by finding the value of q which gave the best fit of the measured data to equation (61). Figure 62 shows the exponent q plotted against $\overline{\alpha}_{ref}$. For the results from the dual-sensor local probe it

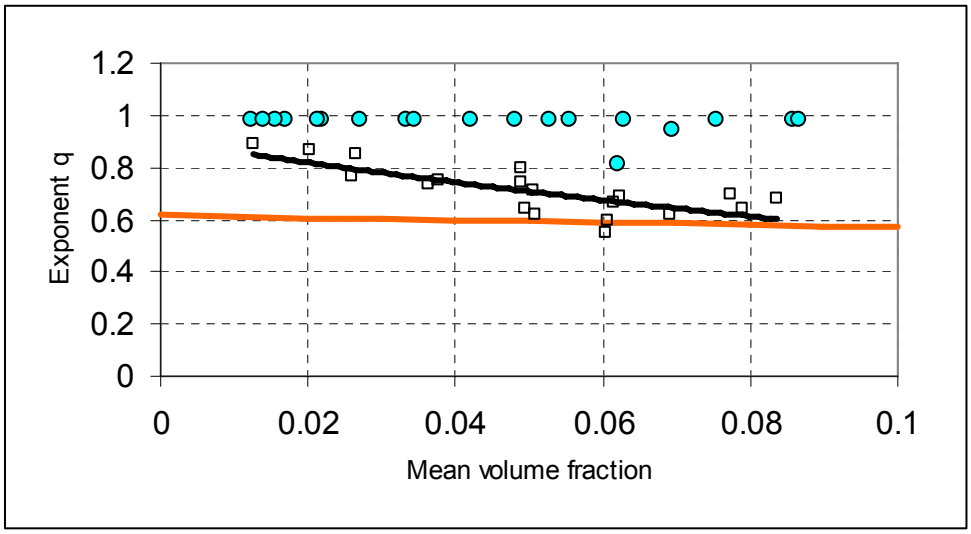

Figure 62. Dots represent ERT exponent (the ERT reconstruction method gave volume fraction profiles which were peakier and which all had the same shape), squares represent dual sensor probe exponents calculated from the formula $\alpha_l = 0.5\overline{\alpha}(1-r/R)^q(q+1)(q+2)$, and orange line represents Van De Welle correlation for q.

is apparent that there is a tendency for q to decrease slowly with increasing $\overline{\alpha}_{ref}$, higher values of q representing more 'peaky' local gas volume fraction distributions.

8.3.2 The gas velocity distribution in vertical upward, bubbly air-water flows.

It is apparent from the figure 40 which shows the velocity distributions in the cross section of the pipe obtained from the dual sensor probe that, for vertical air-water flows, these velocity profiles are much flatter than the volume fraction profiles for vertical air-water flows shown in figure 38 and 39. It is also apparent that, as expected, the velocity profiles for vertical air-water flow are essentially axisymmetric. In figures 60-61 which show the local gas velocity distributions in vertical air-water flows obtained from the dual-plane ERT system, it is apparent that the velocity profiles exhibit large 'flat' regions where the measured velocity is essentially

constant; a result which was not observed for the profiles obtained from the local dual-sensor probe.

Van der Welle [128] proposed that the local axial gas velocity distribution in vertical air-water flows similar to those in the present study could be represented by a power law approximation of the form

$$u_{gl} = u_{gl,\max}(1 - r/R)^{p} \qquad (61)$$

where $u_{gl,\max}$ is the maximum value of the local gas velocity at the pipe centre. By finding the best fit of the experimental data to the relationship given in equation (61) the value of the exponent p was found for the data from the local dual-sensor probe and flow conditions investigated. It was found that for the local dual-sensor probe data, there is some scatter in the value of p about a mean value of 0.173. This is in fair agreement with results obtained by van der Welle [128]. Figure 63 shows the exponent p plotted against u_{gl}.

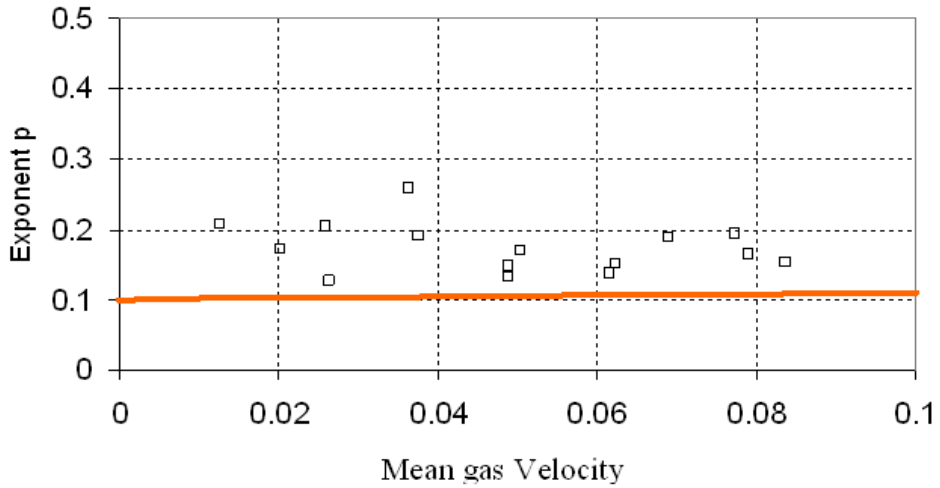

Figure 63. Squares represent dual sensor probe exponents, and orange line represents Van De Welle correlation for p.

For the data from the ERT system, values of p were much lower than the values of p obtained from the local dual-sensor probe due to the fact that the gas velocity profiles obtained from the ERT system are much flatter. Typical values for p for the ERT

system were found to be around 0.02. The very flat profiles obtained from the ERT system are due to the limited frequency at which each plane of data can be acquired. This limited data acquisition frequency does not enable discrimination of small velocity differences in the pipe cross section. Consequently, the same axial gas velocity is measured at many points in the flow cross section, giving rise to the very flat velocity profiles that were observed. It is anticipated that future generations of dual-plane ERT system, with sampling frequencies up to 2000 frames per second, will enable much better discrimination of velocity variations in the flow cross section, hence enabling velocity profiles to be obtained which agree much more closely with those obtained from the local dual-sensor probe.

In general both the gas volume fraction and the gas velocity distributions were approximated by power law functions. The power law exponents q for the local gas volume fraction distributions obtained using the local probe and the ERT system were found to agree fairly closely with each other and with values of q predicted in the literature. The power law exponents p for the gas velocity distributions obtained from the local dual-sensor probe agreed fairly well with values predicted in the literature. However, the gas velocity profiles obtained from the dual-plane ERT system were much flatter than expected due to limited data acquisition speed.

8.4 Dual sensor oil-water results.

A series of experiments was undertaken to measure the local oil volume fraction distribution and the local oil axial velocity distribution in the 80mm internal diameter working section of the flow loop described in chapter 7. Experiments were carried out for values of water superficial velocity u_{ws} in the range $0.276\,\mathrm{ms}^{-1}$ to $0.417\,\mathrm{ms}^{-1}$ and for values of oil superficial velocity u_{os} in the range $0.025\,\mathrm{ms}^{-1}$ to

$0.083\,\mathrm{ms}^{-1}$. At each flow condition a reference measurement $\overline{\alpha}_{ref}$ of the mean oil volume fraction was made using a differential pressure measurement technique, compensated for the effects of frictional pressure loss. For the experiments described herein $\overline{\alpha}_{ref}$ was in the range 0.047 to 0.205. For all of the experiments undertaken the flow regime was 'bubbly oil-in-water' with the oil droplets having an oblate spheroidal shape with the major axis (normal to the direction of motion) approximately 7mm long and the minor axis approximately 6mm long.

Diagrams showing the local oil velocity u_o versus r/D and the local oil volume fraction α versus r/D (where r represents radial probe position and D represents the pipe diameter) are given in figures 64 to 69 (the solid and dotted lines shown in these figures are simply lines connecting adjacent data points).

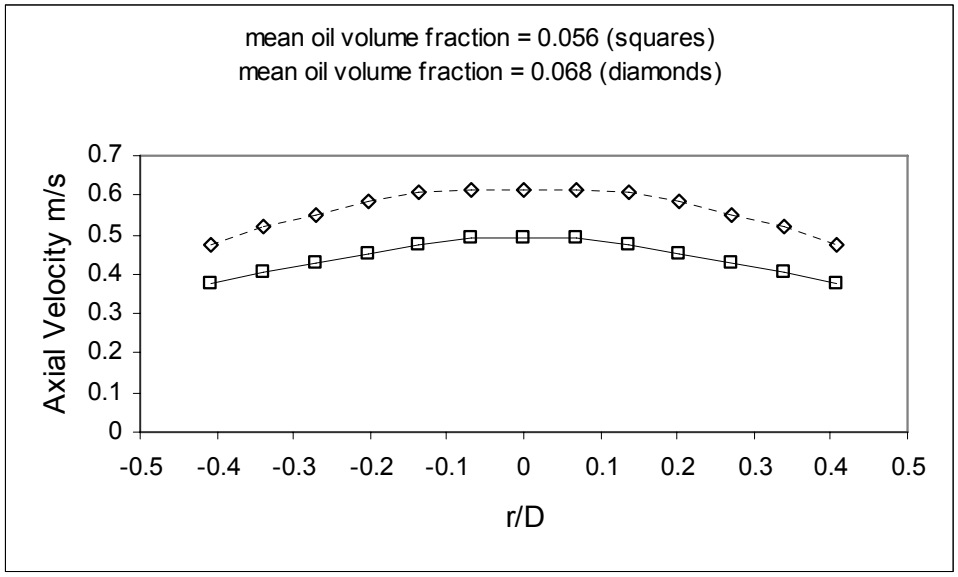

Figure 64. Local oil droplet axial velocity u_o versus r/D for values of mean oil volume fraction less than 0.08. [Squares :- $u_{ws} = 0.276\mathrm{ms}^{-1}$, $u_{os} = 0.027\mathrm{ms}^{-1}$. Diamonds:- $u_{ws} = 0.417\mathrm{ms}^{-1}$, $u_{os} = 0.041\mathrm{ms}^{-1}$].

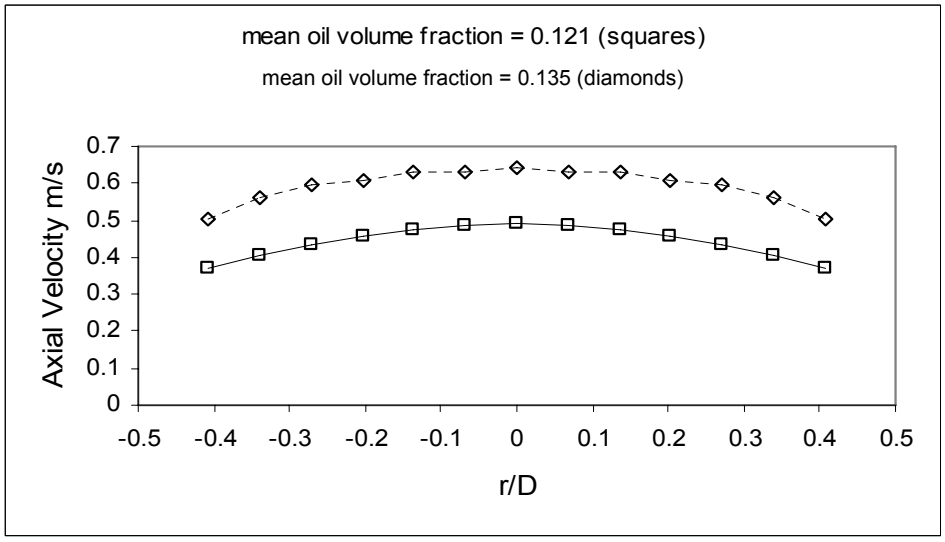

Figure 65. Local oil droplet axial velocity u_o versus r/D for values of mean oil volume fraction between 0.08 and 0.15. [Squares :- $u_{ws} = 0.276\text{ms}^{-1}$, $u_{os} = 0.055\text{ms}^{-1}$. Diamonds:- $u_{ws} = 0.415\text{ms}^{-1}$, $u_{os} = 0.082\text{ms}^{-1}$]

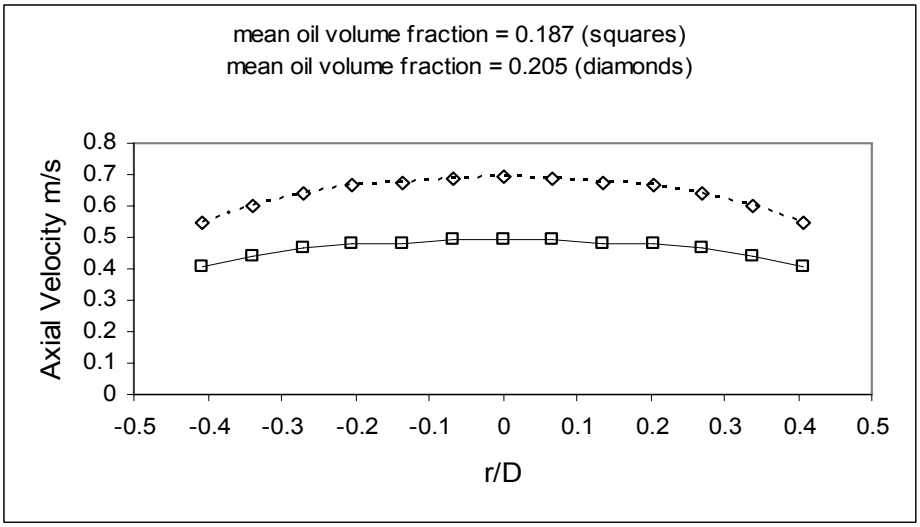

Figure 66. Local oil droplet axial velocity u_o versus r/D for values of mean oil volume fraction greater than 0.15. [Squares :- $u_{ws} = 0.276\text{ms}^{-1}$, $u_{os} = 0.083\text{ms}^{-1}$. Diamonds:- $u_{ws} = 0.416\text{ms}^{-1}$, $u_{os} = 0.124\text{ms}^{-1}$].

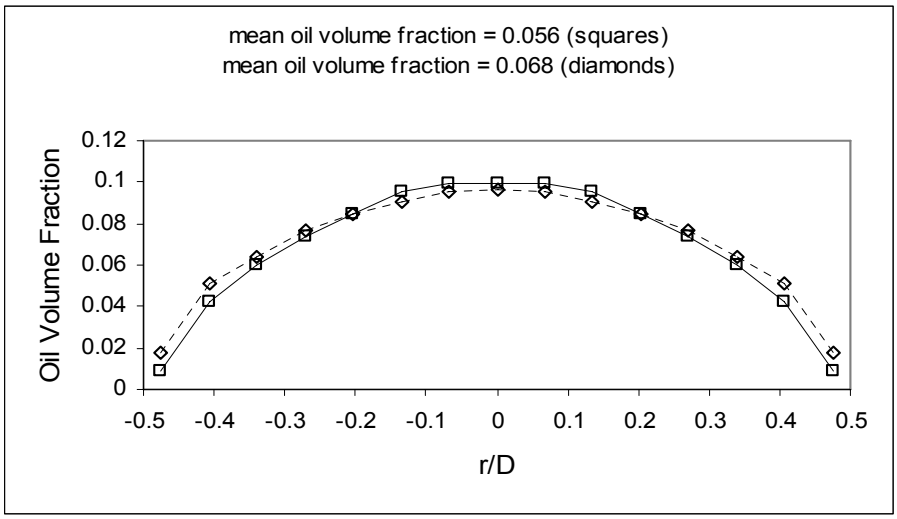

Figure 67. Local oil volume fraction β versus r/D for values of mean oil volume fraction less than 0.08. [Squares :- $u_{ws} = 0.276\text{ms}^{-1}$, $u_{os} = 0.027\text{ms}^{-1}$. Diamonds:- $u_{ws} = 0.417\text{ms}^{-1}$, $u_{os} = 0.041\text{ms}^{-1}$].

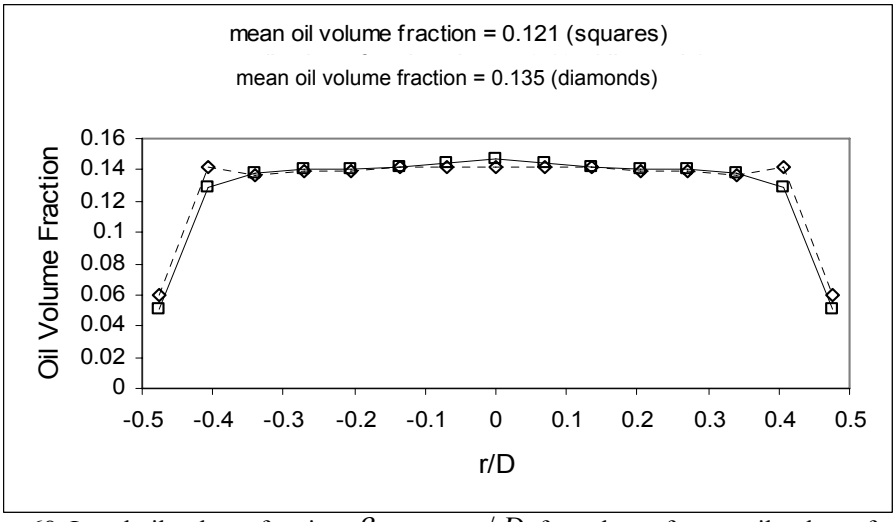

Figure 68. Local oil volume fraction β versus r/D for values of mean oil volume fraction between 0.08 and 0.15. [Squares :- $u_{ws} = 0.276\text{ms}^{-1}$, $u_{os} = 0.055\text{ms}^{-1}$. Diamonds:- $u_{ws} = 0.415\text{ms}^{-1}$, $u_{os} = 0.082\text{ms}^{-1}$].

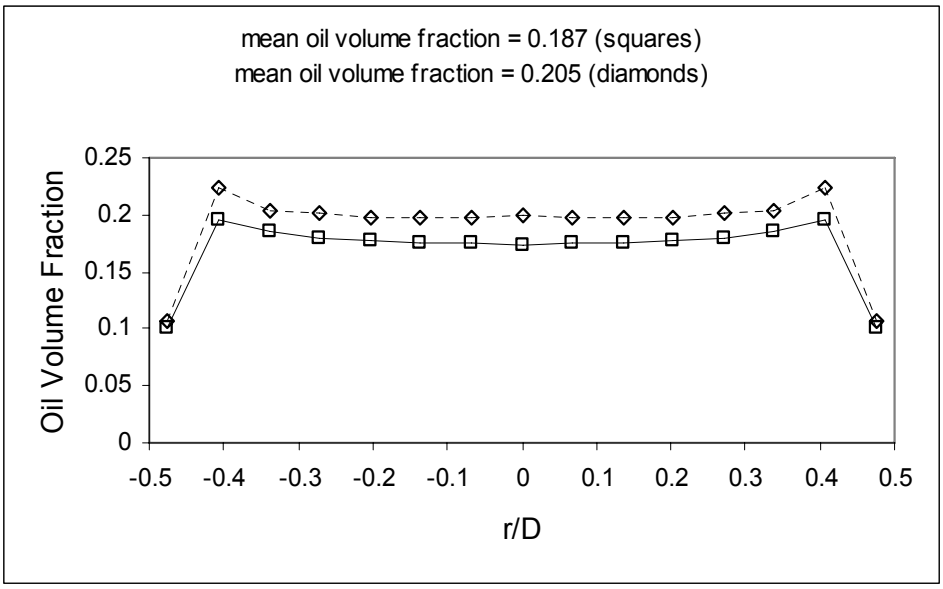

Figure 69. Local oil volume fraction β versus r/D for values of mean oil volume fraction greater than 0.15. [Squares :- $u_{ws} = 0.276\text{ms}^{-1}$, $u_{os} = 0.083\text{ms}^{-1}$. Diamonds:- $u_{ws} = 0.416\text{ms}^{-1}$, $u_{os} = 0.124\text{ms}^{-1}$].

It should be noted that for a given flow condition, the value of u_o or α at a given value of $|r/D|$ in figures 64 to 69 is actually an *averaged* value taken from measurements obtained at the same value of $|r/D|$ for each of the eight radii mentioned above. For reasons described extensively in [129] measurements of u_o taken very close to the pipe wall using a dual-sensor probe *can* be unreliable. Consequently, these 'wall measurements' of u_o have been excluded from the graphs shown in figures 64 to 66.

From figures 64 to 66 it is clear that the local axial oil velocity distributions for all of the flow conditions investigated are 'power law' in shape [129] i.e. the profiles are of the form $u_O = u_{O,\max}(1-r/R)^p$ where $u_{o,\max}$ is the maximum value of the local oil velocity (at the pipe centre), R is the pipe radius and p is an exponent. However, from figures 67 to 69 it is apparent that the shape of the local oil

volume fraction distribution varies significantly with the mean oil volume fraction $\overline{\alpha}_{ref}$. For values of $\overline{\alpha}_{ref}$ less than about 0.08, the local oil volume fraction distribution is approximately 'power law' in shape. For the middle values of $\overline{\alpha}_{ref}$ investigated, i.e. for $\overline{\alpha}_{ref}$ in the approximate range 0.08 to 0.15, the local oil volume fraction distribution is essentially flat, except toward the pipe wall. For higher values of $\overline{\alpha}_{ref}$, i.e. greater than about 0.15, the local oil volume fraction distribution has a shape referred to in [132] as 'intermediate peaked'.

The shapes of the distributions of u_o versus r/D and α versus r/D will be discussed extensively in subsequent sections of this chapter.

8.5 Comparison of Oil Droplet and Air Bubble Velocity Profiles

In section 8.4 it was stated that the oil velocity distribution for each of the flow conditions investigated was 'power law' in shape and of the form $u_O = u_{O,\max}(1-r/R)^p$. The exponent p can be used to characterise the shape of power law profiles because low values of p indicate a relatively flat profile whilst higher values of p indicate a profile with a relatively pronounced peak at the pipe centre [129]. Using curve fitting techniques the value of p was calculated for each of the oil-water flow conditions investigated in the present study. Figure 70 shows p plotted against $\overline{\alpha}_{ref}$ for the oil-water data (diamonds). Also shown in figure 70 are the values of exponent p for velocity profiles of air bubbles in a bubbly air-water flow (crosses) taken in figure 45. [NB: in figure 70, when considering the values of p relevant to air-water flows, the horizontal axis is taken to represent the mean air volume fraction $\overline{\alpha}$].

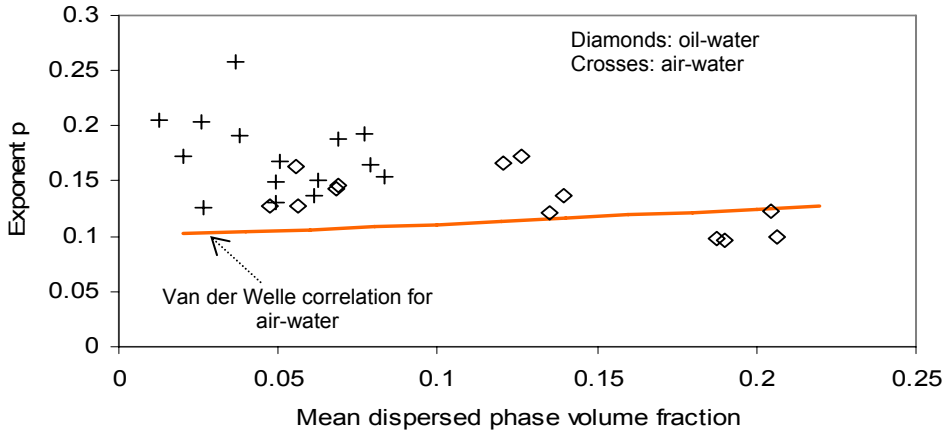

Figure 70. Exponent p versus mean dispersed phase volume fraction for oil-water and air-water bubbly flows.

The air-water data shown in figure 70 (and represented by crosses) was taken at similar flow conditions to those at which the oil-water data was taken (the air-water experiments are described in detail in section 8.3). The air-water data was taken for a more limited range of values of $\overline{\alpha}_{ref}$ because it was necessary to ensure that the air-water flow regime was always bubbly. Inspection of figure 70 shows that the values of p for the oil velocity profiles are quite similar to the values of p for the air velocity profiles. In fact, the mean value of p for the oil data is 0.133 whilst for the air data it is 0.173. For values of dispersed phase volume fraction of about 0.05 to 0.06, where there are several data points for both the air-water and the oil-water experiments, the values of the exponent p are often very similar, indicating that the velocity profiles for the oil droplets and for the air bubbles are very similar in shape. This result is particularly noteworthy given that the oil droplets have a density which is about 630 times greater than the air bubbles.

Also shown in figure 70 in the form of a solid line is the correlation by van der Welle [128] expressing the exponent p as a function of $\overline{\alpha}$ for air-water flows. Although the van der Welle correlation was based on data taken in a vertical, 100mm

internal diameter pipe, and is really only valid for values of gas volume fraction greater than about 0.28, there is still remarkable agreement with the values of p obtained for the oil velocity profiles in the present study. These results suggest that the shape of the velocity profile of the dispersed phase in vertical upward bubbly flows is relatively insensitive to the properties of the dispersed phase, particularly its density.

8.6. Comparison of Oil Droplet and Air Bubble Volume Fraction Profiles

Quantitative comparison of oil volume fraction profiles with air volume fraction profiles in vertical, bubbly, water continuous flows at similar flow conditions is really only feasible when the local volume fraction distribution of the dispersed phase is power law in shape. For other profile shapes (e.g. 'wall peaked' [132]) comparison of the oil and air volume fraction profiles tends to be a qualitative rather than quantitative exercise. In the present investigation power law shaped oil volume fraction distributions were only observed for values of $\overline{\alpha}_{ref}$ less than about 0.08 (see section 8.4). In the literature, although for air-water bubbly flows the local air volume fraction distribution can take a variety of shapes [132], for flows where the air bubble size is about 5mm or greater the air volume fraction profile is generally power law in shape. In the remainder of this section discussion is limited to such power law profiles.

For the oil-water experiments for which $\overline{\alpha}_{ref} < 0.08$ the local oil volume fraction distribution was of the form $\alpha = \alpha_{\max}(1 - r/R)^q$, where $\overline{\alpha}_{ref}$ is the maximum value of the local oil volume fraction which occurs at the pipe centre. In figure 71 the exponent q is shown plotted against $\overline{\alpha}_{ref}$ for five distinct flow conditions. Also

shown in figure 71 (dark line) is a plot of correlation $q = 0.9014e^{-4.823\overline{\alpha}}$, where $\overline{\alpha}$ represents mean air volume fraction, which was obtained for air-water bubbly flows at similar flow conditions (see also section 8.3). [NB: again, in figure 71, when considering air-water data, the horizontal axis must be assumed to represent $\overline{\alpha}$]. A

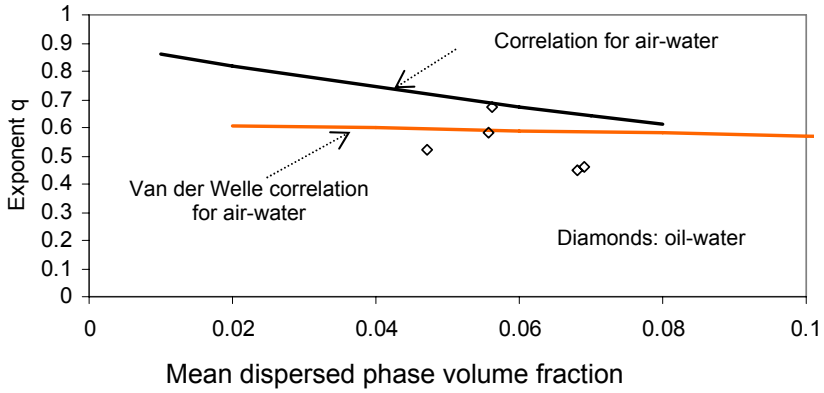

Figure 71. Exponent q versus mean dispersed phase volume fraction for oil-water and air-water bubbly flows.

further correlation relating q to $\overline{\alpha}$, obtained by van der Welle [128] for air-water flows is also shown in figure 71 (orange line). It is apparent that the values of q for the oil-water data are somewhat lower than the values of q for the air-water data, indicating that the oil volume fraction profiles are flatter than the air volume fraction profiles. However, the values of q for the oil-water data are scattered about the van der Welle correlation for q obtained for air-water data. Again, given the large density contrast between air and oil, the similarities in the shapes of the local dispersed phase volume fraction distributions as indicated by figure 71 are very noteworthy.

8.7. The Zuber-Findlay Distribution Parameter C_0

For many two phase flows (both vertical and inclined) the mean velocity $\overline{u}_d$ of the dispersed phase can be obtained from a relationship of the form

$$\overline{u}_d = C_0 u_h + u_{t0}(1-\overline{\alpha}_d)^n \tag{62}$$

where u_{t0} is the velocity of a single particle of the dispersed phase rising through the static continuous phase, n is an exponent, u_h is the homogeneous velocity (or mixture superficial velocity) , $\overline{\alpha}_d$ is the mean volume fraction of the dispersed phase and C_0 is the so called Zuber-Findlay distribution parameter [35]. The terms n and u_{t0} in equation 62 can be obtained from calculation or experiment whilst, under a given set of flow conditions, u_h and $\overline{\alpha}_d$ can often be obtained by measurement [120]. Consequently, if the relevant value of C_0 is known, equation 62 can be used to determine the mean dispersed phase velocity $\overline{u}_d$ (note that for vertical oil-in-water Lucas and Jin [9] found that appropriate values for the terms n and u_{t0} are 2 and $0.167\,\mathrm{ms}^{-1}$ respectively). With reference to [35] the parameter C_0 is given by the expression

$$C_0 = \frac{\overline{\alpha_l j_l}}{\overline{\alpha}_d u_h} \tag{63}$$

where α_l is the local dispersed phase volume fraction, j_l is the local homogeneous velocity and the over bar in the numerator of equation 63 represents averaging in the

flow cross section. The simplifying assumption was made that the local homogeneous velocity can be calculated using the relationship $j_l = (1-\alpha_l)(u_o - u_{slip}) + \alpha_l u_o$ where u_{slip} is the slip velocity between the oil and the water, which was set equal $0.167\,\mathrm{ms}^{-1}$. C_0 can then be calculated from the experimental data according to equation 8.

For the oil-water experiments carried out in the present investigation calculated values of C_0 are shown plotted against the mean oil volume fraction $\overline{\alpha}_{ref}$ in figure 76. Also shown in figure 72 are calculated values of C_0 plotted against the mean air volume fraction $\overline{\alpha}$ for the air-water data described in chapter 8 of this thesis.

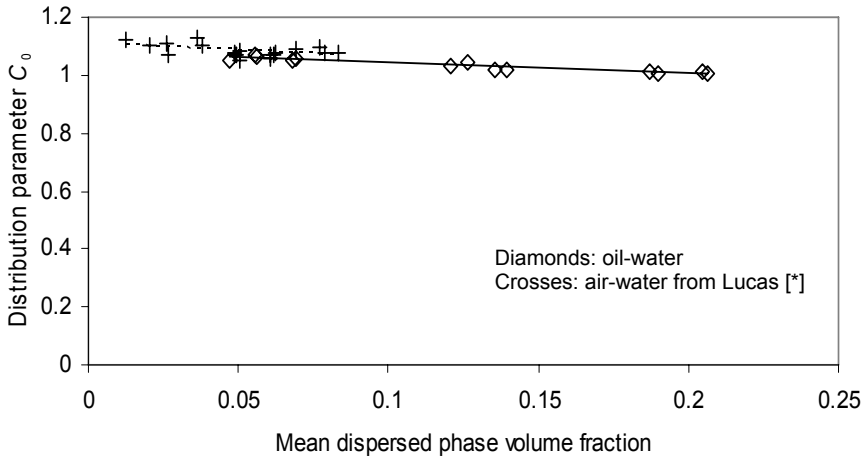

Figure 72. Zuber-Findlay distribution parameter C_0 versus mean dispersed phase volume fraction for oil-water air-water flows. [The dotted line shows the trend of the air-water data. The solid line shows the trend of the oil-water data].

It is clear from figure 72 that, for similar values of the mean dispersed phase volume fraction, the values of C_0 for the oil-water data (diamonds) are very similar to the values of C_0 for the air-water data (crosses). It is also apparent that the trend for C_0 to decrease towards unity with increasing air volume fraction, observed in bubbly air-in-water flows (for values of $\overline{\alpha}$ up to about 0.08), is continued for bubbly oil-in-

water flows (for values of $\overline{\alpha}$ up to about 0.205). The mean value of C_0 for the air-water data shown in figure 72 is 1.084. The mean value of C_0 for the oil-water data is 1.035, which is also remarkably similar to the C_0 value of 1.036 observed by Lucas and Jin [133] for vertical, bubbly oil-in-water flows in a 150mm diameter pipe with a 42.86mm diameter centre body. This suggests that, for vertical, bubbly oil-in water flows, the distribution parameter C_0 may be remarkably insensitive to the pipe diameter and geometry.

8.8. Modelling the Local Oil Volume Fraction Distributions

In an attempt to explain the different shapes of the oil volume fraction profiles in a circular pipe by the use of mathematical modelling, the following oil droplet conservation equation, in cylindrical polar co-ordinates, was used

$$\frac{1}{r}\frac{\partial}{\partial r} r\alpha u_r + \frac{1}{r}\frac{\partial}{\partial \theta}\alpha u_\theta + \frac{\partial}{\partial z}\alpha u_z = 0 \qquad (64)$$

where u_z, u_θ and u_r represent the local oil droplet velocities in the axial, azimuthal and radial directions respectively and where α is the local oil volume fraction. [NB: equation 64 is equivalent to stating that the divergence of the oil droplet flux is equal to zero i.e. $\nabla \cdot (\alpha \mathbf{u}) = 0$]. By making the assumptions that the local oil volume fraction profile is (i) axisymmetric and (ii) fully developed in the axial direction, equation 66 can be simplified to give

$$\frac{1}{r}\frac{d}{dr}(r\alpha u_r) = 0 \qquad (65)$$

or

$$\frac{d}{dr}(r\alpha u_r) = 0 \tag{66}$$

In equation 66, αu_r represents the local oil droplet flux per unit area normal to the radial direction. In the present study it was initially assumed from the work of Beyerlein [134] that this radial flux comprises two components. The first component is a diffusive flux arising from the local droplet diffusivity ε. The second component is due to a circulation induced, local hydrodynamic force [134] acting on the oil droplets which arises from the velocity profile of the continuous water phase. This hydrodynamic force gives rise to a local oil droplet velocity u_{hy} in the positive radial direction which is described in [134] and also discussed in more detail later in this section. Equation 66 can now be rewritten as

$$\frac{d}{dr} r\left\{\alpha u_{hy} - \varepsilon \frac{d\alpha}{dr}\right\} = 0 \tag{67}$$

Integrating equation 67 gives

$$r\left\{\alpha u_{hy} - \varepsilon \frac{d\alpha}{dr}\right\} = K_0 \tag{68}$$

where K_0 is a constant of integration. In equation 68 the quantity $(\alpha u_{hy} - \varepsilon \frac{d\alpha}{dr})$ represents the local *net* flux per unit area, normal to the radial direction, at a given point in the flow. At any given axial location in the pipe (away from the pipe inlet and the pipe outlet) there are no sources or sinks of oil droplets at the pipe centre or the

pipe wall and so $(\alpha u_{hy} - \varepsilon \frac{d\alpha}{dr})$ must always be equal to zero. Thus K_0 must also be equal to zero. Equation 68 may now be manipulated to give

$$\frac{d\alpha}{dr} = \frac{\alpha u_{hy}}{\varepsilon} \tag{69}$$

By considering the lateral forces on a solid sphere in a continuous liquid with shear, Beyerlein et al [134] reported that the local radial velocity u_{hy} imparted to spherical droplets of the dispersed phase in a bubbly two phase flow, as a result of the velocity profile of the continuous liquid phase, is given by

$$u_{hy} = -c_1 \frac{du_L}{dr} \tag{70}$$

where u_L is the local axial liquid velocity and where c_1 is positive, and constant for a given set of flow conditions. In the present study the local axial water velocity u_w may be approximated by the expression

$$u_W = u_O - u_{t0} \tag{71}$$

where u_o is the local axial oil droplet velocity and u_{t0} is the terminal rise velocity of a single oil droplet in stationary water. It was shown in section 8.4 that the local axial oil velocity is of the form

$$u_O = u_{O,\max}(1 - r/R)^p \tag{72}$$

By combining equations 70, 71 and 72 it can be shown that the local radial velocity u_{hy} imparted to the oil droplets as a result of shear in the water phase is given by

$$u_{hy} = K_{hy}(1 - r/R)^{p-1} \tag{73}$$

where K_{hy} is positive and constant for a given set of flow conditions and where p is the exponent defined in section 8.4. Inspection of equation 74 shows that the local radial velocity u_{hy} is always in the direction of increasing r.

With reference to work reported in [134] and [133] the local droplet diffusivity ε in the present investigation was assumed to have a maximum value at the pipe centre and to decay towards the pipe wall. The following expression for ε was adopted

$$\varepsilon = \frac{K_\varepsilon}{r}(1 - r/R)^{1-q} \tag{74}$$

where K_ε is constant for a given set of flow conditions and where q is the exponent defined in section 8.5. [NB: As will be seen later in the section, the assumption of this form of distribution for ε enabled the observed local oil volume fraction distributions to be successfully modelled].

By combining equations 73, 74 and 69 the following expression relating the local oil volume fraction α to radial pipe position r was obtained.

$$\frac{d\alpha}{dr} = \alpha\, r \frac{K_{hy}}{K_{\varepsilon}} (1 - r/R)^{p+q-2} \tag{75}$$

Equation 75 can be used to model the local oil volume fraction distribution in a so-called 'free stream' region of the flow. However, as briefly reported in [134] a 'bubble sub-layer' exists in which the local dispersed phase volume fraction decreases to zero toward the pipe wall. From the experimental data taken in the present study it was assumed that the bubble sub-layer existed in the region for which $|r/D| > 0.405$ and it was further assumed that in this sub-layer the value of α decreased linearly from its free stream value to zero at $|r/D| = 0.5$.

At a given flow condition equation 75 can be solved numerically to determine the free stream local volume fraction distribution provided (i) that α is known at one value of r (the initial condition) and (ii) that the appropriate value for the quantity K_{hy}/K_{ε} is known. At a given flow condition equation 75 was used to simulate the experimentally observed distribution of α with r by using the measured value of the local oil volume fraction at the pipe centre as the initial condition and by adjusting the value of K_{hy}/K_{ε} to give the best fit with the experimental data. A value of $p = 0.133$ was used in equation 75, corresponding to the mean value for this variable for all of the oil-water flow conditions investigated in the present study (see section 8.5). A value of $q = 0.538$ was used in equation 75, this value corresponding to the mean value of q for those flow conditions in which the local oil volume fraction distribution was 'power law' in shape (see section 8.5). It should be noted however that the results predicted by equation 75 were not particularly sensitive to the precise value of q.

For the flow condition where $\overline{\alpha}_{ref} = 0.187$, the value of the quantity K_{hy} / K_{ε} which gave the best agreement with the experimental data was +70. For the flow condition for which $\overline{\alpha}_{ref} = 0.205$ the appropriate value for K_{hy} / K_{ε} was +60. It can be seen from figures 73 and 74 that there is very good agreement between the experimentally observed and the simulated local oil volume fraction distributions.

For the flow conditions at which the local oil volume fraction distributions were 'power law' in shape, i.e. $\overline{\alpha}_{ref} < 0.08$, it was not possible to obtain agreement between the experimentally observed and simulated local oil volume fraction distributions unless *negative* values of K_{hy} / K_{ε} were used. This result indicates that the modelling approach suggested by Beyerlein [134], which proposed a shear induced hydrodynamic force on the droplets in the positive radial direction, is

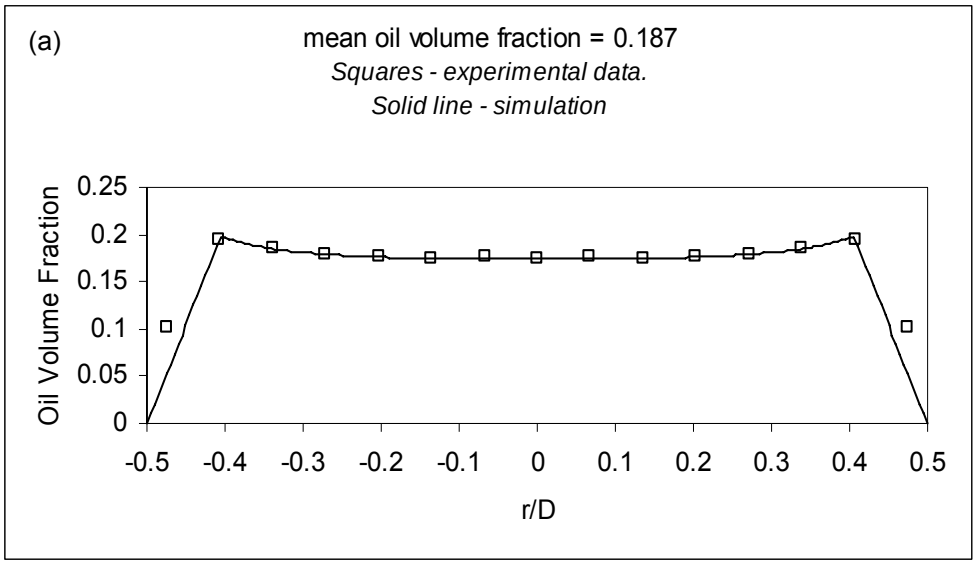

Figure 73. Simulated and experimental local oil volume fraction profiles for values of mean oil volume fraction greater than 0.15. [$u_{ws} = 0.276\text{ms}^{-1}$, $u_{os} = 0.083\text{ms}^{-1}$].

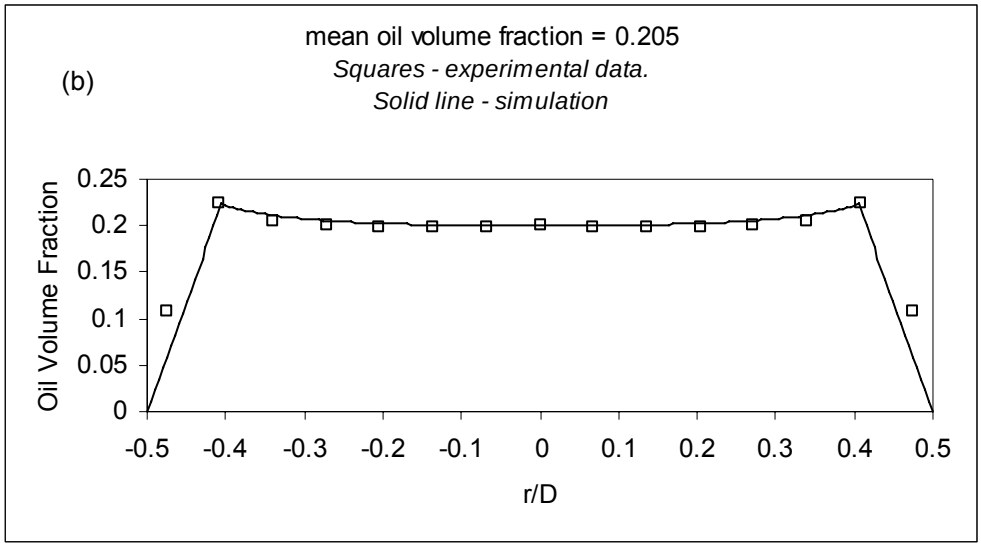

Figure 74. Simulated and experimental local oil volume fraction profiles for values of mean oil volume fraction greater than 0.15. [$u_{ws} = 0.276\text{ms}^{-1}$, $u_{os} = 0.083\text{ms}^{-1}$].

insufficient to explain all of the observed experimental results. In the discussion which follows it will still be assumed that the droplet flux in the radial direction is due to a combination of diffusion and hydrodynamic forces acting on the droplets in the radial direction however, the exact nature of these hydrodynamic forces is not entirely clear (see section 8.8). Since for $\overline{\alpha}_{ref} < 0.08$ negative values of K_{hy} / K_{ε} are required it is apparent that, for such values of the mean oil volume fraction, the resultant of these hydrodynamic forces on the droplets is in the direction of the pipe centre.

Table 9 shows the values of K_{hy} / K_{ε} required to successfully simulate the experimentally observed local volume fraction distributions for six different flow conditions. Also shown in Table 9 are the corresponding values of $\overline{\alpha}_{ref}$. For $\overline{\alpha}_{ref} < 0.08$ the magnitude of the quantity K_{hy} / K_{ε} is significantly greater ($\geq 520m^{-2}$) than the magnitude of this quantity for $\overline{\alpha}_{ref} > 0.15$ ($\leq 70m^{-2}$).

K_{hy}/K_{ε}	$\overline{\alpha}_{ref}$
-600	0.056
-520	0.068
-100	0.121
0	0.135
+70	0.187
+60	0.205

Table 9 Calculated values of K_{hy}/K_{ε} for six different flow conditions and the corresponding values of the mean oil volume fraction $\overline{\alpha}_{ref}$

This strongly suggests that the net hydrodynamic force on the droplets towards the pipe centre for $\overline{\alpha}_{ref} < 0.08$ is significantly greater than the net hydrodynamic force on the droplets toward the pipe wall for $\overline{\alpha}_{ref} > 0.15$ [NB: when K_{hy}/K_{ε} is negative it is implicit that the variation of the radial velocity of the oil droplets with r due to hydrodynamic (as opposed to diffusive) effects will be of the form shown in equation 74 - except with a change of sign. Since the exact nature of this net inward hydrodynamic force on the oil droplets is unknown, the actual variation of the resultant radially inward droplet velocity with r is also unknown].

Experimentally observed and simulated local oil volume fraction distributions for two flow conditions for which $\overline{\alpha}_{ref} < 0.08$ are shown in figures 75 and 76. It is clear that, by using the appropriate values of K_{hy}/K_{ε} from Table 9, there is good agreement between the simulated and experimentally observed distributions. For $0.08 \le \overline{\alpha}_{ref} \le 0.15$ simulated and experimentally observed local oil volume fraction distributions are shown in figures 77 and 78. It can be seen from Table 9 that when $\overline{\alpha}_{ref} = 0.135$ then K_{hy}/K_{ε} is equal to zero, suggesting that the net radial hydrodynamic force on each droplet is also zero and that the shape of the local oil volume fraction profile is purely due to the effects of diffusion.

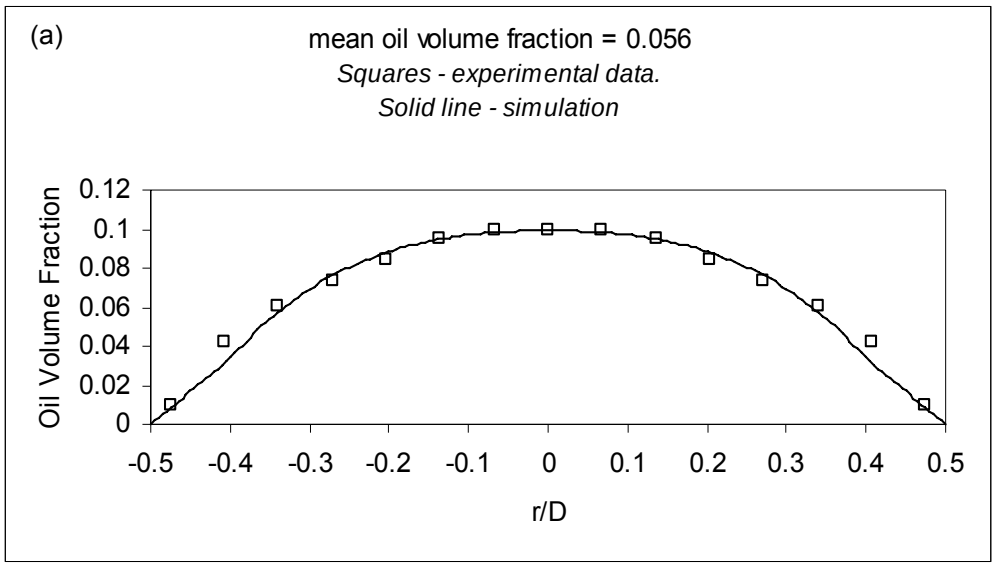

Figure 75. Simulated and experimental local oil volume fraction profiles for values of mean oil volume fraction less than 0.08. [$u_{ws} = 0.276\text{ms}^{-1}$, $u_{os} = 0.027\text{ms}^{-1}$].

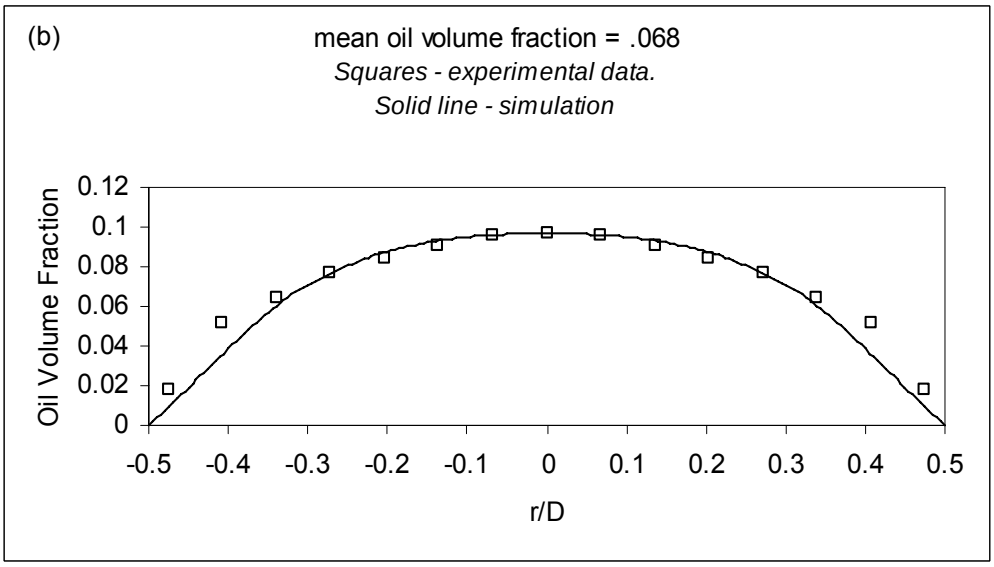

Figure 76. Simulated and experimental local oil volume fraction profiles for values of mean oil volume fraction less than 0.08. [$u_{ws} = 0.417\text{ms}^{-1}$, $u_{os} = 0.041\text{ms}^{-1}$].

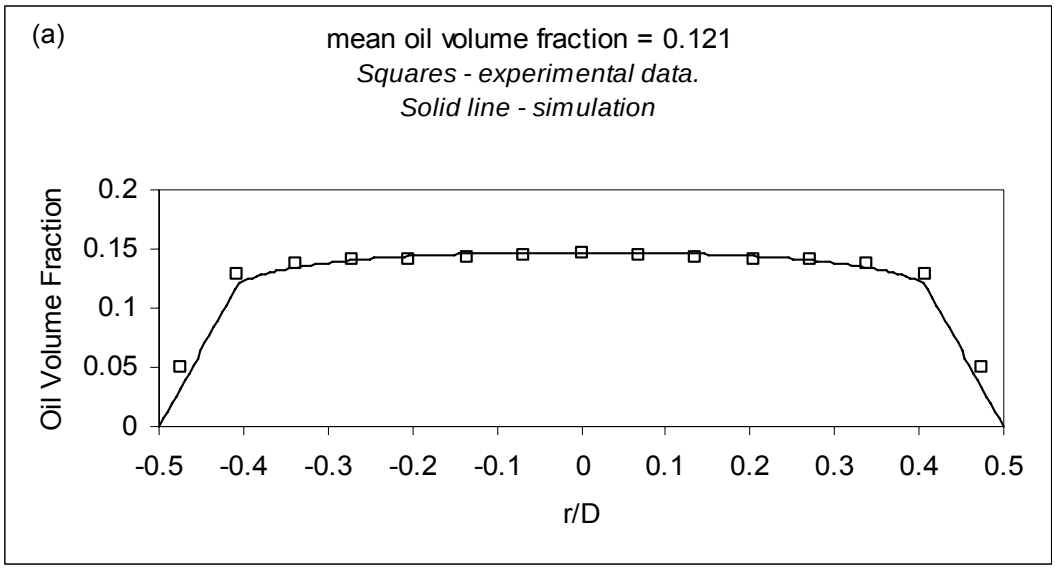

Figure 77. Simulated and experimental local oil volume fraction profiles for values of mean oil volume fraction between 0.08 and 0.15. [$u_{ws} = 0.276\text{ms}^{-1}$, $u_{os} = 0.055\text{ms}^{-1}$].

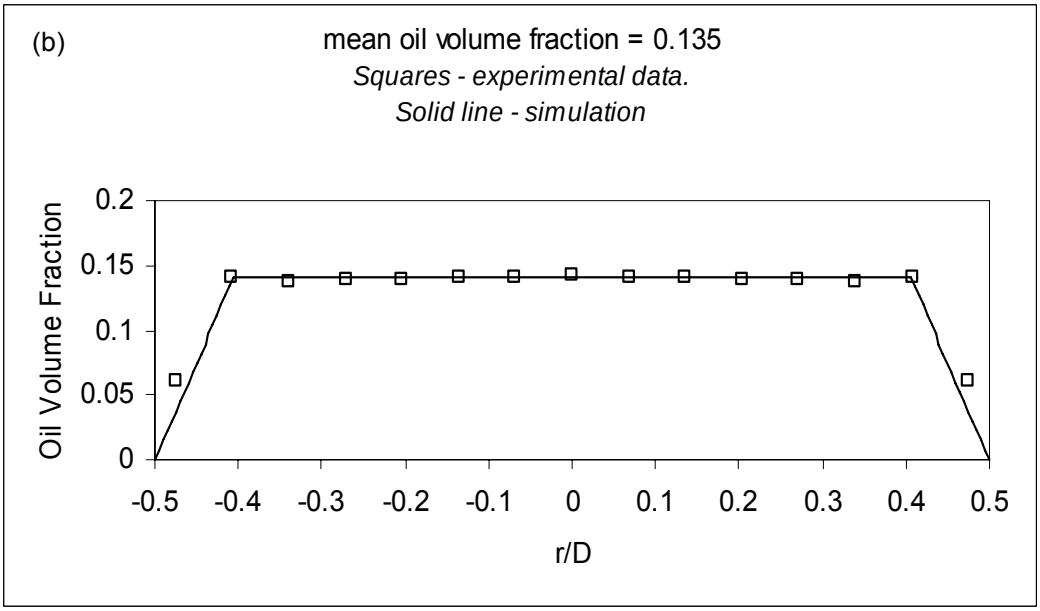

Figure 78. Simulated and experimental local oil volume fraction profiles for values of mean oil volume fraction between 0.08 and 0.15. [$u_{ws} = 0.415\text{ms}^{-1}$, $u_{os} = 0.082\text{ms}^{-1}$].

In the next section the nature of the different hydrodynamic forces acting on the droplets in the radial direction is discussed.

8.9. Radial Forces on Dispersed Phase Particles

In this section a qualitative discussion is given on possible sources of the radial hydrodynamic forces on particles of the dispersed phase in co-current, upward, bubbly two phase flows where the superficial velocity of the continuous phase is greater than zero. For very low dispersed phase volume fraction flows in which the dispersed particles are relatively large compared to the pipe diameter [132], as was the case for the 6mm to 7mm oil droplets in the present investigation, it is widely reported in the literature [132] that the particles will tend to migrate toward the pipe centre. The precise reason for this migration is unclear, but it may be related to the fact that at the pipe centre the velocity gradients in the continuous phase are at a minimum and hence the shear stresses on particles of the dispersed phase are also at a minimum. The pipe centre may therefore represent an equilibrium position for dispersed phase particles in very low volume fraction flows. Once the oil droplets are established at the pipe centre as described above, the low pressure region in their wakes will draw additional oil droplets towards the pipe centre as the oil volume fraction is increased. This could well explain the observed tendency for the oil droplets to accumulate at the pipe centre (against the influence of droplet diffusion) for values of $\overline{\alpha}_{ref}$ less than about 0.08, giving rise to power law shaped profiles.

As the oil volume fraction is increased further the effects of droplet diffusion, and the limited space available for oil droplets at the pipe centre, cause the oil droplets to migrate to those parts of the flow cross section where there is significant shear in the continuous phase velocity profile. Here, circulation induced forces (see section 8.7, [132] and [134]) give rise to radial droplet velocities in the direction of the pipe wall as described by equation 73. This in turn gives rise to the observed ‘intermediate peaked’ oil volume fraction profiles. The modelling work in section 8.7 however

suggests that the net hydrodynamic force moving each droplet toward the pipe centre, for $\overline{\alpha}_{ref}$ less than about 0.08, is significantly greater than the net hydrodynamic force moving each droplet toward the pipe wall for $\overline{\alpha}_{ref}$ greater than about 0.15.

For air-water flows there is a much greater tendency for the air bubbles to agglomerate into larger structures at the pipe centre (such as cap shaped bubbles) rather than to migrate away from the pipe centre. This is the probable reason why power law shaped profiles are observed for wide ranges of values of gas volume fraction in flows where gas is injected in the form of relatively large bubbles ($\geq 5\text{mm}$) [132]. In low volume fraction air-water flows in which the gas bubbles are relatively small (between 0.8mm to 3.6mm) there is a reduced tendency for the migration of bubbles into the wakes of other bubbles at the pipe centre [132], perhaps due to the relatively lower wake size of lower Reynolds number bubbles [135]. At small distances from the pipe inlet these small bubbles may therefore still be present in those parts of the flow cross section where they are subject to circulation induced forces in the direction of the pipe wall. This could well explain why for gas-liquid bubbly flows, in which the bubble size is in the range 0.8mm to 3.6mm, 'intermediate peaked' and 'wall peaked' gas volume fraction distributions are frequently observed [132].

9. Experimental results from the four sensor probe and discussion of results.

Experiments were carried out using the 4-sensor probe in vertical, bubbly oil-water flows both with and without swirl using the flow loop described in section 7.2. The water superficial velocity u_{ws} was set at 0.276ms^{-1}, the oil superficial velocity u_{os} was set at 0.0276ms^{-1} and the mean oil volume fraction $\overline{\alpha}_{ref}$ was always less than 0.1. At each flow condition the 4-sensor probe was used to measure the local axial, radial and azimuthal oil velocity and the local oil volume fraction at 8 locations on a radius (including the pipe centre) equal to 15 points on a pipe diameter. The reason for acquiring data from 1 pipe radius is, as mentioned before (chapter 7), that for vertical flow the flow is axisymmetric. Thus the results presented in this section show the variation of time averaged local flow properties across a single pipe diameter.

It was found, for the flow conditions when a swirler was used the mean axial oil velocity in the flow cross section from the four sensor probe $\overline{u}_{o,probe}$ was always less than $\overline{u}_{o,ref}$ (the mean oil velocity obtained from reference measurements) with $\overline{u}_{o,probe}$ being typically around 60% of the value of $\overline{u}_{o,ref}$. Also, it was found that for the flow condition without swirler the difference between $\overline{u}_{o,probe}$ and $\overline{u}_{o,ref}$ was only 5%. The assumption was made that this was due to a reduction in the magnitude *v* of the velocity of the oil droplets as a result of the 'retarding effect' of the 4-sensor probe on the droplets. The further assumption was made that the probe did not influence the *direction* of motion of the oil droplets. To compensate for the retarding effect, a calibration factor *K* was calculated for both flow conditions investigated (one without swirler and the other flow condition with swirler) such that

$$K\overline{u}_{o,probe} = \overline{u}_{o,ref} \qquad \textbf{(76)}$$

Since it was assumed that the retarding effect of the 4-sensor probe was to reduce the magnitude *v* of the gas bubble velocity vector then in order to obtain calibrated values $v_z^{'}$, $v_r^{'}$ and $v_\theta^{'}$ for the local axial, radial and azimuthal bubble velocities it was necessary to apply the calibration factor K to the calculated values of v_z, v_r and v_θ as follows: $v_z^{'} = Kv_z$, $v_r^{'} = Kv_r$ and $v_\theta^{'} = Kv_\theta$. The value for the calibration factor *K* was 1.42 for the flow condition with swirler and 1.05 for the flow condition without the swirler.

For the flow conditions investigated, both with and without swirl, it was found that the calibrated local radial velocity $v_r^{'}$ was different. Figure 79 shows the variation of $v_r^{'}$ with non-dimensional radial position r/D both with and without swirl for $u_{WS} = 0.276\text{ms}^{-1}$ and $u_{OS} = 0.0276\text{ms}^{-1}$. It is apparent from figure 79 that $v_r^{'}$ for the flow condition without the swirler is positive whilst $v_r^{'}$ for the flow condition with the swirler is relatively small and negative. Based on these results, it can be said that without the swirler the oil droplets have a tendency to move towards the wall (positive radial velocity). But when swirler is present then the oil droplets have a slight trend to go towards the centre of the pipe (negative radial velocity).

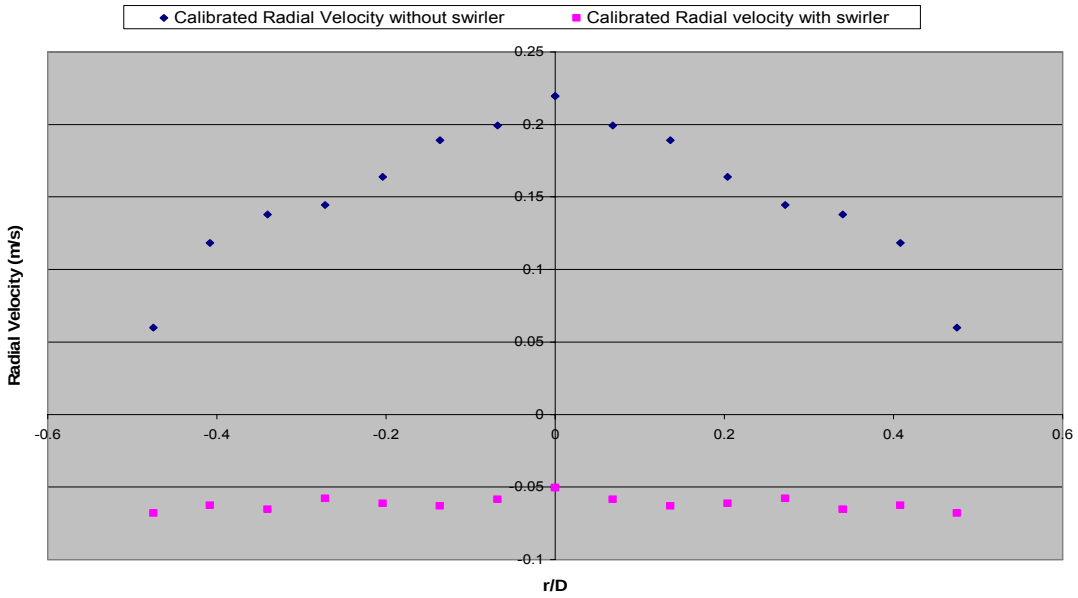

Figure 79. Radial velocity $v_r^{'}$ versus non-dimensional radial position for the same flow condition with swirl [red square dots] and without swirl (blue circle dots).

Figure 794 shows the variation of the calibrated axial velocity $v_z^{'}$ with r/D both with and without swirl for $u_{ws} = 0.276\text{ms}^{-1}$ and $u_{os} = 0.0276\text{ms}^{-1}$.

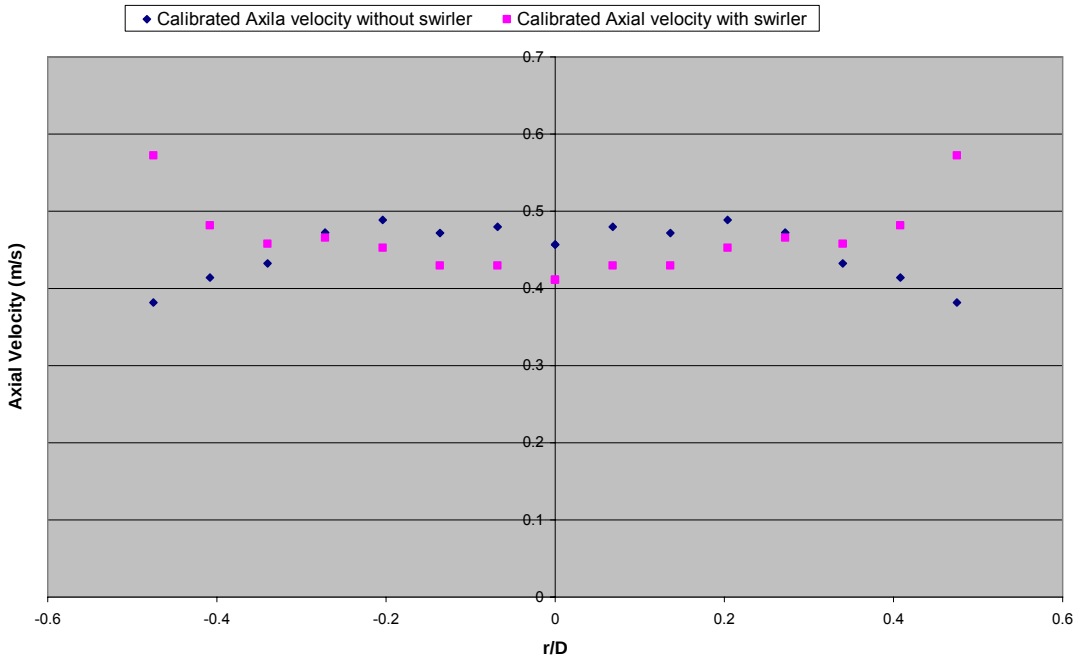

Figure 80. Axial velocity $v_z^{'}$ versus non-dimensional radial position for the same flow condition with swirl [red square dots] and without swirl [blue circle dots].

It is readily apparent from figure 80 that the presence of swirl has a small (but

noticeable) effect on the shape of the axial velocity profile for these values of oil and water superficial velocity. It can be seen that without the swirler the axial velocity profile is relatively flat (with a small variation), whilst the axial velocity profile with the swirler appears to have a curved shape with two peaks at the wall side. This might be an agreement with the observed negative radial velocity, with swirl, where the oil droplets tend to move towards the centre of the pipe. Since most of them accumulate at the centre of the pipe there is less interaction among them at the wall, hence allowing an increased axial velocity at points close to the wall in the presence of swirl. This can be crosschecked with the volume fraction profile shown in figure 82, where the volume fraction profile with swirler is peakier at the centre of the pipe.

Figure 81 shows the variation of the calibrated azimuthal velocity $v_\theta^{'}$ with r/D both with and without swirl for the same values of u_{ws} and u_{os} as before.

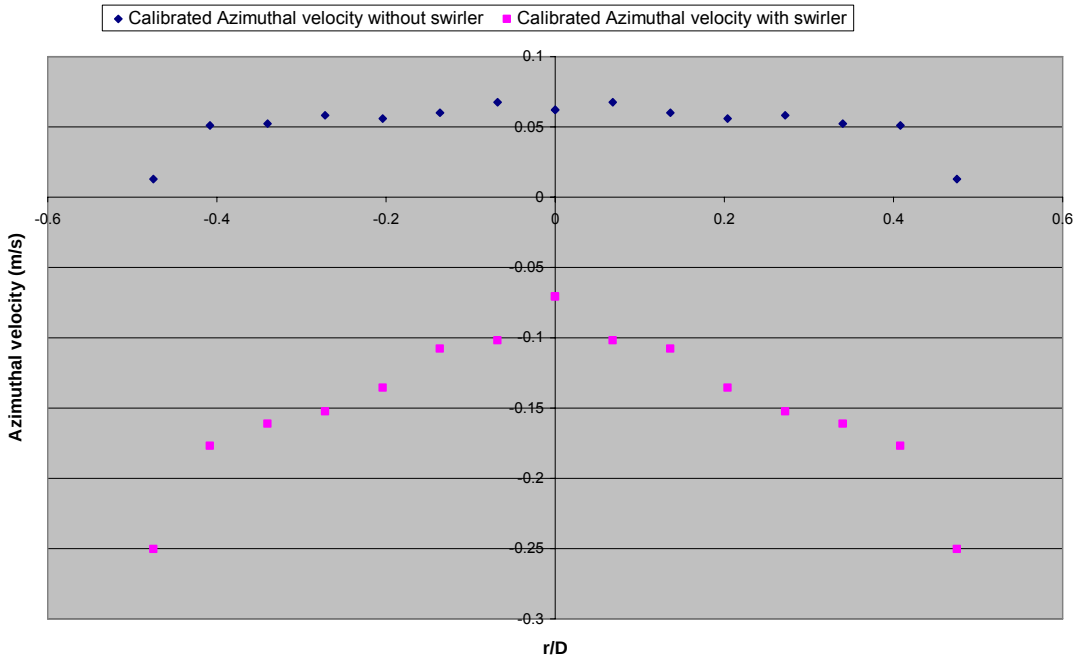

Figure 81. Azimuthal velocity $v_\theta^{'}$ versus non-dimensional radial position for the same flow condition with swirl [red square dots] and without swirl [blue circle dots].

The convention was adopted whereby the local azimuthal velocity is positive for

clockwise swirl and negative for anticlockwise swirl (when the flow is moving upward along the pipe towards the observer). The swirler used in the present investigation induced anticlockwise swirl. It is readily apparent from figure 81 that in the absence of the swirler $v_\theta^{'}$ is relatively close to zero at all positions along the pipe diameter for the flow condition investigated. Without the swirler figure 81 suggests that $v_\theta^{'}$ is slightly positive, suggesting the presence of a low level clockwise swirl which could perhaps be due to the presence of the pipe bends immediately upstream of the inlet to the flow loop working section. In the presence of the swirler it is apparent from figure 81 that there is a marked change in the distribution of $v_\theta^{'}$ across the pipe diameter. It was found that the presence of the swirler causes $v_\theta^{'}$ to be strongly negative close to the pipe walls. It is also apparent from figure 81 that the magnitude of $v_\theta^{'}$ decreases approximately linearly toward the pipe centre. This may suggest that at least part of the multiphase mixture is rotating with approximately constant angular velocity ω (because $v_\theta^{'} = r\omega$). In any case, figure 81 clearly shows that the 4-sensor probe is capable of detecting the azimuthal velocity of the oil bubbles caused by the anticlockwise swirl.

It is believed that the calibration procedure used in this investigation is valid provided that the following assumptions hold true: (i) the *direction* of travel of each bubble is unchanged by the probe and (ii) the calibration factor *K* is the same for all probe positions at a given flow condition. At the pipe wall where the maximum value of $v_\theta^{'}$ occurs, the swirl angle of the flow (defined as $\tan^{-1}(v_\theta^{'}/v_z^{'})$) is -22.6^o in the anticlockwise direction. This is a little of bit more than the 20^o angle of the swirler blades. Nevertheless the agreement is very close. Figure 81 shows the variation of the

local oil volume fraction α with r/D both with and without swirl for the flow condition where $u_{WS} = 0.276\,\text{ms}^{-1}$ and $u_{OS} = 0.0276\,\text{ms}^{-1}$.

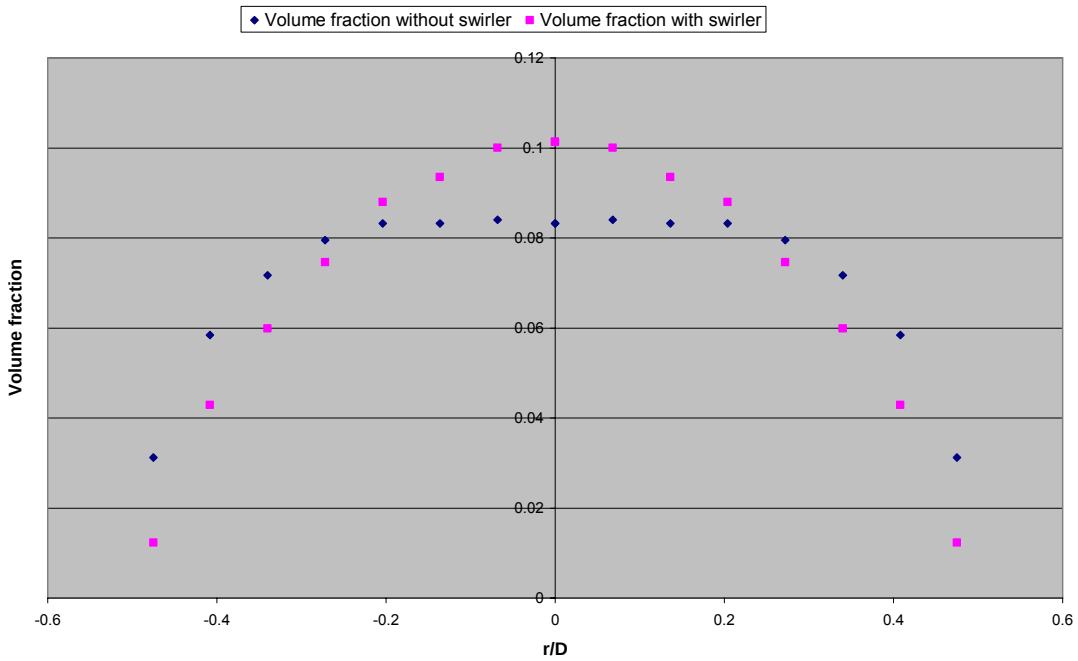

Figure 82. Oil volume fraction versus non-dimensional radial position for the same flow condition, with swirl [red square dots] and without swirl [blue circle dots].

Based on figure 82, it can be seen that there is a small difference between the local oil volume fraction profiles with and without the swirler. As mentioned before, the oil volume fraction profile with the swirler is peakier than the oil volume fraction profile without the swirler. This shows that the oil bubbles tend to accumulate at the centre of the pipe when swirler is present whilst without the swirler they have a weaker tendency (but still present) of accumulating at the centre of the pipe.

Finally, it worth pointing out that the calibration factor *K* is much bigger than the calibration factor used in [119]. The calibration factor for the oil water data with swirler is 1.42, whilst the calibration factor in [119] (air-water data) with swirler is 1.2. Nevertheless these results indicate that for both air bubbles and oil droplets there is a strong influence of the probe on the dispersed phase. There is thus a need for a

better probe design, which affects the motion of the dispersed phase to a much lesser extent.

10. Modification of the four sensor probe model and a rotary index dual sensor probe.

10.1 Reasons for the modifications and the need for a new probe for simulating a four sensor probe.

In previous chapters the use of multi-sensor conductivity probes in bubbly multiphase flows was presented. It shows a method of fabricating two and four sensor probes, their electronic circuits and the resulting voltage waveform at their output. Also, it shows the signal processing scheme for extracting the bubble signature from the acquired signal, and the model for calculating flow properties of the dispersed phase in the pipe.

The multi-sensor probes that have been used were two sensor probes and four sensor probes. In chapters 4 and 6 the description of their fabrication, the supporting electronic circuits, the signal processing and the calculation of the flow properties were described. Several measurements have been acquired using the two types of probes. The outcome of the analysis for the dual sensor probe showed that the whole system (probe, electronics, model, implementation of the algorithm in the computer, and visual presentation) performed very well with a small error.

The four sensor probe showed results that exhibit some ambiguities and as a result a further investigation on the four sensor probe system was undertaken [119]. By comparing the 'volume fraction weighted' mean axial gas velocity in the cross section, obtained from the four-sensor probe, with the mean axial gas velocity obtained from a reference measurement it was found that the four-sensor probe could have a retarding effect on the gas bubbles, reducing the magnitude of their velocity by up to 20%. As mentioned in chapter 9, for 4-sensor probes in a swirling oil-water flow this retarding effect can be even greater (approximately 30%). These results gave rise

to the further suspicion that the interaction of the bubble with the four sensor probe could also alter the *direction* of the bubble as it crossed the probe. It was surmised that, by reducing the physical dimensions of the four-sensor probe, the retarding effect of the probe on the gas bubbles could be lessened. One of the purposes of this chapter is to present the results of an investigation into a rotary index dual-sensor probe which can be used to simulate the measurements that can be obtained from a four-sensor probe whilst significantly reducing the probe size and hence the bubble–probe interaction. It should be noted that the technique described herein is only applicable to bubbly flows in which, at a given spatial location, all bubbles have the same trajectory, size and shape and the same vector velocity and orientation when they strike the probe. The technique is likely to suffer from reduced accuracy in a general, steady state bubbly flow in which these flow conditions are unlikely to be met. The technique is not applicable to unsteady bubbly flows in which the local properties vary with time. So, a new flow rig has been made, new type of probes have been fabricated, and more data sets have been collected. Next, a detailed description of the investigation is presented.

10.2 Derivation of the solutions of the four sensor probe model.

By solving equations (40)–(42) simultaneously, the following expressions for tan β and tan γ are obtained:

$$\tan\beta = \frac{\left(\frac{z_1}{\delta t_{11}} - \frac{z_2}{\delta t_{22}}\right)\left(\frac{y_1}{\delta t_{11}} - \frac{y_3}{\delta t_{33}}\right) - \left(\frac{z_1}{\delta t_{11}} - \frac{z_3}{\delta t_{33}}\right)\left(\frac{y_1}{\delta t_{11}} - \frac{y_2}{\delta t_{22}}\right)}{\left(\frac{z_1}{\delta t_{11}} - \frac{z_3}{\delta t_{33}}\right)\left(\frac{x_1}{\delta t_{11}} - \frac{x_2}{\delta t_{22}}\right) - \left(\frac{z_1}{\delta t_{11}} - \frac{z_2}{\delta t_{22}}\right)\left(\frac{x_1}{\delta t_{11}} - \frac{x_3}{\delta t_{33}}\right)} \qquad (76)$$

$$\tan\,\gamma = \left(\frac{V_{z2} - V_{z1}}{(V_{x1} - V_{x2})\sin\,\beta + (V_{y1} - V_{y2})\cos\,\beta} \right) \tag{77}$$

To obtain the magnitude and direction of the bubble velocity, β is calculated using equation (76) in conjunction with the measured time intervals δt_{ii} and the known sensor coordinates xi, y_i, z_i. Next, γ is calculated using equation (77). Finally, v is calculated using any one of equations (40)–(42). However, this procedure is somewhat complicated by the fact that, for any given value of tan β, there are two possible values of β which lie between 0° and 360° and which can be denoted β_1 and β_2. For example, if tanβ is positive then β_1 will lie between 0° and 90° (first quadrant) and β_2 will lie between 180° and 270° (third quadrant). Similarly if tan β is negative then β_1 will lie between 90° and 180° (second quadrant) and β_2 will lie between 270° and 360° (fourth quadrant). If β_1 is substituted into equation (77) then two possible values for γ denoted γ_1 and γ_2 will result. Similarly, if β_2 is substituted into equation (77) then two further possible values for γ denoted γ_3 and γ_4 will result. These four values of γ thus calculated will all lie in different quadrants. Values of γ lying in quadrants three and four are physically meaningless, and may therefore be rejected, given the definition of γ shown in figures 14 (chapter 5) and 86 (chapter 10) (in which γ can only lie between 0° and 180°). For the experiments described in this paper the bubble velocity vector **V** always made an acute angle with the increasing z-axis of the probe coordinate system. Consequently the value of γ, arising from equation (77), which lies in the second quadrant (90° to 180°) may also be rejected. The remaining value of γ, arising from equation (77), which lies in the first quadrant (0° to 90°) is taken as being the 'correct' polar angle γ_{meas}, as measured by the simulated four-sensor probe. The value of β which gives rise to γ_{meas} is selected as the 'correct' azimuthal angle β_{meas} as measured by the simulated four-sensor probe. Results for

γ_{meas} and β_{meas} are presented in section 10.6 for different directions of the bubbles relative to the probe, obtained by tilting and rotating the probe as will be shown in 10.4.

10.3 Flow chart for solving for β and γ.

Based on the above, the algorithm for the four sensor probe described in chapters 4&5 has been altered and the information that came up from the investigation has been considered. Next, the stages of the new algorithm are summarised below.

Four Sensor Probe Algorithm

1. **Stage 1:** Calculate the numerator and denominator of $\tan\beta$.
2. **Stage 2:** Call N the result of numerator and D the result of denominator.

$$\text{IF N>0 \& D>0 THEN } \beta = \tan^{-1}\left(\frac{|N|}{|D|}\right)$$

$$\text{IF N>0 \& D<0 THEN } \beta = 2\pi - \tan^{-1}\left(\frac{|N|}{|D|}\right)$$

$$\text{IF N<0 \& D<0 THEN } \beta = \pi + \tan^{-1}\left(\frac{|N|}{|D|}\right)$$

$$\text{IF N<0 \& D>0 THEN } \beta = \pi - \tan^{-1}\left(\frac{|N|}{|D|}\right)$$

$$\text{IF N=0 \& D=0 THEN } \beta=0$$

$$\text{IF N=0 \& D>0 THEN } \beta = \frac{\pi}{2}$$

$$\text{IF N=0 \& D<0 THEN } \beta = \frac{3\pi}{2}$$

$$\text{IF N>0 \& D=0 THEN } \beta=0$$

$$\text{IF N<0 \& D=0 THEN } \beta = \pi$$

3. **Stage 3:** Apply stages 1 and 2 to all 6 formulae of β.
4. **Stage 4:** Find the β that gives positive γ angle. Those values are the correct ones.
5. **Stage 5:** Continue with the calculations of velocities (Azimuthial velocity, Radial Velocity, and Axial Velocity).

First of all, it should be mentioned that the algorithm is based on the assumption that the flow has a direction from the front sensor to the rear sensors, or in the case of the current investigation there is upflow direction. This means that it is vital to know the direction of the flow in the pipe before this algorithm is applied. In other words, the polar angle (γ) is always positive.

At the first stage the calculation of numerator and denominator is done separately. Then at the second stage, their signs are considered. Depending on their signs it is possible to locate in which quadrant the angle is positioned. Calculation of the inverse tangent of the absolute values of denominator and numerator is done. The result gives an angle that is positioned in the first quadrant. Then based on the information taken from their signs, multiples of π are added to or subtracted from β in order to put the angle in the proper quadrant. Also, some ill conditioned situations are taken account in the same stage. The third stage is a recursion of the first and second stage. The previous two stages are applied for all 6 formulae of β angles. At the fourth stage, selection of the β angle is done, based on the sign of the γ angle and based on the assumption that was mentioned in the previous paragraph. In other words, since it is known that the direction of flow is upwards, and based on the definition of the γ angle, it is proper and sound to conclude that the sign of γ must be positive. So, the cases where the polar angle is negative are eliminated and with them the formulae that give the corresponding β. Therefore, those formulae of β angle that give positive γ are the ones that are considered and give the correct value. It is important to mention again that although there are 6 formulae for β angle, there are only two unique solutions for β. If one solution of β gives negative γ then instantly three formulae are eliminated and the other three that give the proper and unique solution are taken account. The 6 formulae of the γ angle give always the same magnitude for γ, no

matter which formula of β is used. The only difference is that the wrong values of β (for upward flows) give a negative result and the correct values give a positive γ result. The last stage of the algorithm is the calculation of the velocity components of the vector. The velocity components are the azimuthal velocity, the radial velocity and the axial velocity in a pipe coordinate system (see figure 13 in chapter 5). Assuming that the y axis of the probe coordinate system is always aligned with the radial direction of the pipe coordinate system, then:

$$V_\theta = v \sin\gamma \sin\beta \qquad (78)$$

$$V_r = v \sin\gamma \cos\beta \qquad (79)$$

$$V_z = v \cos\gamma \qquad (80)$$

Where v is the magnitude of the vector velocity and is the average of the vector velocities that are produced by each rear sensor. So:

$$v_1 = \frac{2x_1}{\delta t_{11}} \sin\gamma \sin\beta + \frac{2y_1}{\delta t_{11}} \sin\gamma \cos\beta + \frac{2z_1}{\delta t_{11}} \cos\gamma \qquad (81)$$

$$v_2 = \frac{2x_2}{\delta t_{22}} \sin\gamma \sin\beta + \frac{2y_2}{\delta t_{22}} \sin\gamma \cos\beta + \frac{2z_2}{\delta t_{22}} \cos\gamma \qquad (82)$$

$$v_3 = \frac{2x_3}{\delta t_{33}} \sin\gamma \sin\beta + \frac{2y_3}{\delta t_{33}} \sin\gamma \cos\beta + \frac{2z_3}{\delta t_{33}} \cos\gamma \qquad (83)$$

$$v = \frac{v_1 + v_2 + v_3}{3} \qquad (84)$$

Looking the equations (78)-(80), one observes that due to the fact that γ is always positive then $\sin\gamma$ and $\cos\gamma$ are always positive. Also, v is always positive. So, the β angle is the one that determines if the velocities (azimuthal and radial) have positive or negative direction.

Based on the above, several alterations were made to the old algorithm. The complete set of solutions of the equations (40)-(42) has been found. Based on these

solutions, their corresponding results, and the assumption that the flow is from the front sensor to the rear sensors, the new algorithm has been developed. Changes on the way that β is calculated occurred. A method of choosing the correct values of β and γ angles has been introduced.

10.4 The rotary index dual sensor probe.

The rotary index probe concept is believed to be an original idea. The probe is a dual-sensor probe but the position of the rear sensor with respect to the front sensor can be changed by rotating the lower part of the probe, allowing the simulation of a four-sensor probe. The advantage of this type of probe is that the frontal area is much smaller than that of the equivalent four-sensor probe, thereby causing much less disturbance to the flow. A rotary index dual-sensor probe is also much easier to fabricate than a four-sensor probe. The main disadvantage is that a rotary index dual-sensor probe can only be used in steady state flows.

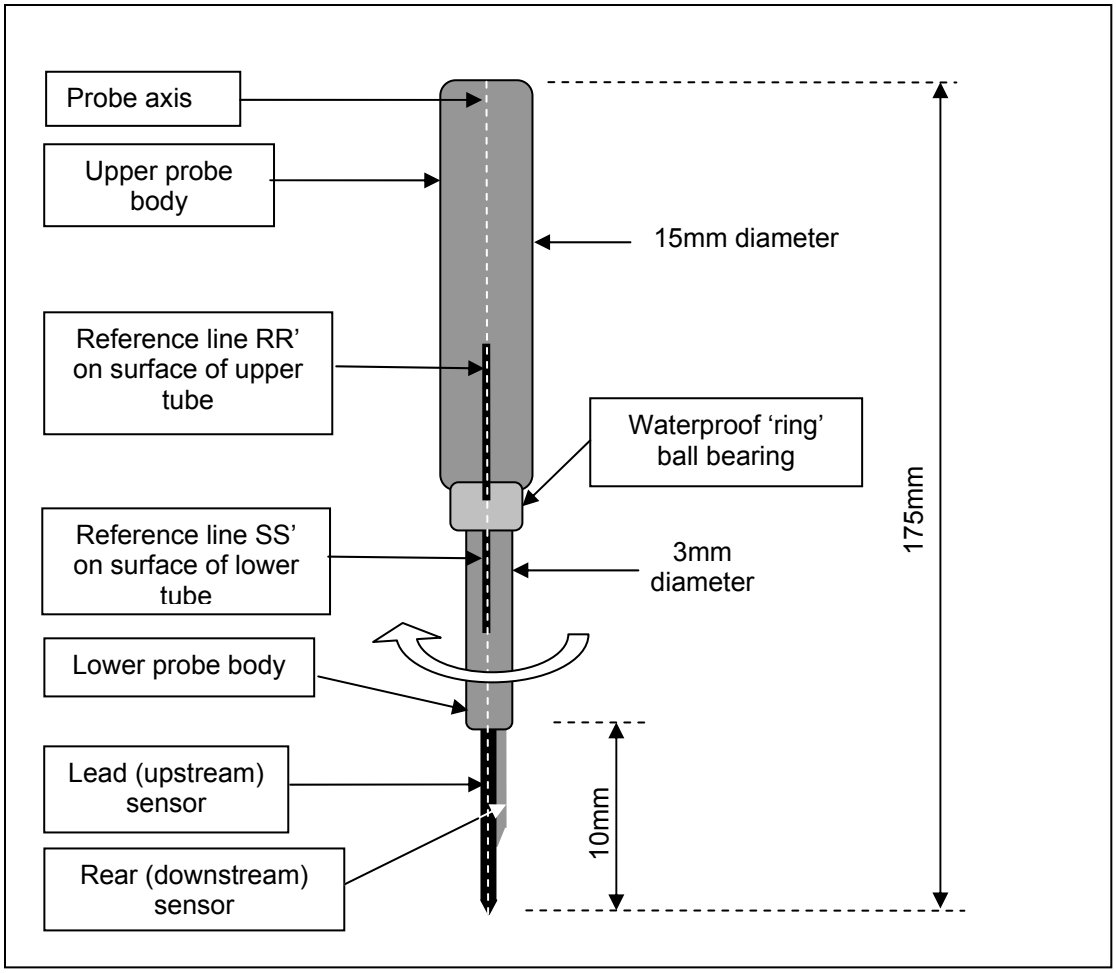

Figure 83. The rotary index dual sensor probe (not to scale)

The rotary index dual-sensor probe used in the experiments described in this thesis consists of an upper probe body, that can be clamped into a hinged platform (described later in the current chapter), and a lower 3mm diameter probe body containing two 0.3mm diameter acupuncture needles coated with an insulating film (see figure 84). The tips of the needles, where the film was removed, formed the two sensors. The upper probe body is connected to the lower probe body by a waterproof ball bearing which allows the lower probe body to be rotated with respect to the upper probe body (see figure 84). The origin of the probe coordinate system is coincident with the position of the lead sensor (as is the case for conventional four-sensor probes) which, for the probe used for the experiments described herein, was located at an axial distance of 1.1765mm upstream of the rear sensor. The z-axis of the probe

coordinate system is coincident with the probe axis thus, as the probe is rotated, the position of the lead sensor in space does not change. The y-axis of the probe coordinate system is defined as the projection onto the x-y plane of any line joining the front sensor to the rear sensor, when the rear sensor is in its initial position relative to the lead sensor. RR' is a reference line on the surface of the upper probe body and SS' is a reference line on the surface of the lower tube body (figure 84). The probe is designed in such a way that when RR' is aligned with SS' (see figure 84) the probe is in its initial position. Thus, if it is required to align the increasing y-axis with the line a-a1 on the hinged platform shown in figure 87 it is merely necessary to align SS' with RR' and to make sure that the line RR' touches a-a1, with RR' facing towards 'a' and away from 'a1'. With the upper probe body clamped in position, a mark on the upper probe body allows the line SS' on the lower probe body to be rotated 120^o anticlockwise (when viewed from above) to give the second rear sensor position in the simulated four-sensor probe (see figure 85). An additional mark allows the line SS' to be rotated 120^o clockwise from its initial position to give the third rear sensor position in the simulated four-sensor probe. With reference to figure 85, for the simulated four-sensor probe used in the experiments described in this thesis, the effective x, y and z coordinates, in the probe coordinate system, of the three rear sensors are as follows (dimensions in mm). Rear sensor 1 (0, 0.7326, 1.1765), rear sensor 2 (0.6344, -0.3663, 1.1765), rear sensor 3 (-0.6344, -0.3663, 1.1765). Measurement of the relative positions of the front and rear sensors from which these coordinates were calculated were made using a calibrated microscope.

The direction of the y-axis of the simulated four-sensor probe was altered by unclamping and rotating the upper probe body then re-clamping it in the hinged platform shown in figure 87. By rotating the y-axis anticlockwise (as viewed from

above) by an angle β^* and by rotating the hinged platform by an angle γ^* the velocity vector $\mathbf{V}$ of bubbles approaching the probe makes an angle γ relative to the z-axis and an angle β with the y-axis where $\gamma = \gamma^*$ and $\beta = \beta^*$.

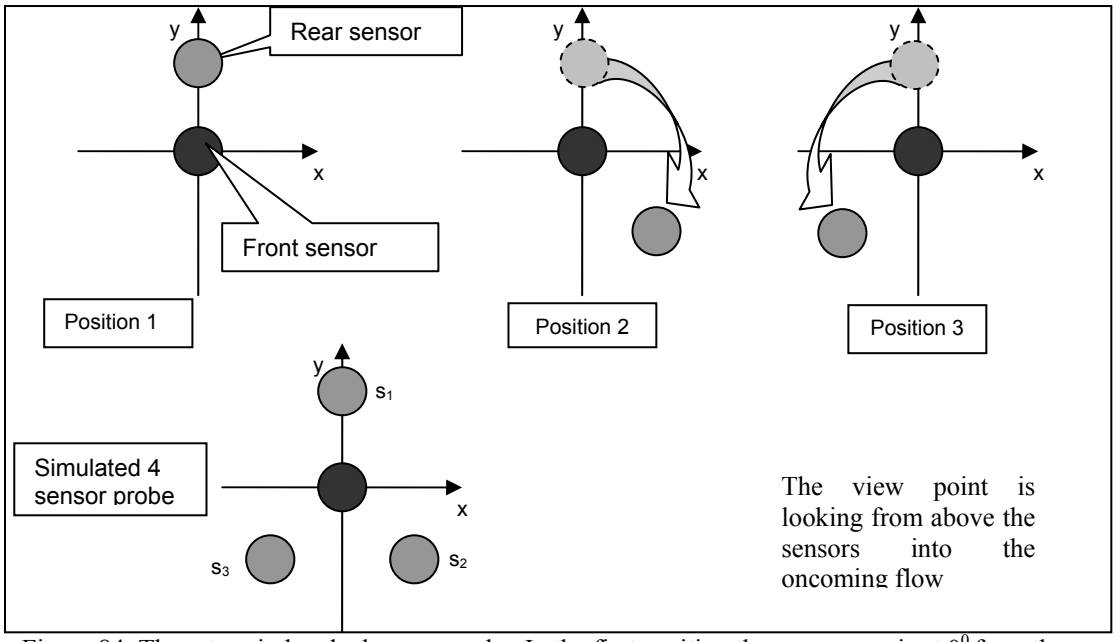

Figure 84. The rotary index dual sensor probe. In the first position the rear sensor is at 0^0 from the y-axis of the probe coordinate system. In the second position it is at 120^0 clockwise from the y-axis. In the third position it is at 120^0 anti-clockwise from the y-axis; s_1, s_2 and s_3 denote the rear sensors in the simulated four-sensor probe.

10.5 Experimental apparatus for the rotary index dual sensor probe.

10.5.1 Bubble Column, Probe Mount and Reference Measurements

In order to test the accuracy with which a conventional or simulated four-sensor probe can measure the bubble velocity vector it must be mounted in a bubble column. In the present investigation, the bubble column consisted of a 750mm long transparent pipe of square cross section with internal side of width 200mm. The pipe was mounted vertically and filled with water. Each probe investigated was clamped to a hinged platform at the top of the pipe, with the probe (when vertical) typically

extending a distance of approximately 100mm below the surface of the water. Air was injected into the pipe using a 2mm internal diameter bubble injector mounted vertically on the base of the tank. The injector was connected to a controllable electric air pump which could be used to vary the flow rate of air to the injector. The position of the bubble injector on the tank base could be varied so that as the orientation of the probe was changed, as described below, it was always possible to ensure that the stream of bubbles emerging from the injector came into contact with the four sensors in the probe. The air bubbles emerging from the injector were typically oblate spheroids with a major diameter of approximately 6mm. The axial separation of the bubbles in the vertically rising stream was of the order of a few bubble diameters and consequently each bubble moved in the wake of the preceding bubble. This meant that the bubble rise velocity was about $0.4\,\mathrm{ms}^{-1}$, significantly higher than the $0.25\,\mathrm{ms}^{-1}$ rise velocity of a single isolated 6mm diameter air bubble in stationary water. A key assumption of the work in this chapter is that the properties of the bubble stream were time invariant i.e. all of the bubbles were the same size and had an identical velocity vector and orientation when they struck the probe.

In an earlier paper [119] Lucas and Mishra defined a local probe coordinate system for four-sensor probes (see figure 86). The origin of the coordinate system is coincident with the position of the lead sensor whilst the z-axis is parallel to the axis of the probe (this axis is vertical for vertically mounted probes such as those described in [119]). The x and y axes are chosen arbitrarily but are orthogonal to each other and to the z-axis. The spatial locations of rear sensors 1, 2 and 3 can be defined using this probe coordinate system. Suppose that an approaching bubble has velocity vector $\mathbf{V}$ relative to the probe coordinate system as shown in figure 86. $\mathbf{V}$ makes a polar angle γ with respect to the z-axis. Furthermore, the projection of $\mathbf{V}$ onto the x-y plane

gives rise to a line that makes an azimuthal angle β to the y-axis (in the direction shown in figure 86). In order to determine the effectiveness with which a four-sensor probe can measure the velocity vector $\mathbf{V}$ of a bubble, using the theory outlined in [119], it is necessary to subject the probe to bubbles approaching with a wide range of values of $\mathbf{V}$. For air bubbles in water it is impractical to attempt to change the direction of the air bubbles, however it is possible to change the direction of $\mathbf{V}$ relative to the probe coordinate system by tilting and rotating the probe as described below.

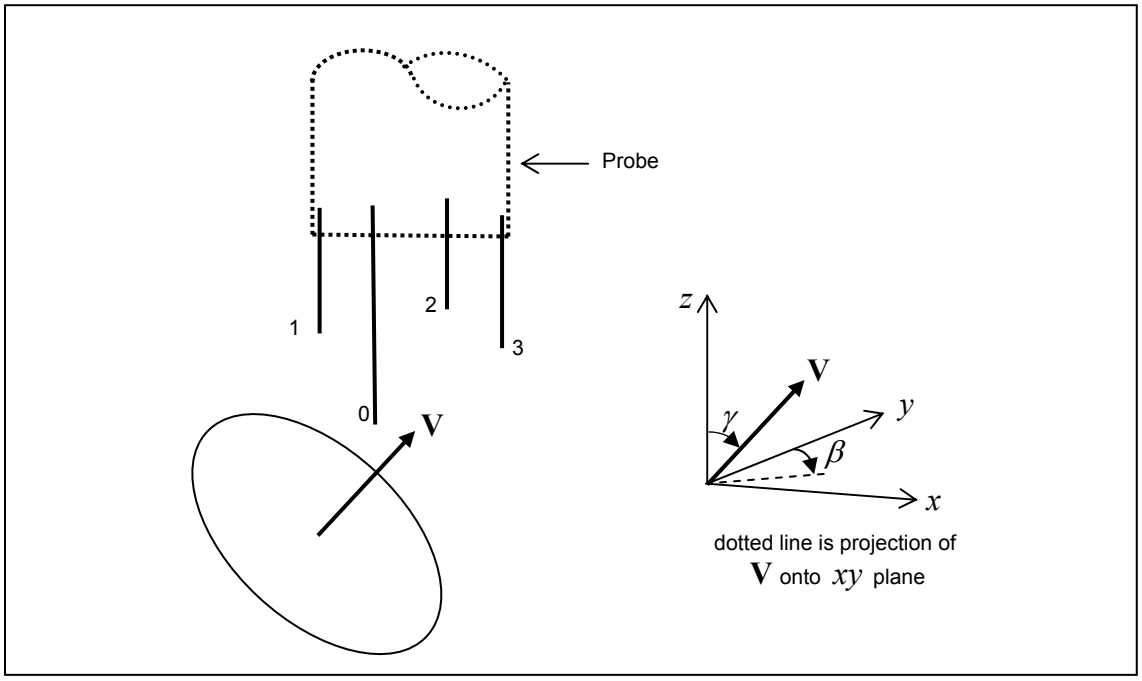

Figure 85. Probe coordinate system. Origin is coincident with sensor 0; z-axis is coincident with that needle of which the tip forms sensor 0 (nb the z-axis is parallel to axis of the probe).

Consider a four-sensor probe mounted on the horizontal, hinged platform at the top of the water filled bubble column as shown in figure 87. A stream of bubbles approaches the probe, and it is assumed here that the velocity of these bubbles is purely vertical. It is further assumed that the y-axis of the probe coordinate system is coincident with the centreline a-a1 of the hinged platform, with the increasing y-axis in the direction

from a to a1. As the hinged platform is rotated through an angle γ^* (in the direction shown in figure 87) the velocity vector $\mathbf{V}$ of the approaching bubbles will now make a polar angle γ relative to the z-axis of the probe where $\gamma = \gamma^*$. If the y-axis of the probe coordinate system is now rotated anticlockwise (as viewed from above) through an angle β^* relative to the line a-a1, the projection of the velocity vector $\mathbf{V}$ (of the bubbles approaching the probe) onto the x-y plane will make an azimuthal angle β relative to the y-axis where $\beta = \beta^*$. By varying the angles γ^* and β^*, the direction of $\mathbf{V}$ relative to the probe coordinate system can be varied for the purposes of testing or calibrating a four-sensor probe. The magnitude v of the bubble velocity vector cannot easily be changed since this is a function of the rise velocity of air bubbles through stationary water, however small variations in v could be achieved by varying the size of the air bubbles via manipulation of the air injection system.

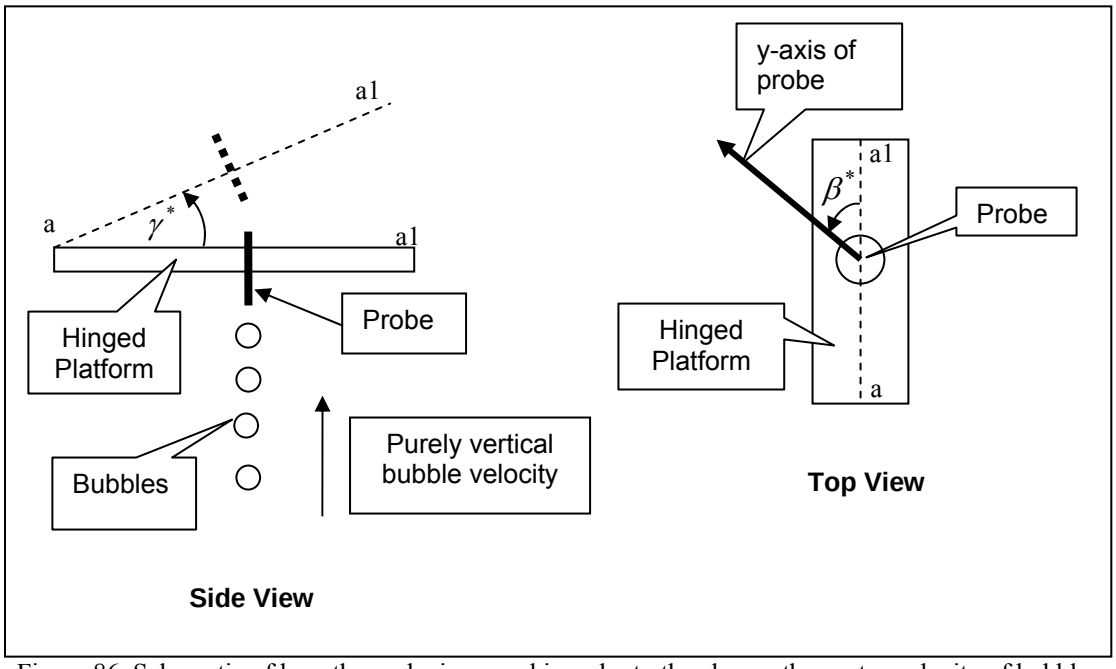

Figure 86. Schematic of how the probe is moved in order to the change the vector velocity of bubbles relative to the probe.

In the present investigation reference measurement of the inclination angle γ^* of the hinged platform was made using an inclinometer. Reference measurement of the angle β^* was made using a simple protractor system. Reference measurement of the bubble vertical rise velocity was made using a cross correlation flow meter [131] the centre of which was placed approximately 100mm below the tip of the probe and through which the bubble stream passed (see figure 89). The cross correlation flow meter consisted of two pairs of copper electrodes separated by an axial distance of 50mm and mounted on the internal circumference of a short length of thin walled 80mm internal diameter plastic pipe (figure 89). This pipe was in turn mounted in the square sided bubble column as shown in figure 89. The conductance between the upstream pair of electrodes and between the downstream pair of electrodes varied due to the passage of the air bubbles and these two conductance variations were measured using inverting amplifier circuits connected to a 2-channel data acquisition system. The signals were then cross correlated using a program written in MATLAB. The reference vertical bubble rise velocity was obtained by dividing the axial separation of the pairs of copper electrodes by the time delay corresponding to the peak of the resultant cross correlation function.

To prevent cross-talk between the two pairs of electrodes, the drive circuit for each pair was alternately switched on and off at high frequency (100kHz) so that when the upstream pair P_u was energised the downstream pair P_d was de-energised and vice-versa (see figure 89). Figure 88 shows the electronic circuit

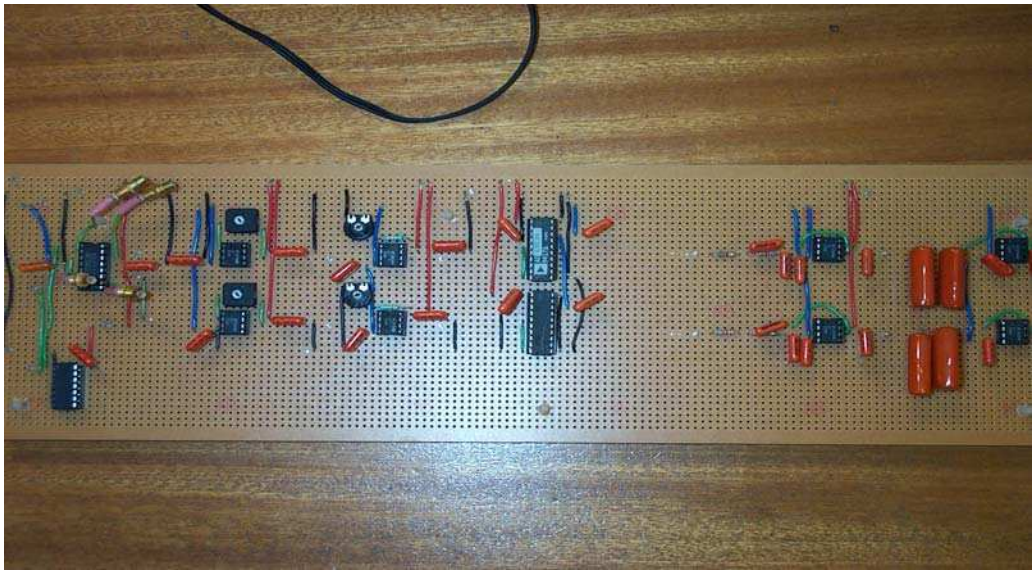

Figure 87. The electronic circuit for cross correlation.

Data acquisition for a given pair was synchronised with the time when that pair was energised. This is an acknowledged method for sharpening the peak of the cross correlation function, enabling the time delay associated with the peak to be determined with greater accuracy.

It should be noted that since both the reference cross correlation velocity measurement and the local probe under test rely on conductance measurements they cannot be used at the same time in case there is interference between the two measurement techniques. Consequently, reference measurements of the bubble velocity magnitude were made just before and just after data was acquired from the local probe.

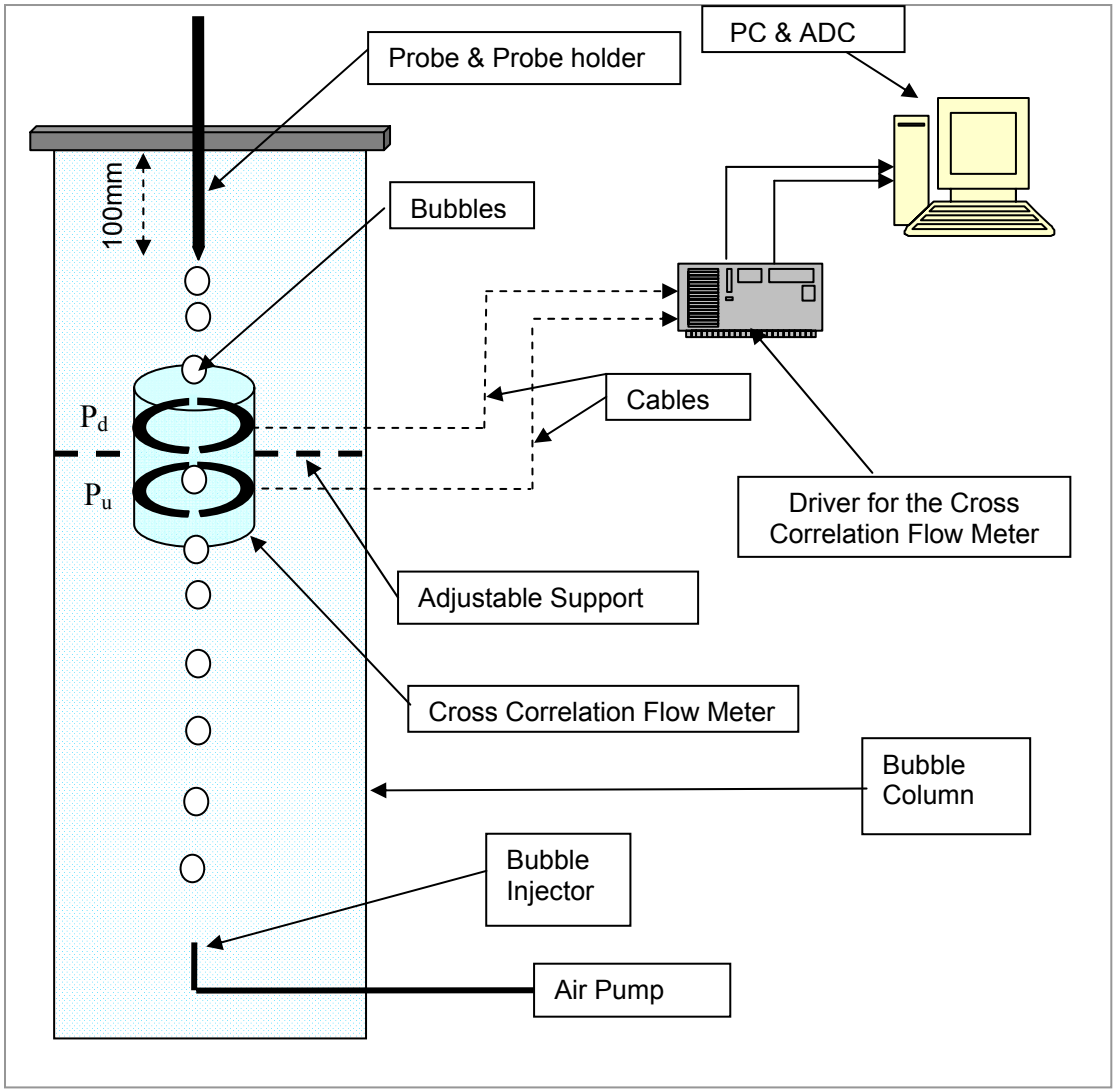

Figure 88. Schematic of the bubble column and instrumentation (not to scale)

10.6 Experimental procedure and Results.

10.6.1 Experimental results.

A series of tests was carried out, with the simulated four-sensor probe positioned at different orientations to the oncoming stream of air bubbles, as described earlier. For each orientation of the probe, reference measurements γ_{ref} and β_{ref} of the polar and azimuthal angles of the bubble velocity vector $\mathbf{V}$ relative to the probe coordinate system were made using the methods described previously. A

reference measurement v_{ref} of the bubble velocity magnitude was also made using the cross correlation flow meter described in 10.5. Variations in v_{ref} that were observed from test to test were due to changes in the water viscosity caused by changes in the ambient temperature of the laboratory. For each orientation of the probe, and for each of the three rotational positions of the lower probe body relative to the upper probe body, conductance data was acquired from the probe for approximately 60 bubbles coming into contact with the probe. This conductance data was acquired at a rate of 250kHz from each of the two sensors using a high speed, pc-based data acquisition system. From this conductance data, average values for the time intervals δt_{ii} (i=1,2,3) were obtained (see equations 37-39) which were used in conjunction with the dimensions of the simulated four sensor probe and the mathematical model outlined in paragraph 10.3 to yield values for γ_{meas} and β_{meas} as well as for v_{meas} the bubble velocity magnitude measured by the probe. It should be noted that when the polar angle γ of the bubble velocity vector relative to the probe coordinate system is equal to zero the azimuthal angle β is unquantifiable. Consequently, for those tests for which $\gamma_{ref} = 0^o$, no values for β_{ref} or β_{meas} are given.

For each of the tests carried out, values of γ_{ref}, β_{ref}, v_{ref}, γ_{meas}, β_{meas} and v_{meas} are given in Table 10. In Table 11 the average values for δt_{11}, δt_{22} and δt_{33} are given for each test. A percentage error ε_v in v_{meas} is defined as

$$\varepsilon_v = \frac{v_{meas} - v_{ref}}{v_{ref}} \times 100 \qquad (89)$$

The value of ε_v for each test undertaken is given in Table 12. Also in Table 12 are the absolute errors $\varepsilon_{abs,\gamma}$ and $\varepsilon_{abs,\beta}$ in degrees for α_{meas} and β_{meas} respectively.

Test	γ_{ref} (degrees)	β_{ref} (degrees)	v_{ref} (m/s)	γ_{meas} (degrees)	β_{meas} (degrees)	v_{meas} (m/s)
1	0	-	0.403	4.844	-	0.427
2	24	0 (=360)	0.403	21.866	358.099	0.397
3	21	180	0.39	19.782	178.375	0.412
4	3	270	0.374	3.181	277.614	0.419
5	0	-	0.41	5.228	-	0.455
6	23	0	0.41	21.832	7.133	0.411
7	23	180	0.41	18.518	171.549	0.438
8	5	270	0.38	2.249	258.903	0.419

Table 10. Values of polar angle, azimuthal angle and velocity magnitude measured by the probe and reference values for these quantities.

Test	δt_{11} (s)	δt_{22} (s)	δt_{33} (s)
1	0.005207	0.005556	0.005675
2	0.006878	0.004833	0.004912
3	0.004164	0.005946	0.005887
4	0.005631	0.005427	0.00576
5	0.005388	0.005182	0.004892
6	0.006627	0.004851	0.004566
7	0.004037	0.005703	0.005433
8	0.00558	0.005502	0.005735

Table 11. Average values for the measured time delays δt_{ii} for each of the tests.

Test	$\varepsilon_{abs,\gamma}$ (degrees)	$\varepsilon_{abs,\beta}$ (degrees)	ε_v (%)
1	4.844	-	5.95
2	-2.134	-1.901	-1.49
3	-1.218	-1.625	5.64
4	0.181	7.614	12.03
5	5.228	-	10.97
6	-1.168	7.133	0.24
7	-4.482	-8.451	6.83
8	-2.751	-11.097	10.26

Table 12. Errors in the values of polar angle, azimuthal angle and velocity magnitude measured by the probe.

From the data given in Table 12, the mean value $\bar{\varepsilon}_{abs,\gamma}$ of the absolute error in γ_{meas} is equal to -0.1875^o. The standard deviation $\sigma_{abs,\alpha}$ of $\varepsilon_{abs,\gamma}$ is equal to 3.271^o. The mean value $\bar{\varepsilon}_{abs,\beta}$ of the absolute error in β_{meas} is equal to -1.388^o. The standard deviation $\sigma_{abs,\beta}$ of $\varepsilon_{abs,\beta}$ is equal to 7.05^o. The relatively low values of $\bar{\varepsilon}_{abs,\gamma}$ and $\bar{\varepsilon}_{abs,\beta}$ indicate that the simulated four-sensor probe can be used to give a reasonably accurate estimate of the polar angle γ and the azimuthal angle β of the bubble velocity vector. The values for the standard deviations $\sigma_{abs,\gamma}$ and $\sigma_{abs,\beta}$ do however indicate that, for some of the individual tests carried out, the errors in γ_{meas} and β_{meas} were somewhat greater than would be suggested by inspection of $\bar{\varepsilon}_{abs,\gamma}$ and $\bar{\varepsilon}_{abs,\beta}$ alone.

The mean value $\bar{\varepsilon}_v$ of the percentage error in the bubble velocity magnitude is 6.304%. The standard deviation σ_v of ε_v is 4.59%. The observed value of $\bar{\varepsilon}_v$

indicates that the simulated four-sensor probe *overestimates* the bubble velocity magnitude and this result is somewhat surprising because, as stated in section 10.1, it was previously found that a conventional four-sensor probe had a *retarding* effect of up to about 20% (in air) on the bubble velocity magnitude. Nevertheless it can be concluded that the simulated four-sensor probe, consisting of two needle sensors, has a much smaller influence on the bubble velocity magnitude than a conventional four-sensor probe which contains four needle sensors.

10.7 Possible Sources of Error

When a gas bubble comes into contact with one of the conductance sensors there is an abrupt reduction in the measured conductance from S_w the water conductance to S_g the gas conductance. A threshold conductance S_{th} such that $S_g < S_{th} < S_w$ is introduced to help define the precise time at which the bubble surface makes first contact with the sensor (a similar method is used to determine the precise time at which the bubble surface makes last contact with the sensor). In reference [119] it is demonstrated that, provided the transient responses of all sensors in the probe are similar, then the measurement technique is relatively insensitive to the choice of threshold conductance. Issues associated with thresholding are therefore unlikely to be major sources of the observed errors in γ_{meas}, β_{meas} and v_{meas}.

The mathematical model described in chapters 5 and 10 and discussed extensively in reference [119] requires that each gas bubble contacting the probe has a plane of symmetry normal to its direction of motion. High speed filming of the gas bubbles in the experiments described in this thesis suggests that this requirement was generally fulfilled. Consequently, an error in this assumption associated with the

mathematical model is unlikely to be a major source of the observed measurement errors.

A more likely source of error is that the effective axial separation of the two sensors in the rotating dual-sensor probe has been overestimated. This overestimate could be due to measurement errors associated with the use of the calibrated microscope to measure the relative positions of two sensors. An overestimate of 6% (about 60 microns) in the measured axial separation of the two sensors could easily account for the observed mean overestimate of 6.304% in the bubble velocity magnitude.

Perhaps the most likely source of the observed errors in γ_{meas}, β_{meas} and v_{meas} is the assumption that the trajectory of the bubbles in the bubble stream is time invariant such that all of the bubbles have an identical velocity vector and orientation relative to the probe. Although the flow is 'steady state' it is nevertheless possible that some time-dependent variations in the bubble velocity vector may occur. If so, the rotating dual-sensor probe does not truly mimic the operation of a conventional four-sensor probe and errors associated with the mathematical model used to determine γ_{meas}, β_{meas} and v_{meas} will arise.

11. General Conclusions.

A dual sensor conductance probe has been designed and built and used, with appropriate signal processing techniques, to obtain distributions of the local gas volume fraction and the local gas velocity in vertical upward, bubbly air–water flows in which the mean gas volume fraction was less than 0.1. Both the gas volume fraction and the gas velocity distributions were approximated by power law functions. The power law exponents q for the local gas volume fraction distributions were found to be higher than the values predicted by van der Welle. For $\overline{\alpha} = 0.02$, the exponent q was 30% higher than predicted by van der Welle indicating that, for this low value of $\overline{\alpha}$ the local gas volume fraction distribution is much less uniform than previously thought, with the gas preferentially clustering at the pipe centre. The power law exponents p for the gas velocity distributions were on average slightly higher than the values predicted by van der Welle. This may be due to the fact that van der Welle's predictions were based on data taken at much higher values of $\overline{\alpha}$. However, it is also possible that this discrepancy may be due to signal processing errors arising from an axial sensor separation s which was inappropriately large.

For the vertical bubbly oil-liquid flows investigated, the local oil volume fraction and axial velocity distributions were axisymmetric. As the inclination angle of the flow away from the vertical was increased, the oil droplets tended to migrate towards the upper side of the inclined pipe. However hydrodynamic forces on the droplets, arising from shear in the liquid phase, caused the oil droplets to become confined into a smaller region of the flow cross section at the upper side of the pipe as the liquid superficial velocity was increased. The lower density of the oil-liquid mixture at the upper side of the inclined pipe gave rise to relatively high axial

velocities in this part of the flow cross section. The effect of pipe inclination on the maximum axial gas velocity must be taken into consideration, for example, when modeling oil well 'blowouts'.

A series of experiments was carried out on vertical, bubbly oil-in-water flows in an 80mm internal diameter pipe for values of water superficial velocity in the range $0.276\,\mathrm{ms}^{-1}$ to $0.417\,\mathrm{ms}^{-1}$, for values of oil superficial velocity in the range $0.025\,\mathrm{ms}^{-1}$ to $0.083\,\mathrm{ms}^{-1}$ and for values of the mean oil volume fraction $\overline{\alpha}_{ref}$ in the range 0.047 to 0.205. The oil droplets were about 6mm to 7mm in size. For all of the flow conditions investigated, it was found that the velocity profile of the oil droplets was 'power law' in shape, with the peak velocity at the pipe centre and with the velocity declining to zero at the pipe wall. The shapes of the observed oil velocity distributions were very similar to the shapes of air velocity distributions obtained in bubbly air-water flows at similar flow conditions and with 5mm air bubbles. Values of the Zuber-Findlay distribution parameter C_0 for the oil-water flows were very similar to values of C_0 obtained for bubbly air-water flows at similar flow conditions. These results are noteworthy given the large density ratio contrast between oil-water (0.8) and air-water (0.0012).

The shape of the local oil volume fraction distribution for the oil-in-water flows investigated was found to be dependent upon $\overline{\alpha}_{ref}$. For values of $\overline{\alpha}_{ref}$ less than about 0.08, the local oil volume fraction distribution was observed to be 'power law' in shape. For values of $\overline{\alpha}_{ref}$ in the range 0.08 to 0.15 the local oil volume fraction distribution was found to be essentially flat apart from within the so-called bubble sub-layer adjacent to the wall. For values of $\overline{\alpha}_{ref}$ greater than about 0.15 the local oil volume fraction distribution had an 'intermediate peak' shape. Modelling work that

was undertaken suggests that the shape of the local oil volume fraction distribution is the result of droplet diffusion and radial hydrodynamic forces acting on the oil droplets. For $\overline{\alpha}_{ref} < 0.08$ the net hydrodynamic force is relatively strong and acts in the direction of the pipe centre. For $0.08 \le \overline{\alpha}_{ref} \le 0.15$ the net hydrodynamic force can be close to zero with the resultant oil volume fraction distribution being purely a function of the droplet diffusion process. For $\overline{\alpha}_{ref} > 0.15$ the net hydrodynamic force on each droplet is relatively weak and in the direction of the pipe wall. For $\overline{\alpha}_{ref} > 0.15$ one component of the net hydrodynamic force is probably a "circulation induced" radial force acting on each droplet as a result of shear in the continuous water phase. [128][139]

It was found that the gas volume fraction profiles in vertical air-water flows obtained from electrical resistance tomography (ERT) all had similar shapes irrespective of the flow conditions suggesting that the gas volume fraction profiles were highly depended upon the "conjugate gradient" image reconstruction method that was used. The gas velocity profiles obtained from dual plane ERT failed to show the same level of detail as the velocity profiles obtained from the dual sensor probe. This suggests that dual plane ERT averages out (or smears out) the local gas velocity distribution. Whereas ERT may be useful in determining the mean gas velocity and mean gas volume fraction, as yet it appears to be unable to accurately measure the gas velocity and volume fraction profiles.

A novel technique, requiring the measurement of seven time delays obtained from a local 4-sensor conductance probe, has been developed for measuring the velocity vectors of individual oil bubbles in bubbly oil-liquid flows. The technique has been found to be relatively insensitive to assumptions made, when processing the

probe output signals, regarding the precise times at which each of the sensors comes into contact with the surface of the bubble. A study has been carried out using the technique to investigate the distribution of the mean local axial, radial and azimuthal bubble velocities in vertical upward, bubbly air-water flows both with a 20^{o} swirler and without swirl. The distribution of the local gas volume fraction in such flows was also investigated. For the range of flow conditions studied the following key results were observed. (i) The measured radial velocity of the gas bubbles was always close to zero, both with and without swirl. (ii) The presence of the swirl had very little effect on the distribution of the local axial velocity of the gas bubbles. (iii) For a given set of flow conditions, the introduction of swirl causes a significant increase in the azimuthal velocity of the gas bubbles in the direction of the swirl. Although this result could have been predicted qualitatively in advance, the novel measurement technique described herein allowed the variation of the azimuthal velocity $v_{\theta}^{'}$ across the pipe diameter to be measured. It was found that the magnitude of $v_{\theta}^{'}$ was a maximum at the pipe wall but decreased toward the pipe centre. (iv) For most of the flow conditions investigated it was found that the presence of swirl had very little effect on the distribution of the local gas volume fraction α_{l} in the flow cross section. However at the highest value of water superficial velocity investigated ($u_{ws} = 0.91\text{ms}^{-1}$) it was found that the presence of swirl caused the gas bubbles to preferentially accumulate at the pipe centre, due to a 'centrifuge' effect.

It was found that the 4-sensor probe used in the present investigation could cause the magnitude *v* of the bubble velocity vector to be reduced in the presence of swirl to 70% of its true value. This effect had to be compensated for by the use of a flow dependent calibration factor *K*. Further work is necessary to investigate whether

the calibration factor K is actually the same for all probe positions, at a given flow condition, or whether its value changes as the probe is moved from the pipe centre to the pipe wall. Future work will also concentrate on reducing the physical dimensions of the 4-sensor probe to minimize this 'retarding effect' of the probe on the gas bubbles.

A rotary index dual-sensor probe has been used to simulate a four sensor probe in order to measure the velocity vectors of bubbles in a time invariant bubbly air–water flow. The rotary index dual sensor probe has a smaller frontal area than the equivalent conventional four-sensor probe and thereby interferes less with the motion of the oncoming bubbles. By changing the orientation of the axes of the rotary index dual-sensor probe, relative to a stream of vertically rising air bubbles, the velocity vector **V** of these bubbles relative to the probe coordinate system was varied. Experiments were carried out in which the probe was used to measure the polar angle α of the bubble velocity vector relative to the probe coordinate system, the azimuthal angle β of the bubble velocity vector relative to the probe coordinate system and the magnitude v of the bubble velocity vector, for different values of γ in the range 0^0 to 24^0, for reference values of β in the range 0^0 to 270^0 and for reference values of v of about $0.4 ms^{-1}$. It was found that the mean absolute error $\bar{\varepsilon}_{abs,\alpha}$ in the measured polar angle was equal to -0.1875^0 whilst the mean absolute error $\bar{\varepsilon}_{abs,\beta}$ in the measured azimuthal angle was equal to -1.388^0. The mean percentage error $\bar{\varepsilon}_v$ in the measured bubble velocity magnitude was +6.304%. This value of $\bar{\varepsilon}_v$ compares very favourably with results for a conventional four-sensor probe in the literature which reported percentage errors as large as −20% for the bubble velocity magnitude (no estimates were reported for the errors in the measured values of polar and azimuthal angles).

This suggests that the rotary index dual- sensor probe has a much smaller retarding effect on the bubbles than an equivalent conventional four-sensor probe and implies that future work on four-sensor probes must address the issue of probe intrusiveness, either through probe design or calibration. Errors in the measurement of γ, β and v using the rotating dual sensor probe may be due (i) to minor errors in measurement of the relative positions of the two sensors and (ii) to variations with time of the trajectory of the bubbles, thereby violating the assumption of time invariant flow conditions.

12. Further Work.

As a result of the current investigation, and the conclusions reached, a number of suggestions for further work can be made. These are listed below:

- *Use of an AC excitation signal to the probes*.

  As mentioned in chapters 4 and 6, the electronic circuit responsible for detecting the conductivity changes of the dual and four sensor probes uses a DC input. The constant DC current from the source propagates through the probe's electrodes (the acupuncture needles) then through the medium between the sensors and then back to the DC source. The probe is connected with a DC amplifier and acts as a resistor. The changes in the resistor's value depend on the medium between the electrodes. When the medium is water the resistance is low (high conductance) and when the medium is oil or air the resistance is high (low conductance). These resistance changes are detected by the DC amplifier and it outputs a voltage linearly dependent on the resistance values. But when DC current is applied across the electrodes then electrolysis occurs in an aqueous environment. The outcome of this electro-chemical activity is that solid corrosion products form on the electrodes' surface. These corrosion products have a very high resistance. The overall result of the corrosion is the total resistance of the probe will significantly be increased. But if an AC current is applied, the electrodes of the probe change polarity according to the frequency of the applied AC source. This has the effect of reducing (but not eliminating; both electrodes will still suffer corrosion damage) the effect of corrosion, prolonging the life of the probe, maintaining for longer periods the quality of signals produced by the probe-signal

conditioner system, and reducing maintenance costs of the probe. Of course, the change from DC source to AC source has the effect of building a new electronic circuit that is able to detect the probe's conductance changes. A new signal processing scheme must also be developed.

- *Local probes optimization*.

  Based on the experimental results shown in chapters 8, 9, and 10, the retarding effect that the probes introduced to the environment has a significant negative role to the quality of the data, and the errors of the measurements. This retarding effect is highly dependent (but not only) on the size of the probe. Minimization of its geometry (without having a negative impact to the probe's functionality) will reduce the negative impact of this retardation.

  Regarding the rotating dual sensor probe, an extra optimization that may be achieved is to build an automatic control system for its rotation and positioning. The result will be to minimize the errors introduced by the manual rotation of the probe during the experiments (something that was performed in the current investigation), and to have more (known) accurate positioning of its geometry during the tests. A new traverse mechanism that is able to host the new automated rotating dual sensor probe must also be part of the optimization. Note, as it was mentioned in chapter 10, that the rotating dual sensor probe is proper for steady state flows.

- *Experimental use of the optimized probes.*

  A new set of experiments, in oil-water and air water flows, can be performed in order to quantify the performance of the optimized probes, and increase the accuracy of the measurements.

- *Uncertainty budget of the measuring system.*

  Since the primary purpose of the local sensor probes is to provide a benchmark against which ERT data can be validated, it is vital to create the uncertainty budget of the probes measurement system. The uncertainty budget is a table which identifies all the sources of errors that are present to the measurement chain and gives an uncertainty value for each one. A list of errors that are present to the measurement chain is shown below. This is by no means an exhaustive list and a considerable amount of work must be performed for completing the task.

  1. Uncertainties of the reference data.
  2. Uncertainties of the electronic circuits.
  3. Uncertainties of the probe's geometry.
  4. Uncertainties of the position of the probe.
  5. Uncertainties of the A/D converters (quantization noise).

  After quantifying the identified sources of errors, several statistical tools should be applied to the values in order to calculate the final uncertainty of the measurement chain. Of course, cooperation with the National Physical Laboratory (NPL) could be used in order to have traceability of the measurements and a complete picture of the accuracy of the system.

REFERENCES

[1] G. F. HEWITT, J. M. DELHAYE, N. ZUBER, "*Multiphase Science and technology*", volume 2, Hemisphere Publishing Corporation, pages 1-94, 1986.

[2] Govier G. W., Aziz K., "The flow of complex Mixtures in pipes", Van Nostrand Reinhold Company, pages 322-329, 1982.

[3] J. M. COULSON & J. F. RICHARDSON, "*Chemical engineering*", SIXTH EDITION, Butterworth Heinemann, volume 1, pages 181-231, 1999.

[4] Beggs, H. D., "*An experimental study of two phase flow in inclined pipes*", Pd.D. dissertation, University of Tulsa, OK, 1972.

[5] Beggs, H. D., Brill, J. P., "*A study of two-phase flow in inclined pipes*.", J. Pet. Technol., (MAY), 607-617, 1973.

[6] P. Vigneaux, P. Chenais, J. P. Hulin, "*Liquid-liquid flows in an inclined pipe.*", AIChE Journal, volume 34, No.5, pages 781-789, May 1988.

[7] Z. X. Ding, K. Ullah, and Y. Huang, "*A comparison of predictive oil/water holdup models for production log interpretation in vertical and deviated wellbores*", SPWLA 35th Annual Logging Symposium, June 19-22, 1994.

[8] A. R. Hasan, SPE, U. of North Dakota, and C. S. Kabir, SPE, Chevron Overseas Petroleum Technology Company, "*A simplified model for oil-water flow in vertical and deviated wellbores*", SPE 49163, 1998.

[9] G. P. Lucas and N. D. Jin, "*Investigation of a drift velocity model for predicting superficial velocities of oil and water in inclined oil-water pipe flows with a centre body*", Meas. Sci. Technol., Volume 12, pages 1546-1554, 2001.

[10] G. Oddie, H. Shi, L. J. Durlofsky, K. Aziz, B. Pfeffer, J. A. Holmes, "*Experimental study of two and three phase flows in large diameter inclined pipes.*", International Journal of Multiphase Flow, volume 29, pages 527-558, 2003.

[11] Christophe Boyer, Anne-Marie Duquenne, Gabriel Wild, "*Measuring techniques in gas-liquid-solid reactors*", Chemical Engineering Science, volume 57, pp 3185-3215, 2002.

[12] Takashi Hibiki, Rong Situ, Ye Mi, Mamoru Ishii, "*Local flow measurements of vertical upward bubbly flow in an annulus*", Heat and Mass Transfer, volume 46, pp 1479-1496, 2002.

[13] N. Panayotopoulos, G. P. Lucas, R. Mishra, "*Calculation of Volume fraction and mean bubble vector velocity using two and four sensor conductivity probes in vertical and inclined bubble air-water flows.*", School of computing & engineering Researchers' Conference, University of Huddersfield, Nov 2005.

[14] Jim Cory, "*The measurement of volume fraction and velocity profiles in vertical and inclined multiphase flow*", PhD thesis, December 1999.

[15] http://science.howstuffworks.com/oil-drilling2.htm, Craig C. Freudenrich, Ph.D., 19/07/2006.

[16] http://science.howstuffworks.com/oil-drilling4.htm, Craig C. Freudenrich, Ph.D., 19/07/2006.

[17] S. R. Wylie, A. Shaw and A. I. Al-Shamma'a, "*RF sensor for multiphase flow measurement through an oil pipeline.*", Meas. Sci. Technol., volume 17, pages 2141-2149, 2006.

[18] Subhashini Ghorai, Visual Suri, K. D. P. Nigam, "*Numerical modelling of three-phase stratified flow in pipes.*", Chemical Engineering Science, volume 60, pages, 6637-6648, 2005.

[19] V. Seshadri, S. N. Singh, Charau Fabien, and R. Mishra, "*Hold-up in multi-sized particulate solid-liquid flow through horizontal pipes.*", Indian Journal of Engineering & Materials Sciences, volume 8, pages 84-89, April 2001.

[20] J. Ling, P. V. Skudarnov, C. X. Lin, M. A. Ebadian, "*Numerical Investigations of liquid-solid slurry flows in a fully developed turbulent flow region.*", International Journal of Heat and Fluid Flow, volume 24, pages 389-398, 2003.

[21] Suhashini Ghorai, K. D. P. Nigam, "*CFD modelling and interfacial phenomena in two-phase flow in pipes.*", Chemical engineering and Processing, volume 45, pages 55-65, 2006.

[22] Dirk Lucas, Eckhard Krepper, Horst-Michael Prasser, "*Prediction of radial gas profiles in vertical pipe flow on the basis of bubble size distribution.*", Int. J. Therm. Sci., volume 40, pages 217-225, 2001.

[23] Jürgen Steinemann and Rainer Buchholz, "*Application of an electrical conductivity microprobe for the characterization of bubble behaviour in gas-liquid bubble flow.*", Verlag Chemie GmbH, D-6940 Weinheim, pages 102-107, 1984.

[24] Severin Waelchli, Philipp Rudolf von Rohr, "*Two-phase flow characteristics in gas-liquid microreactors.*", International journal of multiphase flow, volume 32, issue 7, pages 791-806, 2006.

[25] Wei Feng, Jianping Wen, Jinghua Fan, Qing Yuan, Xiaoqiang Jia, Yan Sun, "*Local hydrodynamics of gas-liquid-nanoparticles three-phase fluidization.*", Chemical engineering science, volume 60, pages 6887-6898, 2005.

[26] J. Varley, J. W. R. Boyd, S. Gallagher, A. K. Brown, P. W. Dodd, "*Correlation between conductivity and liquid hold-up for a multi-segment industrial foam probe for fermentation.*", Biochemical engineering journal, volume 19, pages 199-210, 2004.

[27] Bouchaib Gourich, Christophe Vial, Abel Hafid Essadki, Fouad Allam, Mohammed Belhaj, Mahfud Ziyad, "*Identification of flow regimes and transition points in a bubble column through analysis of differential pressure signal – Influence of the coalescence behaviour of the liquid phase.*", Chemical engineering and processing, volume 45, issue 3, pages 214-223, 2006.

[28] Yu Zheng, Xiaotao Wan, Zhen Qian, Fei Wei, Yong Jin, "*Numerical simulation of the gas-particle turbulent flow in riser reactor based on κ-ε-κ_p-ε_p-θ two fluid model.*", Chemical engineering science, volume 56, pages 6813-6822, 2001.

[29] R. Pohorecki, W. Moniuk, P. Bielski, P. Sobieszuk, G. Dąbrowiecki, "*Bubble diameter correlation via numerical experiment.*" Chemical engineering journal, volume 113, pages 35-39, 2005.

[30] Moshe Favelukis, Cam Hung Ly, "*Unsteady mass transfer around spheroidal drops in potential flow.*", chemical engineering science, volume 60, pages 7011-7021, 2005.

[31] GAO Xiqum, MA Youguang, ZHU Chunying, and YU Guocong, "*Towards the mechanism of mass transfer of a single bubble.*", Chinese journal of Chemical Engineering, volume 14, pages 158-163, 2006.

[32] Pyung Seob Song, Chan Gi Lee, Suk Hwan Kang, Sung Mo Son, Yong Kang, Sang Done Kim, "*Drop properties and pressure fluctuations in liquid-liquid-solid fluidized-bed reactors.*", Chemical engineering and processing, volume 44, pages 1296-1305, 2005.

[33] G. P. Lucas, J. C. Cory, R. C. Waterfall, Loh W. W., and Dickin F. J., "*Measurement of the solids volume fraction and velocity distributions in solids-*

liquid flows using dual-plane electrical resistance tomography", J. Flow Meas. Instrum., volume 10, pages 249-258, 1999.

[34] Chistophe Boyer, Anne-Marie Dquenne, Gabriel Wild, "*Measuring techniques in gas-liquid and gas-liquid-solid reactors.*", Chemical engineering Science, volume 57, pages 3185-3215, 2002.

[35] Züber N., Findlay J. A., "*Average volumetric concentration in two-phase flow systems.*" Journal of heat transfer, volume 87, pages 453-468, 1965.

[36] Matsui G., "*Identification of flow regimes in vertical gas-liquid two-phase flow using differential pressure fluctuations.*", International journal of multiphase flow, volume 10, pages 711-720, 1984.

[37] Glasqow L. A., Erickson L. E., Lee C. H., & Patel S. A., "*Wall pressure fluctuations and bubble size distributions at several positions in an airlift fermentor.*", Chemical engineering communications, volume 29, pages 311-336, 1984.

[38] Drahos J. & Cermak J., "*Diagnostics of gas-liquid flow patterns in chemical engineering systems.*", Chemical engineering and processing, volume 26, pages 4069-4075, 1992.

[39] Drahos J., Zadradnik J., Puncochar M., Fialova M., & Bradka F., "*Effect of operating conditions of the characteristics of pressure fluctuations in a bubble column.*", Chemical engineering and processing, volume 29, pages 107-115, 1991.

[40] Drahos J., Bradka F., & Puncochar M., "*Fractal behaviour of pressure fluctuations in a bubble column.*", Chemical engineering science, volume 47, pages 4069-4075, 1992.

[41] Vial C., Camarasa E., Poncin S., Wild G., Midoux N., & Bouillard J., "*Study of hydrodynamic behaviour in bubble columns and external loop airlift reactors through analysis of pressure fluctuations.*", Chemical engineering science, volume 55, pages 2957-2973, 2000.

[42] Jonhsson F., Zijerveld R. C., Schouten J. C., van den Bleek C. M., and Leckner B., "*Characterization of fluidization regimes by time-series analysis of pressure fluctuations.*", International journal of multiphase flow, volume 26, pages 663-715, 2000.

[43] Letzel H. M., Schouten J. C., Krisma R., van den Bleek C. M., "*Characterisation of regimes and regime transitions in bubble columns by chaos analysis of pressure signals.*", Chemical engineering science, volume 52, pages 4447-4459, 1997.

[44] Latifi M. A., Rode S., Midoux N, Storck A., "*The use of microelectrodes for the determination of flow regimes in a trickle-bed reactor.*", Chemical engineering Science, volume 47, pages 1955-1961, 1992.

[45] Brians L. A., Briens C. L., Margaritis A., Hay J., "*Minimum liquid fluidization velocity in gas-liquid-solid fluidized beds.*", American Institute of chemical engineers journal, volume 43, pages 1180-1189, 1997b.

[46] Maucci E., Briens C. L., Martinuzzi R. J., Wild G., "*Detection and characterization of piston flow regime in three-phase fluidized beds.*", Powder technology, volume 103, pages 243-259, 1999.

[47] Latifi M. A., Naderifar A., Midoux N., Le Méhauté A., "*Fractal behaviour of local liquid-solid mass transfer fluctuations at the wall of a trickle-bed reactor.*", Chemical engineering science, volume 49, pages 3823-3829, 1994b.

[48] Luewisuthichat W., Tsutsumi A., Yoshida K., "*Deterministic chaos analysis of particle dynamics in three-phase systems.*", Journal of chemical engineering of japan, volume 29, pages 675-682, 1996.

[49] Lin T. –J., Juang R., -C., Chen Y. –C., Chen C. –C., "*Predictions of flow transitions in a bubble column by chaotic time series analysis of pressure fluctuation signals.*", Chemical engineering science, volume 56, pages 1057-1065, 2001.

[50] Bakshi B. R., Zhong H., Jiang P., Fan L-S., "*Analysis of flow in gas-liquid bubble columns using multi-resolution methods.*", Transactions of the institution of chemical engineers, A: Chemical engineering research and design, volume 73, pages 608-614, 1995.

[51] Daly J. G., Patel S. A., Bukur D. B., "*Measurement of gas holdups and Sauter mean bubble diameters in bubble column reactors by dynamic gas disengagement method.*", Chemical engineering science, volume 47, pages 3647-3654, 1992.

[52] Camarasa E., Vial C., Poncin S., Wild G., Midoux N., Bouillard J., "*Influence of coalescence behaviour of the liquid and of gas sparging on hydrodynamics and bubble characteristics in a bubble column.*", Chemical engineering and processing, volume 38, pages 329-344, 1999.

[53] Lee D. j., Luo X., Fan L. –S., "*Gas disengagement technique in a slurry bubble column operated in the coalesced bubble regime.*", Chemical engineering science, volume 54, pages 2227-2236.

[54] Levespiel O., "*Chemical reaction engineering.*", (3rd edition), New York: Wiley.

[55] Shah Y. T., Stiegel G. J., Sharma M. M., "*Backmixing in gas-liquid reactors.*", American Institute of chemical engineers journal, volume 24, pages 221-259, 1978.

[56] Buffham B. A., Mason G., "*Hold-up and dispersion: Tracer residence times, moments and inventory measurements.*", Chemical engineering science, volume 48, pages 3879-3887, 1993.

[57] Blet V., Berne P., Chaussy C., Perrin S., Schweich D., "*Characterization of a packed column using radioactive tracers.*", Chemical engineering science, volume 54, pages 91-101, 1999.

[58] Pant H. J., Saroha A. K., Nigam K. D. P., "*Measurement of liquid holdup and axial dispersion in trickle bed reactors using radiotracer technique.*", Nukleonika, volume 45, pages 235-241, 2000.

[59] Sakai N., Onozaki M., Saegusa H., Ishibashi H., Hayashi T., Kobayashi M., Tachikawa N., Ishikawa I., Morooka S., "*Fluid dynamics in coal liquefaction reactors using neutron absorption tracer technique.*", American institute of chemical engineers journal, volume 46, pages 1688-1693, 2000.

[60] Larachi F., Laurent A., Wild G., Midoux N., "*Some experimental liquid saturation results in fixed-bed reactors operated under elevated pressure in cocurrent upflow and downflow of the gas and the liquid.*", Industrial and engineering chemistry research, volume 30, pages 2404-2410, 1991.

[61] Garcia Ochoa J., Khalfet R., Poncin S., Wild G., "*Hydrodynamics and mass transfer in a suspended solid bubble column with polydispersed high density particles.*", Chemical engineering science, volume 52, pages 3827-3834, 1997.

[62] Joseph S., Shah Y. T., "*Errors caused by tracer solubility in the measurement of gas phase axial dispersion.*", Canadian journal of chemical engineering, volume 64, pages 380-386, 1986.

[63] Lübbert A., "*Characterization of bioreactors."*, in H.J. Rehm, G. Reed, A. Pühler, & P. Stadler (Eds.), *Biotechnology* (2nd edition). Vol4. (pp. 107-148). Weinheim, New York: Verlag Chemie. 1991.

[64] Begovich J. M., Watson J. S., "*An electroconductivity method for the measurement of axial variation of holdups in three-phase fluidized beds.*", American institute of chemical engineers journal, volume 24, pages 351-354, 1978.

[65] Uribe-Sales A., Gomez C. O., Finch J. A., "*A conductivity technique for gas and solids holdup determination in three-phase reactors.*", Chemical engineering science, volume 49, pages 1-10, 1994.

[66] Shen G., Finch J. A., "*Bubble swarm velocity in a column.*", Chemical engineering science, volume 51, pages 3665-3674, 1996.

[67] Lage P. L. C., Espocito R. O., "*Experimental determination of bubble size distributions in bubble columns: Prediction of mean bubble diameter and gas holdup.*", Powder technology, volume 101, pages 142-150, 1999.

[68] Bendjaballah N., Dhaouadi H., Poncin S., Midoux N., Hornut J. M., Wild G., "*Hydrodynamics and flow regimes in external loop airlift reactors.*", Chemical engineering science, volume 54, pages 5211-5221, 1999.

[69] Lin T. –J., Tsuchiya K., Fan L. –S., "*Bubble flow characteristics in bubble columns at elevated pressure and temperature.*", American institute of chemical engineers journal, volume 44, pages 545-560, 1998.

[70] Heindel T. J., "*Gas flow regime changes in a bubble column filled with a fibre suspension.*", Canadian journal of chemical engineering, volume 78, pages 1017-1022, 2000.

[71] Murai Y., Song X. Q., Tagari T., Ishikawa M., Yamamoto F., Ohta J., "*Inverse energy cascade structure of turbulence in bubbly flow. PIV measurement and results.*", Japanese society of mechanical engineers international journal series B, Fluids and thermal engineering, volume 43, pages 188-196, 2000.

[72] Reese J., Muddle R. F., Lee D. J., Fan L. –S., "*Analysis of multiphase systems through particle image velocimetry.*", American institute of chemical engineers symposium series, volume 92, pages 161-167, 1996.

[73] Delnoij E., Kuipers J. A. M., van Swaaij W. P. M., Westerweel J., "*Measurement of gas-liquid two-phase flow in bubble columns using ensemble correlation PIV.*", Chemical engineering science, volume 55, pages 3385-3395, 2000.

[74] Callaghan P. T., "*Principles of nuclear magnetic resonance microscopy.*", New York: Oxford University Press, 1991.

[75] Chaouki J., Larachi F., Dudukovic M. P., "*Noninvasive tomographic and velocimetric monitoring of multiphase flows.*", Industrial and engineering chemistry research, volume 36, pages 4476-4503, 1997.

[76] Sharma S., Mantle M. D., Gladden L. F., Winterbottom J. M., "*Determination of bed voidage using water substitution and 3D magnetic resonance imaging, bed density and pressure drop in packed-bed reactors.*", Chemical engineering science, volume 56, pages 587-593, 2001.

[77] Becker S., De Bie H., Sweeney J., "*Study on the flow structure in an aerated flat apparatus using lase Doppler anemometry.*", Chemical engineering and technology, volume 23, pages 222-226, 2000.

[78] Vial C., Lainé R., Poncin S., Midoux N., Wild G., "*Influence of gas distribution and regime transition on liquid velocity and turbulence in a 3D bubble column.*", Chemical engineering science, volume 56, pages 1085-1093, 2001.

[79] Vial C., Poncin S., Wild G., Midoux N., "*A simple method for regime identification and flow characterisation in bubble columns and airlift reactors.*", Chemical engineering and processing, volume 40, pages 35-151, 2001.
[80] Reiss L. P., Hanratty T. J., "*An experimental study of the unsteady nature of the viscous sublayer.*", A.I.Ch.E. journal, volume 9, pages 154-160, 1963.
[81] Rode S., Midoux N., Latifi M. A., Storck A., "*Hydrodynamics and liquid-solid mass transfer mechanisms in packed beds operating in cocurrent gas-liquid downflow: An experimental study using electrochemical shear stress sensors.*" Chemical engineering science, volume 49, pages 1383-1401, 1994.
[82] Chen J., Kemoun A., Al-Dahhan M. H., Dudukovic M. P., Lee D. J., Fan L. –S., "*Comparative hydrodynamics study in bubble columns using computer-automated radioactive particle tracking (CARPT)/computed tomography (CT) and particle image velocimetry (PIV).*", Chemical engineering science, volume 54, pages 2199-2207, 1999.
[83] Chaouki J., Larachi F., Dudukovic M. P., "*Noninvasive tomographic and velocimetric monitoring of multiphase flows.*", Industrial and engineering chemistry research, volume 36, pages 4476-4503, 1997.
[84] Kak A. C., Slaney M., "*Computerized tomographic imaging.*", New York: IEEE press, 1987.
[85] Kumar S. B., Moslemian D., Dudukovic M. P., "*A gamma ray tomographic scanner for imaging voidage distribution in two-phase flow systems.*", Flow measurement instrumentation, volume 6, pages 61-73, 1995.
[86] Froystein T., "*Flow imaging by gamma-ray Tomography: Data processing and reconstruction techniques.*", Frontiers in industrial process tomography II, Delft, pages 8-12, 1997.
[87] Mann R., Dickin F. J., Wang M., Dyakowski T., Williams R. A., Edwards R. B., Forrest A. E., Holden P. J., "*Application of electrical resistance tomography to interrogate mixing processes at plant scale.*", Chemical engineering science, volume 52, pages 2087-2097, 1997.
[88] Schmitz D., Mewes D., "*Tomographic imaging of transient multiphase flow in bubble columns.*", Chemical engineering journal, volume 77, pages 99-104, 2000.
[89] Prasse H. –M., Böttger A., Zschau J., "*A new electrode-mesh tomography for gas-liquid flows.*", Flow measurement and instrumentation, volume 9, pages 111-119, 1998.
[90] Fraser D., Wang M., "*Electrical resistance tomography for process applications.*", Measurement science technology, volume 7, pages 247-260, 1996.
[91] Wang M., "*Inverse solutions for electrical impendance tomography based on conjugate gradients methods.*", Measurement science technology, volume 13, pages 101-117, 2001.
[92] Utiger M., Stüber F., Duquenne A. M., Delmas H., Guy C., "*Local measurements for the studey of external loop airlift hydrodynamics.*", Canadian journal of chemical engineering, colume 77, pages 375-382, 1999.
[93] Young M. A., Carbonell R. G., Ollis D. F., "*Airlift bioreactors: Analysis of local two-phase hydrodynamics.*", American institute of chemical engineers journal, volume 37, pages 403-428, 1991.
[94] Hosgett S., Ishii M., "*Local two-phase flow measurement using sensor techniques.*", Nuclear engineering and design, volume 175, pages 15-24, 1997.

[95] Menzel T., In Der Weide T., Staudacher O., Wein O., Onken U., "*Reynolds shear stress for modelling of bubble column reactors.*", Industrial and engineering chemical research, volume 29, pages 988-994, 1990.

[96] Roig V., Larrieu N., Suzanne C., "*Turbulent length scales in bubbly mixing layer.*", International symposium on two-phase flow modelling and experimentation, Rome, 1995.

[97] Bruuns H. H., "*Hot wire anemometry. Principles and signal analysis.*", New York: Oxford University Press Inc., 1995.

[98] Lance M., Bataille J., "*Turbulence in the liquid phase of a bubbly air-water flow.*", Advances in two-phase flow and heat transfer, volume 1, pages 403-427, NATO Specialist Meeting, Nato Advances Science Institute Series, West Germany, 1983.

[99] Pannek S., Pauli J., Onken U., "*Determination of local hydrodynamicparameters in bubble columns by the electrodiffusion method with oxygen as depolarizer.*", Journal of applied electrochemistry, volume 24, pages 666-669, 1994.

[100] Pauli J., Onken U., Sobolik V., "*Electrodiffusional direction-specific probe for measuring local velocity of aerated aqueous systems.*", Journal of applied electrochemistry, volume 21, pages 1073-1076, 1991.

[101] Mitchell J. E., Harnatty T. J., "*A study of turbulence at a wall using an electrochemical wall shear stress meter.*", Journal of fluid mechanics, volume 26, pages 199-221, 1966.

[102] Bröring F. J., Fischer J., Korte T., Sollinger S., Lübbert A., "*Flow structure of the dispersed gasphase in real multiphase chemical reactors investigated by a new ultrasound-Doppler technique.*", Canadian journal of chemical engineering, volume 69, pages 1247-1256, 1991.

[103] Bouillard J., Alban B., Jacques P., Xuereb C., "*Liquid flow velocity measurements in stirred tanks by ultra-sound Doppler velocimetry.*", Chemical engineering Science, volume 56, pages 747-754, 2001.

[104] Stravs A. A., von Stockar U., "*Measurement of interfacial areas in gas-liquid dispersions by ultrasonic pulse transmission.*", Chemical engineering science, volume 40, pages 1169-1175, 1985.

[105] Stravs A. A., Wahl J., von Stokar U., Reilly P. J., "*Development of ultrasonic pulse reflection method for measuring relative size distributions of air bubbles inaqueous solutions.*", Chemical engineering science, volume 42, pages 1677-1987, 1987.

[106] Nicol R. S., Davidson J. F., "*Gas holdup in circulating bubble columns.*", Transactions of the institute of chemical engineer, A: Chemical engineering research and design, volume 68, pages 13-21, 1988.

[107] Groen J .S., Mudde R. F., van den Akker H. E. A., "*Time dependant behaviour of the flow in a bubble column.*", Transactions of the institute of chemical engineer, A: Chemical engineering research and design, volume 73, pages 615-620, 1995.

[108] Chabot J., Farag H., De Lasa H., "*Fluid dynamics of bubble columns at elevated temperature modelling and investigation with refractive fibre optic sensor.*", The chemical engineering journal, volume 70, pages 105-113, 1998.

[109] Burgess J. M., Caldebank P. H., "*The measurement of bubble parameters in two-phase dispersions-I: The development of an improved probe technique.*", Chemical engineering science, volume 30, pages 743-750, 1975.

[110] Jürgen Steinmann, Rainer Buchholz, "*Application of an electrical conductivity microprobe for the characterization of bubble behaviour in gas-liquid bubble flow.*", Verlag Chemie GmbH, d-6940 Weinheim, pages 102-107, 1984.

[111] Saito Y., Mishima K., Tobita Y., Suzuki T., Matsubayashi M., "*Measurements of liquid-metal two-phase flow by using neutron radiography and electrical conductivity probe.*", Experimental thermal and fluid science, xx, xxxx, 2004.

[112] Ishii M., Kim S., "*Micro four-sensor probe measurement of interfacial area transport for bubbly flow in round pipes.*", Nuclear engineering and design, volume 205, pages 123-131, 2001.

[113] Kim S., Fu X. Y., Wang X., Ishii M., "*Development of the miniaturised four-sensor conductivity probe and the signal processing scheme.*", International journal of heat and mass transfer, volume 43, pages 4101-4118, 2000.

[114] Steinemann J., Buchholz R., "*Application of an electrical conductivity microprobe for the characterization of bubble behaviour in gas-liquid bubble flow.*", Part. Charct. 1, pages 102-107, 1984.

[115] Wu Q., Welter K., McCreary D., Reyes J. N., "*Theoretical studies on the design criteria of double-sensor probe for the measurement of bubble velocity.*", J. Flow Meas. Instrum., volume 12 (issue 1), pages 43-51, 2001.

[116] John Parry Lewis, Alsdair Trail, "*Statistics explained.*", Addison-Wesley, pages 95-98, 1999.

[117] Liu T. –J., "*An effective signal processing method for resistivity probe measurements in a two phase bubbly flow.*", Meas. Sci. Technol., volume 13, pages 206-217, 2002.

[118] Mishra R., Lucas G. P., Kieckhoefer H., "*A model for obtaining the velocity vectors of spherical droplets in multiphase flows from measurements using an orthogonal four-sensor probe.*", Meas. Sci. Technol, volume 13, pages 1488-1498, 2002.

[119] Lucas G. P., Mishra R., "*Measurement of bubble velocity components in a swirling gas-liquid pipe flow using a local four-sensor conductance probe.*", Meas. Sci. Technol., volume 16, pages 749-758, 2004.

[120] Lucas G. P., Jin N. D., "*Measurement of the homogeneous velocity of inclined oi-in-water flows using a resistance cross correlation flow meter.*", Meas. Sci. Technol., volume 12, pages 1529-1536, 2001.

[121] M. L. Mathur, "*A new design of vanes for swirl generation.*", IE(I) Journal ME, volume 55, pages 93-96, 1974.

[122] Fraser Dickin and Mi Wang, "*Electrical resistance tomography for process applications.*", Meas. Sci. Technol., volume 7, pages 247-260, 1996.

[123] J. R. Grace and D. Harrison, "*The influence of bubble shape on the rising velocities of large bubbles*", Chemical Eng. Science, vol. 22, pages 1337-1347, 1967.

[124] J. R. Crabtree and J. Bridgwater, "*Bubble coalescence in viscous liquids*", Chemical Eng. Science, vol. 26, pages 839-851, 1970.

[125] Moshe Favelukis, Cam Hung Ly, "*Unsteady mass transfer around spheroidal drops in potential flow*", Chemical Eng. Science, vol. 60, pages 7011-7021, 2005.

[126] Sergio Bordel, Rafael Mato, Santiago Villaverbe, "*Modeling of the evolution with length of bubble size distributions in bubble column*", Chemical Eng. Science, vol. 61, pages 3663-3673, 2006.

[127] Salese A., Larue de Tournemine A., Roig V., "*Development of bubble cluster detection and identification method.*", Fifth world conference on experimental

heat transfer, fluid mechanics and thermodynamics, Thessaloniki, Greece, pages 24-28, September 2001.

[128] Van der Welle R 1985 "*Void fraction, bubble velocity and bubble size in two phase flow Int. J. Multiphase Flow.*" **11** 317-345

[129] G. P. Lucas, R. Mishra and N. Panayotopoulos, "*Volume Fraction and Velocity Profile Measurement in Low Void Fraction Gas-Liquid Flows using a Dual-Sensor Conductance Probe*", Journal of **Flow Measurement and Instrumentation** Volume 15, Issues 5-6 , October-December 2004, Pages 271-283.

[130] G. P. Lucas, M. Wang, R. Mishra, Y Dai and N. Panayotopoulos, "*Quantitative comparison of gas velocity and volume fraction profiles obtained from a dual-plane ERT system with profiles obtained from a local dual-sensor conductance probe, in a bubbly gas-liquid flow*", Conference on Tomography, Lodz, Poland, September 2004.

[131] Beck and Plaskowski Cross correlation Flow Meters.

[132] Hibiki T and Ishii M, "*Distribution parameter and drift velocity of drift-flux model in bubbly flow*", Int. J. Heat and Mass Transfer, **5**, (2001), 707-721.

[133] Lucas G P, "*Modelling velocity profiles in inclined multiphase flows to provide a priori information for flow imaging*", The Chemical Engineering Journal **56** (1995) 167-173.

[134] Beyerlein S W, Cossmann R K and Richter H J, "*Prediction of bubble concentration profiles in vertical turbulent two-phase flow.*" Int. J. Multiphase Flow, **11**, Issue 5, (1985), 629-641.

[135] Brennen C E, fundamentals of multiphase flow, (2005) Cambridge University Press.

[136] F A Hamad, F Imberton and H H Bruun, "*An optical probe for measurements in liquid - liquid two-phase flow*", 1997 *Meas. Sci. Technol.* **8** 1122-1132.

[137] MiWang, Gary Lucas, YunfengDai, Nikolaos Panayotopoulos ,RichardAWilliams, "*Visualisation of Bubbly Velocity Distribution in a Swirling Flow using Electrical Resistance Tomography*", Part. Part. Syst. Charact. *23* (2006) 321–329.

[138] M. Wang, Inverse Solutions for Electrical ImpedanceTomography Based on Conjugate Gradients Methods,*Meas. Sci. Technol.*, IOP, **2000**, *13*, 101–117.

[139] G.P. Lucas and N. Panagiotopoulos, "*Measurement of oil volume fraction and velocity profiles in vertical, bubbly oil-in-water flows*", **Flow Measurement and Instrumentation** Volume 15, Issues 5-6, October-December 2004, Pages 271-283.

[140] http://www.grc.nasa.gov/WWW/K-12/airplane/pitot.html, January 2009.

[141] **King, L V** "*On the Convection of Heat From Small Cylinders in a Stream of Fluid: Determination of the Convection Constants of Small Platinum Wires, with Applications to Hot-wire Anemometry*" . Proc. R. Soc. London (1914), Vol 90, pp 563-570.

APENDICES

APPENDIX I

Software for controlling DAQ2006 and acquiring data.

```
Dim tempstring As String
Dim Voltage_Range As Integer, Card_Number As Integer
Dim box As Integer, result As Integer, temp_channel As Integer
Dim Number_of_channels As Integer, tempint As Integer
Dim Sampling_frequency As Long, Sampling_Time As Long
Dim Data_pathway As String, Total_number_samples As Long
Dim Total_number_of_bytes As Long, Scan_Interval As Long
Dim Number_of_points As Integer, Number_of_diameters As Integer
Dim Total_number_of_all_data As Double
Dim Traverse_check As Boolean
Dim Number_of_points_at_boundary As Integer
Dim Vmax As Single, Vmin As Single
Dim Ymax As Single, Ymin As Single
Dim X0 As Long, Xmax As Long, Number_of_samples_on_screen As Long
Dim Voltage_array() As Double
Dim Buffer1() As Integer, Buffer2() As Integer
Dim Buffer_index As Integer, Buffer_size As Long
Dim Samples_per_buffer As Long
Dim Stop_async As Byte, Access_count As Long
Dim Channels() As Integer, temp_time As Long
Dim T1 As Double, T2 As Double, DT As Double
```

Private Sub Acquire_Data_Command_Click()

```
Set_up_DAQ_Command.Enabled = False
Restart_Command.Enabled = False
Acquire_data_Command.Enabled = False
Four_Sensor_probe_app_Command.Enabled = False
Exit_Acquire_Command.Enabled = False

If (Traverse_mechanism_Check.Value = 0) Then

   ReDim Voltage_array(Number_of_channels)

   'For temp = 1 To Number_of_channels
   '    Channels(temp) = temp
   'Next temp
'For temp_time = (Sampling_Time - 1) To 0 Step -1

'    Sampling_time_Label1.Caption = Str$(temp_time)
   Buffer_size = Number_of_channels * 16
   ReDim Buffer1(Buffer_size) '(Samples_per_buffer)

   result = D2K_AI_AsyncDblBufferMode(Card_Number, 0)
   If (result < 0) Then
      tempstring = Str$(result)
      Error_messages_Label.Caption = tempstring
      Current_status_Label.Caption = "Error in setting D2K_AI_AsyncDblBufferMode()
function"
   Else
      result = D2K_AI_ContBufferSetup(Card_Number, Buffer1(0), Buffer_size, Buffer_index)
      If (result < 0) Then
         tempstring = Str$(result)
         Error_messages_Label.Caption = tempstring
```

```
        Current_status_Label.Caption = "Error in D2K_AI_ContBufferSetup() function"
      Else
        temp_channel = Number_of_channels - 1
        Read_scans = Buffer_size / Number_of_channels
        temp_time = Sampling_Time - 1
        While (temp_time > 0)
          T1 = Timer
          result = D2K_AI_ContScanChannels(Card_Number, temp_channel, Buffer_index,
Read_scans, Scan_Interval, 0, 0) 'ASYNCH_OP)
          'result = D2K_AI_SimuReadChannel(Card_Number, Number_of_channels,
Channels(), Buffer1())
          If (result < 0) Then
            tempstring = Str$(result)
            Error_messages_Label.Caption = tempstring
            Current_status_Label.Caption = "Error in D2K_AI_ContScanChannels()
function!"
          Else
            'Current_status_Label.Caption = Str$(Buffer1(1))
            For dummy = 0 To Number_of_channels
              result = D2K_AI_VoltScale(Card_Number, Voltage_Range, Buffer1(dummy),
Voltage_array(dummy))
            Next dummy
            Current_status_Label.Caption = Str$(Voltage_array(1))
            Stop_async = 0
            While (Stop_async = 0)
              result = D2K_AI_AsyncCheck(Card_Number, Stop_async, Access_count)
            Wend
            result = D2K_AI_AsyncClear(Card_Number, 0, Access_count)
          End If
          T2 = Timer
          DT = T2 - T1
          temp_time = temp_time - DT
          Sampling_time_Label1.Caption = Str$(temp_time)
        Wend
      End If
    End If
  '  Next temp_time
Else
    Current_status_Label.Caption = "Wrong Button pressed. Traverse mechanism checkbox is
checked!"
End If

result = D2K_AI_ContBufferReset(Card_Number)
Set_up_DAQ_Command.Enabled = False
Restart_Command.Enabled = True
Acquire_data_Command.Enabled = True
Four_Sensor_probe_app_Command.Enabled = True
Exit_Acquire_Command.Enabled = True
End Sub

Private Sub EXIT_ACQUIRE_Command_Click()
result = D2K_Release_Card(ByVal Card_Number)
ACQUIRE_FORM.Visible = False
ACQUIRE_FORM.Enabled = False

DacProc_Form.Enabled = True
DacProc_Form.Visible = True

End Sub
```

```
Private Sub Form_Load()
Restart_Command.Enabled = False
Set_up_DAQ_Command.Enabled = True
Exit_Acquire_Command.Enabled = True
Acquire_data_Command.Enabled = False
Four_Sensor_probe_app_Command.Enabled = False

End Sub

Private Sub Restart_Command_Click()
result = D2K_Release_Card(ByVal Card_Number)
If (result < 0) Then
   tempstring = Str$(result)
   Error_messages_Label.Caption = tempstring
   Current_status_Label.Caption = "Error in releasing DAQ 2006"
Else
   Current_status_Label.Caption = "DAQ 2006 has been released"
End If
Set_up_DAQ_Command.Enabled = True
Restart_Command.Enabled = False
Point_number_Label.Caption = "0"
Size_of_data_file_Label.Caption = "0"
Sampling_time_Label1.Caption = "0"
Acquire_data_Command.Enabled = False
Four_Sensor_probe_app_Command.Enabled = False

End Sub

Private Sub Set_up_DAQ_Command_Click()
Card_Number = D2K_Register_Card(DAQ_2006, 0)
tempstring = Str$(Card_Number)
Error_messages_Label.Caption = tempstring
If (Card_Number < 0) Then
   box = MsgBox("Error registering the card!", vbOKOnly, "Error")
   tempstring = Str$(Card_Number)
   Error_messages_Label.Caption = tempstring
Else
   tempstring = Voltage_Range_Combo.Text
   If (tempstring = "+-10Volts") Then
      Voltage_Range = AD_B_10_V
      Vmax = 10
      Vmin = -10
   ElseIf (tempstring = "+-5Volts") Then
      Voltage_Range = AD_B_5_V
      Vmax = 5
      Vmin = -5
   ElseIf (tempstring = "+-2.5Volts") Then
      Voltage_Range = AD_B_2_5_V
      Vmax = 2.5
      Vmin = -2.5
   ElseIf (tempstring = "+-1.25Volts") Then
      Voltage_Range = AD_B_1_25_V
      Vmax = 1.25
      Vmin = -1.25
   ElseIf (tempstring = "+5Volts") Then
      Voltage_Range = AD_U_5_V
      Vmax = 5
      Vmin = 0
   ElseIf (tempstring = "+10Volts") Then
      Voltage_Range = AD_U_10_V
```

```
      Vmax = 10
      Vmin = 0
   ElseIf (tempstring = "+2.5Volts") Then
      Voltage_Range = AD_U_2_5_V
      Vmax = 2.5
      Vmin = 0
   ElseIf (tempstring = "+1.25Volts") Then
      Voltage_Range = AD_U_1_25_V
      Vmax = 1.25
      Vmin = 0
   Else
      Voltage_Range = AD_B_10_V
      Vmax = 10
      Vmin = -10
   End If
   Number_of_channels = Number_of_channels_Text.Text
   For tempint = 0 To (Number_of_channels - 1)
      result = D2K_AI_CH_Config(ByVal Card_Number, ByVal tempint, ByVal
Voltage_Range)
   Next tempint
   If (result < 0) Then
      box = MsgBox("Error configuring the card!", vbOKOnly, "Error")
      tempstring = Str$(result)
      Error_messages_Label.Caption = tempstring
   Else
      result = D2K_AI_Config(ByVal Card_Number, DAQ2K_AI_ADCONVSRC_Int, ByVal
DAK2K_AI_TRGMOD_POST Or DAQ2K_AI_TrgPositive Or DAQ2K_AI_TRGSRC, 0, 0, 0, 1)
      tempstring = Str$(result)
      Error_messages_Label.Caption = tempstring
      If (result < 0) Then
         box = MsgBox("Error in AI configuration!", vbOKOnly, "Error")
         tempstring = Str$(result)
         Error_messages_Label.Caption = tempstring
      Else
         Number_of_points = Number_of_points_Text.Text
         Number_of_diameters = Number_of_diameters_Text.Text
         Sampling_frequency = Sampling_frequency_Text.Text
         Sampling_Time = Sampling_Time_Text.Text
         Data_pathway = Data_Pathway_Text.Text
         Scan_Interval = 40000000 / Sampling_frequency
         Number_of_points_at_boundary = Number_of_points_at_boundary_Text.Text
         Total_number_of_samples = Sampling_frequency * Sampling_Time *
Number_of_channels
         Total_number_of_bytes = Total_number_of_samples * 2
         tempstring = Str$(Total_number_of_bytes)
         Size_of_data_file_Label.Caption = tempstring
         If (Traverse_mechanism_Check.Value = 1) Then
            Traverse_check = True
         Else
            Traverse_check = False
         End If
         Samples_per_buffer = Sampling_ferquency * Number_of_channels
         Current_status_Label.Caption = "DAQ 2006 has been successfully set up."
      End If
   End If
End If

Set_up_DAQ_Command.Enabled = False
Restart_Command.Enabled = True
Acquire_data_Command.Enabled = True
```

```
Four_Sensor_probe_app_Command.Enabled = True
Call Set_up_sensor_screens
Current_status_Label.Caption = "DAQ 2006 is ready and screens have been adjusted."
End Sub


Private Sub Set_up_sensor_screens()
X0 = 0
Number_of_samples_on_screen = Sampling_frequency
Xmax = Number_of_samples_on_screen
Ymax = Vmax
Ymin = Vmin

sensor1_screen.Scale (X0, Ymin)-(Xmax, Ymax)
sensor2_screen.Scale (X0, Ymin)-(Xmax, Ymax)
sensor3_screen.Scale (X0, Ymin)-(Xmax, Ymax)
sensor4_screen.Scale (X0, Ymin)-(Xmax, Ymax)

End Sub
```

APPENDIX II

The following files were used in the analysis of dual sensor data in air and oil water flows:

- Thresnew.m
- Thres_gdn1.m
- Scan_stream.m
- Get_time_of_contact.m
- Find_pairs.m
- Thdplotnewvel.m
- Thdplotnewvol.m
- Volint88new.m.

Thresnew.m

```
% program using thres_gdn1 as sobroutine
function[]=thresnew();
period=30;
fs=3750;
s=2000;
dt1max=0.05;
Dvnf=1.0
Dvrf=0.5
Dvnr=1.0
Dvrr=0.5
M=load('datad001.dat');
[v_mean,dtn_mean,NoB_1f,alpha_f,NoB_1r,alpha_r,NoB_2]=thres_gdn1(peri
od,fs,s,dt1max,Dvnf,Dvrf,Dvnr,Dvrr,M);
save v_meanres1.dat v_mean  -ascii -double;
save alphres1.dat NoB_1f alpha_f NoB_1r alpha_r NoB_2 -ascii -double;
M=load('datad002.dat');
[v_mean,dtn_mean,NoB_1f,alpha_f,NoB_1r,alpha_r,NoB_2]=thres_gdn1(peri
od,fs,s,dt1max,Dvnf,Dvrf,Dvnr,Dvrr,M);
save v_meanres2.dat v_mean  -ascii -double;
save alphres2.dat NoB_1f alpha_f NoB_1r alpha_r NoB_2 -ascii -double;
M=load('datad003.dat');
[v_mean,dtn_mean,NoB_1f,alpha_f,NoB_1r,alpha_r,NoB_2]=thres_gdn1(peri
od,fs,s,dt1max,Dvnf,Dvrf,Dvnr,Dvrr,M);
save v_meanres3.dat v_mean  -ascii -double;
save alphres3.dat NoB_1f alpha_f NoB_1r alpha_r NoB_2 -ascii -double;
M=load('datad004.dat');
[v_mean,dtn_mean,NoB_1f,alpha_f,NoB_1r,alpha_r,NoB_2]=thres_gdn1(peri
od,fs,s,dt1max,Dvnf,Dvrf,Dvnr,Dvrr,M);
save v_meanres4.dat v_mean  -ascii -double;
save alphres4.dat NoB_1f alpha_f NoB_1r alpha_r NoB_2 -ascii -double;
M=load('datad005.dat');
```

```
[v_mean,dtn_mean,NoB_1f,alpha_f,NoB_1r,alpha_r,NoB_2]=thres_gdn1(peri
od,fs,s,dt1max,Dvnf,Dvrf,Dvnr,Dvrr,M);
save v_meanres5.dat v_mean  -ascii -double;
save alphres5.dat NoB_1f alpha_f NoB_1r alpha_r NoB_2 -ascii -double;
M=load('datad006.dat');
[v_mean,dtn_mean,NoB_1f,alpha_f,NoB_1r,alpha_r,NoB_2]=thres_gdn1(peri
od,fs,s,dt1max,Dvnf,Dvrf,Dvnr,Dvrr,M);
save v_meanres6.dat v_mean  -ascii -double;
save alphres6.dat NoB_1f alpha_f NoB_1r alpha_r NoB_2 -ascii -double;
M=load('datad007.dat');
[v_mean,dtn_mean,NoB_1f,alpha_f,NoB_1r,alpha_r,NoB_2]=thres_gdn1(peri
od,fs,s,dt1max,Dvnf,Dvrf,Dvnr,Dvrr,M);
save v_meanres7.dat v_mean  -ascii -double;
save alphres7.dat NoB_1f alpha_f NoB_1r alpha_r NoB_2 -ascii -double;
M=load('datad008.dat');
[v_mean,dtn_mean,NoB_1f,alpha_f,NoB_1r,alpha_r,NoB_2]=thres_gdn1(peri
od,fs,s,dt1max,Dvnf,Dvrf,Dvnr,Dvrr,M);
save v_meanres8.dat v_mean  -ascii -double;
save alphres8.dat NoB_1f alpha_f NoB_1r alpha_r NoB_2 -ascii -double;
M=load('datad009.dat');
[v_mean,dtn_mean,NoB_1f,alpha_f,NoB_1r,alpha_r,NoB_2]=thres_gdn1(peri
od,fs,s,dt1max,Dvnf,Dvrf,Dvnr,Dvrr,M);
save v_meanres9.dat v_mean -ascii -double;
save alphres9.dat NoB_1f alpha_f NoB_1r alpha_r NoB_2 -ascii -double;
M=load('datad010.dat');
[v_mean,dtn_mean,NoB_1f,alpha_f,NoB_1r,alpha_r,NoB_2]=thres_gdn1(peri
od,fs,s,dt1max,Dvnf,Dvrf,Dvnr,Dvrr,M);
save v_meanres10.dat v_mean -ascii -double;
save alphres10.dat NoB_1f alpha_f NoB_1r alpha_r NoB_2 -ascii -
double;
M=load('datad011.dat');
[v_mean,dtn_mean,NoB_1f,alpha_f,NoB_1r,alpha_r,NoB_2]=thres_gdn1(peri
od,fs,s,dt1max,Dvnf,Dvrf,Dvnr,Dvrr,M);
save v_meanres11.dat v_mean -ascii -double;
save alphres11.dat NoB_1f alpha_f NoB_1r alpha_r NoB_2 -ascii -
double;
M=load('datad012.dat');
[v_mean,dtn_mean,NoB_1f,alpha_f,NoB_1r,alpha_r,NoB_2]=thres_gdn1(peri
od,fs,s,dt1max,Dvnf,Dvrf,Dvnr,Dvrr,M);
save v_meanres12.dat v_mean -ascii -double;
save alphres12.dat NoB_1f alpha_f NoB_1r alpha_r NoB_2 -ascii -
double;
M=load('datad013.dat');
[v_mean,dtn_mean,NoB_1f,alpha_f,NoB_1r,alpha_r,NoB_2]=thres_gdn1(peri
od,fs,s,dt1max,Dvnf,Dvrf,Dvnr,Dvrr,M);
save v_meanres13.dat v_mean -ascii -double;
save alphres13.dat NoB_1f alpha_f NoB_1r alpha_r NoB_2 -ascii -
double;
M=load('datad014.dat');
[v_mean,dtn_mean,NoB_1f,alpha_f,NoB_1r,alpha_r,NoB_2]=thres_gdn1(peri
od,fs,s,dt1max,Dvnf,Dvrf,Dvnr,Dvrr,M);
save v_meanres14.dat v_mean -ascii -double;
save alphres14.dat NoB_1f alpha_f NoB_1r alpha_r NoB_2 -ascii -
double;
M=load('datad015.dat');
[v_mean,dtn_mean,NoB_1f,alpha_f,NoB_1r,alpha_r,NoB_2]=thres_gdn1(peri
od,fs,s,dt1max,Dvnf,Dvrf,Dvnr,Dvrr,M);
save v_meanres15.dat v_mean -ascii -double;
save alphres15.dat NoB_1f alpha_f NoB_1r alpha_r NoB_2 -ascii -
double;
M=load('datad016.dat');
```

```
[v_mean,dtn_mean,NoB_1f,alpha_f,NoB_1r,alpha_r,NoB_2]=thres_gdn1(peri
od,fs,s,dt1max,Dvnf,Dvrf,Dvnr,Dvrr,M);
save v_meanres16.dat v_mean -ascii -double;
save alphres16.dat NoB_1f alpha_f NoB_1r alpha_r NoB_2 -ascii -
double;
M=load('datad017.dat');
[v_mean,dtn_mean,NoB_1f,alpha_f,NoB_1r,alpha_r,NoB_2]=thres_gdn1(peri
od,fs,s,dt1max,Dvnf,Dvrf,Dvnr,Dvrr,M);
save v_meanres17.dat v_mean -ascii -double;
save alphres17.dat NoB_1f alpha_f NoB_1r alpha_r NoB_2 -ascii -
double;
M=load('datad018.dat');
[v_mean,dtn_mean,NoB_1f,alpha_f,NoB_1r,alpha_r,NoB_2]=thres_gdn1(peri
od,fs,s,dt1max,Dvnf,Dvrf,Dvnr,Dvrr,M);
save v_meanres18.dat v_mean -ascii -double;
save alphres18.dat NoB_1f alpha_f NoB_1r alpha_r NoB_2 -ascii -
double;
M=load('datad019.dat');
[v_mean,dtn_mean,NoB_1f,alpha_f,NoB_1r,alpha_r,NoB_2]=thres_gdn1(peri
od,fs,s,dt1max,Dvnf,Dvrf,Dvnr,Dvrr,M);
save v_meanres19.dat v_mean -ascii -double;
save alphres19.dat NoB_1f alpha_f NoB_1r alpha_r NoB_2 -ascii -
double;
M=load('datad020.dat');
[v_mean,dtn_mean,NoB_1f,alpha_f,NoB_1r,alpha_r,NoB_2]=thres_gdn1(peri
od,fs,s,dt1max,Dvnf,Dvrf,Dvnr,Dvrr,M);
save v_meanres20.dat v_mean -ascii -double;
save alphres20.dat NoB_1f alpha_f NoB_1r alpha_r NoB_2 -ascii -
double;
M=load('datad021.dat');
[v_mean,dtn_mean,NoB_1f,alpha_f,NoB_1r,alpha_r,NoB_2]=thres_gdn1(peri
od,fs,s,dt1max,Dvnf,Dvrf,Dvnr,Dvrr,M);
save v_meanres21.dat v_mean -ascii -double;
save alphres21.dat NoB_1f alpha_f NoB_1r alpha_r NoB_2 -ascii -
double;
M=load('datad022.dat');
[v_mean,dtn_mean,NoB_1f,alpha_f,NoB_1r,alpha_r,NoB_2]=thres_gdn1(peri
od,fs,s,dt1max,Dvnf,Dvrf,Dvnr,Dvrr,M);
save v_meanres22.dat v_mean  -ascii -double;
save alphres22.dat NoB_1f alpha_f NoB_1r alpha_r NoB_2 -ascii -
double;
M=load('datad023.dat');
[v_mean,dtn_mean,NoB_1f,alpha_f,NoB_1r,alpha_r,NoB_2]=thres_gdn1(peri
od,fs,s,dt1max,Dvnf,Dvrf,Dvnr,Dvrr,M);
save v_meanres23.dat v_mean -ascii -double;
save alphres23.dat NoB_1f alpha_f NoB_1r alpha_r NoB_2 -ascii -
double;
M=load('datad024.dat');
[v_mean,dtn_mean,NoB_1f,alpha_f,NoB_1r,alpha_r,NoB_2]=thres_gdn1(peri
od,fs,s,dt1max,Dvnf,Dvrf,Dvnr,Dvrr,M);
save v_meanres24.dat v_mean -ascii -double;
save alphres24.dat NoB_1f alpha_f NoB_1r alpha_r NoB_2 -ascii -
double;
M=load('datad025.dat');
[v_mean,dtn_mean,NoB_1f,alpha_f,NoB_1r,alpha_r,NoB_2]=thres_gdn1(peri
od,fs,s,dt1max,Dvnf,Dvrf,Dvnr,Dvrr,M);
save v_meanres25.dat v_mean -ascii -double;
save alphres25.dat NoB_1f alpha_f NoB_1r alpha_r NoB_2 -ascii -
double;
M=load('datad026.dat');
```

```
[v_mean,dtn_mean,NoB_1f,alpha_f,NoB_1r,alpha_r,NoB_2]=thres_gdn1(peri
od,fs,s,dt1max,Dvnf,Dvrf,Dvnr,Dvrr,M);
save v_meanres26.dat v_mean -ascii -double;
save alphres26.dat NoB_1f alpha_f NoB_1r alpha_r NoB_2 -ascii -
double;
M=load('datad027.dat');
[v_mean,dtn_mean,NoB_1f,alpha_f,NoB_1r,alpha_r,NoB_2]=thres_gdn1(peri
od,fs,s,dt1max,Dvnf,Dvrf,Dvnr,Dvrr,M);
save v_meanres27.dat v_mean  -ascii -double;
save alphres27.dat NoB_1f alpha_f NoB_1r alpha_r NoB_2 -ascii -
double;
M=load('datad028.dat');
[v_mean,dtn_mean,NoB_1f,alpha_f,NoB_1r,alpha_r,NoB_2]=thres_gdn1(peri
od,fs,s,dt1max,Dvnf,Dvrf,Dvnr,Dvrr,M);
save v_meanres28.dat v_mean  -ascii -double;
save alphres28.dat NoB_1f alpha_f NoB_1r alpha_r NoB_2 -ascii -
double;
M=load('datad029.dat');
[v_mean,dtn_mean,NoB_1f,alpha_f,NoB_1r,alpha_r,NoB_2]=thres_gdn1(peri
od,fs,s,dt1max,Dvnf,Dvrf,Dvnr,Dvrr,M);
save v_meanres29.dat v_mean -ascii -double;
save alphres29.dat NoB_1f alpha_f NoB_1r alpha_r NoB_2 -ascii -
double;
M=load('datad030.dat');
[v_mean,dtn_mean,NoB_1f,alpha_f,NoB_1r,alpha_r,NoB_2]=thres_gdn1(peri
od,fs,s,dt1max,Dvnf,Dvrf,Dvnr,Dvrr,M);
save v_meanres30.dat v_mean -ascii -double;
save alphres30.dat NoB_1f alpha_f NoB_1r alpha_r NoB_2 -ascii -
double;
M=load('datad031.dat');
[v_mean,dtn_mean,NoB_1f,alpha_f,NoB_1r,alpha_r,NoB_2]=thres_gdn1(peri
od,fs,s,dt1max,Dvnf,Dvrf,Dvnr,Dvrr,M);
save v_meanres31.dat v_mean  -ascii -double;
save alphres31.dat NoB_1f alpha_f NoB_1r alpha_r NoB_2 -ascii -
double;
M=load('datad032.dat');
[v_mean,dtn_mean,NoB_1f,alpha_f,NoB_1r,alpha_r,NoB_2]=thres_gdn1(peri
od,fs,s,dt1max,Dvnf,Dvrf,Dvnr,Dvrr,M);
save v_meanres32.dat v_mean  -ascii -double;
save alphres32.dat NoB_1f alpha_f NoB_1r alpha_r NoB_2 -ascii -
double;
M=load('datad033.dat');
[v_mean,dtn_mean,NoB_1f,alpha_f,NoB_1r,alpha_r,NoB_2]=thres_gdn1(peri
od,fs,s,dt1max,Dvnf,Dvrf,Dvnr,Dvrr,M);
save v_meanres33.dat v_mean  -ascii -double;
save alphres33.dat NoB_1f alpha_f NoB_1r alpha_r NoB_2 -ascii -
double;
M=load('datad034.dat');
[v_mean,dtn_mean,NoB_1f,alpha_f,NoB_1r,alpha_r,NoB_2]=thres_gdn1(peri
od,fs,s,dt1max,Dvnf,Dvrf,Dvnr,Dvrr,M);
save v_meanres34.dat v_mean  -ascii -double;
save alphres34.dat NoB_1f alpha_f NoB_1r alpha_r NoB_2 -ascii -
double;
M=load('datad035.dat');
[v_mean,dtn_mean,NoB_1f,alpha_f,NoB_1r,alpha_r,NoB_2]=thres_gdn1(peri
od,fs,s,dt1max,Dvnf,Dvrf,Dvnr,Dvrr,M);
save v_meanres35.dat v_mean  -ascii -double;
save alphres35.dat NoB_1f alpha_f NoB_1r alpha_r NoB_2 -ascii -
double;
M=load('datad036.dat');
```

```
[v_mean,dtn_mean,NoB_1f,alpha_f,NoB_1r,alpha_r,NoB_2]=thres_gdn1(peri
od,fs,s,dt1max,Dvnf,Dvrf,Dvnr,Dvrr,M);
save v_meanres36.dat v_mean  -ascii -double;
save alphres36.dat NoB_1f alpha_f NoB_1r alpha_r NoB_2 -ascii -
double;

M=load('datad037.dat');
[v_mean,dtn_mean,NoB_1f,alpha_f,NoB_1r,alpha_r,NoB_2]=thres_gdn1(peri
od,fs,s,dt1max,Dvnf,Dvrf,Dvnr,Dvrr,M);
save v_meanres37.dat v_mean  -ascii -double;
save alphres37.dat NoB_1f alpha_f NoB_1r alpha_r NoB_2 -ascii -
double;

M=load('datad038.dat');
[v_mean,dtn_mean,NoB_1f,alpha_f,NoB_1r,alpha_r,NoB_2]=thres_gdn1(peri
od,fs,s,dt1max,Dvnf,Dvrf,Dvnr,Dvrr,M);
save v_meanres38.dat v_mean  -ascii -double;
save alphres38.dat NoB_1f alpha_f NoB_1r alpha_r NoB_2 -ascii -
double;

M=load('datad039.dat');
[v_mean,dtn_mean,NoB_1f,alpha_f,NoB_1r,alpha_r,NoB_2]=thres_gdn1(peri
od,fs,s,dt1max,Dvnf,Dvrf,Dvnr,Dvrr,M);
save v_meanres39.dat v_mean  -ascii -double;
save alphres39.dat NoB_1f alpha_f NoB_1r alpha_r NoB_2 -ascii -
double;

M=load('datad040.dat');
[v_mean,dtn_mean,NoB_1f,alpha_f,NoB_1r,alpha_r,NoB_2]=thres_gdn1(peri
od,fs,s,dt1max,Dvnf,Dvrf,Dvnr,Dvrr,M);
save v_meanres40.dat v_mean  -ascii -double;
save alphres40.dat NoB_1f alpha_f NoB_1r alpha_r NoB_2 -ascii -
double;

M=load('datad041.dat');
[v_mean,dtn_mean,NoB_1f,alpha_f,NoB_1r,alpha_r,NoB_2]=thres_gdn1(peri
od,fs,s,dt1max,Dvnf,Dvrf,Dvnr,Dvrr,M);
save v_meanres41.dat v_mean  -ascii -double;
save alphres41.dat NoB_1f alpha_f NoB_1r alpha_r NoB_2 -ascii -
double;

M=load('datad042.dat');
[v_mean,dtn_mean,NoB_1f,alpha_f,NoB_1r,alpha_r,NoB_2]=thres_gdn1(peri
od,fs,s,dt1max,Dvnf,Dvrf,Dvnr,Dvrr,M);
save v_meanres42.dat v_mean  -ascii -double;
save alphres42.dat NoB_1f alpha_f NoB_1r alpha_r NoB_2 -ascii -
double;

M=load('datad043.dat');
[v_mean,dtn_mean,NoB_1f,alpha_f,NoB_1r,alpha_r,NoB_2]=thres_gdn1(peri
od,fs,s,dt1max,Dvnf,Dvrf,Dvnr,Dvrr,M);
save v_meanres43.dat v_mean  -ascii -double;
save alphres43.dat NoB_1f alpha_f NoB_1r alpha_r NoB_2 -ascii -
double;

M=load('datad044.dat');
[v_mean,dtn_mean,NoB_1f,alpha_f,NoB_1r,alpha_r,NoB_2]=thres_gdn1(peri
od,fs,s,dt1max,Dvnf,Dvrf,Dvnr,Dvrr,M);
save v_meanres44.dat v_mean  -ascii -double;
save alphres44.dat NoB_1f alpha_f NoB_1r alpha_r NoB_2 -ascii -
double;
```

```
M=load('datad045.dat');
[v_mean,dtn_mean,NoB_1f,alpha_f,NoB_1r,alpha_r,NoB_2]=thres_gdn1(peri
od,fs,s,dt1max,Dvnf,Dvrf,Dvnr,Dvrr,M);
save v_meanres45.dat v_mean  -ascii -double;
save alphres45.dat NoB_1f alpha_f NoB_1r alpha_r NoB_2 -ascii -
double;

M=load('datad046.dat');
[v_mean,dtn_mean,NoB_1f,alpha_f,NoB_1r,alpha_r,NoB_2]=thres_gdn1(peri
od,fs,s,dt1max,Dvnf,Dvrf,Dvnr,Dvrr,M);
save v_meanres46.dat v_mean  -ascii -double;
save alphres46.dat NoB_1f alpha_f NoB_1r alpha_r NoB_2 -ascii -
double;

M=load('datad047.dat');
[v_mean,dtn_mean,NoB_1f,alpha_f,NoB_1r,alpha_r,NoB_2]=thres_gdn1(peri
od,fs,s,dt1max,Dvnf,Dvrf,Dvnr,Dvrr,M);
save v_meanres47.dat v_mean  -ascii -double;
save alphres47.dat NoB_1f alpha_f NoB_1r alpha_r NoB_2 -ascii -
double;

M=load('datad048.dat');
[v_mean,dtn_mean,NoB_1f,alpha_f,NoB_1r,alpha_r,NoB_2]=thres_gdn1(peri
od,fs,s,dt1max,Dvnf,Dvrf,Dvnr,Dvrr,M);
save v_meanres48.dat v_mean  -ascii -double;
save alphres48.dat NoB_1f alpha_f NoB_1r alpha_r NoB_2 -ascii -
double;

M=load('datad049.dat');
[v_mean,dtn_mean,NoB_1f,alpha_f,NoB_1r,alpha_r,NoB_2]=thres_gdn1(peri
od,fs,s,dt1max,Dvnf,Dvrf,Dvnr,Dvrr,M);
save v_meanres49.dat v_mean  -ascii -double;
save alphres49.dat NoB_1f alpha_f NoB_1r alpha_r NoB_2 -ascii -
double;

M=load('datad050.dat');
[v_mean,dtn_mean,NoB_1f,alpha_f,NoB_1r,alpha_r,NoB_2]=thres_gdn1(peri
od,fs,s,dt1max,Dvnf,Dvrf,Dvnr,Dvrr,M);
save v_meanres50.dat v_mean  -ascii -double;
save alphres50.dat NoB_1f alpha_f NoB_1r alpha_r NoB_2 -ascii -
double;

M=load('datad051.dat');
[v_mean,dtn_mean,NoB_1f,alpha_f,NoB_1r,alpha_r,NoB_2]=thres_gdn1(peri
od,fs,s,dt1max,Dvnf,Dvrf,Dvnr,Dvrr,M);
save v_meanres51.dat v_mean  -ascii -double;
save alphres51.dat NoB_1f alpha_f NoB_1r alpha_r NoB_2 -ascii -
double;

M=load('datad052.dat');
[v_mean,dtn_mean,NoB_1f,alpha_f,NoB_1r,alpha_r,NoB_2]=thres_gdn1(peri
od,fs,s,dt1max,Dvnf,Dvrf,Dvnr,Dvrr,M);
save v_meanres52.dat v_mean -ascii -double;
save alphres52.dat NoB_1f alpha_f NoB_1r alpha_r NoB_2 -ascii -
double;

M=load('datad053.dat');
[v_mean,dtn_mean,NoB_1f,alpha_f,NoB_1r,alpha_r,NoB_2]=thres_gdn1(peri
od,fs,s,dt1max,Dvnf,Dvrf,Dvnr,Dvrr,M);
save v_meanres53.dat v_mean  -ascii -double;
```

```
save alphres53.dat NoB_1f alpha_f NoB_1r alpha_r NoB_2 -ascii -
double;

M=load('datad054.dat');
[v_mean,dtn_mean,NoB_1f,alpha_f,NoB_1r,alpha_r,NoB_2]=thres_gdn1(peri
od,fs,s,dt1max,Dvnf,Dvrf,Dvnr,Dvrr,M);
save v_meanres54.dat v_mean  -ascii -double;
save alphres54.dat NoB_1f alpha_f NoB_1r alpha_r NoB_2 -ascii -
double;

M=load('datad055.dat');
[v_mean,dtn_mean,NoB_1f,alpha_f,NoB_1r,alpha_r,NoB_2]=thres_gdn1(peri
od,fs,s,dt1max,Dvnf,Dvrf,Dvnr,Dvrr,M);
save v_meanres55.dat v_mean  -ascii -double;
save alphres55.dat NoB_1f alpha_f NoB_1r alpha_r NoB_2 -ascii -
double;
M=load('datad056.dat');
[v_mean,dtn_mean,NoB_1f,alpha_f,NoB_1r,alpha_r,NoB_2]=thres_gdn1(peri
od,fs,s,dt1max,Dvnf,Dvrf,Dvnr,Dvrr,M);
save v_meanres56.dat v_mean  -ascii -double;
save alphres56.dat NoB_1f alpha_f NoB_1r alpha_r NoB_2 -ascii -
double;
M=load('datad057.dat');
[v_mean,dtn_mean,NoB_1f,alpha_f,NoB_1r,alpha_r,NoB_2]=thres_gdn1(peri
od,fs,s,dt1max,Dvnf,Dvrf,Dvnr,Dvrr,M);
save v_meanres57.dat v_mean  -ascii -double;
save alphres57.dat NoB_1f alpha_f NoB_1r alpha_r NoB_2 -ascii -
double;
M=load('datad058.dat');
[v_mean,dtn_mean,NoB_1f,alpha_f,NoB_1r,alpha_r,NoB_2]=thres_gdn1(peri
od,fs,s,dt1max,Dvnf,Dvrf,Dvnr,Dvrr,M);
save v_meanres58.dat v_mean  -ascii -double;
save alphres58.dat NoB_1f alpha_f NoB_1r alpha_r NoB_2 -ascii -
double;
M=load('datad059.dat');
[v_mean,dtn_mean,NoB_1f,alpha_f,NoB_1r,alpha_r,NoB_2]=thres_gdn1(peri
od,fs,s,dt1max,Dvnf,Dvrf,Dvnr,Dvrr,M);
save v_meanres59.dat v_mean  -ascii -double;
save alphres59.dat NoB_1f alpha_f NoB_1r alpha_r NoB_2 -ascii -
double;

M=load('datad060.dat');
[v_mean,dtn_mean,NoB_1f,alpha_f,NoB_1r,alpha_r,NoB_2]=thres_gdn1(peri
od,fs,s,dt1max,Dvnf,Dvrf,Dvnr,Dvrr,M);
save v_meanres60.dat v_mean  -ascii -double;
save alphres60.dat NoB_1f alpha_f NoB_1r alpha_r NoB_2 -ascii -
double;
M=load('datad061.dat');
[v_mean,dtn_mean,NoB_1f,alpha_f,NoB_1r,alpha_r,NoB_2]=thres_gdn1(peri
od,fs,s,dt1max,Dvnf,Dvrf,Dvnr,Dvrr,M);
save v_meanres61.dat v_mean  -ascii -double;
save alphres61.dat NoB_1f alpha_f NoB_1r alpha_r NoB_2 -ascii -
double;
M=load('datad062.dat');
[v_mean,dtn_mean,NoB_1f,alpha_f,NoB_1r,alpha_r,NoB_2]=thres_gdn1(peri
od,fs,s,dt1max,Dvnf,Dvrf,Dvnr,Dvrr,M);
save v_meanres62.dat v_mean  -ascii -double;
save alphres62.dat NoB_1f alpha_f NoB_1r alpha_r NoB_2 -ascii -
double;
M=load('datad063.dat');
```

```
[v_mean,dtn_mean,NoB_1f,alpha_f,NoB_1r,alpha_r,NoB_2]=thres_gdn1(peri
od,fs,s,dt1max,Dvnf,Dvrf,Dvnr,Dvrr,M);
save v_meanres63.dat v_mean  -ascii -double;
save alphres63.dat NoB_1f alpha_f NoB_1r alpha_r NoB_2 -ascii -
double;
M=load('datad064.dat');
[v_mean,dtn_mean,NoB_1f,alpha_f,NoB_1r,alpha_r,NoB_2]=thres_gdn1(peri
od,fs,s,dt1max,Dvnf,Dvrf,Dvnr,Dvrr,M);
save v_meanres64.dat v_mean  -ascii -double;
save alphres64.dat NoB_1f alpha_f NoB_1r alpha_r NoB_2 -ascii -
double;
M=load('datad065.dat');
[v_mean,dtn_mean,NoB_1f,alpha_f,NoB_1r,alpha_r,NoB_2]=thres_gdn1(peri
od,fs,s,dt1max,Dvnf,Dvrf,Dvnr,Dvrr,M);
save v_meanres65.dat v_mean  -ascii -double;
save alphres65.dat NoB_1f alpha_f NoB_1r alpha_r NoB_2 -ascii -
double;
M=load('datad066.dat');
[v_mean,dtn_mean,NoB_1f,alpha_f,NoB_1r,alpha_r,NoB_2]=thres_gdn1(peri
od,fs,s,dt1max,Dvnf,Dvrf,Dvnr,Dvrr,M);
save v_meanres66.dat v_mean  -ascii -double;
save alphres66.dat NoB_1f alpha_f NoB_1r alpha_r NoB_2 -ascii -
double;
M=load('datad067.dat');
[v_mean,dtn_mean,NoB_1f,alpha_f,NoB_1r,alpha_r,NoB_2]=thres_gdn1(peri
od,fs,s,dt1max,Dvnf,Dvrf,Dvnr,Dvrr,M);
save v_meanres67.dat v_mean  -ascii -double;
save alphres67.dat NoB_1f alpha_f NoB_1r alpha_r NoB_2 -ascii -
double;
M=load('datad068.dat');
[v_mean,dtn_mean,NoB_1f,alpha_f,NoB_1r,alpha_r,NoB_2]=thres_gdn1(peri
od,fs,s,dt1max,Dvnf,Dvrf,Dvnr,Dvrr,M);
save v_meanres68.dat v_mean  -ascii -double;
save alphres68.dat NoB_1f alpha_f NoB_1r alpha_r NoB_2 -ascii -
double;
M=load('datad069.dat');
[v_mean,dtn_mean,NoB_1f,alpha_f,NoB_1r,alpha_r,NoB_2]=thres_gdn1(peri
od,fs,s,dt1max,Dvnf,Dvrf,Dvnr,Dvrr,M);
save v_meanres69.dat v_mean  -ascii -double;
save alphres69.dat NoB_1f alpha_f NoB_1r alpha_r NoB_2 -ascii -
double;
M=load('datad070.dat');
[v_mean,dtn_mean,NoB_1f,alpha_f,NoB_1r,alpha_r,NoB_2]=thres_gdn1(peri
od,fs,s,dt1max,Dvnf,Dvrf,Dvnr,Dvrr,M);
save v_meanres70.dat v_mean  -ascii -double;
save alphres70.dat NoB_1f alpha_f NoB_1r alpha_r NoB_2 -ascii -
double;
M=load('datad071.dat');
[v_mean,dtn_mean,NoB_1f,alpha_f,NoB_1r,alpha_r,NoB_2]=thres_gdn1(peri
od,fs,s,dt1max,Dvnf,Dvrf,Dvnr,Dvrr,M);
save v_meanres71.dat v_mean  -ascii -double;
save alphres71.dat NoB_1f alpha_f NoB_1r alpha_r NoB_2 -ascii -
double;
M=load('datad072.dat');
[v_mean,dtn_mean,NoB_1f,alpha_f,NoB_1r,alpha_r,NoB_2]=thres_gdn1(peri
od,fs,s,dt1max,Dvnf,Dvrf,Dvnr,Dvrr,M);
save v_meanres72.dat v_mean  -ascii -double;
save alphres72.dat NoB_1f alpha_f NoB_1r alpha_r NoB_2 -ascii -
double;
M=load('datad073.dat');
```

```
[v_mean,dtn_mean,NoB_1f,alpha_f,NoB_1r,alpha_r,NoB_2]=thres_gdn1(peri
od,fs,s,dt1max,Dvnf,Dvrf,Dvnr,Dvrr,M);
save v_meanres73.dat v_mean  -ascii -double;
save alphres73.dat NoB_1f alpha_f NoB_1r alpha_r NoB_2 -ascii -
double;
M=load('datad074.dat');
[v_mean,dtn_mean,NoB_1f,alpha_f,NoB_1r,alpha_r,NoB_2]=thres_gdn1(peri
od,fs,s,dt1max,Dvnf,Dvrf,Dvnr,Dvrr,M);
save v_meanres74.dat v_mean  -ascii -double;
save alphres74.dat NoB_1f alpha_f NoB_1r alpha_r NoB_2 -ascii -
double;
M=load('datad075.dat');
[v_mean,dtn_mean,NoB_1f,alpha_f,NoB_1r,alpha_r,NoB_2]=thres_gdn1(peri
od,fs,s,dt1max,Dvnf,Dvrf,Dvnr,Dvrr,M);
save v_meanres75.dat v_mean  -ascii -double;
save alphres75.dat NoB_1f alpha_f NoB_1r alpha_r NoB_2 -ascii -
double;
M=load('datad076.dat');
[v_mean,dtn_mean,NoB_1f,alpha_f,NoB_1r,alpha_r,NoB_2]=thres_gdn1(peri
od,fs,s,dt1max,Dvnf,Dvrf,Dvnr,Dvrr,M);
save v_meanres76.dat v_mean  -ascii -double;
save alphres76.dat NoB_1f alpha_f NoB_1r alpha_r NoB_2 -ascii -
double;
M=load('datad077.dat');
[v_mean,dtn_mean,NoB_1f,alpha_f,NoB_1r,alpha_r,NoB_2]=thres_gdn1(peri
od,fs,s,dt1max,Dvnf,Dvrf,Dvnr,Dvrr,M);
save v_meanres77.dat v_mean  -ascii -double;
save alphres77.dat NoB_1f alpha_f NoB_1r alpha_r NoB_2 -ascii -
double;
M=load('datad078.dat');
[v_mean,dtn_mean,NoB_1f,alpha_f,NoB_1r,alpha_r,NoB_2]=thres_gdn1(peri
od,fs,s,dt1max,Dvnf,Dvrf,Dvnr,Dvrr,M);
save v_meanres78.dat v_mean  -ascii -double;
save alphres78.dat NoB_1f alpha_f NoB_1r alpha_r NoB_2 -ascii -
double;
M=load('datad079.dat');
[v_mean,dtn_mean,NoB_1f,alpha_f,NoB_1r,alpha_r,NoB_2]=thres_gdn1(peri
od,fs,s,dt1max,Dvnf,Dvrf,Dvnr,Dvrr,M);
save v_meanres79.dat v_mean  -ascii -double;
save alphres79.dat NoB_1f alpha_f NoB_1r alpha_r NoB_2 -ascii -
double;
M=load('datad080.dat');
[v_mean,dtn_mean,NoB_1f,alpha_f,NoB_1r,alpha_r,NoB_2]=thres_gdn1(peri
od,fs,s,dt1max,Dvnf,Dvrf,Dvnr,Dvrr,M);
save v_meanres80.dat v_mean  -ascii -double;
save alphres80.dat NoB_1f alpha_f NoB_1r alpha_r NoB_2 -ascii -
double;
M=load('datad081.dat');
[v_mean,dtn_mean,NoB_1f,alpha_f,NoB_1r,alpha_r,NoB_2]=thres_gdn1(peri
od,fs,s,dt1max,Dvnf,Dvrf,Dvnr,Dvrr,M);
save v_meanres81.dat v_mean  -ascii -double;
save alphres81.dat NoB_1f alpha_f NoB_1r alpha_r NoB_2 -ascii -
double;
M=load('datad082.dat');
[v_mean,dtn_mean,NoB_1f,alpha_f,NoB_1r,alpha_r,NoB_2]=thres_gdn1(peri
od,fs,s,dt1max,Dvnf,Dvrf,Dvnr,Dvrr,M);
save v_meanres82.dat v_mean  -ascii -double;
save alphres82.dat NoB_1f alpha_f NoB_1r alpha_r NoB_2 -ascii -
double;
M=load('datad083.dat');
```

```
[v_mean,dtn_mean,NoB_1f,alpha_f,NoB_1r,alpha_r,NoB_2]=thres_gdn1(peri
od,fs,s,dt1max,Dvnf,Dvrf,Dvnr,Dvrr,M);
save v_meanres83.dat v_mean  -ascii -double;
save alphres83.dat NoB_1f alpha_f NoB_1r alpha_r NoB_2 -ascii -
double;
M=load('datad084.dat');
[v_mean,dtn_mean,NoB_1f,alpha_f,NoB_1r,alpha_r,NoB_2]=thres_gdn1(peri
od,fs,s,dt1max,Dvnf,Dvrf,Dvnr,Dvrr,M);
save v_meanres84.dat v_mean  -ascii -double;
save alphres84.dat NoB_1f alpha_f NoB_1r alpha_r NoB_2 -ascii -
double;
M=load('datad085.dat');
[v_mean,dtn_mean,NoB_1f,alpha_f,NoB_1r,alpha_r,NoB_2]=thres_gdn1(peri
od,fs,s,dt1max,Dvnf,Dvrf,Dvnr,Dvrr,M);
save v_meanres85.dat v_mean  -ascii -double;
save alphres85.dat NoB_1f alpha_f NoB_1r alpha_r NoB_2 -ascii -
double;
M=load('datad086.dat');
[v_mean,dtn_mean,NoB_1f,alpha_f,NoB_1r,alpha_r,NoB_2]=thres_gdn1(peri
od,fs,s,dt1max,Dvnf,Dvrf,Dvnr,Dvrr,M);
save v_meanres86.dat v_mean  -ascii -double;
save alphres86.dat NoB_1f alpha_f NoB_1r alpha_r NoB_2 -ascii -
double;
M=load('datad087.dat');
[v_mean,dtn_mean,NoB_1f,alpha_f,NoB_1r,alpha_r,NoB_2]=thres_gdn1(peri
od,fs,s,dt1max,Dvnf,Dvrf,Dvnr,Dvrr,M);
save v_meanres87.dat v_mean  -ascii -double;
save alphres87.dat NoB_1f alpha_f NoB_1r alpha_r NoB_2 -ascii -
double;
M=load('datad088.dat');
[v_mean,dtn_mean,NoB_1f,alpha_f,NoB_1r,alpha_r,NoB_2]=thres_gdn1(peri
od,fs,s,dt1max,Dvnf,Dvrf,Dvnr,Dvrr,M);
save v_meanres88.dat v_mean  -ascii -double;
save alphres88.dat NoB_1f alpha_f NoB_1r alpha_r NoB_2 -ascii -
double;
```

Listing of Thres_gdn1.m

```
function[v_mean,dtn_mean,NoB_1f,alpha_f,NoB_1r,alpha_r,NoB_2]=thres_g
dn1(period,fs,s,dt1max,Dvnf,Dvrf,Dvnr,Dvrr,M);

%Vnoise_p3,Vref_p3,Vnoise_p4,Vref_p4,(this was before dt1max)
%thres_g(period,fs,s,Vnoise_f,Vref_f,Vnoise_r,Vref_r);
%
%A function to analyse the data obtained from dual probes using
circuit 3 and GLOBAL Lab.
%It will calculate various bubble parameters using a combination of
fixed level thresholding
%and the gamma criterion (e.g. angle criterion). Data are assumed to
be in ASCII format in
%a file called 'bubble_ac.dat', whos 1st column holds the front
sensor data and the 2nd
%column holds the rear sensor data. When the two data streams are
initially scanned, the
%number of bubbles detected in each stream will be displayed and
updated.
%
%thres_g will call the following subfunctions diricty or indirectly:
%          -   scan_stream
%          -   get_time_of_contact
%          -   find_pairs
%
%INPUT PARAMETERS
%================
%period    -   total sampling period [sec]
%fs        -   sampling frequency used to acquire data [Hz]
%s         -   scaling factor that gives 45° between 1 unit voltage
and 1 unit time
%              i.e. s=1000 for 1V/1msec
%Vnoise_f  -   (lower) noise limit for front sensor data [V]
%Vref_f    -   front sensor reference voltage (center voltage in
noise band) [V]
%Vnoise_r  -   (lower) noise limit for rear sensor data [V]
%Vref_r    -   rear sensor reference voltage (center voltage in noise
band) [V]
%dt1max    -   parameter to decide if bubble signatures are caused by
same bubble
%
%OUTPUT
%======
%This m-file will compute and display the following parameters:
%NoB_1f    -   number of bubbles that hit front sensor
%alpha_f   -   volume fraction on front sensor
%NoB_1r    -   number of bubbles that hit rear sensor
%alpha_r   -   volume fraction on rear sensor
%NoB_2     -   number of bubbles that hit both front and rear sensor
%dt1_mean  -   mean time delay for 1st contact [sec]
%dt1_min   -   shortest time delay for 1st contact [sec]
%dt1_max   -   longest time delay for 1st contact [sec]
%dt2_mean  -   mean time delay for 2nd contact [sec]
%dt2_min   -   shortest time delay for 2nd contact [sec]
%dt2_max   -   longest time delay for 2nd contact [sec]
%
%Furthermore, the delay times for 1st and 2nd contact will be saved
in an ASCII file along
%with the corresponding time of first contact with the front sensor.
This is helpful for
```

```
%inspection of the original data file if in doubt about any of the
results. The ASCII file
%is called 'dt_res.dat' and is organised into 3 columns (time of 1st
contact with front
%sensor, delay time for 1st contact, delay time for 2nd contact).
%
%The LOAD and SAVE statements used in this m-file may need
modification depending on the
%version of MATLAB used.

format long;      %use 15 digit precision

%M=load('probe_ac.dat');
%M=load('datad001.dat');

A=M(:,1);         %load data from front sensor
B=M(:,2);         %load data from rear sensor
%p3=M(:,3);
%p4=M(:,4);
%A=A*1000;
%B=B*1000;
N=length(A);      %determine number of data

N                 %output no. of data


A_max=min(A)
B_max=min(B)

Vnoise_f=A_max+Dvnf;
Vref_f=A_max+Dvrf;
Vnoise_r=B_max+Dvnr;
Vref_r=B_max+Dvrr;

[alpha_f,NoB_1f,times]=scan_stream(A,Vnoise_f,Vref_f,N,period,fs,s);

c_times_f=times

[alpha_r,NoB_1r,times]=scan_stream(B,Vnoise_r,Vref_r,N,period,fs,s);

c_times_r=times;


[c_times,NoB_2]=find_pairs(c_times_f,c_times_r,dt1max);
if (NoB_2>0.0)

dt1_mean=0;
dt2_mean=0;
dtn_mean=0;
dt1i_mean=0;
dt2i_mean=0;
dtni_mean=0;
an1=0.0
an2=0.0
an3=0.0
for n=1:NoB_2        %find mean delay times and min and max delay
times
   dt1=c_times(n,2)-c_times(n,1);
   dt2=c_times(n,4)-c_times(n,3);
   dtn=(dt1+dt2)/2;
   if dt1<=0.000267;
```

```
      dt1i=0.0
      an1=an1+1
      else
         dt1i=1/dt1;
      end
      if dt2<=0.000267;
         dt2i=0.0;
         an2=an2+1;
         else
            dt2i=1/dt2;
         end
         if dtn<=0.000267;
            dtni=0.0
            an3=an3+1
         else
            dtni=1/dtn;
            end
   dt1_mean=dt1_mean+dt1;
   dt2_mean=dt2_mean+dt2;
   dtn_mean=dtn_mean+dtn;
   dt1i_mean=dt1i_mean+dt1i;
   dt2i_mean=dt2i_mean+dt2i;
   dtni_mean=dtni_mean+dtni;
   if n==1
      dt1_min=dt1; dt1_max=dt1;
      dt2_min=dt2; dt2_max=dt2;
   else
      if dt1<dt1_min
         dt1_min=dt1;
      end
      if dt1>dt1_max
         dt1_max=dt1;
      end
      if dt2<dt2_min
         dt2_min=dt2;
      end
      if dt2>dt2_max
         dt2_max=dt2;
      end
   end
   vn(n,1)=.0048866/dtn;
   dt(n,1)=c_times(n,1);
   dt(n,2)=dt1;
   dt(n,3)=dt2;
   dt(n,4)=dtn;
end
dt1_mean=dt1_mean/NoB_2;
dt2_mean=dt2_mean/NoB_2;
dtn_mean=dtn_mean/NoB_2;
dt1i_mean=dt1i_mean/(NoB_2-an1);
dt2i_mean=dt2i_mean/(NoB_2-an2);
dtni_mean=dtni_mean/(NoB_2-an3);
v_mean(:,1)=.0048866/dt1_mean;
v_mean(:,2)=.0048866/dt2_mean;
v_mean(:,3)=.0048866/dtn_mean;
v_mean(:,4)=.0048866*dt1i_mean;
v_mean(:,5)=.0048866*dt2i_mean;
v_mean(:,6)=.0048866*dtni_mean;
save dt_rescheck.dat dt -ascii -double;
save v_rescheck.dat vn -ascii -double;
%save v_meanrescheck.dat v_mean dtn_mean -ascii -double;
```

```
%save alphrescheck.dat NoB_1f alpha_f NoB_1r alpha_r NoB_2 -ascii -
double;

%display results
NoB_1f
alpha_f
NoB_1r
alpha_r

%NoB_1p3
%alpha_p3
%NoB_1p4
%alpha_p4

NoB_2
dt1_mean
dt1_min
dt1_max
dt2_mean
dt2_min
dt2_max
dtn_mean
v_mean
else
   dtn_mean1=0.048866
   dtn_mean=dtn_mean1
   v_mean(:,1)=.0048866/dtn_mean;
   v_mean(:,2)=.0048866/dtn_mean
   v_mean(:,3)=.0048866/dtn_mean
   v_mean(:,4)=.0048866/dtn_mean
   v_mean(:,5)=.0048866/dtn_mean
   v_mean(:,6)=.0048866/dtn_mean

end
```

Listing of Scan_stream.m

```
function[alpha,NoB,times]=scan_stream(D,Vnoise,Vref,N,period,fs,s);

%[alpha,NoB,times]=scan_stream(D,Vnoise,Vref,N,period,fs,s)
%
%This function scans a data stream and will detect the bubbles.
%
%INPUT PARAMETERS
%================
%D       -  data stream to be scaned
%Vnoise  -  (lower) noise limit for data [V]
%Vref    -  center voltage in noise band [V]
%N       -  no. of data points in data stream D
%period  -  sampling period [sec]
%fs      -  sampling frequency [Hz]
%
%RETURNED PARAMETERS
%===================
%alpha   -  volume fraction
%NoB     -  no. of bubbles detected based on Vthres criterion
%times   -  holds two columns with the 1st and 2nd time of contact
for each bubble respectively

Vthres=Vref+0.1

NoB=0;                %no bubbles detected yet
alpha=0;
r=1;                  %preload counter, start with first data point
while r<=N            %repeat loop till end of data stream hit
   if D(r)>Vthres
   %   D(r)
   %  Vthres
      NoB=NoB+1;
      NoB;

[r_new,check,t1,t2]=get_time_of_contact(r,fs,D,s,Vthres,Vnoise,N);
      if check==1                %bubble contact times were
identified
         r=r_new;
         times(NoB,1)=t1;
         times(NoB,2)=t2;
         alpha=alpha+(t2-t1);    %accumulate bubble resident time
      else
         r=r_new;
      end
   else
      r=r+1;

   end
end

alpha=alpha/period
```

Listing of get_time_of_contact.m

```
function[r_new,check,t1,t2]=get_time_of_contact(r,fs,D,s,Vthres,Vnois
e,N);

%[r_new,check,t1,t2]=get_time_of_contact(r,fs,D,s,Vthres,Vnoise,N);
%
%Once a bubble has been detected, this function will find the
associated times of 1st and 2nd
%contact of the bubble with the sensor tip.
%
%INPUT PARAMETERS
%================
%r        -  data point index
%fs       -  sampling frequency [Hz]
%D        -  data stream
%s        -  scaling factor
%Vthres   -  threshold voltage [V]
%Vnoise   -  (lower) noise limit for data
%N        -  total number of data in data stream
%
%RETURNED PARAMETERS
%===================
%r_new    -  new data index, from where scanning will be continued
%check    -  indicates if both times of 1st and 2nd contact were found
%t1       -  time of 1st contact with sensor tip [sec]
%t2       -  time of 2nd contact with sensor tip [sec]

p=r;     %use new counter, keep old one as reference
t1=0;
t2=0;
check1=0; %contact times not identified yet
check2=0;


%loop to detect 1st time of contact
while p>2               %smallest data index is 1; however, gamma
cannot be calculated for 1st data point,
   p=p-1;               %only for 2nd and following points
   %gamma=180-atan((D(p)-D(p-1))/(s/fs))*180/pi +atan((D(p+1)-
D(p))/(s/fs))*180/pi;

   %if gamma >= 90
    %       if gamma <= 160
     %          t1=(p-1)/fs;  %subtract 1 as data index p starts with
1 but time with 0sec
      %   check1=1;
       %  break
      %end
   %end
   if D(p)<=Vnoise      %if transients are not rapid (flat signal) we
identify time of contact this way
      t1=(p-1)/fs;
      check1=1;
      break
   end

end


%loop to detect 2nd time of contact
```

```
p=r;
while p<N
   p=p+1;
   if D(p)<=Vthres
%      gamma=180-atan((D(p)-D(p-1))/(s/fs))*180/pi +atan((D(p+1)-
D(p))/(s/fs))*180/pi;

%     if gamma >= 90
 %       if gamma <= 160
  %          t2=(p-1)/fs;  %subtract 1 as data index p starts with 1
but time with 0sec
   %         check2=1;
    %        r_new=p+1;    %commence scanning with next data point
     %      break
      %  end
      %end
       if D(p)<=Vnoise      %if transients are not rapid (flat signal)
we identify time of contact this way
          t2=(p-1)/fs;
          check2=1;
          r_new=p+1;        %commence scanning with next data point
          break
       end

   end
end

check=check1 & check2;     %if both t1 and t2 detected, set check

if p==N                    %if end of data is hit befor t2 could be
detected
   r_new=N+1;
end
```

Listing of find pairs.m

```
function[c_times,NoB_2]=find_pairs(t_f,t_r,dt1max);

%[c_times,NoB_2]=find_pairs(t_f,t_r)
%
%From all the individual bubbles that hit front and rear sensor, this
function detects which
%bubbles hit both front and rear sensor.
%
%INPUT PARAMETERS
%================
%t_f     -  matrix that holds front sensor contact times (e.g. times
of 1st and 2nd contacts)
%t_r     -  matrix that holds rear sensor contact times (e.g. times
of 1st and 2nd contacts)
%dt1max  -  signal processing parameter, if dt1 > dt1max we assume
signatures are from different
%           bubbles
%
%RETURNED PARAMETERS
%===================
%c_times -  a four column matrix, holds the contact times associated
with a bubble that hits
%           both front and rear sensor, e.g.
%           time of 1st contact with front sensor, time of 1st
contact with rear sensor,
%           time of 2nd contact with front sensor, time of 2nd
contact with rear sensor
%NoB_2   -  no. of bubbles that hit both front and rear sensor

F=length(t_f)
R=length(t_r)
if (F>5) & (R>5)
NoB_2=0;       %no matching pairs found yet
r=1;
for f=1:F
   %r=1;
   while t_r(r,1)<t_f(f,1)
            if r>=R
         r=R;
        break
     end
     r=r+1;
  end
  if r>=R
     break
  end
     %if (t_r(r,1)>=t_f(f,1)) & (t_r(r,1)<=t_f(f,2))  %check all 3
criteria, USE THIS FOR 2.5mm probes
   if (t_r(r,1)>=t_f(f,1)) & (t_r(r,1)<=t_f(f,1)+dt1max) %check all 3
criteria, USE FOR 5mm probes
      if t_r(r,2)-t_f(f,2)>=0
         if f==F
            NoB_2=NoB_2+1;
            c_times(NoB_2,1)=t_f(f,1);
            c_times(NoB_2,2)=t_r(r,1);
            c_times(NoB_2,3)=t_f(f,2);
            c_times(NoB_2,4)=t_r(r,2);
            r=r+1;
            r %we do not want to assign same bubble again
```

```
         elseif t_r(r,2)<t_f(f+1,2)
            NoB_2=NoB_2+1;
            c_times(NoB_2,1)=t_f(f,1);
            c_times(NoB_2,2)=t_r(r,1);
            c_times(NoB_2,3)=t_f(f,2);
            c_times(NoB_2,4)=t_r(r,2);
            r=r+1;
         end
      end
   end
end

else

   NoB_2=0;
   c_times(1,1)=0
            c_times(1,2)=0
            c_times(1,3)=0
            c_times(1,4)=0
            end
```

listing of thdplotnewvolfr.m

```
%3d graphics
function[]=thdplotnewvolfr()
r=[0.475;.380;.285;0.190;0.095;0.;-0.095;-0.190;-0.285;-0.380;-0.475;
   0.475;.380;.285;0.190;0.095;0.;-0.095;-0.190;-0.285;-0.380;-0.475;
   0.475;.380;.285;0.190;0.095;0.;-0.095;-0.190;-0.285;-0.380;-0.475;
   0.475;.380;.285;0.190;0.095;0.;-0.095;-0.190;-0.285;-0.380;-0.475;
   0.475;.380;.285;0.190;0.095;0.;-0.095;-0.190;-0.285;-0.380;-0.475;
   0.475;.380;.285;0.190;0.095;0.;-0.095;-0.190;-0.285;-0.380;-0.475;
   0.475;.380;.285;0.190;0.095;0.;-0.095;-0.190;-0.285;-0.380;-0.475;
   0.475;.380;.285;0.190;0.095;0.;-0.095;-0.190;-0.285;-0.380;-
0.475;]
p1=load('alphres1.dat');
p2=load('alphres2.dat');
p3=load('alphres3.dat');
p4=load('alphres4.dat');
p5=load('alphres5.dat');
p6=load('alphres6.dat');
p7=load('alphres7.dat');
p8=load('alphres8.dat');
p9=load('alphres9.dat');
p10=load('alphres10.dat');
p11=load('alphres11.dat');
p12=load('alphres12.dat');
p13=load('alphres13.dat');
p14=load('alphres14.dat');
p15=load('alphres15.dat');
p16=load('alphres16.dat');
p17=load('alphres17.dat');
p18=load('alphres18.dat');
p19=load('alphres19.dat');
p20=load('alphres20.dat');
p21=load('alphres21.dat');
p22=load('alphres22.dat');
p23=load('alphres23.dat');
p24=load('alphres24.dat');
p25=load('alphres25.dat');
p26=load('alphres26.dat');
```

```
p27=load('alphres27.dat');
p28=load('alphres28.dat');
p29=load('alphres29.dat');
p30=load('alphres30.dat');
p31=load('alphres31.dat');
p32=load('alphres32.dat');
p33=load('alphres33.dat');
p34=load('alphres34.dat');
p35=load('alphres35.dat');
p36=load('alphres36.dat');
p37=load('alphres37.dat');
p38=load('alphres38.dat');
p39=load('alphres39.dat');
p40=load('alphres40.dat');
p41=load('alphres41.dat');
p42=load('alphres42.dat');
p43=load('alphres43.dat');
p44=load('alphres44.dat');
p45=load('alphres45.dat');
p46=load('alphres46.dat');
p47=load('alphres47.dat');
p48=load('alphres48.dat');
p49=load('alphres49.dat');
p50=load('alphres50.dat');
p51=load('alphres51.dat');
p52=load('alphres52.dat');
p53=load('alphres53.dat');
p54=load('alphres54.dat');
p55=load('alphres55.dat');
p56=load('alphres56.dat');
p57=load('alphres57.dat');
p58=load('alphres58.dat');
p59=load('alphres59.dat');
p60=load('alphres60.dat');
p61=load('alphres61.dat');
p62=load('alphres62.dat');
p63=load('alphres63.dat');
p64=load('alphres64.dat');
p65=load('alphres65.dat');
p66=load('alphres66.dat');
p67=load('alphres67.dat');
p68=load('alphres68.dat');
p69=load('alphres69.dat');
p70=load('alphres70.dat');
p71=load('alphres71.dat');
p72=load('alphres72.dat');
p73=load('alphres73.dat');
p74=load('alphres74.dat');
p75=load('alphres75.dat');
p76=load('alphres76.dat');
p77=load('alphres77.dat');
p78=load('alphres78.dat');
p79=load('alphres79.dat');
p80=load('alphres80.dat');
p81=load('alphres81.dat');
p82=load('alphres82.dat');
p83=load('alphres83.dat');
p84=load('alphres84.dat');
p85=load('alphres85.dat');
p86=load('alphres86.dat');
p87=load('alphres87.dat');
```

```
p88=load('alphres88.dat');
pz1=[p1,p2,p3,p4,p5,p6,p7,p8,p9,p10];
pz2=[p11,p12,p13,p14,p15,p16,p17,p18,p19,p20];
pz3=[p21,p22,p23,p24,p25,p26,p27,p28,p29,p30];
pz4=[p31,p32,p33,p34,p35,p36,p37,p38,p39,p40];
pz5=[p41,p42,p43,p44,p45,p46,p47,p48,p49,p50];
pz6=[p51,p52,p53,p54,p55,p56,p57,p58,p59,p60];
pz7=[p61,p62,p63,p64,p65,p66,p67,p68,p69,p70];
pz8=[p71,p72,p73,p74,p75,p76,p77,p78,p79,p80];
pz9=[p81,p82,p83,p84,p85,p86,p87,p88];
Pz=[pz1,pz2,pz3,pz4,pz5,pz6,pz7,pz8,pz9];

Zn=Pz';
Z=Zn(:,2);
ZZ1=Zn(:,4);

for n=1:88;
         if n<=11
            n
            theta=0;
         end
         if (n>11) &(n<=22);
            n
            theta=(pi/8);
         end
         if (n>22) &(n<=33);
            n
   theta=(pi/4);
 end

if (n>33) &(n<=44);
            n
   theta=(3*pi/8);
end
  if (n>44) &(n<=55);
            n
   theta=(pi/2);
 end
   if (n>55) &(n<=66);
            n
   theta=(5*pi/8);
end
  if (n>66) &(n<=77);
            n
   theta=(6*pi/8);
end

if n>77;
    n
   theta=(7*pi/8);
end
X(n,1)=r(n)*cos(theta);
X(n,2)=r(n)*sin(theta);
X(n,3)=Z(n);
X(n,4)=ZZ1(n);
X1(n)=X(n,1);
Y1(n)=X(n,2);
Z1(n)=X(n,3);
Zp(n)=X(n,4);
%next n;
X1;
```

```
end

for ii=1:360;
   jj=ii-1;
   xo(ii)=0.5*cos(jj);
   yo(ii)=0.5*sin(jj);
   zo(ii)=0;
end
xx1=[X1,xo];
yy1=[Y1,yo];
zz1=[Z1,zo];
zz2=[Zp,zo];
xa=-0.5:.002:.5;
ya=-0.5:.002:.5;
[xa,ya]=meshgrid(xa,ya);
[xa,ya,alpha]=griddata(xx1,yy1,zz1,xa,ya,'cubic');
[xa,ya,alpha1]=griddata(xx1,yy1,zz2,xa,ya,'cubic');
subplot(2,1,1);
%plot3(xa,ya,alpha);
mesh(xa,ya,alpha);;
title('Mean volume fraction=1.09%, Mean velocity=0.64 m/s');
xlabel('X-coordinate(r/D)');
ylabel('Y-coordinate(r/D)');
zlabel ('Volume fraction front sensor');
subplot(2,1,2);
mesh(xa,ya,alpha1);;
%plot3(xa,ya,alpha1);
title('Mean volume fraction=1.09%, Mean velocity=0.64 m/s');
xlabel('X-coordinate(r/D)');
ylabel('Y-coordinate(r/D)');
zlabel ('Volume fraction rear sensor');
%mesh(xa,ya,alpha)
%holdon
%plot3(X1,Y1,Z1)
%surfc(xa,ya,alpha)
%X1n=X1';
%Y1n=Y1;
%DmatrixZ1=diag(Z1');
%DmatrixZ2=diag(Zv);
%DmatrixZ3=DmatrixZ1/0.65;
%DmatrixZ4=DmatrixZ2/1.09;
%X=X'
%Y=Y'
%z=z'
%h1=interp3(X1n,Y1,DmatrixZ2)
%mesh(h1),
%surfc(X1n,Y1,DmatrixZ4)
%title('non dimensional velocity profile');
%plot3(X1,Y1,Z1):


%%plot3(X1,Y1,Zv);

%[xx,yy]=meshgrid(X1n,Y1);
%mesh(xx,yy,DmatrixZ1);
%title('velocity profile');


save xy.dat X  -ascii -double
save volfr.dat Zn  -ascii –double
```

listing of thdplotnewvelz.m (this program can be used for plotting velocity based on six time function)

```
function[]=thdplotnewvel()
r=[0.475;.380;.285;0.190;0.095;0.;-0.095;-0.190;-0.285;-0.380;-0.475;
   0.475;.380;.285;0.190;0.095;0.;-0.095;-0.190;-0.285;-0.380;-0.475;
   0.475;.380;.285;0.190;0.095;0.;-0.095;-0.190;-0.285;-0.380;-0.475;
   0.475;.380;.285;0.190;0.095;0.;-0.095;-0.190;-0.285;-0.380;-0.475;
   0.475;.380;.285;0.190;0.095;0.;-0.095;-0.190;-0.285;-0.380;-0.475;
   0.475;.380;.285;0.190;0.095;0.;-0.095;-0.190;-0.285;-0.380;-0.475;
   0.475;.380;.285;0.190;0.095;0.;-0.095;-0.190;-0.285;-0.380;-0.475;
   0.475;.380;.285;0.190;0.095;0.;-0.095;-0.190;-0.285;-0.380;-
0.475;]
p1=load('v_meanres1.dat');
p2=load('v_meanres2.dat');
p3=load('v_meanres3.dat');
p4=load('v_meanres4.dat');
p5=load('v_meanres5.dat');
p6=load('v_meanres6.dat');
p7=load('v_meanres7.dat');
p8=load('v_meanres8.dat');
p9=load('v_meanres9.dat');
p10=load('v_meanres10.dat');
p11=load('v_meanres11.dat');
p12=load('v_meanres12.dat');
p13=load('v_meanres13.dat');
p14=load('v_meanres14.dat');
p15=load('v_meanres15.dat');
p16=load('v_meanres16.dat');
p17=load('v_meanres17.dat');
p18=load('v_meanres18.dat');
p19=load('v_meanres19.dat');
p20=load('v_meanres20.dat');
p21=load('v_meanres21.dat');
p22=load('v_meanres22.dat');
p23=load('v_meanres23.dat');
p24=load('v_meanres24.dat');
p25=load('v_meanres25.dat');
p26=load('v_meanres26.dat');
p27=load('v_meanres27.dat');
p28=load('v_meanres28.dat');
p29=load('v_meanres29.dat');
p30=load('v_meanres30.dat');
p31=load('v_meanres31.dat');
p32=load('v_meanres32.dat');
p33=load('v_meanres33.dat');
p34=load('v_meanres34.dat');
p35=load('v_meanres35.dat');
p36=load('v_meanres36.dat');
p37=load('v_meanres37.dat');
p38=load('v_meanres38.dat');
p39=load('v_meanres39.dat');
p40=load('v_meanres40.dat');
p41=load('v_meanres41.dat');
p42=load('v_meanres42.dat');
p43=load('v_meanres43.dat');
p44=load('v_meanres44.dat');
p45=load('v_meanres45.dat');
p46=load('v_meanres46.dat');
p47=load('v_meanres47.dat');
p48=load('v_meanres48.dat');
p49=load('v_meanres49.dat');
```

```
p50=load('v_meanres50.dat');
p51=load('v_meanres51.dat');
p52=load('v_meanres52.dat');
p53=load('v_meanres53.dat');
p54=load('v_meanres54.dat');
p55=load('v_meanres55.dat');
p56=load('v_meanres56.dat');
p57=load('v_meanres57.dat');
p58=load('v_meanres58.dat');
p59=load('v_meanres59.dat');
p60=load('v_meanres60.dat');
p61=load('v_meanres61.dat');
p62=load('v_meanres62.dat');
p63=load('v_meanres63.dat');
p64=load('v_meanres64.dat');
p65=load('v_meanres65.dat');
p66=load('v_meanres66.dat');
p67=load('v_meanres67.dat');
p68=load('v_meanres68.dat');
p69=load('v_meanres69.dat');
p70=load('v_meanres70.dat');
p71=load('v_meanres71.dat');
p72=load('v_meanres72.dat');
p73=load('v_meanres73.dat');
p74=load('v_meanres74.dat');
p75=load('v_meanres75.dat');
p76=load('v_meanres76.dat');
p77=load('v_meanres77.dat');
p78=load('v_meanres78.dat');
p79=load('v_meanres79.dat');
p80=load('v_meanres80.dat');
p81=load('v_meanres81.dat');
p82=load('v_meanres82.dat');
p83=load('v_meanres83.dat');
p84=load('v_meanres84.dat');
p85=load('v_meanres85.dat');
p86=load('v_meanres86.dat');
p87=load('v_meanres87.dat');
p88=load('v_meanres88.dat');

pz1=[p1;p2;p3;p4;p5;p6;p7;p8;p9;p10];
psize1=size(pz1)
pz2=[p11;p12;p13;p14;p15;p16;p17;p18;p19;p20];
psize2=size(pz2)
pz3=[p21;p22;p23;p24;p25;p26;p27;p28;p29;p30];
psize3=size(pz3)
pz4=[p31;p32;p33;p34;p35;p36;p37;p38;p39;p40];
psize4=size(pz4)
pz5=[p41;p42;p43;p44;p45;p46;p47;p48;p49;p50];
psize5=size(pz5)
pz6=[p51;p52;p53;p54;p55;p56;p57;p58;p59;p60];
psize6=size(pz6)
pz7=[p61;p62;p63;p64;p65;p66;p67;p68;p69;p70];
psize7=size(pz7)
pz8=[p71;p72;p73;p74;p75;p76;p77;p78;p79;p80];
psize8=size(pz8)
pz9=[p81;p82;p83;p84;p85;p86;p87;p88];
psize9=size(pz9)
Pz=[pz1;pz2;pz3;pz4;pz5;pz6;pz7;pz8;pz9];
psize=size(Pz)
Zn=Pz';
```

```
Z=Pz(:,1);
zz=Pz(:,2);
zzz=Pz(:,3)
z8=zzz(88)
for n=1:88;
         if n<=11
            n
            theta=0;
         end
         if (n>11) &(n<=22);
            n
            theta=(pi/8);
         end
         if (n>22) &(n<=33);
            n
   theta=(pi/4);
 end

if (n>33) &(n<=44);
            n
   theta=(3*pi/8);
end
  if (n>44) &(n<=55);
            n
   theta=(pi/2);
 end
   if (n>55) &(n<=66);
            n
   theta=(5*pi/8);
end
  if (n>66) &(n<=77);
            n
   theta=(6*pi/8);
end

if n>77;
    n
   theta=(7*pi/8);
end

X(n,1)=r(n)*cos(theta);
X(n,2)=r(n)*sin(theta);
X(n,3)=Z(n);
X(n,4)=zz(n);
X(n,5)=zzz(n);
X1(n)=X(n,1);
Y1(n)=X(n,2);
Z1(n)=X(n,3);
ZZ1(n)=X(n,4);
ZZZ1(n)=X(n,5);
%next n;
X1;
end

for ii=1:36;
   jj=ii-1;
   xo(ii)=0.5*cos(jj);
   yo(ii)=0.5*sin(jj);
   zo(ii)=0;
end
xx1=[X1,xo];
```

```
yy1=[Y1,yo];
Zx1=[Z1,zo];
Zy1=[ZZ1,zo];
Zz1=[ZZZ1,zo];
%zz2=[Zv',zo];
%xx1=[X1];
%yy1=[Y1];
%zz1=[Z1];
xa=-0.5:.002:.5;
ya=-0.5:.002:.5;
l1=length(xx1)
l2=length(yy1)
l3=length(Zx1)
[xa,ya]=meshgrid(xa,ya);
[xa,ya,alpha]=griddata(xx1,yy1,Zx1,xa,ya,'cubic');
[xa,ya,alpha1]=griddata(xx1,yy1,Zy1,xa,ya,'cubic');
[xa,ya,alpha2]=griddata(xx1,yy1,Zz1,xa,ya,'cubic');

mesh(xa,ya,alpha2);
%plot3(xa,ya,alpha1);

xlabel('X-coordinate(r/D)');
ylabel('Y-coordinate(r/D)');
zlabel ('Vz');

save xy.dat X  -ascii -double
```

listing of volint88new.m

```
%3d graphics
function[]=volint88new()
r=[0.475;.380;.285;0.190;0.095;0.;-0.095;-0.190;-0.285;-0.380;-0.475;
   0.475;.380;.285;0.190;0.095;0.;-0.095;-0.190;-0.285;-0.380;-0.475;
   0.475;.380;.285;0.190;0.095;0.;-0.095;-0.190;-0.285;-0.380;-0.475;
   0.475;.380;.285;0.190;0.095;0.;-0.095;-0.190;-0.285;-0.380;-0.475;
   0.475;.380;.285;0.190;0.095;0.;-0.095;-0.190;-0.285;-0.380;-0.475;
   0.475;.380;.285;0.190;0.095;0.;-0.095;-0.190;-0.285;-0.380;-0.475;
   0.475;.380;.285;0.190;0.095;0.;-0.095;-0.190;-0.285;-0.380;-0.475;
   0.475;.380;.285;0.190;0.095;0.;-0.095;-0.190;-0.285;-0.380;-
0.475;];
p1=load('alphres1.dat');
p2=load('alphres2.dat');
p3=load('alphres3.dat');
p4=load('alphres4.dat');
p5=load('alphres5.dat');
p6=load('alphres6.dat');
p7=load('alphres7.dat');
p8=load('alphres8.dat');
p9=load('alphres9.dat');
p10=load('alphres10.dat');
p11=load('alphres11.dat');
p12=load('alphres12.dat');
p13=load('alphres13.dat');
p14=load('alphres14.dat');
p15=load('alphres15.dat');
p16=load('alphres16.dat');
p17=load('alphres17.dat');
p18=load('alphres18.dat');
p19=load('alphres19.dat');
p20=load('alphres20.dat');
p21=load('alphres21.dat');
p22=load('alphres22.dat');
p23=load('alphres23.dat');
p24=load('alphres24.dat');
p25=load('alphres25.dat');
p26=load('alphres26.dat');
p27=load('alphres27.dat');
p28=load('alphres28.dat');
p29=load('alphres29.dat');
p30=load('alphres30.dat');
p31=load('alphres31.dat');
p32=load('alphres32.dat');
p33=load('alphres33.dat');
p34=load('alphres34.dat');
p35=load('alphres35.dat');
p36=load('alphres36.dat');
p37=load('alphres37.dat');
p38=load('alphres38.dat');
p39=load('alphres39.dat');
p40=load('alphres40.dat');
p41=load('alphres41.dat');
p42=load('alphres42.dat');
p43=load('alphres43.dat');
p44=load('alphres44.dat');
p45=load('alphres45.dat');
p46=load('alphres46.dat');
p47=load('alphres47.dat');
p48=load('alphres48.dat');
```

```
p49=load('alphres49.dat');
p50=load('alphres50.dat');
p51=load('alphres51.dat');
p52=load('alphres52.dat');
p53=load('alphres53.dat');
p54=load('alphres54.dat');
p55=load('alphres55.dat');
p56=load('alphres56.dat');
p57=load('alphres57.dat');
p58=load('alphres58.dat');
p59=load('alphres59.dat');
p60=load('alphres60.dat');
p61=load('alphres61.dat');
p62=load('alphres62.dat');
p63=load('alphres63.dat');
p64=load('alphres64.dat');
p65=load('alphres65.dat');
p66=load('alphres66.dat');
p67=load('alphres67.dat');
p68=load('alphres68.dat');
p69=load('alphres69.dat');
p70=load('alphres70.dat');
p71=load('alphres71.dat');
p72=load('alphres72.dat');
p73=load('alphres73.dat');
p74=load('alphres74.dat');
p75=load('alphres75.dat');
p76=load('alphres76.dat');
p77=load('alphres77.dat');
p78=load('alphres78.dat');
p79=load('alphres79.dat');
p80=load('alphres80.dat');
p81=load('alphres81.dat');
p82=load('alphres82.dat');
p83=load('alphres83.dat');
p84=load('alphres84.dat');
p85=load('alphres85.dat');
p86=load('alphres86.dat');
p87=load('alphres87.dat');
p88=load('alphres88.dat');
pz1=[p1,p2,p3,p4,p5,p6,p7,p8,p9,p10];
pz2=[p11,p12,p13,p14,p15,p16,p17,p18,p19,p20];
pz3=[p21,p22,p23,p24,p25,p26,p27,p28,p29,p30];
pz4=[p31,p32,p33,p34,p35,p36,p37,p38,p39,p40];
pz5=[p41,p42,p43,p44,p45,p46,p47,p48,p49,p50];
pz6=[p51,p52,p53,p54,p55,p56,p57,p58,p59,p60];
pz7=[p61,p62,p63,p64,p65,p66,p67,p68,p69,p70];
pz8=[p71,p72,p73,p74,p75,p76,p77,p78,p79,p80];
pz9=[p81,p82,p83,p84,p85,p86,p87,p88];
Pz=[pz1,pz2,pz3,pz4,pz5,pz6,pz7,pz8,pz9];
Zn=Pz';
z=Zn(:,2);
%ZZ1=Zn(:,4);
pp1=load('v_meanres1.dat');
pp2=load('v_meanres2.dat');
pp3=load('v_meanres3.dat');
pp4=load('v_meanres4.dat');
pp5=load('v_meanres5.dat');
pp6=load('v_meanres6.dat');
pp7=load('v_meanres7.dat');
pp8=load('v_meanres8.dat');
```

```
pp9=load('v_meanres9.dat');
pp10=load('v_meanres10.dat');
pp11=load('v_meanres11.dat');
pp12=load('v_meanres12.dat');
pp13=load('v_meanres13.dat');
pp14=load('v_meanres14.dat');
pp15=load('v_meanres15.dat');
pp16=load('v_meanres16.dat');
pp17=load('v_meanres17.dat');
pp18=load('v_meanres18.dat');
pp19=load('v_meanres19.dat');
pp20=load('v_meanres20.dat');
pp21=load('v_meanres21.dat');
pp22=load('v_meanres22.dat');
pp23=load('v_meanres23.dat');
pp24=load('v_meanres24.dat');
pp25=load('v_meanres25.dat');
pp26=load('v_meanres26.dat');
pp27=load('v_meanres27.dat');
pp28=load('v_meanres28.dat');
pp29=load('v_meanres29.dat');
pp30=load('v_meanres30.dat');
pp31=load('v_meanres31.dat');
pp32=load('v_meanres32.dat');
pp33=load('v_meanres33.dat');
pp34=load('v_meanres34.dat');
pp35=load('v_meanres35.dat');
pp36=load('v_meanres36.dat');
pp37=load('v_meanres37.dat');
pp38=load('v_meanres38.dat');
pp39=load('v_meanres39.dat');
pp40=load('v_meanres40.dat');
pp41=load('v_meanres41.dat');
pp42=load('v_meanres42.dat');
pp43=load('v_meanres43.dat');
pp44=load('v_meanres44.dat');
pp45=load('v_meanres45.dat');
pp46=load('v_meanres46.dat');
pp47=load('v_meanres47.dat');
pp48=load('v_meanres48.dat');
pp49=load('v_meanres49.dat');
pp50=load('v_meanres50.dat');
pp51=load('v_meanres51.dat');
pp52=load('v_meanres52.dat');
pp53=load('v_meanres53.dat');
pp54=load('v_meanres54.dat');
pp55=load('v_meanres55.dat');
pp56=load('v_meanres56.dat');
pp57=load('v_meanres57.dat');
pp58=load('v_meanres58.dat');
pp59=load('v_meanres59.dat');
pp60=load('v_meanres60.dat');
pp61=load('v_meanres61.dat');
pp62=load('v_meanres62.dat');
pp63=load('v_meanres63.dat');
pp64=load('v_meanres64.dat');
pp65=load('v_meanres65.dat');
pp66=load('v_meanres66.dat');
pp67=load('v_meanres67.dat');
pp68=load('v_meanres68.dat');
pp69=load('v_meanres69.dat');
```

```
pp70=load('v_meanres70.dat');
pp71=load('v_meanres71.dat');
pp72=load('v_meanres72.dat');
pp73=load('v_meanres73.dat');
pp74=load('v_meanres74.dat');
pp75=load('v_meanres75.dat');
pp76=load('v_meanres76.dat');
pp77=load('v_meanres77.dat');
pp78=load('v_meanres78.dat');
pp79=load('v_meanres79.dat');
pp80=load('v_meanres80.dat');
pp81=load('v_meanres81.dat');
pp82=load('v_meanres82.dat');
pp83=load('v_meanres83.dat');
pp84=load('v_meanres84.dat');
pp85=load('v_meanres85.dat');
pp86=load('v_meanres86.dat');
pp87=load('v_meanres87.dat');
pp88=load('v_meanres88.dat');
qz1=[pp1;pp2;pp3;pp4;pp5;pp6;pp7;pp8;pp9;pp10];
qz2=[pp11;pp12;pp13;pp14;pp15;pp16;pp17;pp18;pp19;pp20];
qz3=[pp21;pp22;pp23;pp24;pp25;pp26;pp27;pp28;pp29;pp30];
qz4=[pp31;pp32;pp33;pp34;pp35;pp36;pp37;pp38;pp39;pp40];
qz5=[pp41;pp42;pp43;pp44;pp45;pp46;pp47;pp48;pp49;pp50];
qz6=[pp51;pp52;pp53;pp54;pp55;pp56;pp57;pp58;pp59;pp60];
qz7=[pp61;pp62;pp63;pp64;pp65;pp66;pp67;pp68;pp69;pp70];
qz8=[pp71;pp72;pp73;pp74;pp75;pp76;pp77;pp78;pp79;pp80];
qz9=[pp81;pp82;pp83;pp84;pp85;pp86;pp87;pp88];
%qpz=[qz1;qz2,qz3;qz4;qz5;qz6;qz7;qz8;qz9]
qqz=[qz1;qz2;qz3;qz4;qz5;qz6;qz7;qz8;qz9]
pp88
%qzn=qqz';
qz=qqz(:,6)
if qz(1)<=0.1
   qz(1)=(0.0+qz(2))/2
   qz(1)
end
if qz(11)<=0.1
   qz(11)=(0.0+qz(10))/2
end
if qz(12)<=0.1
   qz(12)=(0.0+qz(13))/2
end
if qz(22)<=0.1
   qz(22)=(0.0+qz(21))/2
end
if qz(23)<=0.1
   qz(23)=(0.0+qz(24))/2
end
if qz(33)<=0.1
   qz(33)=(0.0+qz(32))/2
end
if qz(34)<=0.1
   qz(34)=(0.0+qz(35))/2
end
if qz(44)<=0.1
   qz(44)=(0.0+qz(43))/2
end
if qz(45)<=0.1
   qz(45)=(0.0+qz(46))/2
end
```

```
if qz(55)<=0.1
   qz(55)=(0.0+qz(54))/2
end
if qz(56)<=0.1
   qz(56)=(0.0+qz(57))/2
end
if qz(66)<=0.1
   qz(66)=(0.0+qz(65))/2
end
if qz(67)<=0.1
   qz(67)=(0.0+qz(68))/2
end
if qz(77)<=0.1
   qz(77)=(0.0+qz(76))/2
end
if qz(78)<=0.1
   qz(78)=(0.0+qz(79))/2
end
if qz(88)<=0.1
   qz(88)=(0.0+qz(87))/2
end
qz
fq=z.*qz;
%q=ZZ1.*qz;
l=fq(2);
a6=pi*(.0038*.0038);
a5=pi*(.0038+.0076)*(.0038+.0076)-a6;
a4=pi*(.0038+(2*.0076))*(.0038+(2*.0076))-a6-a5;
a3=pi*(.0038+(3*.0076))*(.0038+(3*.0076))-a6-a5-a4;
a2=pi*(.0038+(4*.0076))*(.0038+(4*.0076))-a6-a5-a4-a3;
a1=pi*((.040*.040)-((.040-.002-.0038)*(.040-.002-.0038)));

v11=(z(1)+z(12)+z(23)+z(34)+z(45)+z(56)+z(67)+z(78));
v12=(z(11)+z(22)+z(33)+z(44)+z(55)+z(66)+z(77)+z(88));
v21=(z(2)+z(13)+z(24)+z(35)+z(46)+z(57)+z(68)+z(79));
v22=(z(10)+z(21)+z(32)+z(43)+z(54)+z(65)+z(76)+z(87));
v31=(z(3)+z(14)+z(25)+z(36)+z(47)+z(58)+z(69)+z(80));
v32=(z(9)+z(20)+z(31)+z(42)+z(53)+z(64)+z(75)+z(86));
v41=(z(4)+z(15)+z(26)+z(37)+z(48)+z(59)+z(70)+z(81));
v42=(z(8)+z(19)+z(30)+z(41)+z(52)+z(63)+z(74)+z(85));
v51=(z(5)+z(16)+z(27)+z(38)+z(49)+z(60)+z(71)+z(82));
v52=(z(7)+z(18)+z(29)+z(40)+z(51)+z(62)+z(73)+z(84));
v6=(z(6)+z(17)+z(28)+z(39)+z(50)+z(61)+z(72)+z(83))/8;
v1=(v11+v12)/16;
v2=(v21+v22)/16;
v3=(v31+v32)/16;
v4=(v41+v42)/16;
v5=(v51+v52)/16;
av=(a1*v1)+(a2*v2)+(a3*v3)+(a4*v4)+(a5*v5)+(a6*v6);
aa=pi*.040*.040;
a=a1+a2+a3+a4+a5+a6;
volumefraction=av/aa
%vol=av';
%volume1=vol(:,2);
%volume2=vol(:,4);
volumefraction;
f11=(fq(1)+fq(12)+fq(23)+fq(34)+fq(45)+fq(56)+fq(67)+fq(78));
f12=(fq(11)+fq(22)+fq(33)+fq(44)+fq(55)+fq(66)+fq(77)+fq(88));
f21=(fq(2)+fq(13)+fq(24)+fq(35)+fq(46)+fq(57)+fq(68)+fq(79));
f22=(fq(10)+fq(21)+fq(32)+fq(43)+fq(54)+fq(65)+fq(76)+fq(87));
f31=(fq(3)+fq(14)+fq(25)+fq(36)+fq(47)+fq(58)+fq(69)+fq(80));
```

```
f32=(fq(9)+fq(20)+fq(31)+fq(42)+fq(53)+fq(64)+fq(75)+fq(86));
f41=(fq(4)+fq(15)+fq(26)+fq(37)+fq(48)+fq(59)+fq(70)+fq(81));
f42=(fq(8)+fq(19)+fq(30)+fq(41)+fq(52)+fq(63)+fq(74)+fq(85));
f51=(fq(5)+fq(16)+fq(27)+fq(38)+fq(49)+fq(60)+fq(71)+fq(82));
f52=(fq(7)+fq(18)+fq(29)+fq(40)+fq(51)+fq(62)+fq(73)+fq(84));
f6=(fq(6)+fq(17)+fq(28)+fq(39)+fq(50)+fq(61)+fq(72)+fq(83));
f1=(f11+f12)/16;
f2=(f21+f22)/16;
f3=(f31+f32)/16;
f4=(f41+f42)/16;
f5=(f51+f52)/16;
ff6=f6/8;
fav=(a1*f1)+(a2*f2)+(a3*f3)+(a4*f4)+(a5*f5)+(a6*ff6);
fav
av
mean_gas_velocity=fav/av
%'mixturevelocity(front)'
superficial_gas_velocity=fav/(pi*0.04*0.04)
%'gasvelocity(front)'
volume_fraction_front=volumefraction
```

APENDIX III

Code for calculating the reference data. Two files have been used. Below are the code lines of each of them.

Listing of reference.m

```
function[]=reference()


alpha1=0;
vm1=0;
vws1=0;
vgs1=0;
M=load('chec01.dat');
[alpha,vm,vws,vgs]=check(M);
alpha2=alpha1+alpha;
vm2=vm1+vm;
vws2=vws1+vws;
vgs2=vgs1+vgs;
M=load('chec02.dat');
[alpha,vm,vws,vgs]=check(M);
alpha3=alpha2+alpha;
vm3=vm2+vm;
vws3=vws2+vws;
vgs3=vgs2+vgs;
M=load('chec03.dat');
[alpha,vm,vws,vgs]=check(M);
alpha4=alpha3+alpha;
vm4=vm3+vm;
vws4=vws3+vws;
vgs4=vgs3+vgs;
M=load('chec04.dat');
[alpha,vm,vws,vgs]=check(M);
alpha5=alpha4+alpha;
vm5=vm4+vm;
vws5=vws4+vws;
vgs5=vgs4+vgs;
M=load('chec05.dat');
[alpha,vm,vws,vgs]=check(M);
alpha6=alpha5+alpha;
vm6=vm5+vm;
vws6=vws5+vws;
vgs6=vgs5+vgs;

M=load('chec06.dat');
[alpha,vm,vws,vgs]=check(M);
alpha7=alpha6+alpha;
vm7=vm6+vm;
vws7=vws6+vws;
vgs7=vgs6+vgs;
M=load('chec07.dat');
[alpha,vm,vws,vgs]=check(M);
alpha8=alpha7+alpha;
vm8=vm7+vm;
vws8=vws7+vws;
vgs8=vgs7+vgs;
M=load('chec08.dat');
```

```
[alpha,vm,vws,vgs]=check(M);
alpha9=alpha8+alpha;
vm9=vm8+vm;
vws9=vws8+vws;
vgs9=vgs8+vgs;
M=load('chec09.dat');
[alpha,vm,vws,vgs]=check(M);
alpha10=alpha9+alpha;
vm10=vm9+vm;
vws10=vws9+vws;
vgs10=vgs9+vgs;

volume_fraction=alpha10/9
mixture_velocity=vm10/9
superficial_gas_velocity=vgs10/9
superficial_water_velocity=vws10/9
mean_gas_velocity=superficial_gas_velocity/volume_fraction


function[alpha,vm,vws,vgs]=check(M);


format long;      %use 15 digit precision



A=M(:,1);         %load data from front sensor
B=M(:,2);         %load data from rear sensor
p3=M(:,3);
p4=M(:,4);
dp2=mean(A);
p2=1+(mean(B)*10);
t2=273.15+(mean(p3)*10);
Qg1=mean(p4)*40;
e=M(:,5);
m1=length(e);
no=0.0;
for nn=1:m1-1
   mult=e(nn)*e(nn+1);
   if mult < 0.0;
      no=no+1;
   end
end
Qt1=no/(30*2);

p1=1.00996;
t1=273.15;

dp1=1.01168;   %insert pressuredrop when no water flows in voltage


Qt2=Qt1*.0468/3600;
%'qt2'
Qg2=p1*t2*Qg1/(p2*t1*60000.0);
%'qg2'
area=0.00502;
Qt=Qt2+Qg2;
vm=Qt/area;
%'vm'
vws=Qt2/area;
%'vws'
```

```
vgs=Qg2/area;
%'vgs'
f=0.013;
dpt=(dp2-dp1)*1000*9.9696/4.;
wpt=2.*1000.*0.77*0.013*(vm*vm)/0.08;
alpha=(wpt-dpt)/(1000.*9.81*0.77)%the equation for normal water like
characteristic
%'alpha'
%alpha=(wpt+dpt)/(1000.*9.81*0.77);%the equation for high volume
fraction to make hp at top
%'alpha'
```

When a upstream pressure is less than down stream pressure

```
function[alpha,vm,vws,vgs]=check(M);


format long;      %use 15 digit precision



A=M(:,1);         %load data from front sensor
B=M(:,2);         %load data from rear sensor
p3=M(:,3);
p4=M(:,4);
dp2=mean(A);
p2=1+(mean(B)*10);
t2=273.15+(mean(p3)*10);
Qg1=mean(p4)*40;
e=M(:,5);
m1=length(e);
no=0.0;
for nn=1:m1-1
   mult=e(nn)*e(nn+1);
   if mult < 0.0;
      no=no+1;
   end
end
Qt1=no/(30*2);

p1=1.00996;
t1=273.15;

dp1=1.01168;   %insert pressuredrop when no water flows in voltage


Qt2=Qt1*.0468/3600;
%'qt2'
Qg2=p1*t2*Qg1/(p2*t1*60000.0);
%'qg2'
area=0.00502;
Qt=Qt2+Qg2;
vm=Qt/area;
%'vm'
vws=Qt2/area;
%'vws'
vgs=Qg2/area;
%'vgs'
f=0.013;
dpt=(dp2-dp1)*1000*9.9696/4.;
wpt=2.*1000.*0.77*0.013*(vm*vm)/0.08;
```

```
%alpha=(wpt-dpt)/(1000.*9.81*0.77)%the equation for normal water like
characteristic
%'alpha'
alpha=(wpt+dpt)/(1000.*9.81*0.77);%the equation for high volume
fraction to make hp at top
```